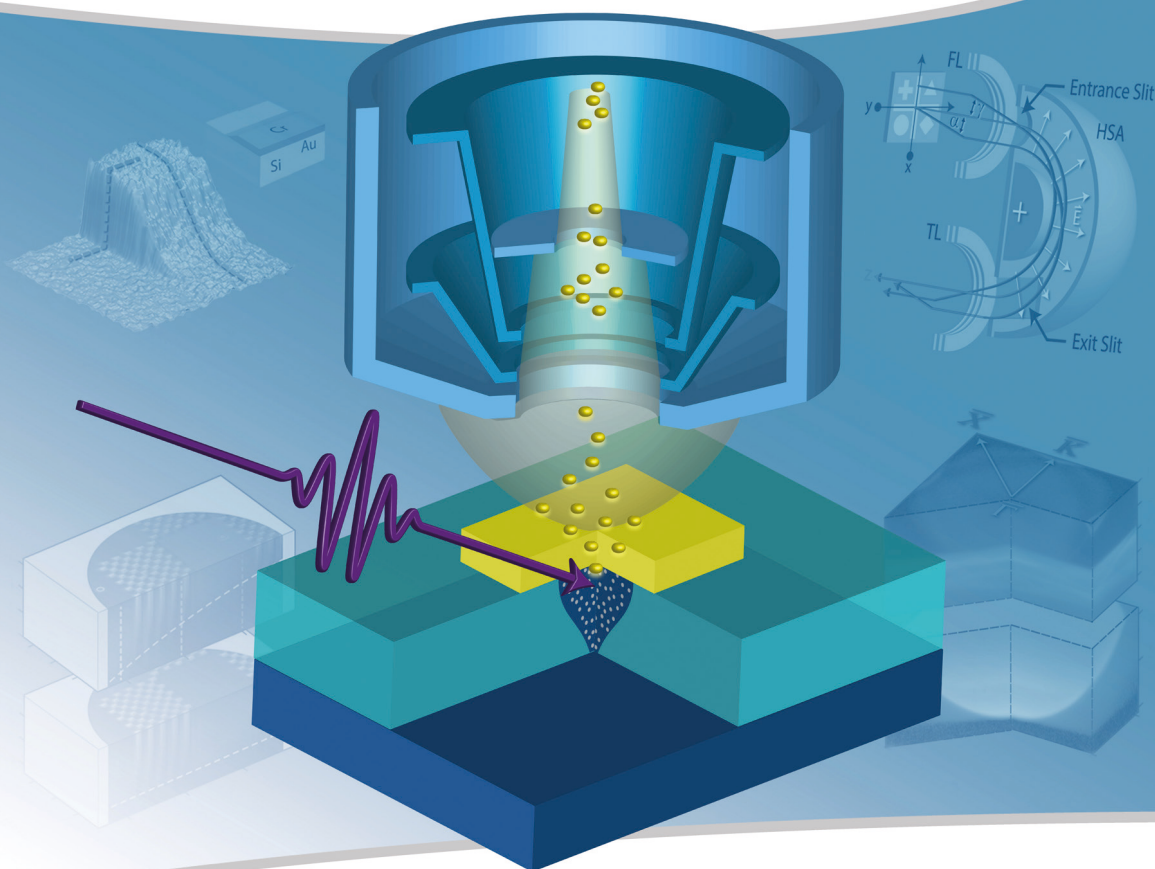


Bulk and surface sensitive energy-filtered photoemission microscopy using synchrotron radiation for the study of resistive switching memories

Marten Christopher Patt



Forschungszentrum Jülich GmbH
Peter Grünberg Institute (PGI)
Electronic Properties (PGI-6)

Bulk and surface sensitive energy-filtered photoemission microscopy using synchrotron radiation for the study of resistive switching memories

Marten Christopher Patt

Schriften des Forschungszentrums Jülich
Reihe Schlüsseltechnologien / Key Technologies

Band / Volume 122

ISSN 1866-1807

ISBN 978-3-95806-130-9

Bibliographic information published by the Deutsche Nationalbibliothek.
The Deutsche Nationalbibliothek lists this publication in the Deutsche
Nationalbibliografie; detailed bibliographic data are available in the
Internet at <http://dnb.d-nb.de>.

Publisher and
Distributor: Forschungszentrum Jülich GmbH
Zentralbibliothek
52425 Jülich
Tel: +49 2461 61-5368
Fax: +49 2461 61-6103
Email: zb-publikation@fz-juelich.de
www.fz-juelich.de/zb

Cover Design: Grafische Medien, Forschungszentrum Jülich GmbH

Printer: Grafische Medien, Forschungszentrum Jülich GmbH

Copyright: Forschungszentrum Jülich 2016

Schriften des Forschungszentrums Jülich
Reihe Schlüsseltechnologien / Key Technologies, Band / Volume 122

D 464 (Diss., Duisburg, Univ., 2016)

ISSN 1866-1807
ISBN 978-3-95806-130-9

The complete volume is freely available on the Internet on the Jülicher Open Access Server (JuSER)
at www.fz-juelich.de/zb/openaccess.



This is an Open Access publication distributed under the terms of the [Creative Commons Attribution License 4.0](https://creativecommons.org/licenses/by/4.0/),
which permits unrestricted use, distribution, and reproduction in any medium, provided the original work is properly cited.

Zusammenfassung

In dieser Arbeit wird die Anwendbarkeit von energiegefilterter Photoemissionsmikroskopie zur Analyse zukünftiger elektronischer Bausteine für die Informationstechnologie untersucht. Die langfristige Perspektive ist dabei die Untersuchung von Schaldynamiken in nichtflüchtigen widerstandsbasierten Speichern auf Oxid-Basis. Diese werden als eine vielversprechende Komponente in der Entwicklung leistungsfähigerer Prozessoren oder Speicher gesehen, seit die Fortschritte der klassischen Silizium oder Magnetismus basierten Technologien ihre physikalischen Grenzen erreichen. Dennoch hängen die Effizienz und Funktionalität geeigneter Materialsysteme stark von Qualität und den Eigenschaften ihrer Oberflächen und Grenzflächen ab. Die energiegefilterte Photoemissionsmikroskopie ermöglicht eine ortsaufgelöste chemische Studie dieser Systeme, insbesondere wenn sie mit hoch-brillanten Synchrotron Lichtquellen kombiniert wird. Die hohen Photonenintensitäten werden notwendig, wenn charakteristische kernnahe Elektronenzustände mit hoher Orts- und Energieauflösung untersucht werden sollen. Studien an auf Valenzbandänderungen in Strontium-Titanat basierenden Metall-Isolator-Metall Bauelementen, welche ein Modellsystem für widerstandsbasierte Speicher darstellen, haben gezeigt, dass Ortsauflösungen um 100 nm und Energieauflösungen um 100 meV benötigt werden, um die relevanten Änderungen bei jedem Schaltzyklus sichtbar zu machen. Daher wird in dieser Arbeit ein großer Wert auf die Bestimmung der dafür benötigten experimentellen Parameter gelegt.

Eine weitere Herausforderung stellt die Untersuchung der funktionalen Schichten solcher Bauelemente durch ihre Top-Elektrode hindurch dar. Der Einsatz harter Röntgenstrahlung ermöglicht die Verwendung von Photoelektronen mit hoher kinetischer Energie, die eine bis zu zehnfach größere Informationstiefe bieten. In dieser Arbeit wird zum ersten Mal gezeigt, mit welcher Ortsauflösung chemisch unterschiedliche Regionen durch eine bis zu 15 nm dicke Deckschicht abgebildet werden können. Mikroskopierelevante Themen wie Transmission und Aberrationen werden mit Hinblick auf die Verwendung hoch energetischen Elektronen diskutiert und durch Berechnungen veranschaulicht.

Abstract

In this thesis the applicability of energy-filtered photoemission microscopy for the analysis of future electronic devices for the information technology is studied. The long-term perspective is the analysis of the switching-dynamics in oxide-based non-volatile resistive memories. These are regarded as promising new components in the development of more powerful processing units or storage devices, since the improvements of the classical silicon or magnetism-based technologies are approaching their physical limits. Nevertheless, the efficiency and functionality of suitable material systems strongly depend on the quality and properties of their surfaces and interfaces. The energy-filtered photoemission microscopy provides a spatially resolved chemical study of these systems, especially in combination with high brilliance synchrotron light sources. The high photon intensities are needed, if characteristic core levels of a specimen should be analyzed with a high spatial and energy resolution. Studies of metal-insulator-metal structures based on the valence change effect in strontium titanate, which is a model system for resistive switching devices, showed that the spatial resolution needs to be in the 100 nm regime and the energy-resolution in the 100 meV regime to resolve the relevant changes in a switching cycle. Therefore, a big focus of this thesis lies on the determination of the relevant experimental parameters which are needed to fulfill these requirements.

Another challenging task is to study the functional layer of such a device through a capping electrode. Hard X-ray synchrotron radiation allows the use of high kinetic energy photoelectrons with an up to ten times larger information depth. In this thesis it is shown for the first time, which spatial resolution can be achieved when detecting chemically different regions through cover layer thicknesses of up to 15 nm. Microscope-relevant topics like transmission and aberration effects are discussed with respect to the use of high kinetic electrons and illustrated by calculations.

Contents

1. Introduction	1
2. Fundamental aspects of energy-filtered photoemission microscopy	7
2.1. Photoemission spectroscopy	10
2.1.1. Penetration of the incoming photons and photo-ionization cross section	13
2.1.2. The photo-excitation process	14
2.1.3. Photoelectron transport to the surface and inelastic mean free path	17
2.1.4. Transmission through the surface and momentum conservation	19
2.2. Angular and momentum resolved photoemission	21
2.3. X-ray absorption spectroscopy	23
2.4. Work function	24
2.4.1. Work function and contact potential	25
2.4.2. Influence of an accelerating field	26
2.5. Conclusions	28
3. Instrumental aspects	29
3.1. Instrumental aspects of the NanoESCA microscope	30
3.1.1. The objective	30
3.1.2. The Projection column	32
3.1.3. The energy filter	33
3.1.4. The image detection	37
3.1.5. The channeltron detection	39
3.1.6. Photoemission microscopy and momentum microscopy	39
3.2. Light sources	41
3.2.1. UV excitation	41
3.2.2. Soft X-ray and hard x-ray synchrotron sources	43
3.3. Conclusions	47

4. Evaluation methods	49
4.1. Work function analysis	50
4.1.1. About the nature of the work function edge	50
4.1.2. Fit model for the work function edge	52
4.1.3. The fitting procedure	55
4.1.4. Applicability and robustness of the procedure	55
4.2. Principal Component Analysis	56
4.3. Conclusions	58
5. Objective lens calculations	59
5.1. Basic calculations	59
5.1.1. Electron kinetics between sample and extractor	60
5.1.2. Conversion from the electron emission angle α to the microscope entrance angle α'	64
5.1.3. Estimation of relativistic corrections	65
5.2. Acceptance angle of the objective lens	66
5.2.1. Relation between contrast aperture and energy analyzer entrance slit	68
5.3. Transmission of the objective lens	70
5.4. Spatial resolution of the objective lens	73
5.4.1. Spherical aberration of the accelerating field	75
5.4.2. Chromatic aberration of the acceleration field	78
5.4.3. Aberrations of the objective lens	79
5.4.4. Diffraction at the contrast aperture	81
5.4.5. The total aberration of the objective	84
5.5. Conclusions	85
6. Non - Isochromaticity of the Energy Filter	89
6.1. Non-Isochromaticity analysis and correction	90
6.1.1. Impact of the energy shift on the intensity distribution of a photoemission image	90
6.1.2. Determination of the energy shift by a work function analysis	92
6.1.3. Energy shift correction of the image spectrum	94
6.2. Energy filter calculations	96
6.2.1. The set of transfer functions to calculate the electron trajectories	96
6.2.2. Calculating the electron trajectories passing the filter	97
6.2.3. Analysis of the calculated trajectories	100

6.2.4.	Simulation of energy-filtered PEEM images	102
6.2.5.	The footprint of the non-isochromaticity in energy-filtered images	103
6.3.	Calibration of the intermediate image plane	107
6.3.1.	Magnification of the intermediate image plane	108
6.3.2.	Non-Isochromaticity dependence on the projective magnification	109
6.4.	Experimental characterization of the Non-isochromaticity	114
6.4.1.	Effects of the analyzer pass-energy and slit configuration	115
6.4.2.	An interpretation of the energy-shift dependencies	119
6.5.	A generalized fit model for the intensity shift	123
6.6.	Conclusions	124
7.	Instrumental characterization measurements	127
7.1.	Detection of the photoelectrons	127
7.1.1.	Flat field, Dark field and Image-Correction in the analogue imaging mode	128
7.1.2.	Image intensity and its dependency on the MCP voltage	129
7.1.3.	Single Event Counting	133
7.2.	Momentum microscopy and k-Calibration	136
7.2.1.	Calibration of the k_{\parallel} scale with the photoemission horizon	141
7.2.2.	Energy resolution	142
7.2.3.	Relation between the contrast aperture and the momentum space	144
7.3.	Spatial resolution in spectro-microscopy	146
7.3.1.	A test sample for spatial resolution	146
7.3.2.	Microspectroscopy and chemical analysis	150
7.4.	Conclusions	154
8.	Hard x-ray photoemission electron microscopy	157
8.1.	Preliminary aspects of HAXPEEM experiments	157
8.1.1.	Experimental peculiarities	157
8.1.2.	Sample design	159
8.2.	Work function analysis with high kinetic photoelectrons	160
8.3.	Space-Charge influence on the spatial resolution	167
8.4.	Bulk sensitive imaging and chemical imaging	171
8.5.	Accessing buried interfaces	176
8.5.1.	EAL determination	178
8.5.2.	Lateral Resolution and Probing Depth	183
8.6.	Conclusions	185

9. Outlook: Towards time-resolved device analysis	187
9.1. First HAXPEEM results on STO	188
9.2. Towards time resolved studies	190
10. Summary	195
A. Often used equations	199
A.1. Gauss/Step-Function	199
A.2. Spatial Calibration	199
A.3. Spectral fits with a Voigt profile	201
A.4. Energy resolution with a Fermi/Gauss convolution	201
B. Complementary objective lens calculations	203
B.1. Conversion between start angle and entrance angle	203
B.2. Maximum accepted emission angle	204
Danksagungen	207
Bibliography	224
List of figures and tables	227
List of own publications	231
Curriculum Vitae	237
List of Abbreviations	242
Index	247

1. Introduction

We live in a time of stunning technological improvements, especially in the field of information technology. An exemplary development which unifies the progress of the last decade in a broad field of technology is the *smartphone*. Its steady improvements are very present to and in the urgent interest of a huge amount of customers, which makes it a driving force of technological development. This small pocket device integrates in a very limited space a computing power which easily exceeds that of any 10 year old personal computer. The resolution of its screen, especially the pixel density, exceeds that of actual televisions. Enormous amounts of data are stored on tiny flash-storages. And despite of all this technological potential its power consumption is small enough that it can be run by a light battery for several days.

For each field of the mentioned technologies (computing power, human interface device, data storage, energy storage), several other examples can be named. Especially an efficient energy storage and production will be of growing interest for the next decades, if renewable and clean electric energy should replace the fossil energy sources. The common aspect for an improvement of efficiency in all fields often is a development to smaller device scales. For microprocessors, for example, this trend was described by G. Moore [Moo98] and R. Dennard [DGR⁺74] and is nowadays known as *Moore's law*. The simplified essence of this prediction was that the computing performance would double each 18 months, which could be reached for some time by shrinking the size and increasing the number of the transistors on a chip [Sti15]. In the last decade, CPUs or GPUs, for example, made a big step in efficiency by reducing the scale of transistor-elements in the fabrication process of silicon-based semiconductor units from 90 nm (2004) to 14 nm (2014). However, the traditional *MOSFET* scaling already ran into physical limits because of quantum mechanical effects like the exponential increase of gate oxide leakage. The increase of the CPU operating frequency stopped at around 4 GHz. An improvement of performance then is only possible by introducing new materials and device structures (strained silicon, high-k metal gate, multi-gate devices) [Boh11]. The future of such develop-

ment is proposed to lie even in more exotic devices like *carbon nanotubes* [DDS95], *spin-based logic* [DDCS07] or *memristors*. The latter means a device the resistance of which depends on the amount of current which previously flowed through it. Its conductive state can be changed by electrical pulses between a low resistive (on) and a high resistive (off) state which offers the on/off distinction which is needed to store digital data. Additionally, this state persists if the current is switched off, which means it is a nonvolatile memory. Such an device was predicted in 1971 [Chu71] and firstly build in 2007 [SSSW08]. A *memristor* can be also seen as an artificial synapse which would provide more *brain-like* abilities to future computing devices (complex learning, adaptive and spontaneous behaviour)[PDV10]. Especially the combination with volatile memory could dramatically increase the efficiency of such processors [Pav15].

A variety of materials is known, called *resistive switching materials*, which could serve in a *memristor* [Chu11]. The devices are in general build as a capacitor-like *MIM structures* (metal, insulator, metal), where the resistive material is deposited between two electron conductors. Also the different physical phenomena which lead to a non-volatile resistive switching memory effect are numerous [WDSS09], including *phase change*-, *thermochemical*- and *valency change*- memory effects. Among the latter, strontium titanate (SrTiO_3 , STO) is a typical model system. Here, the valence change memory effect is based on the movement of *oxygen vacancies*. These vacancies create two free electrons in the Ti conduction band which lower the resistance of the material. If the vacancies connect the electrodes of the MIM cell, the cell is set to its low resistive state. This connection, mostly regarded as thin filaments along highly defective areas [SLD⁺12], can be established by applying a voltage and interrupted by applying a voltage of opposite sign. While this general mechanism is known, many unsolved questions remain, especially regarding its applicability as a device: How big are the filaments and how small could a typical memory cell be? What is the exact (stoichiometric) difference between the on and the off state? Do filaments completely vanish when switching to the off-state or is the connection only interrupted near one of the electrodes? What is the dynamic of the switching process? Does the filament forming appear at equal positions in the active layer with each layer or randomly?

Finding answers to these questions is the general motivation of this thesis. The investigation of the relevant mechanisms defining the functionality of such devices is the key to improve them. At the same time, the complexity of the devices and its processes ask for powerful and flexible analytic methods. One of the most promising methods which is able to take into account a huge amount of the relevant factors is

the *energy-filtered photoemission microscopy*. It combines a chemical analysis of the stoichiometry of the devices and the relevant electronic structure with a spatially resolved analysis. This way, changes in an operation step of this device can be assigned to the location in the device where this change happened. The energy-filtered photoemission microscopy unifies two technical approaches of the last decades, which is the development of *microscopy with photo-excited electrons* (PEEM) and the *spectroscopy of photoelectrons* (PES). The first issue goes back to E. Brüche in the early 1930s [Brü33] and was developed until today [Bau12] with respect to an improved spatial resolution. A lot of theoretical and instrumental design work was done in the 1980s by G.F. Rempfer [RNG80, RG89, RSHG91]. The latest improvements in this field were achieved by introducing an *electrostatic electron mirror* to correct *spherical and chromatic aberrations* of the microscope which lead to a calculated resolution limit of 4 nm [THE⁺10]. Only 34 nm were reported so far for this instrument [GDN⁺15] in combination with synchrotron radiation. A limiting factor for the spatial resolution seems to be space charge effects[Bau12], which can appear directly above the sample or in the instrument [LMNB11, NJP⁺09, PWW⁺14]. An analysis of these effects was recently published in [SMT⁺15] and may lead to improvements in the future.

For the imaging of sample surfaces a couple of contrast mechanisms can be used in PEEM (topological contrast, work function contrast, chemical contrast, magnetic contrast) [SS02]. In combination with *synchrotron light sources*, which offer a tunable photon energy for the electron excitation, element selective studies based on *absorption spectroscopy* (XAS) became available. A more direct access to a spatially resolved chemical analysis could be provided by filtering the photoelectrons by their kinetic energy, like it is done in *photoemission spectroscopy* [Hüf03], by introducing an image conserving *energy filter*. The first working instrument was presented in the beginning of the 1990s [Ven91]. Another concept is the separation of the different kinetic energies by their *time-of-flight* (time-of-flight PEEM) [SSZ⁺98]. Besides an imaging with chemical contrast, such instruments can also be used for momentum resolved studies [KKO⁺03], which allow the analysis of the electronic *band structure* of a material [ML12]. A promising instrument which can use the imaging and the momentum mode in a complementary way was introduced in 2005 as *NanoESCA* [EWM⁺05, EWRB10]. It uses a double-hemispherical energy analyzer concept to avoid chromatic aberrations in the filter. The microscope module in this instrument was already used for *time-resolved studies* of dynamic processes in magnetic materials using the time structure of synchrotron light pulses [WKCS12]. The time resolution

of such experiments reach down to the lower 10 ps-regime [NGK⁺13]. Another highly interesting new application for this setup is to place an *imaging spin-filter* behind the energy-filter, which is based on the spin-dependent reflectivity of electrons on special scattering targets at a suitable scattering energy [TEU⁺11, TEK⁺13].

A couple of recent advances in this experimental field are reviewed in [LB08] and [SWP⁺12]. A drawback of the analysis based on photoemission for many years was the limited depth information due to the inelastic mean free path (IMFP) of electrons. Photoelectrons, which are used for the chemical analysis described above could only be detected from near surface regions of a specimen. First successful attempts to study the aforementioned STO - device structures by means of PEEM employed pre-switched resistive switching cells, in which the top-electrodes were either removed by local *Joule heating* during the switching process [LPM⁺14] or by wiping it away with a cotton swap [LKS⁺15]. The *redox process* coming along with the oxygen vacancies forming the conductive filaments could be identified in localized XAS-spectra of the Ti L₃ as well as of the Fe L edge in Fe-doped STO. The growth of these filaments seems to be initiated in confined pre-filaments which are related to local differences in the doping level or structural defects. An increasing current density in these pre-filaments leads to a localized Joule heating, which increases the mobility of oxygen ions and accelerates the reduction process. The size of the filaments could be estimated to 100 nm or less. It could be furthermore shown that indeed multiple filaments are active at the same time.

The next step would be to study such devices in-operando, especially if dynamic processes should be examined. This requires an intact device and forbids the aforementioned removal of the top-electrodes. The development of highly energetic light sources which provide hard X-rays led to more bulk sensitive studies (HAXPES), since the excited electrons have higher kinetic energies and longer IMFPs [Fad10]. Only then it was possible to access and study device layers buried deeper than a nanometer, which is a crucial condition for the analysis of real technological devices. Spatially integrated HAXPES studies have been already performed on large arrays of switched STO-cells [LKP⁺14]. A much more precise study can be expected, if HAXPES is combined with a microscopic approach. First pioneering experiments with photoemission microscopy in the total electron yield mode [WTO⁺06] or energy-filtered mode [YYK⁺06] using hard x-rays were published in 2006. In 2011 we performed the first tests with a modified NanoESCA at the P09 hard x-ray beamline at the DESY synchrotron in Hamburg [WPC⁺12]. With regard to device engineering, a detailed characterization of this method, called HAXPEEM (hard x-ray photoemis-

sion electron microscopy), was done on the basis of idealized test samples, showing that a spatial resolution of around 500 nm can be reached through a 15 nm thick top-electrode [PWW⁺14].

The main focus of this thesis is to study the energy filtered photoemission microscopy especially with respect to the use with hard x-ray excitation as well as to the feasibility for the analysis of devices like resistive switching memories. A high *energy resolution* of only a few 100 meV together with a good *spatial resolution* is needed to detect spectroscopic changes in areas which have dimensions around 100 nm. These high resolutions naturally come along with a reduction in *electron transmission* and thus long exposure times have to be taken into account for the measurements. Applications like HAXPEEM, time-resolved measurements and spin-filtered measurements each for itself lead to an additional reduction in signal intensity. Therefore, it is important to know, how the components of the experiment operate together and which effects influence the resolutions and the transmissions, to find optimized settings for each measurement. A part of this thesis will therefore analyze instrumental details and provide calculations, which are used to explain the experiments.

In **Chapter 2** I will first introduce the concept of *energy filtered photoemission microscopy* and explain the main aspects of *photoemission-* and *photoabsorption spectroscopy*, which are the fundamental physical methods used in this thesis. All experimental details are presented in **Chapter 3** including the fundamental aspects of *photoemission microscopy* and *imaging energy-filters*, but also the function and possibilities of *synchrotron light sources* which are used as main photo excitation source in this thesis. The fact that energy filtered photoemission microscopy in combination with such powerful light sources easily produces a huge amount of data is considered in **Chapter 4** by presenting methods which allow *automatized data evaluation* and concepts for a *statistical treatment*. Since the combination of photoemission microscopy with high energetic light sources is a new approach, the consequences of the use of *high kinetic electrons* for microscopy (transmission, acceptance angle, resolution) are studied in **Chapter 5** on the basis of *analytic electrostatic model calculations*. During my studies I found that also an exact understanding of the *non-isochromaticity* introduced by the imaging energy filter is of significant importance for a correct interpretation of the measured data, especially if they have an impact on the intensity distribution of energy-filtered microscopic images. **Chapter 6** is therefore dedicated to an comprehensive analysis of this part of the instrumental setup. The issue is especially important for the *HAXPEEM* approach, since a naturally small transmission forces us to use experimental settings with a high

non-isochromaticity of the analyzer.

In **Chapter 7** a variety of characterization measurements is shown which cover all important aspects of *spectro-microscopy*. Also *momentum resolved measurements* are discussed as far as they shed light on real-space microscopic issues. It is then demonstrated, how precise spatial and spectroscopic data can be gathered from structures with length scales down to 30 nm. While these experiments were performed with *surface sensitive* soft x-ray synchrotron light, the *hard x-ray approach* is presented and studied in **Chapter 8** on the basis of dedicated test-samples. Potentials and challenges of this method are identified with the help of the calculations in the former chapters. **Chapter 9** finally gives an outlook to future *in operando* studies of electronic devices like *memristors*. First results on STO-devices with the HAX-PEEM method are presented as well as instrumental tests of time-resolved studies with the same instrument.

Naturally, there will be still some way to go until the combination of time-resolved studies with energy-filtered hard x-ray photoemission microscopy will allow us to dynamically see the changes which appear in electronic devices below the electrodes. The results in this thesis are nevertheless promising and show how this method can help to understand and develop the complex material systems which are expected to dominate the future technological advances in non-volatile memory cells but also spin transistors, photovoltaic elements or batteries.

2. Fundamental aspects of energy-filtered photoemission microscopy

As described in the introduction, the spatially resolved spectroscopic examination of nano-technological devices will become more important in the near future if the stoichiometry of solids and molecules and their electronic states play the dominant role in the functional design of these elements. One of the methods with a high potential to fulfill the given requests is *energy-filtered photoemission electron microscopy* (EF-PEEM). It can be seen as an evolution of the classical powerful photoemission spectroscopy (PES) [Hüf03] which is extended with a system of electrostatic and/or magnetic lenses to collect a huge variety of photoelectrons emitted from a sample. The important information from which position of the sample and under which initial angle an electron was emitted is preserved to some extent. On the one hand, this allows for fast and coherent measurements of spectroscopic images of a sample or device under investigation. On the other hand some instrumental effort is needed to transfer all necessary phase space information undisturbed through the magnification stages of the microscope and the energy filter. Most of the measurements in this thesis were performed with a modified version of the *NanoESCA*¹ instrument[EWM⁺05] so that exemplary values are often given for this machine. Nevertheless, many statements are also true for microscopes from other manufacturers.

An overview of what can be measured with energy-filtered photoemission microscopy is shown in Fig. 2.1. The schematic distinguishes between a *real-space microscopy* mode and a *momentum microscopy* mode. In both modes electrons in the sample are excited by photons (which can originate from a variety of different possible light-sources). The energy of a photon can be absorbed by an electron and converts to kinetic energy (*photoelectric effect*). If the kinetic electron energy is big enough to overcome its *binding energy* in the atom/crystal and the work function barrier of the specimen it can travel into the vacuum as a free electron and leaves

¹distributed by *Scienta Omicron GmbH[Sci]/Focus GmbH[Foc]*

the specimen with a specific kinetic energy and start angle. A strong electric *extractor field* between the specimen and the objective lens is used to accelerate the free electrons into the microscope.

After passing several electron lenses inside the microscope and the energy filter, the electron distribution is projected onto a two dimensional screen and can be acquired as an image. The microscope can

- either map a spatial resolved image of the sample while integrating over all emission angles in each point (real-space microscopy)
- or map the momentum distribution of all electrons² leaving the sample while integrating over all sample area (momentum microscopy).

The angular space or the projected sample area respectively can be reduced by apertures inside the objective lens to reduce the phase space over which is integrated. Momentum microscopy as a consequence is only possible for highly ordered systems like *single crystals* [KKO⁺03] , graphene [BCWK12] or molecules [WHS⁺12] which arrange themselves in a periodic structure³. If for example momentum maps from amorphous solids are measured they differ so much inside the measured area that the integrated distribution is completely smeared out⁴.

In both modes image series can be acquired. They consist of energy filtered images which were measured over a full spectrum of kinetic electron energies, like it is shown in Fig. 2.1(c,d). In the real-space mode single photoemission spectra can then be extracted from lateral coordinates along the sample (*region of interests*, ROI) and subsequently compared to find chemical differences (e). In the momentum mode cuts through the image spectrum perpendicular to the image plane are of interest (f), because they show energy-momentum relations like it is known from calculated band-structures. An important difference is that not all transitions are allowed in the photoemission process and therefore not all existing bands are visible in such *energy dispersion curves* (EDC). But also the energy-filtered momentum distribution for a specific kinetic electron energy (*constant energy distribution* (CED)) is of interest (e.g. for all electrons excited from the Fermi level).

In this chapter, I first introduce the basic concepts of the classical photoemission spectroscopy because they have the same importance for the data acquired in the

²the momentum distribution is directly connected to the angle distribution, as is explained in Sec. 2.2.

³here also a single crystal as substrate is needed

⁴The measured sample area in the *NanoESCA* can be reduced to a minimum of approx. 6 μm in diameter. Structures for momentum microscopy needs to be at least in the order of this size.

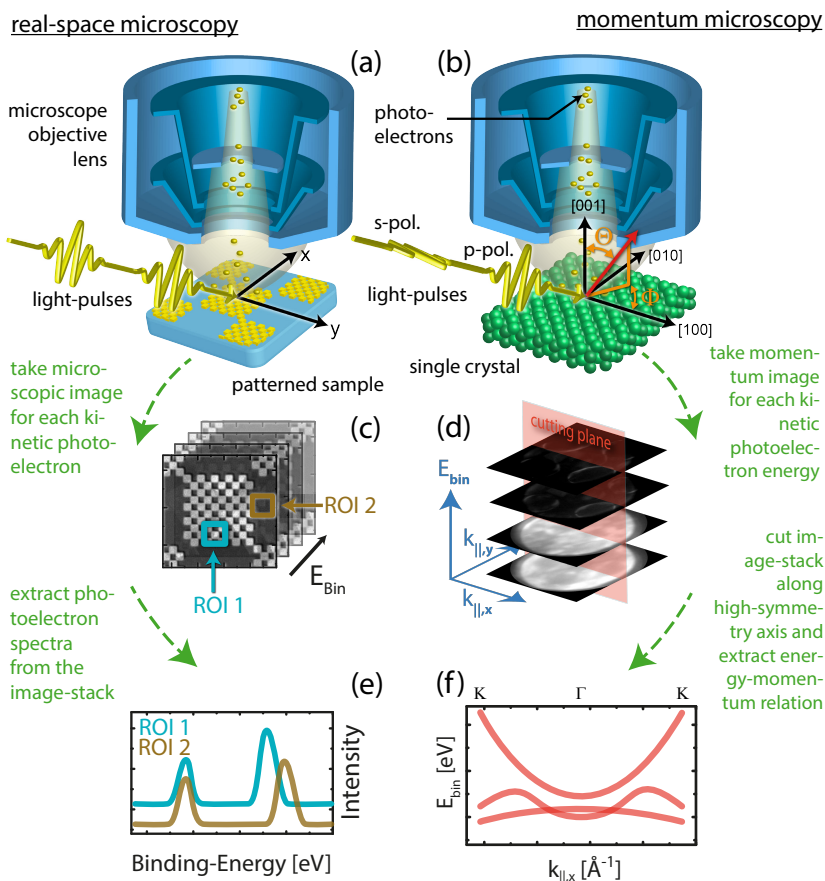


Figure 2.1.: The scheme compares the two operation modes of energy-filtered photoemission microscopy and the process of data acquisition. In the real space mode (a) spatial resolved image spectra are acquired from a specimen (c). The chemical information can be evaluated for different sample positions (e). In momentum microscopy (b) the energy dispersion curve (f) is often of interest, which can be extracted from a stack of constant energy distributions (d).

microscopy approach. Afterwards the instrumental aspects of the energy-filtered photoemission microscopy are explained for the *NanoESCA* concept and the light-sources used in this thesis are presented. The chapter closes with a description of representative evaluation methods used in this thesis.

2.1. Photoemission spectroscopy

The photoemission electron spectroscopy (PES) is the basic method used in this thesis, while the microscopy approach can be seen as a powerful upgrade of this technique. The interpretation of the image spectra acquired by an energy-filtered photoemission electron microscope (EF-PEEM) implies the same knowledge about the photoemission processes as is needed for the spectroscopy. Since the development of the photoemission electron spectroscopy already started at the end of the 1950's [NSS57] there is nowadays a lot of literature available (see for example [Hüf03] for a comprehensive overview). In this section I will introduce the fundamental aspects of the method with a focus on issues connected with the measurements presented in this thesis.

The photoelectron emission spectroscopy as a method has its origin in the *photoelectric effect*, which was discovered by H. Hertz in 1887 [Her87] and led to the famous interpretation of A. Einstein [Ein05] who explained the effect by an energy-quantization of the electro-magnetic field. R.A. Millikan finally verified experimentally [Mill6] that the proportionality factor in Einstein's equation is the *Planck's constant* h . According to Einstein's theory, photons therefore are quantized with the energy $h \cdot \nu$, which is a function of the frequency ν of their electro-magnetic wave. The maximum kinetic energy $E_{kin,max}$ of electrons which are excited by these photons and are able to leave a solid due to the photoelectric effect is

$$E_{kin,max} = \frac{1}{2} m_e \cdot v^2 = e \cdot V = h \cdot \nu - \Phi \quad (2.1)$$

with the electron mass m_e its velocity v and its charge e . This kinetic energy is equivalent to the kinetic energy of an electron accelerated by a potential difference V . The *work function* Φ is a material specific value. In a metal it is mainly determined by the surface potential barrier of the solid which electrons have to overcome to leave the specimen.

Equation (2.1) describes the situation for electrons which are easiest to free from a solid because they have the weakest binding state. That is true for the highest occupied bands in the *band structure* of a solid. In the ground state of a metal⁵,

⁵For semiconductors and insulators the Fermi level lies in a band gap between the valence band and

the electronic valence states are filled up to the *Fermi level* E_F , like it is shown in Fig. 2.2. While electrons at the Fermi level only have to overcome the work function to reach the *vacuum level* E_{vac} and become free electrons, other electrons are more strongly bound in the Coulomb potentials of the atoms in so-called localized *core levels*. Electrons which are excited from a core level need to overcome an additional *binding energy* E_{bin} and therefore higher photon energies to be released from the solid. The general relation between the kinetic energy of photoelectrons and the frequency of the electromagnetic wave to excite them can be written as

$$E_{kin} = \frac{1}{2} m_e \cdot v^2 = e \cdot V = h \cdot \nu - E_{bin} - \Phi. \quad (2.2)$$

By using a fixed monochromatic photon energy and by filtering the excited photoelectrons according to their kinetic energy with a spectrometer, the binding energies of a solid can be measured which are characteristic for each solid and can unveil the prevailing elemental components and the chemical bonds. Hence, photoelectron emission spectroscopy is also called *Electron Spectroscopy for Chemical Analysis* (ESCA).

A quantitative interpretation of photoemission spectra is in principle possible with the so called *one-step model* of the photoemission [MBME11], which treats the photoemission process as a single quantum-mechanical process. For this purpose, a time-reversed LEED⁶ formalism can be used. In the LEED formalism, a free electron wave enters a crystal and goes through multiple scattering processes. The time-reversed process gives a good description for the photoemission process. *Density Functional Theory* (DFT) can be used to calculate a realistic band-structure for the system under investigation, from which transition probabilities for all possible electronic excitations can be derived.

Nevertheless, the historically first and more intuitive model to describe the photoemission process is the *three-step model* which is presented here in greater detail. The three steps cover the photo-excitation of the electrons, the transport of the electrons to the surface and the transmission through the surface. The scheme presented in Fig. 2.2 adds two steps for the description of the incoming electro-magnetic wave, which also have to be taken into account during an experiment. All steps are discussed separately in the following sections.

the conduction band and the electronic states are only filled the valence band edge. Additional effects like band bending hamper the interpretation of photoemission results [Hor90]

⁶Low Energy Electron Diffraction

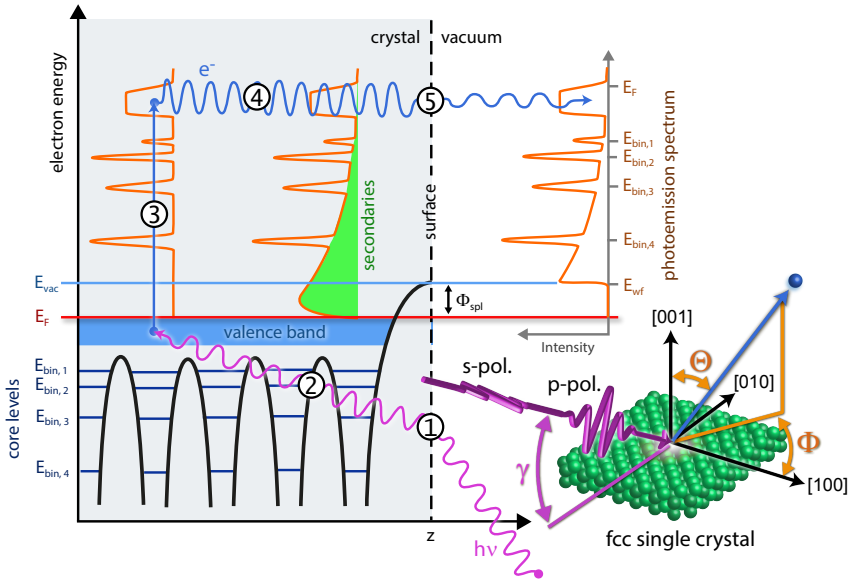


Figure 2.2.: Scheme of the photoemission three-step model. An electromagnetic wave is refracted at the surface (1) and penetrates through the solid (2) and excites a photoelectron (3). The photoelectron propagates through the solid to the surface (4) and might undergo elastic and inelastic scattering processes. The latter generates secondary electrons. The electron wave is finally refracted at the surface (5). If its energy is high enough to overcome the surface potential barrier it escapes into the vacuum and can be detected by a photoelectron analyzer. The 3D sketch shows a photoemission process seen from outside the solid. The incident angle γ and the polarization of the electromagnetic wave have an influence on which electron orbitals in the crystal are addressed and under which solid angles the excited photoelectrons escape the crystal.

2.1.1. Penetration of the incoming photons and photo-ionization cross section

Nowadays, a variety of different monochromatic photon sources are in use, each with different advantages and disadvantages. The choice of the optimal *light source* depends on the goal of the concrete experiment. The important properties are the maximal photon energy of the light source, the possibility to vary the photon energy in a certain range and the energy resolution of the light source. The available flux and the extent to which the beam can be focused on a small spot of the sample, determines the electron excitation rate. For many experiments the variability of the *light polarization* (linear, circular) is of importance. Finally, a pulsed light source allows to perform time resolved pump-probe studies. To just mention a few examples: laser-based systems promise the best *time resolution* (< 1 fs), the polarization can be tuned but they do not reach high photon energies. Discharge lamps (e.g. He I) offer very good energy resolutions but have a fixed photon energy and are not polarized nor do they have a time-structure. Synchrotron sources reach very high energies, good energy resolutions, medium pulse-width (10 ps), high intensities and can be polarized. New approaches like lasers with high harmonic generation (HHG) [PSG06] or synchrotron-sources with time-domain slicing [KHK⁺06] overcome limitations of their basic method: With HHG the benefits of a laser system can be used with higher photon energies and time-domain slicing improves the time resolution of synchrotron light pulses. Free electron lasers reach the highest brilliance and good time resolution but have a very low repetition rate.

If an electromagnetic wave reaches the surface of a specimen under an angle γ (see inset in Fig. 2.2), it is refracted at the surface Fig. 2.2(1) and subsequently travels through the solid (2) until it excites an electron. The degree of refraction is a function of the wavelength and the optical constants of the material and is stronger for lower energetic photons.

The probability that a photon of a certain wavelength is absorbed by an electron is described by the *photo-ionization cross section*. It differs for different materials, electron orbitals and light polarizations [GFK81] and is a function of the photon energy. As an example calculated curves are shown in Fig. 2.3 for different Au and Si states. The data is taken from the Elettra ionization cross section database [Rob] which refers to the tables given in [J.J93] and [YL85]. The vertical lines mark the energetic position of the binding energies of the related core level and was taken from the NIST XPS database [NIS12]. In general, the chosen photon energy needs to be larger than the binding energy of the core level which should be excited, but

in many cases a cross section maximum exists, which lies for example 236 eV above the binding energy for the Au 4f_{7/2} core level. A tunable light source could match this value exactly.

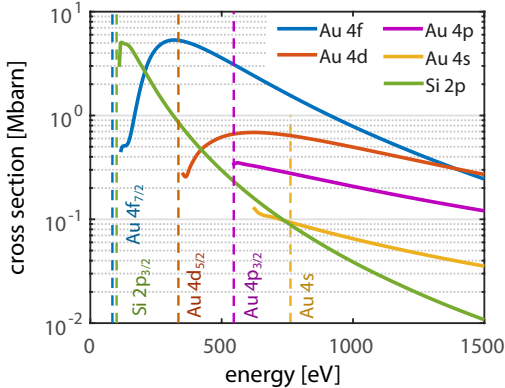


Figure 2.3: Photoionization Cross Sections for selected core levels of Au and Si as a function of the exciting photon energy. The vertical lines mark the binding energy of the related core levels. The Au 4f_{7/2} core level has a binding energy of 83.95 eV. The cross section maximum to excite photoelectrons from this core level lies at a photon energy of $h\nu = 320$ eV. Data taken from [Rob] and [NIS12].

For higher photon energies the photo-ionization cross section is rapidly decreasing. Regarding hard x-ray photoemission, this is a major drawback, because it strongly suppresses the count-rates which can be achieved from shallow core levels. The cross section σ_{nl} approx. decreases as

$$\sigma_{nl}(h\nu) \approx (h\nu)^{-3.5-l} \quad (2.3)$$

where (n and l denote the main and angular momentum quantum numbers of the electronic level excited)[Dru05].

2.1.2. The photo-excitation process

The electronic states in a solid are described by bands and the wave functions of electrons in the periodic lattice of a crystal can be described with *Bloch functions*, formally written as

$$|\Psi_{n,l,s}(\vec{k})\rangle = |n, l, \vec{k}, s\rangle \quad (2.4)$$

which have eigenstates $E_{n,l,s}(\vec{k})$, where n is the band index, l the orbital momentum quantum number, \vec{k} the electron wave vector and s the spin quantum number. With the knowledge of the lattice structure these wave functions can be calculated by solving a Schrödinger (nonrelativistic) or Dirac-type (relativistic interactions included) equation in the framework of the density functional theory (DFT). The correct Hamiltonian thereby needs to include a vector potential \vec{A} for a system subjected to an electromagnetic field, a potential $V(\vec{r})$, which contains the crystalline

symmetries, the Pauli matrices $\vec{\sigma}$ to describe interactions of the spins with an external magnetic field \vec{B} and further terms describing relativistic corrections to the electron energy (Darwin term), spin-orbit coupling and the exchange correlation potential [Blü10, p. B6.4].

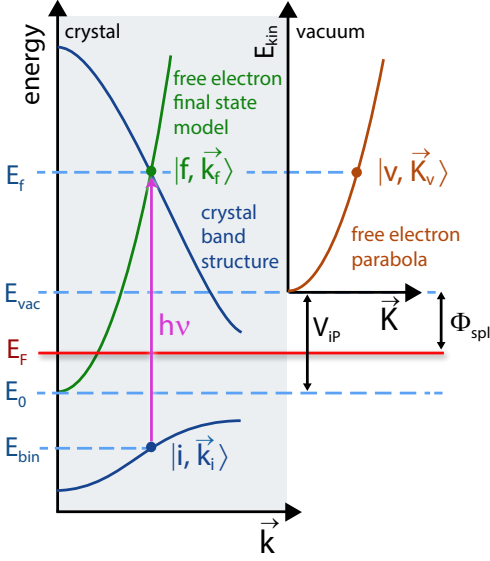


Figure 2.4: Scheme of the photoexcitation process in the momentum space with the notation used in the text. An electron in an initial state of the crystal band structure is transferred into a final state of the crystal band structure above the Fermi level via an optical transition. The free electron final state model is used to explain the transition between the final state in the crystal and the vacuum state of the free electron. Adapted from [Hüf03].

In the *photo-excitation* process, the electron is transferred from an initial state $|i, \vec{k}_i\rangle$ in the occupied band structure of the solid into an unoccupied final state $|f, \vec{k}_f\rangle$ via an optical transition (Fig.2.4). It is usually described as a direct (momentum conserving) transition in the reduced zone scheme of a bandstructure [Hüf03, P. 350]. The correct conservation law for the electron momentum $\hbar \vec{k}$ for the transition is

$$\vec{k}_f = \vec{k}_i + \vec{q} \pm \vec{G} \quad (2.5)$$

and includes the photon momentum \vec{q} and the reciprocal lattice vector \vec{G} . The transition probability between these states is given by *Fermi's golden rule* [FO74] which can be written in the linear response theory as

$$P_{i \rightarrow f} = \frac{2\pi}{\hbar} \cdot \underbrace{|\langle f, \vec{k}_f | H_{int} | i, \vec{k}_i \rangle|^2}_{=M_{fi}^2} \cdot \delta(E_f - E_i - h\nu) \quad (2.6)$$

$$\text{with } H_{int} = \frac{-e}{m c} \cdot \vec{A}(\vec{r}) \cdot \vec{p} \quad (2.7)$$

with the vector potential \vec{A} of the electric field and the momentum operator \vec{p} and the binding energies E_i and E_f . The δ -function describes the energy conservation in the excitation. If the wavelength of the electromagnetic field is large compared to the inter-atomic distances of the lattice, the matrix element M_{fi} can be simplified (*dipole approximation*) to

$$M_{fi} = \frac{ie}{\hbar c} \cdot A_0(E_f - E_i) \cdot \langle f, \vec{k}_f | \vec{e} \cdot \vec{r} | i, \vec{k}_i \rangle \quad (2.8)$$

with the amplitude of the vector potential A_0 and its polarization vector \vec{e} .

If this transition matrix is evaluated for high symmetries of the wave functions, so called *selection rules* can be deduced [EH80, WB81], which describe allowed and forbidden transitions between the initial and final states. The fact that not all transitions are allowed makes it impossible to map the complete band-structure of a solid by means of photoemission.

The wave-functions of atomic core levels can be expressed by a radial part, spherical harmonics (see e.g. [Nol06, p. 104]) and a spin part as

$$|\Psi_{n,l,m,s}\rangle = |R(r)\rangle |Y_{l,m_l}(\theta, \phi)\rangle |\chi(s)\rangle. \quad (2.9)$$

The advantage of the *dipole approximation* is that the operator $\vec{e} \cdot \vec{r}$ can also be expressed in spherical harmonics ($Y_{1,0}$ for linear and $Y_{1,\pm m}$ for circularly polarized light). The transition matrix element in Eq. (2.8) as a pure product of spherical harmonics is only non-zero for special relations between the indices l and m of the harmonics and the dipole selection rules for photo-excitation can be expressed as

$$\Delta L = \pm 1 \quad \text{and} \quad \Delta m_L = 0, \pm 1 \quad (2.10)$$

for the angular quantum number L and the magnetic quantum number m_L . The selection rule for the angular quantum number, for example, tells us that a Si 2p level can only be excited into an s or d level. Note that in the case of spin-orbit coupling the combined angular quantum number $J = L + S$ with the spin quantum number S has to be used. The scheme in Fig. 2.5 shows the allowed transitions between spin-orbit split states for circularly polarized light.

The transitions shown in the figure have different probabilities, which can be calculated by *Clebsch-Gordon* coefficients (see e.g. [Nol06, p. 88]). Because the spin is tied to specific orbitals due to the spin-orbit coupling, the excitation with a particular light-polarization can lead to a net spin-polarization of the excited photoelectrons even in non-magnetic materials, which is, e.g., used in spin-polarized electron guns [PCW⁺80].

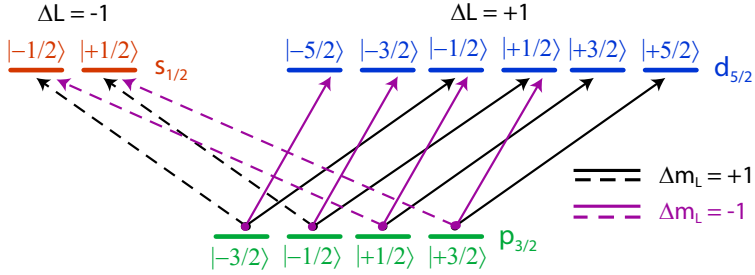


Figure 2.5.: Allowed photo-excitation transitions for a spin-orbit split $p_{3/2}$ state excited by left- or right circular polarized light. In the case of linear polarized light ($\Delta m_L = 0$) the combined quantum number J of the wave functions is conserved.

The total photo-current produced by the photo excitation process is proportional to the sum of Eq. (2.6) over all allowed transitions. The presented equations thereby describe a single particle approximation, whereas the photoemission process is more correctly described in the many-body theory, including electronic correlations between the electrons. Especially, a photoemission process leaves behind a hole in the electronic system, which alters its ground state until the hole is filled again. Photoemission therefore never measures the ground-state but an excited system. Theoretical approaches to handle this issue in the framework of the DFT are for example the *local density approximation* (LDA) which can be extended with a Hubbard term U to cover the effects in strongly correlated systems (LDA+U) [Ani97].

2.1.3. Photoelectron transport to the surface and inelastic mean free path

The excited (“hot”) electron with the wave function $|f, \vec{k}_f\rangle$ is subsequently transported to the surface of the solid (see Fig.2.2(4)). On its way it might undergo various elastic and inelastic scattering processes. The most probable ones are electron-electron scattering or scattering on crystal defects. On each scattering process, the electron can change its trajectory (its momentum \vec{k}). In the case of inelastic scattering it additionally loses kinetic energy and will not longer contribute to sharp emission lines in a photoemission spectrum, but to a featureless secondary background (green area in Fig. 2.2). The secondary yield increases to the low energetic part of the spectrum. It can be calculated, for example, by the theory of S. Tougaard [Tou88] and subtracted from the photoemission spectrum for a more reliable peak-

analysis ⁷. The photoemission intensity of the not scattered or elastically scattered photoelectrons greatly depends on the way λ , which the electron has to travel to the surface. It can be treated in the framework of an exponential damping as a function of the layer thickness t in which the photoelectrons were excited and their emission angle α with respect to the surface normal:

$$I(t, E_{kin}, \alpha) = I_0 \cdot \exp\left(-\frac{t}{\lambda(E_{kin}) \cdot \cos(\alpha)}\right). \quad (2.11)$$

The parameter λ is called the inelastic mean free path (IMFP) and depends on the kinetic energy E_{kin} of the transported electron and the material through which it is transported. It is usually much smaller than the penetration depth of the photons. After comparing the measured kinetic energy dependance of λ for a huge variety of materials, a *universal curve* was proposed by Seah and Dench [SD79], with a minimum of only a few Ångstroms around a kinetic electron energy of 100 eV. Photoemission with kinetic energies in this range exhibits maximum *surface sensitivity*. Lower and higher kinetic electron energies have larger IMFPs for most of the materials. This property is especially used in the hard x-ray photoemission spectroscopy which can reach up to $\lambda = 10$ nm for kinetic energies of 10 keV [Fad10]. This aims at a high *bulk sensitivity* and the possibility to perform photoemission through capping layers.

Theoretical models to calculate the IMFP as a function of the electron energy for each element are presented in [TPP11]. The calculated values above $E_{kin} = 50$ eV could be fitted⁸ with a modified *Bethe equation* of the form

$$\lambda(E_{kin}) = \frac{E_{kin}}{E_p^2 \cdot \left(\beta \cdot \ln(\gamma \cdot E_{kin}) - \frac{C}{E_{kin}} + \frac{D}{E_{kin}^2}\right)}, \quad (2.12)$$

including the element specific bulk plasmon energy E_p and further parameters given in the article. Example curves for materials used in this thesis are plotted in Fig. 2.6.

⁷While Tougaard calculates the complete background of a photoemission experiment on the basis of known experimental settings and an universal differential inelastic scattering cross-section, the background subtraction algorithm proposed by Shirley [Shi72] simply assumes that the background at a given point of a core level peak is proportional to the area beneath the peak above this point (to higher kinetic energies). It is easier to determine, although the Tougaard procedure is closer to the theoretical prediction [Rep92].

⁸The authors states that satisfactory fits with Eq. (2.12) were made in the range between $E_{kin} = 50..2000$ eV. While the curves also represent the calculated curves reasonably well for higher energies, they typically give wrong values for energies below 50 eV.

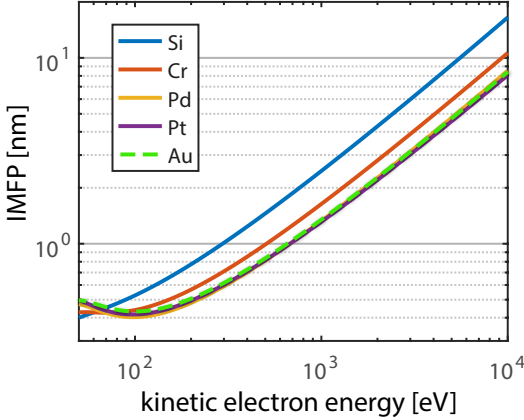


Figure 2.6: Inelastic mean free paths (IMFP) as a function of the kinetic electron energy for selected materials, calculated with the modified Bethe equation and parameters given in [TPP11]. The curves for heavy elements are quite similar and have a minimum around $E_{kin} = 100$ eV, whereas they differ for light elements like Si and Cr.

The $\cos(\alpha)$ -term in Eq. (2.11) takes into account that photoelectrons with higher emission angles α relative to the surface normal have to travel longer distances to the surface than just the layer thickness t . The same can be true for electrons which do not lose kinetic energy but change their trajectories several times due to elastic scattering processes. If the distances traveled inside the material become longer on average, the effective λ in Eq.(2.11) seems to be smaller. This factor is then called *effective attenuation length* (EAL) and is the value which can be measured in a real experiment, for example with the *overlayer film method* in photoemission experiments [PJ99a]. The difference between EAL and IMFP is extensively described in [JP99]. Without elastic scattering effects both values would be identical [BN82] whereas with these effects the EAL can be smaller than the calculated IMFP by up to 30 % [Pow84].

2.1.4. Transmission through the surface and momentum conservation

In the last step of the three-step model of the photoemission process, the electron needs to overcome the surface potential barrier which matches the periodic potential inside the crystal to the vacuum outside. The shape of this potential depends on the material, on an potential surface adsorbate and on additional electrostatic fields in the vacuum (see Sec. 2.4). Photoelectrons inside the crystal after the photo-excitation process travel in a potential with the depth $V_{iP} = E_{vac} - E_0$ between the vacuum level E_{vac} and the bottom of the valence band E_0 . The simplified picture of the *free electron final-state model* (see 2.4) assumes that the final states of the photo-excitation process can be described by a *free electron parabola* $E_f =$

$(\hbar k_f)^2/2 m^*$) with an effective electron mass m^* and its zero at E_0 . After leaving the crystal potential, the magnitude of the electron momentum $|\vec{K}|$ is described by the intersection of the same final state energy with a free-electron parabola $E_f = ((\hbar K)^2/2 m^*)$ starting at E_{vac} [Hüf03]. The condition for the component of the electron momentum perpendicular to the surface k_{\perp} to overcome the potential is

$$E_{kin,\perp} = \frac{(\hbar k_{\perp})^2}{2 m_e} \geq E_{vac} - E_0. \quad (2.13)$$

Electrons which have insufficient kinetic energy to overcome the barrier will not leave the solid which leads to a relatively sharp work function edge in the photoemission spectrum (see Fig. 2.2, step (5)). The surface-parallel component $k_{f,\parallel}$ of the final state electron momentum is conserved during the refraction at the surface potential, as is shown in Fig. 2.7. For the surface parallel momentum in the vacuum we can write

$$K_{\parallel} = k_{f,\parallel} + G_{f,\parallel} \quad (2.14)$$

with the surface parallel component of a reciprocal lattice vector $G_{f,\parallel}$. If a homogeneous electric field is applied between the sample and the extractor of a photoemission microscope, the photoelectron is accelerated in the direction perpendicular to the surface and only the perpendicular component of the momentum K_{\perp} is increased, whereas the parallel component is conserved again $K'_{\parallel} = K_{\parallel}$. Consequently, the distribution of the parallel momenta of the photoelectrons detected by momentum microscopy corresponds to the momenta of the final states in the crystal.

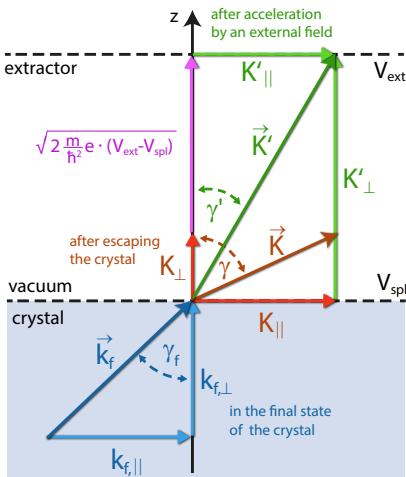


Figure 2.7: The final state wave vector \vec{k}_f of an electron inside the crystal is diffracted by the surface potential and leaves the crystal with the wave vector \vec{K} , whereby its component parallel to the surface is conserved $K_{\parallel} = k_{f,\parallel}$. The emission angle outside the crystal becomes bigger $\gamma > \gamma_f$. In the immersion lens of a photoemission microscope, the electrons are accelerated by an electric field perpendicular to the surface after leaving the crystal, which again only changes the perpendicular component of the electron momentum. The surface-parallel photoelectron momentum detected by the microscope equals the parallel final state momentum in the crystal.

2.2. Angular and momentum resolved photoemission

In the classical *angular resolved photoemission spectroscopy* (ARPES) setup the outer emission angle γ and the kinetic energy E_{kin} of the escaping photoelectrons can be measured. Since these values are directly connected with the electron momenta in the framework of the *nearly free electron model* (see Fig. 2.7) one can deduce the final state momenta as

$$k_{f,\perp}^2 = \underbrace{\frac{2m_e}{\hbar^2} \cdot E_{kin} \cdot \cos^2 \gamma}_{=K_{\perp}^2} + \frac{2m_e}{\hbar^2} \cdot \underbrace{(E_{vac} - E_0)}_{\equiv V_{iP}} \quad (2.15)$$

$$k_{f,\parallel}^2 = \frac{2m_e}{\hbar^2} \cdot (E_f - E_0) \cdot \sin^2(\gamma_f) = \frac{2m_e}{\hbar^2} \cdot E_{kin} \cdot \sin^2(\gamma) = K_{\parallel}^2 \quad (2.16)$$

with the final state energy E_f , the energy of the bottom of the valence band E_0 and the vacuum level energy E_{vac} (see Sec.2.1.4). The term $V_{iP} = E_{vac} - E_0$ describes the mean inner potential which can be calculated [San85] or determined from the comparison of measured and calculated band-structures. Note that the nearly free electron picture can strongly deviate from the real final state band-structure, especially if hybridization of the electron orbitals plays a role. In this case, calculated band-structures have to be used for a proper qualitative interpretation of the measured data.

In the energy filtered momentum microscope, the parallel momentum K_{\parallel} of the electron is directly measured together with its kinetic energy E_{kin} which are related as

$$E_{kin} = \frac{\hbar^2}{2m_e} \cdot (K_{\parallel}^2 + K_{\perp}^2) = E_f(\vec{k}) - E_{vac}. \quad (2.17)$$

If the inner potential V_0 is known, the perpendicular final state component $k_{f,\perp}$ can therefore be calculated [KKO+03] with

$$k_{f,\perp}^2 = \frac{2m_e}{\hbar^2} \cdot (E_{kin} + V_{iP}) - K_{\parallel}^2. \quad (2.18)$$

The description of momentum-related effects in a periodic crystal can be done within a reduced zone scheme in the first *Brillouin zone*, because all effects are repeated periodically and a particle with the momentum $\hbar \vec{k}_1$ behaves identically to a particle with the momentum $\hbar \vec{k}_2$ if the wave numbers just differ by a specific reciprocal lattice vector \vec{G} like $\vec{k}_1 = \vec{k}_2 + \vec{G}$. Such a three-dimensional *Brillouin zone* is shown in Fig. 2.8(a) for a face centered cubic (fcc) crystal structure, as it is relevant for all noble metals. Energy dispersion curves (EDCs) are classically shown in an energy versus momentum diagram for high symmetry directions between high symmetry points (indicated in the figure), e.g. $\Gamma - K$ or $K - W$, where Γ always

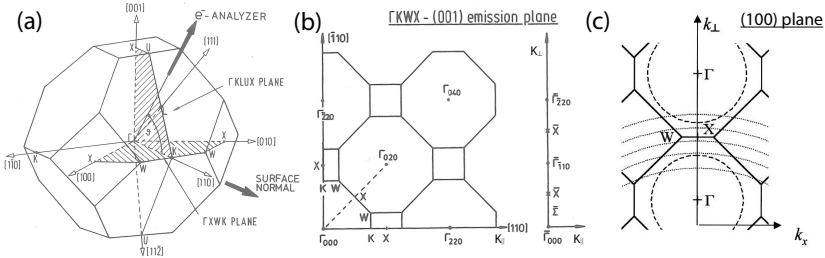


Figure 2.8.: (a) Brillouin Zone Scheme of a fcc lattice. (b) The (001) emission plane. (c) The (100) emission plane. (a,b) taken from [Hüf03], (c) taken from [KKO⁺03]

denotes the center of the *Brillouin zone* whereas the other letters denotes points at the border. Often the direction between two points is also indicated with a letter. An example is the $\Gamma - X$ direction, which e.g. goes along the [010] and the [100] direction of the fcc crystal, indicated as Δ . As mentioned earlier, the momentum microscope maps the component of the electron wave vector parallel to the surface. Which direction is mapped is therefore determined by the orientation of the crystal surface. The measurement presented in Sec. 7.2 shows for example data on a Ag (001) crystal, which means that a projection of the $\Gamma K W X$ - emission plane can be studied, which is shown as an extended zone scheme in Fig.2.8(b). Note that which part of the 3D *Brillouin zone* is accessed by the transition from a initial to a final state within the crystal still also depends on the perpendicular component of the electron wave vector k_{\perp} and according to Eq. 2.18 therefore on the kinetic energy of the electron. Fig. 2.8(c) for example shows the (100) emission plane which can be seen as a cut through the fcc *Brillouin zone* perpendicular to the (001) surface. The electrons in a photoemission experiment with the highest kinetic energy come from the lowest bound state (Fermi edge in a metal). This maximal kinetic energy is determined by the energy of the exciting photon $h\nu$. By varying the photon energy one can therefore determine, which plane in the k_{\perp} direction is accessed (dotted lines). Note that in the reciprocal 3D space, the cutting plane is a sphere with radius $\sqrt{k_{\perp}^2 + k_{\parallel}^2}$. By mapping the Fermi edge with a sufficient range of photon energies, the whole 3D Fermi surface can be measured [KKO⁺03].

2.3. X-ray absorption spectroscopy

X-ray absorption spectroscopy (XAS) is an alternative spectroscopic method which is based on photoemission and is often used in microscopy approaches. Not the kinetic electron energies of photoelectrons are analyzed, but how the photoemission yield changes with the photon energy. Tunable light-sources like synchrotrons are mandatory. If an electron from a core level is excited by a photon it undergoes a photoemission process (see Sec.2.1.2) and can leave the sample, if the photon energy is high enough. If the photon energy is quasi-continuously tuned to higher energies, it will be able to excite core levels with higher binding energies. If such a new binding state is reached, the photoemission yield will rise abruptly. This rise in the spectrum is called absorption edge. The increased photoemission can also be directly measured by an increase in the sample current which flows to balance the lost electrons.

The emitted photoelectron leaves a hole in its subshell which will be filled by electrons from lower bound states. The energy which is released by this process usually excites another electron (*Auger* process). These *Auger electrons* have very specific energies, because their excitation energies are defined by transitions between energetic sharply defined levels. Since the Auger electrons can be inelastically scattered in the solid, they increase the secondary electron yield. Fast Auger electrons leaving the sample are mainly excited from surface near regions. Electrons which are very slow have a larger IMFP and also may come from deeper layers.

Since the low energy electron yield nevertheless is proportional to the absorption rate, a photoemission microscope can measure the low secondary electrons to gather an image absorption spectrum. The strong secondary electron yield gives a high count-rate which is advantageous for microscopic methods and the probing depth can be higher than for direct photoemission microscopy. An additional imaging energy filter is in general not needed, since the chemical contrast in an image is provided by the different absorption rates of different region of interests, but it can increase the contrast.

The absorption spectroscopy is usually performed at the absorption edge of a core level. The analysis of the spectrum directly above the edge gives information about unoccupied electron states, into which core level electrons are excited after the photoabsorption⁹ and is used to study the orbitals of atoms or molecules at the surface. The further fine structure¹⁰ of the spectrum is caused by interference of the excited electron wave with the surrounding atoms and can be used to analyze the

⁹this detail of the spectrum is called near-edge x-ray absorption fine structure (NEXAFS)

¹⁰The so called *extended X-ray absorption fine structure* (EXAFS)

ligands around atom of the excited electron.

Finally, dichroism effects which result from light-polarization dependent transition probabilities in the photo-excitation process (see Sec. 2.1.2) give a usable absorption spectroscopy contrast for microscopy. For example, the x-ray magnetic circular dichroism (XMCD) is often used to image ferromagnetic domains. The spin orbit split $2p_{1/2}$ and $2p_{3/2}$ states of Fe exhibits a net spin-polarization when it is excited into the 3d bands by circularly polarized light. Due to the exchange splitting of the 3d bands in magnetic materials, the density of states are different for spin-up and spin-down electrons, which serves as a filter for the spin-polarized electrons. Different magnetic domains therefore have a different absorption rate, which is the contrast mechanism for magnetic imaging. Other dichroism effects are the *X-ray magnetic linear dichroism* (XMLD) and the *X-ray natural linear dichroism*(XNLD).

2.4. Work function

The *work function* Φ of a material is a highly interesting quantity because it is related to many chemical and electrical properties of the material's interface. Photoelectron spectroscopy with UV light is generally accepted as a basic technique to measure it [HGWL10]. In photoemission experiments it is an energy barrier electrons have to overcome when they travel from inside the material to the outside vacuum level. The measured value of the work function of a sample region depends on the material and its surface orientation and is furthermore effected by possible adsorbates (impurities, deliberately placed molecules, etc.). In energy-filtered photoemission microscopy, work function differences $\Delta\Phi$ along a sample surface are a well detectable contrast mechanism and are therefore a preferable technique to analyze the surface of a sample and to find interesting regions for a more intense examination. Furthermore in most of the cases a *work function analysis* can be performed with low energetic lab sources like a mercury discharge lamp (see Sec. 3.2.1). In this section, I give a short overview of the origin of the work function. How the work function can be evaluated in photoemission microscopy will be described in Sec. 4.1. The knowledge of the spatial distribution of the work function in a sample region is also of interest, if the exact kinetic energy of the emitted photoelectrons plays a role, because a lower work function leads to higher kinetic energies of the photoelectrons leaving the sample according to $E - E_F = h \cdot \nu - E_{bin} = E_{kin} + \Phi$. The spatial distribution of the work function should therefore be taken into account, if spectra from different sample positions are compared in great detail.

Adsorbed atoms or molecules (for example, carbon and oxygen on “dirty” samples) can influence the work function of the underlying material. Such a behavior is well known and understood for adsorbed Cs as cover layer, which is placed on purpose to reduce the work function for technical or experimental reasons. The work function changes can be described by a classical point-dipole model for a coverage significantly below one Cs atom per 30 \AA^2 and an orbital-overlap model for a more dense coverage [CVB⁺12]. Because of these electrostatic and orbital effects the work function decreases for low coverages and increases again to match the work function of the cover material, if the layer becomes thick enough to dominate the surface. The responsible dipole moment is governed by the difference between the electronegativities of the adsorbate and the substrate.

2.4.1. Work function and contact potential

The work function Φ can be most simply defined for an infinite, clean single crystal surface without any external electric field. It is then the energy difference between the electrochemical potential $\bar{\mu}$ of the electrons inside the metal and the energy level of the electrostatic potential Φ_0 of an electron just outside the surface and can be written as [Kna73]

$$\Phi = -e\phi_0 - \bar{\mu}. \quad (2.19)$$

For crystalline solid state bodies at a temperature $T = 0 \text{ K}$ the electrochemical potential $\bar{\mu}$ equals the *Fermi energy* E_F . The minimum energy level of the electrons outside the surface is the aforementioned vacuum level $E_{vac} = -e\phi_0$ and is usually considered as the “zero point” of the energy scale ($-e\phi_0 = 0 \text{ eV}$). The electrochemical potential $\bar{\mu}$ consists of two parts: the chemical potential μ of electrons in the metal which is a bulk property and the surface potential $\chi = \phi_0 - \phi_i$ (see Fig. 2.9(a)). The work function can therefore be written as

$$\Phi = -\mu - e\chi = -\mu + e(\phi_i - \phi_0). \quad (2.20)$$

The surface potential arises from electron wave functions which spread beyond the boundary of the bulk (thanks to their kinetic energy) and cause an asymmetric electron charge distribution at the surface. This electric double layer varies for different crystal orientations of the same material, because it depends on the geometry of the atomic positions at the surface [EK74].

If two conductors (A and B) are brought into contact, the electrochemical potentials of the materials change due to charge transfer until the Fermi energies of both

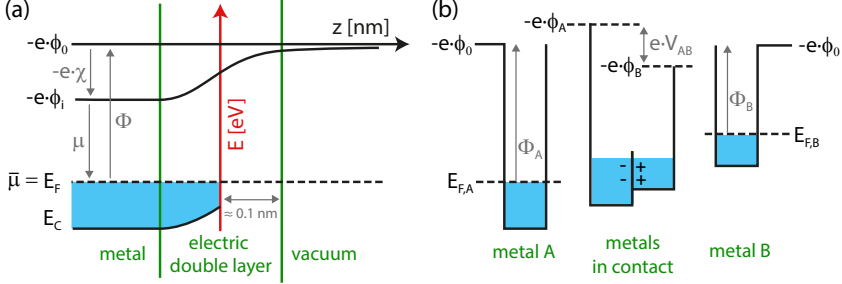


Figure 2.9.: (a) Potential energy diagram of a metal/vacuum interface including an electric double layer with the surface potential χ , the chemical potential of the electrons μ , the work function Φ , the Fermi level E_F , the bottom of the conduction band E_C , the electrostatic potential outside (ϕ_0) and inside (ϕ_i) the solid. If this metal is brought into contact with another conductor (b), the Fermi energies of the conductors change due to charge transfer until they reach an equal level. A voltage potential $V_{AB} = \phi_B - \phi_A$ called the Volta potential appears at the surface, which is directly connected to the work function difference $\Delta\Phi = \Phi_A - \Phi_B = e V_{AB}$ of the conductors.

materials are on the same level (see Fig. 2.9(b)). An electrical potential difference

$$V_{AB} = \phi_B - \phi_A = \frac{1}{e} \cdot (\Phi_A - \Phi_B) \quad (2.21)$$

called the *contact potential* (or *Volta potential*) arises at the contact region, which is equal to the difference of the work functions of the two conductors divided by the elementary charge e . In photoemission experiments like the *NanoESCA* energy-filtered measurements are performed with the Fermi energy E_F of the sample as reference level for the energy scale. With a correct instrumental calibration, the absolute work functions of the different materials can be directly measured. The work function Φ_i of a material (with index i) is then equal to that specific energy above the Fermi level $E_i - E_F$ where the first electrons (with the lowest binding energy) manage to reach the vacuum and can be detected in the experiment. The work function difference $\Delta\Phi = \Phi_A - \Phi_B$ between two materials is usually a good contrast mechanism which can be used to distinguish them.

2.4.2. Influence of an accelerating field

The electrostatic potential of an electron outside a surface can be described with the image potential

$$V(r) = -\frac{e}{16 \pi \epsilon_0 r} \quad (2.22)$$

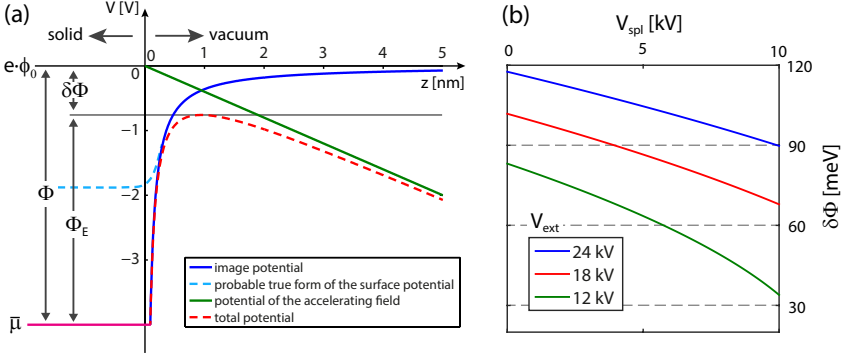


Figure 2.10.: (a) Calculated potential of an electron in the vicinity of a surface of a solid with the work function $\phi = 4$ V (adapted from [Kna73]). The image potential was calculated with Eq. (2.22). The potential of the accelerating field E_{acc} (see Eq. (2.23)) was calculated with an unnaturally high extractor voltage of $V_{ext} = 1$ MV to see a distinguished Schottky-effect. For the immersion lens of a photoemission microscope the effect is smaller. It is shown for the *NanoESCA* instrument in (b) for three different extractor voltages V_{ext} according to Eq. (2.23). The sample voltage V_{spl} varies in the energy filter mode with the kinetic energy of the filtered photoelectrons $E_{kin} = e \cdot V_{spl}$.

with the distance r between the surface and the electron. This function reaches its asymptotic value zero at infinite distances r of the electron from the surface. The vacuum level is therefore more precisely defined as $\phi_0 = V(r = \infty)$ like it is shown in Fig. 2.10(a)(blue curve).

If a constant electrical accelerating field E_{acc} is applied outside the sample surface, as is usually the case in immersion lens microscopy, this field alters the potential energy of the electrons outside the surface (*Schottky effect*) as it is shown in 2.10(red curve). The new total potential is the sum of the image potential in Eq. 2.22 and the potential of the accelerating field $-E_{acc} \cdot r$. The maximum of this potential defines the new work function Φ_E which the electrons inside the crystal have to overcome to reach the vacuum level. It is smaller than the work function without accelerating field. The difference $\delta\Phi$ between both work functions can be calculated as [Kna73]

$$\delta\Phi = \sqrt{\frac{e}{4\pi\epsilon_0}} \cdot \sqrt{E_{acc}}, \quad \text{with } E_{acc} = \frac{V_{ext} - V_{spl}}{d_{obj}}. \quad (2.23)$$

The formula of the accelerating field E_{acc} is given here for the immersion lens of the *NanoESCA* (see also Sec. 5.1). Typical values are an acceleration potential of $V_{ext} - V_{spl} = 24$ kV and a distance $d_{obj} = 2.5$ mm between sample and extractor, which results in a field strength of $E_{acc} = 9.6 \cdot 10^6$ V/m and a work function reduction

of $\delta\Phi = 117.57$ meV. Fig. 2.10(b) shows calculated values for additional extractor voltages as a function of the sample potential V_{spl} , which varies in the energy filtered mode according to the kinetic energy $E_{kin} = e \cdot V_{spl}$ of the photoelectrons which should be filtered. If measurements with different accelerating fields are compared to each other, the Schottky effect should be taken into account.

2.5. Conclusions

Photoemission- and photo-absorption spectroscopy offer a huge variety of possibilities to analyze the electronic structure of material systems and to draw conclusions about their stoichiometry. Often this is only possible in comparison to theoretical models and calculations. Due to the small inelastic mean free path of electrons this methods are nevertheless very surface sensitive. The use of high kinetic electrons is a possibility to become more bulk sensitive. Highly energetic and brilliant light sources like electron-synchrotrons are needed to provide intense, polarized and time-structured photons with variable energy.

All benefits of these methods can be applied to spatial- or momentum resolved approaches in the form of energy filtered photoemission microscopies. The microscopic approach is nevertheless more complicated to handle than spectrometers, but it has the benefit that the measured signal can be related to a concrete region of interest on the specimen, which allows an improved goal-oriented study of nano-devices.

3. Instrumental aspects

The *NanoESCA* is a *photoemission microscope* with an aberration corrected energy filter and electrostatic objective and projective lenses. It was introduced in 2005 [EWM⁺05]. The main idea is to cover two aspects at the same time: a microscope with a good spatial resolution and a spectroscopic resolution sufficient for chemical analysis in each point of the image. In this section I will give an overview over the instrument. On this basis, further details, calculations and characterization measurements are discussed in the subsequent chapters 5 and 6. A precise understanding of the instrument is necessary for the analysis of data acquired. The most important parts of the microscope are the immersion objective lens and the energy filter. Other parts are discussed briefly, as far as they are of interest for the later studies.

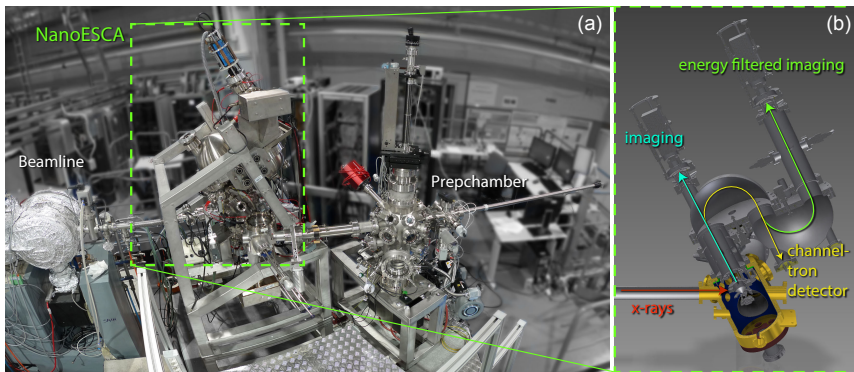


Figure 3.1.: (a) Photography of the *NanoESCA* setup, which is a permanent end-station at the 3rd generation synchrotron Elettra in Trieste, Italy [WPK⁺11]. The UHV-facility is equipped with a preparation chamber for in-situ preparations. The microscope itself can be run in different operation-modes (b). The synchrotron light hits the sample in a 65° angle relative to the sample normal. The microscopy of the escaping photoelectrons can be performed with the full electron yield in the imaging mode or by using an image-conserving double-hemispherical energy-filter. Behind the first hemisphere a channeltron detector is installed, which can acquire photoemission spectra.

3.1. Instrumental aspects of the NanoESCA microscope

Introduced in 2005 [EWM+05] the *NanoESCA* is one representative of commercially available PEEMs. Its outstanding property is to combine a relatively good energy resolution with an adequate spatial resolution¹. The NanoESCA consists of a microscope column with a subsequent energy-filter, which is supposed to preserve the PEEM-image during the filter process. Three operation modes can be used:

- The *PEEM mode* just uses the microscope itself without the energy-filter. An image of the full photoelectron yield which leaves the sample in a certain area can be magnified and projected on a 2D detector. Usually, secondary electrons are dominant. This mode is often used in absorption spectroscopy (see Sec. 2.3).
- The *energy-filtered PEEM mode* transmits the PEEM image of the microscope through a double-hemispherical energy filter. Only photoelectrons with a defined kinetic energy can pass the filter. This allows element-selective imaging.
- A *channeltron* can be used in combination with the first hemisphere of the energy filter. All photoelectrons of a predefined kinetic energy which pass the filter are counted and the spatial resolution is neglected. The benefit of a *channeltron* is a more reliable counting statistic.

The NanoESCA consists of a variety of elements which are necessary for a proper function of these three general operation modes. Furthermore some optional elements are available which allow some more specific operation modes. They will be discussed in the context of the following more detailed description of the instrument. The schematic in Fig. 3.2 shows the essential parts of the NanoESCA which can be grouped in five categories: The *objective*, the *projection column*, the *energy filter*, the *image detection* and the *channeltron detection*. In the following I will explain the function of the groups and the elements they contain:

3.1.1. The objective

The *objective* is, like in any microscope, the essential part to image and magnify a region of interest (ROI) of the sample under investigation. It strongly determines

¹Other representatives of commercially available PEEMs are the Elmitec LEEM/PEEM and the SPECS LEEM/PEEM, which have a somewhat better spatial resolution performance, but a less powerful energy-filter concept

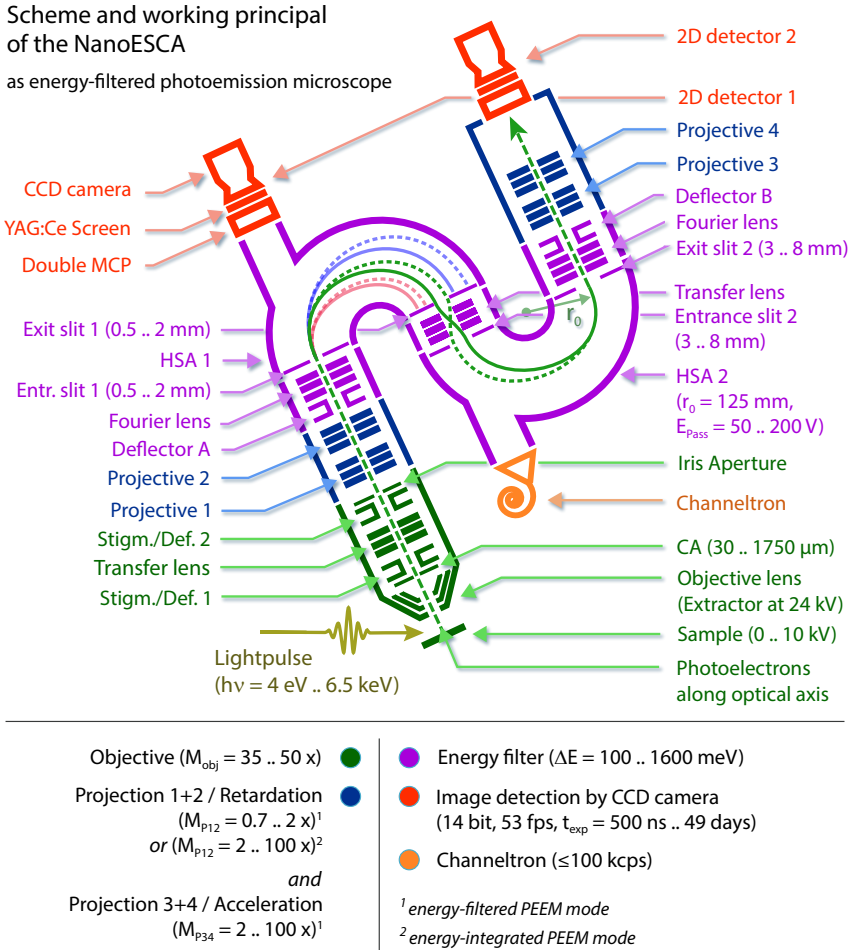


Figure 3.2.: The sketch shows the concept of the NanoESCA as an example for an energy-filtered photoemission microscope. The photoelectrons are excited by a lightpulse and travel through four main instrument parts: objective, projection, energy-filter and again projection until they reach the imaging detector. Two more measurement modes can be used: either if imaging is proceeded without the energy-filter or if just the first HSA is used for energy-filtering and electrons are counted with the channeltron while neglecting the spatial information.

the resolution and the transmission of the microscope². The immersion *objective lens* applies a strong electric field between the *sample* and the *extractor*³, which draws photoelectrons into the microscope column and creates a first intermediate image (with a magnification factor of $M_{obj} \approx 35..50$, depending on the settings) at the position of the iris aperture. The iris aperture can be closed so that only a defined part of the spatially resolved photoelectron distribution can pass further into the microscope. A strong extractor field bends the trajectories of the photoelectrons, which are leaving the sample, towards the optical axis of the microscope. More photoelectrons enter the microscope (higher transmission) while their angular spread is reduced. The latter is a necessary condition for a proper function of the microscope, because a reduction of the angular photoelectron spread reduces the effect of aberrations of the electron optical elements and therefore improves the resolution of the microscope (See Sec. 5.4). A *contrast aperture* (CA) is placed at the position of the back focal plain of the objective lens, which can limit the angular spread of photoelectrons additionally. This leads to a even higher spatial resolution but at the same time lowers the transmission of the microscope. The octupole *Stigmators/Deflectors* correct the trajectories of the photoelectrons and an eventual astigmatism⁴. The *transfer lens* is an optional element. It is needed to map the momentum distribution of the photoelectrons onto the second image plane⁵ instead of the spatial distribution (see Sec. 3.1.6). Chapter 5 explains the objective lens in detail.

3.1.2. The Projection column

There are two *projection* elements in the NanoESCA. The first one is placed behind the objective. Its function differs slightly for the PEEM mode and the energy-filtered PEEM mode:

- In the PEEM mode the projective lenses 1 and 2 project the first intermediate image onto the first 2D detector. They can be used for an additional magnification $M_{P12} \approx 2 .. 100$. In the highest combined magnification

²Note, that the subsequent energy-filter, if used, influences the resolution and the transmission additionally to the microscope column.

³The NanoESCA objective lens is a *tetrode lens* consisting of an extractor potential, a focus potential and a column potential. The extractor faces the sample and lies on a high positive potential compared to the sample.

⁴This correction becomes necessary, if the sample surface under investigation is not perfectly plane-parallel to the extractor plane and photoelectrons leaving the sample perpendicular to the surface are tilted against the optical axis of the microscope. The deflector corrects this tilt.

⁵The second image plane is located in *deflector A*.

($M_{obj} \cdot M_{P12} \approx 4000$), a ROI of 5 μm diameter can be projected onto the image detector with 19.1 mm diameter.

- In the energy-filtered mode, the projective lenses project the first intermediate image into a second intermediate image which lies in the deflector A plane in front of the energy-filter entrance slit. The magnification is rather small ($M_{P12} \approx 1..5$), but the main task is the retardation of the photoelectrons from a column drift velocity ($E_{kin} \approx 1..2 \text{ keV}$) to the pass-energy E_{pass} of the energy-filter ($E_{Pass} \approx 50..200 \text{ eV}$).

The second projection element sits behind the energy-filter. It projects the third intermediate image, which is formed in the Fourier lens behind the exit slit of the energy filter, onto the second 2D detector. The electrons are accelerated from E_{pass} to a column drift velocity ($E_{kin} \approx 1.2 \text{ keV}$) and the magnification factor M_{P34} of the projective lenses can be set between 2 and 20. Again, in the highest combined magnification ($M_{obj} \cdot M_{P12} \cdot M_{P34} \approx 4000$) a ROI of approx. 5 μm diameter can be projected onto the detector.

3.1.3. The energy filter

The *energy filter* consists of two (mostly identical) *hemispherical sector analyzers* (HSA) in a point-symmetrical configuration. In the first HSA photoelectrons are separated by their kinetic energy due to the dispersive effect of an electric field applied between an inner and outer hemisphere. An entrance and an exit slit of limited size define a small bandwidth of kinetic electron energies which travel on the correct trajectories to pass both slits and the electric field. The task of the second HSA is to neutralize the dispersive effect of the first HSA to avoid chromatic errors in a PEEM image sent through the filter [EWM⁺05].

The mean radius of the hemispheres, on which the slits are centered, is $r_0 = 125 \text{ mm}$. An electron which enters the HSA centered and perpendicular to the entrance slit plane has to have a defined kinetic *pass energy* E_{pass} to stay on this radius and to leave the exit slit as well centered and perpendicular to it. This pass energy can be varied by the electric field between the hemispheres between $E_{pass} \approx 50..200 \text{ eV}$. A smaller pass energy leads to a stronger dispersion and a better energy separation. The exit slit of the first HSA can be varied between $w_{exit} = 0.5..8 \text{ mm}$ and cuts out a certain bandwidth ΔE of the kinetic energy separated electrons. The entrance slit is a round aperture with a diameter w_{entr} equal to the exit slit width.

While the trajectory of an electron entering the energy filter along the optical axis of the microscope is easy to understand, the transfer of a complete image is more complicated. Each electron trajectory building up an image in the intermediate image plane in front of the analyzer is defined by a certain distance x, y from the optical axis and certain angles α, β to it, as well as its kinetic energy E_{kin} which can be expressed relative to the pass energy of the filter $\varepsilon = (E_{kin} - E_{pass})/E_{pass}$. Here (x, α) are the coordinates in the dispersive plane of the analyzer and (y, β) are the coordinates perpendicular to it. While the (y, β, α) coordinates are in first order not altered by the transfer through the analyzer except for a sign change [Ton90]

$$y_{exit} = -y_{entr} \quad \mathbf{and} \quad \beta_{exit} = -\beta_{entr} \quad \mathbf{and} \quad \alpha_{exit} = -\alpha_{entr}, \quad (3.1)$$

the distance x from the optical axis undergoes an energy and α dependent shift

$$x_{exit} = -x_{entr} + 2 \cdot r_0 \cdot (\varepsilon - \alpha^2). \quad (3.2)$$

The energy separation by the ε term is used for the energy filtering. For equal slit sizes $d = w_{entr} = w_{exit}$ the energies passing the filter are distributed between

$$E_{min} = E_{pass} \cdot \left(1 - \frac{d}{2 \cdot r_0} + \dots\right) \quad \mathbf{and} \quad E_{max} = E_{pass} \cdot \left(1 + \frac{d}{2 \cdot r_0} + \alpha_{max}^2 + \dots\right) \quad (3.3)$$

in a triangular shape with an asymmetric tail towards higher energies [IAK76]. The angle α_{max} describes the maximal half angle of the pencil ray which can enter the HSA through the entrance slit. The energy resolution of the HSA is the FWHM of this energy distribution which can be approximated as

$$\Delta E_{1/2} \approx E_{pass} \cdot \left(\frac{d}{2 \cdot r_0} + \frac{\alpha_{max}^2}{4}\right) \quad (3.4)$$

and depends linearly on the pass energy and the slit width. With the slit widths and pass energies mentioned above energy resolutions in the range of $\Delta E_{1/2} \approx 0.1..6.4$ eV are possible.

Because the value of the trajectory angle α is not altered by the HSA in Eq. (3.1) in contrast to the lateral x position, the important lateral coordinates of the image are translated into angles and vice versa by a *Fourier lens* in front of the entrance slit according to

$$x_{out} = \tan(\alpha_{in}) \cdot f \quad \mathbf{and} \quad \alpha_{out} = -\arctan(x_{in}/f), \quad (3.5)$$

where f is the focal length which is equal on both sides of this lens. For small angles α and $f \gg x$ this translation can be expressed with a matrix

$$\begin{pmatrix} x_{out} \\ \alpha_{out} \end{pmatrix} = \begin{pmatrix} 0 & f \\ -1/f & 0 \end{pmatrix} \cdot \begin{pmatrix} x_{in} \\ \alpha_{in} \end{pmatrix}. \quad (3.6)$$

The reciprocal image is sent through the analyzer and transferred back by an identical lens behind the exit of the second HSA. The transfer between both hemispheres is performed by a *transfer lens*, which projects the electron vectors in the exit plane of the first HSA to the entrance plane of the second HSA like

$$\begin{pmatrix} x_{out} \\ \alpha_{out} \end{pmatrix} = \begin{pmatrix} -1 & 0 \\ 0 & -1 \end{pmatrix} \cdot \begin{pmatrix} x_{in} \\ \alpha_{in} \end{pmatrix}. \quad (3.7)$$

The deflectors at the beginning and the end of this filter system adjust the electron trajectories correctly along the optical axis. The image in the deflector plane needs to be correctly focused into the entrance slit of the analyzer by the Fourier lens. Note, that due to this setup a *non-isochromaticity* [EWRB10] is introduced into the transmitted image, which will be analyzed in Chap. 6 and can be corrected in an energy-filtered image-stack.

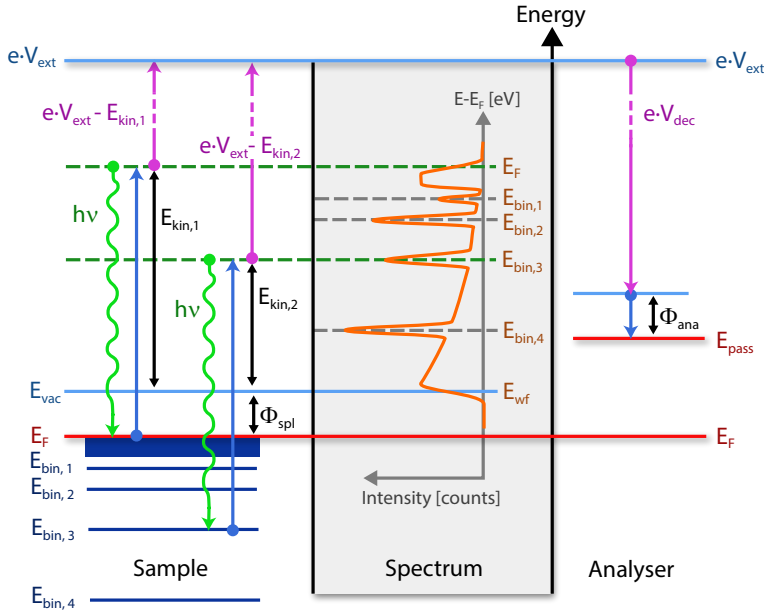


Figure 3.3.: Energy diagram and working principle of the NanoESCA energy filter. Photoelectrons which are excited from different core levels inside a sample by a monochromatic light source $h\nu$ will have different kinetic energies E_{kin} in the vacuum. By changing the acceleration potential V_{acc} the energy level which will have the right pass energy E_{pass} inside the analyzer can be varied. The deceleration potential V_{dec} remains unchanged during an energy sweep. The sample and the analyzer are electrical connected so that all energy scales can be related to the Fermi level of the sample as $E - E_F$.

While the filter settings (pass energy, slits) and the retarding projective lenses in front of it stay unchanged during an energy-filtered measurement, the kinetic photoelectron energy, which should pass the filter, is set by the immersion objective lens. An energy scheme of the filtering process in the NanoESCA is shown in Fig. 3.3. Photoelectrons which are excited by monochromatic photons with energy $h\nu$ have to overcome the work function Φ_{spl} of the sample and will have different kinetic energies

$$E_{kin,i} = h\nu - E_{bin,i} - \Phi_{spl}, \quad (3.8)$$

depending on the binding energy level $E_{bin,i}$ inside the sample, from which they were excited. The accelerating field of the immersion objective lens between the sample potential V_{spl} and the extractor potential V_{ext} increases the kinetic energy of the photoelectrons to

$$E'_{kin,i} = E_{kin,i} + e \cdot V_{acc,i} = E_{kin,i} + e \cdot (V_{ext} - V_{spl,i}) \underset{e \cdot V_{spl,i} = E_{kin,i}}{=} e \cdot V_{ext}. \quad (3.9)$$

That means that by adjusting the sample voltage to a defined kinetic photoelectron energy ($e \cdot V_{spl,i} = E_{kin,i}$) a constant final kinetic energy value $E'_{kin,i} = e \cdot V_{ext} = const.$ is reached for each initial kinetic energy. From this constant energy level the electrons are decelerated inside the microscope to match the pass energy E_{pass} of the HSA

$$E_{pass} = e \cdot V_{ext} - e \cdot V_{dec} - \Phi_{ana}, \quad (3.10)$$

where Φ_{ana} is the work function of the analyzer which has to be calibrated prior to an experiment. By sweeping the sample voltage V_{spl} each kinetic photoelectron energy can be addressed by the energy-filter and a spectrum can be acquired. The decelerating field in the microscope remains unchanged. The sample and the analyzer are electrically connected so that all energy scales can be related to the Fermi level E_F of the sample so that a spectrum is usually measured as energy above Fermi level

$$E - E_F = h\nu - E_{bin,i} = E_{kin,i} + \Phi_{spl} = \underbrace{e \cdot (V_{dec} - V_{ext} + V_{spl,i})}_{=R_i} + E_{pass} + \Phi_{ana} \quad (3.11)$$

with the kinetic energy *retardation* R_i of the microscope. The sample potential can be set between $V_{spl} = -5..10000$ V, i.e., a kinetic energy spectrum can be acquired over a wide range.

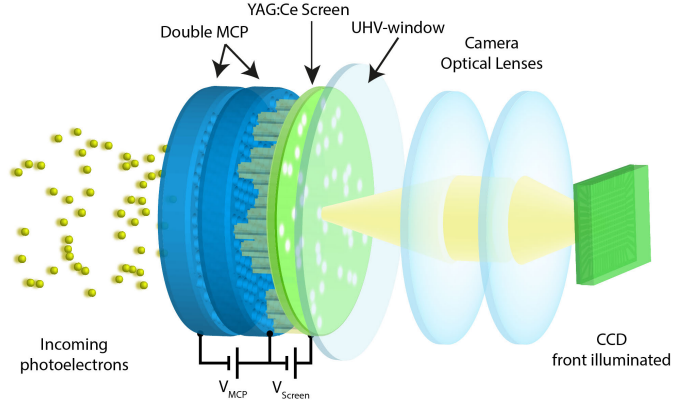


Figure 3.4.: Sketch of the NanoESCA detection system: the photoelectron image is projected onto a double microchannel plate (Chevron), which amplifies the electron current. The amplified electron bunches are accelerated against a YAG:Ce screen which serves as scintillator and produces light-blobs from the electron bunches. The screen is finally photographed by a fast acquisition camera and the images are send to a computer. The parts left of the UHV-window are operated in ultra high vacuum, the parts right of the window work under normal pressure. Taken from [PWW⁺14].

3.1.4. The image detection

After the photoelectrons pass the microscope and the energy filter, the two dimensional photoelectron distribution has to be detected and saved for computational post-processing and analysis. A sketch of the detection setup is shown in Fig. 3.4.

After leaving the energy-filter, the photoelectrons are projected by projective lenses onto a double microchannel plate (MCP) in *Chevron* configuration. The MCP multiplies single electrons to electron bunches. The gain can be adjusted by the potential difference across the microchannels (ranging from $V_{MCP} = 1.3$ to 1.9 kV) and reaches values between $10^5..10^7$ [LW79]. The electron bunches are then accelerated towards a scintillator-screen, which is made of Cerium-doped Yttrium Aluminum Garnet (YAG:Ce). The acceleration potential can be tuned between $V_{Scr} = 3.5$ kV ⁶. At the positions, where the electron bunches hit the screen, Gaussian shaped light signals are produced by the scintillator material. The image

⁶The screen intensity and the resolution of the detection system are increasing as a function of V_{Scr} [Foc12]. For the sake of a longer screen life-time (e.g. avoiding the risk of sparkovers), $V_{Scr} = 4$ kV is used as a standard, whereas $V_{Scr} = 5$ kV is used for low photoelectron fluxes in the *single event counting* .

of these light signals is acquired by a digital fast-acquisition camera. The scintillator-screen, which is operated in UHV, is separated by a UHV-window from the camera, which works under atmospheric pressure. The images produced by the camera are subsequently transferred to a computer memory for further evaluation.

A YAG:Ce screen (see for example [Sai14]) has some advantageous for our application (compared with the often used phosphor): the emission wavelength of 550 nm perfectly matches the quantum efficiency maximum of the used front-illuminated CCD-sensor (Kodak KAI-2001) of approximately 55% [PCO14]. The decay time of the excited states in the screen is relatively short (70 ns), which reduces the background signal. The spatial resolution of YAG:Ce was determined to be below 10 μm for electrons with a kinetic energy of $E_{kin} = 20 \text{ keV}$ [SB13] and decreases with lower kinetic energies. Furthermore its mechanical properties allow one to reduce the screen thickness down to 30 μm . This is advantageous for the spatial resolution, since a blur of the spatial position of the incoming electron bunch due to electron scattering along the screen thickness is reduced. The light output is around 8 photons per keV kinetic electron energy. Its refractive index (1.82) is relatively high, which slightly blurs the spatial resolution of the outgoing light.

The fast acquisition camera *PCO.1600* [PCO14] has a maximal frame rate of 29.8 fps in the full frame mode (1600 x 1200 px²) and 53.4 fps in the 2x2 - binning mode. The latter is the standard mode and a resolution of 800 x 600 px² is used in our experiments. The minimum exposure time for single shot-images is 500 ns. The dynamic range of the camera is 14 bit, which allows $n = 2^{14} = 16384$ intensity steps for each pixel of the image. The amount of distinguishable intensity steps in one pixel can in principal be related to the real counts of detected electrons in the accordant MCP channel, but because of several non-linearities in the electron-light-electron conversions between the MCP and the CCD, the gathered intensity distribution is more appropriate for a qualitative than a quantitative analysis, except for the case, where the single event counting is used (see Sec. 7.1.3).

The diameter of the excited YAG-screen is $d_{Screen} = 19.1 \text{ mm}$. On the CCD camera it is projected onto an area of $d_{img} = 1124 \text{ px}$. Throughout this work the camera is used in the above mentioned 2x2 - binning mode so that the effective projection area on the CCD camera has a diameter of $d_{img,eff} = 562 \text{ px}$. These values are important for the calibration of the microscope's magnification and its *field of view* (FOV). A characterization of the imaging system is presented in Sec. 7.1.

3.1.5. The channeltron detection

As mentioned above, the benefit of the *channeltron* is its counting statistics. Incoming electrons, without respect to their spatial distribution, are collected, multiplied and counted. It is a more simple detection system which does not require such a complicated set-up like the image detection and therefore does not have elements, which add errors to the counting statistics. The amount of counted electrons is linear to the amount of incoming electrons, which makes it useable for quantitative spectrum analysis. Although the channeltron has no spatial resolution by itself, inside the NanoESCA it can be used for quasi spatial resolved measurements. For this *micro spectroscopy mode* a region of interest on the sample is chosen with the image detector and the iris aperture in the first image plane can be closed around this region of interest. Only electrons from that defined region will then be counted by the channeltron. The iris aperture can be closed down to a region of interest of approximately 6 μm in diameter.

3.1.6. Photoemission microscopy and momentum microscopy

The photoemission distribution from the sample can be either mapped as a spatially resolved *real space* image onto the imaging unit or as the reciprocal momentum distribution image (see Fig. 2.1). The latter only makes sense in combination with the energy filter and allows the acquisition of energy distribution curves for all k_{\parallel} directions (see Sec. 2.2). The distribution to be mapped is chosen by the correct lens settings in the objective and projection part of the microscope [EWRB10]. The three usual combinations are shown in Fig. 3.5 including the simplified schematic trajectories for electrons with different start position in real space and for different start angles. The settings are shown for the energy-filtered mode of the *NanoESCA*. For the non-filtered mode only setting (a) is used with the difference that the projection lenses transfer the the final image on a screen instead into the intermediate image plane on the height of *deflector A*.

The standard imaging mode is shown in (a) where the electron trajectories arriving from the sample are imaged by the *objective lens* onto the first intermediate image plane, which is positioned on the height of the *field aperture* (FA). The *objective lens* has its *back focal plane* at the *contrast aperture*. Therefore, the spatial field of view can be limited by the FA and the angular phase space can be limited by the CA. The transfer lens is not used in this mode. Both projection lenses transfer the first intermediate image onto the second intermediate image. The image can also be

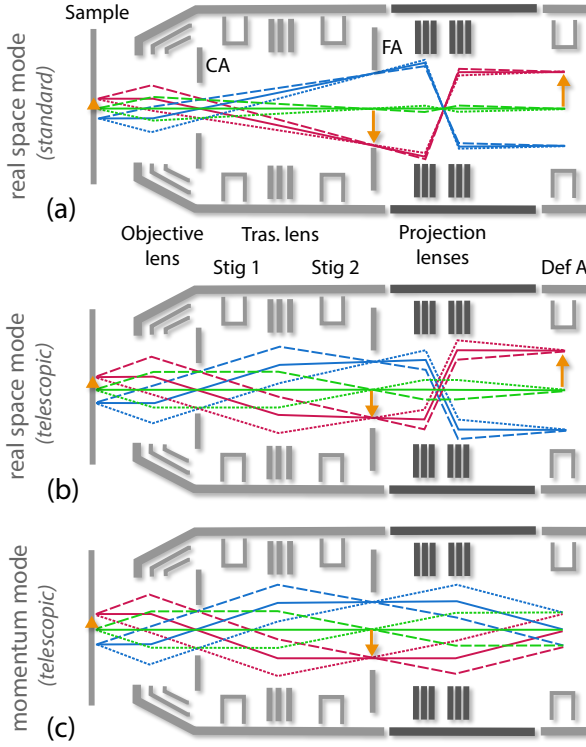


Figure 3.5: The sketch shows schematically, how electron trajectories of different lateral positions and different start angles are transferred through the microscope part of the *NanoESCA* for the three main operating modes: *standard real space*, *telescopic real space* and *momentum space*. The *contrast aperture* (CA) and the *field aperture* (FA) have an equal phase space limiting effect in all mode. Intermediate image planes are indicated with arrows. Adapted from [EWRB10].

magnified. The electrons are at the same time retarded to the pass energy of the analyzer.

For the momentum mode (c) a *telescopic image* is needed in the first intermediate image, which means that the correct angular distribution is maintained in all image points. This is not the case in (a). To fulfill this condition, an additional transfer lens is used behind the objective lens. The reciprocal image of the first intermediate image is then mapped into the second intermediate image plane. Besides the retardation, the projective lens then serves as a Fourier lens (see Eq. (3.6)).

The telescopic image in the first intermediate plane can also be projected as a real space image into the second image plane, which is shown in (b). One can therefore easily switch between a real-space and a momentum image, while the electron distributions in the back focal plane and in the first image plane remain equal in either mode. This is important, if the phase space limiting apertures are used. For example, in the momentum mode it might be reasonable to limit the area on the sample, from where a momentum resolved signal is acquired (for example graphene

flakes of limited size [BWKC13]). By switching into the telescopic real space mode one can close the field aperture in a controlled way around the region of interest.

If only the real-space mode is needed, the standard mode (a) is preferable because one lens is less used and the angular spread is smaller, which both reduce spherical aberration effects which limit the resolution. Additionally, the telescopic mode slightly decreases the magnification in the microscope column by a factor 0.461 compared to the standard mode.

3.2. Light sources

Light sources are an essential part of a photoemission experiment, as I described in Sec. 2.1.1 and a big variety of different light-sources with different properties are available nowadays. In the following I describe the relevant features of the sources used in this thesis, starting from a comparison of the spectral differences of two laboratory UV sources (a discharge lamp and a laser) and subsequently explaining the features of soft- and hard X-ray synchrotron sources.

3.2.1. UV excitation

The *NanoESCA* instrument is equipped with a high-pressure *mercury lamp* with a luminous flux of 3000 lm. Compared to the synchrotron light sources the lamp has a wide spot size which nearly homogeneously illuminates the sample and is therefore used for overview imaging. For photoelectron spectroscopy issues it has the disadvantage of having a not monochromatic spectral distribution. In the following measurement I compare PES data of an epitaxial Au-film excited by either a mercury lamp or a two times frequency doubled *Nd:YAG Laser*, which provides a sharp monochromatic spectral distribution. Laser light-sources are additionally polarized and can be pulsed for time-resolved measurements.

For this experiment I used a non-cleaned Chessy-patterned sample (100 nm thick, epitaxial grown Au structure on Si (111) wafer) (see Fig. 6.1). The microscope's field aperture was closed to a 10 μm diameter window to only obtain the photoemission signal from the Au-covered region (*micro-spectroscopy* mode). The photoelectrons were excited by either the mercury lamp or the Nd:YAG laser and energy filtered spectra were taken in the channeltron-mode of the NanoESCA. The mercury lamp is of the high-pressure mercury plasma arc-discharge lamp type HBO 103. The corresponding radiation spectrum was adapted from [Dav14] and is shown in Fig. 3.6. The laser radiation spectrum was considered to be a Lorentzian profile with the

mean-value $\lambda=266$ nm and the spectral broadening $\Delta\lambda = 0.54$ nm. This corresponds to $h\nu = 4.661$ eV and $\Delta(h\nu) = 9.4$ meV. For a better comparison, its peak-intensity was arbitrarily set to the mercury spectrum intensity at $\lambda = 253.7$ nm. The contrast aperture of the microscope was set to $30 \mu\text{m}$, which allows only a small angular spread of the photoelectrons to enter the microscope. The energy-filter was run with a pass-energy of 50 eV and an exit-slit of 0.5 mm. The calculated energy-resolution of this setting is approx. 100 meV. The energy scale used in Fig. 3.6 is the energy above the Au Fermi-level ($E - E_F = h \cdot \nu - E_{bin} = E_{kin} + \Phi$). The photon excitation energies can be directly compared to the photoelectron kinetic energies on this scale.

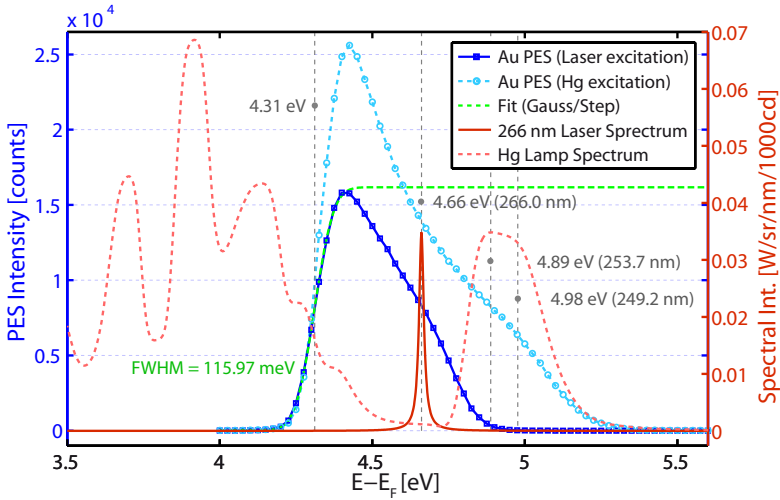


Figure 3.6.: Photoemission spectra of a 100 nm Au layer (on Si), excited by either a high pressure mercury lamp or a two times frequency doubled Nd:YAG laser.

The photoelectron spectra of the Au-sample are also shown in Fig. 3.6 for the laser and for the mercury lamp excitation. The spectra were normalized such that their intensities at $h \cdot \nu - (E - E_F) = 0$ are equal, as we would expect for two equal light sources. The excitation energy of the laser has its well defined maximum at $h \cdot \nu = 4.66$ eV. The mercury-lamp has a broader spectrum at its high-energy edge with a maximum at $h \cdot \nu = 4.89$ eV. This point was used for the normalization of the photoelectron spectra. Additionally the mercury spectrum has an only slightly less intense peak at $h \cdot \nu = 4.98$ eV and a tail reaching up to approximately $h \cdot \nu = 5.4$ eV. Higher energetic lines of the Hg spectrum are filtered out by the encasing quartz-

glass of the lamp to avoid ozone production. The mercury lamp spectrum shown in Fig. 3.6 has a full width half max of approx. $\text{FWHM} = 265 \text{ meV}$ at its high-energy excitation end, compared to 10 meV for the laser excitation.

In both photoelectron spectra the low-energy cut-off defined by the work-function Φ is clearly visible. A convolution of a Gauss-profile and a step-function was fitted to the *work function edge* of the laser-excited photoemission spectrum. The center of the edge of this fit (4.31 eV) is a rough guess for the position of the real work function edge Φ . The energy resolution is approximately given by the FWHM of the Gaussian profile (115.97 meV), which very well fits to the expected energy-resolution of the analyzer. A more exact explanation of this fit method is given in Sec. 4.1. The high-energetic end of the spectra for metallic conductors is defined by the photoelectrons which are directly excited from the Fermi-level (zero binding energy) with $E_{kin} = h \cdot \nu - \Phi$. This Fermi-edge of the laser excited spectrum is convoluted with a non-trivial DOS contribution because of the uncleaned surface. Nevertheless one can try to fit a similar Gauss/Step-function like at the work-function-edge. The result is a center of the Fermi-edge at $E - E_F = 4.76 \text{ eV}$ and a $\text{FWHM} = 174.21 \text{ meV}$. Note that since the *Fermi-edge* is convoluted with the steep slope of the DOS, this value is also only a rough guess. The FWHM is obviously broader than the FWHM at the work-function-edge. At the Fermi-edge, the thermal broadening and the spectral broadening of the laser have to be taken into account in addition to the instrumental broadening

$$\Delta E_{total} = \sqrt{\Delta E_{inst}^2 + (4 \cdot k_B \cdot T)^2 + (h \nu)_{laser}^2} \quad (3.12)$$

which is $\Delta E_{total} = 155.70 \text{ meV}$ in this case. On the chosen $E - E_F$ -scale the center of the Fermi-edge should be actually equal to the excitation energy of $E - E_F = 4.66 \text{ eV}$. Compared to this value it is shifted by 100 meV to higher energies in our experiment, which may be caused by a slight miss-calibration of the energy-analyzer work function Φ_{ana} in Eq. (3.10). As a consequence the value of the measured work-function-edge would have to be decreased by the same value. Finally, the Fermi-edge of the mercury lamp excited spectrum is significantly broader than the Fermi-edge of the laser excited spectrum which is a consequence of the broad excitation band-width.

3.2.2. Soft X-ray and hard x-ray synchrotron sources

Electron- or positron-synchrotrons which are dedicated to x-ray photon production provide some of the most powerful and diversified light sources in the world. Our measurements were performed at the 3rd generation synchrotrons *Elettra* in Trieste (Italy) and at *PETRA-III* in Hamburg (Germany).

Particle acceleration in the synchrotron

Their basic idea is that electrons (positrons) are accelerated to velocities close to the speed of light which are subsequently sent through a strong magnetic field B . Due to the *Lorentz force* the charged particles move on radial trajectories inside the magnetic field and emit a continuous spectrum of *bremsstrahlung* with a critical photon energy⁷ of

$$\hbar \omega_c [eV] = 665 \cdot E_e^2 [GeV] \cdot B [T] \quad (3.13)$$

with the electron energy E_e . The radiant power P_r of this particle on a curve with radius r is [FM10]

$$P_r = \frac{c q^2 E_e}{6 \pi \epsilon_0 r^2 \cdot (m c^2)^4} \quad (3.14)$$

with the light velocity c , the particle charge q and mass m and the vacuum permittivity ϵ_0 . Electrons and positrons are therefore in general equally suitable except for two points: Electrons are easier to generate (hot tungsten cathode instead of pair-production by bombarding atom cores with electrons) but they attract positively charged particles in the storage ring of the synchrotron (ionized rest gas particles or dust) which shorten their life-times due to an increased scattering rate. *Elettra* works with electrons, *PETRA-III* with positrons.

The way from accelerated electrons to x-ray radiation used in our experiments should be described in short: Electrons are emitted by a hot tungsten cathode and pre-accelerated by an electric field. The second step is a *linear accelerator* which consists of a row of *cavities* in which an oscillating electromagnetic field is used for the acceleration of the electrons. Only a short time window of the electric field can be used for this purpose, therefore the electron beam will be split into bunches with the right *time structure*. The so-called *radio frequency* (RF) of the electromagnetic field determines this time structure. In *Elettra* and *PETRA-III* a RF of 500 MHz is used which leads to *gaps* of 2 ns between the bunches. The *bunch length*, which limits the *time resolution* of this light source, is approximately 42 ps [LMNB11]. The last acceleration step is performed in a synchrotron, in which the bunches are sent several times through the same set of cavities in a ring. Since the velocity of the electrons is increasing, also the magnetic field of the *bending magnets*, which keep the electrons in the ring, have to increase synchronous⁸. If the electrons have reached their final kinetic energy, they are deflected into the storage ring. The storage ring is a synchrotron which works on a constant kinetic energy level. Nevertheless, the

⁷the intensity of the emitted spectrum significantly but slowly drops above the critical energy

⁸which gives a synchrotron its name

energy loss of the electrons in the bending magnets of the ring, which is also used for the production of synchrotron radiation, has to be compensated by cavities. The *ring energy* for *Elettra* is 2 or 2.4 GeV, for *PETRA-III* it is 6 GeV. The electron beam in the storage ring has a limited life time so that the beam current decays with the time. Nowadays, most synchrotrons work in a *top-up mode* in which missing electrons are constantly injected to keep the *ring current* on the same level (100 mA at PETRA-III, 140-300 mA at Elettra).

Adjusting light properties in the undulator and the beamline

The most efficient way to produce x-ray radiation from the electrons inside the storage ring is to send them through an *undulator*. It (see Fig. 3.7) consists of two arrays of magnets with periodically alternating field directions, which forces the electrons between them on sinus shaped or spiral trajectories. This causes an emission of radiation in the propagation direction of the electron. With an appropriate *phase shift* of the two arrays of magnets, the polarization of the emitted photons can be switched between *horizontal linear*, *vertical linear* and *right* or *left circular*. The experimental setup of the *NanoESCA* is oriented in such a way that *horizontal linear* polarized light corresponds to *s-polarization* and *vertical linear* polarized light corresponds to *p-polarization* of the light on the specimen. In *undulators* the periodicity λ_U of the magnetic field is chosen such way that the photon wave front emitted by an electron on one part of the sinus curve can interfere constructively with the photon wave front emitted from the same electron after one period. The emitted photon spectrum is then reduced to an energetic sharp line and its higher harmonics instead of a continuous spectrum. This sharp line can be energetically shifted by changing the *gap* between the magnet arrays, so that any photon energy can be reached.

The *undulator* is followed by a *beamline*. The *Nanospectroscopy/NanoESCA* beamline at *Elettra*, for example, consists of several focusing mirrors (approx. 10 μm *beam spot diameter* (FWHM) on the sample) and a variable line space (VLS) plane grating monochromator. The scattering angle of the grating needs to be adjusted to the used photon energy and the width of the *exit slit* w_{slit} defines the *energetic bandwidth* of the filtered radiation which can be calculated via

$$\Delta(\hbar\omega) = \frac{\hbar\omega}{RP} \cdot \frac{w_{slit}[\mu\text{m}]}{10} \quad (3.15)$$

where the resolution power $RP = \hbar\omega/\Delta(\hbar\omega)$ as a function of the photon energy is tabulated for different gratings in use [CMK+99]⁹. The beamline works with

⁹An example: $RP=6000$ at $\hbar\omega = 100$ eV. An exit slit of $w_{slit} = 20$ μm results in a photon energy

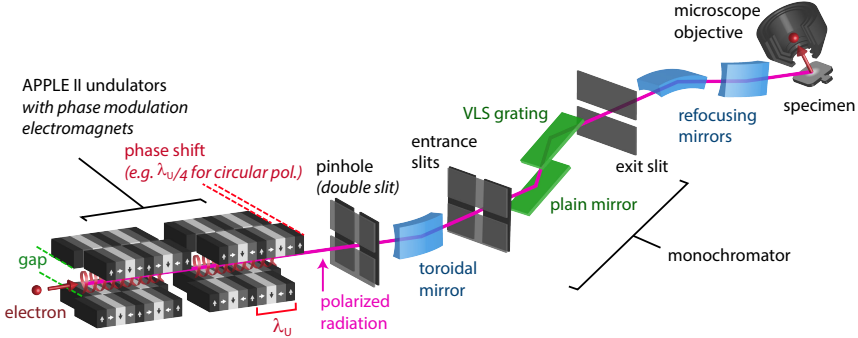


Figure 3.7.: Scheme of the *NanoESCA* beamline at the 3rd generation synchrotron *ELETTRA* in Trieste, Italy. The *gap* and the *phase shift* of the two undulator columns can be adjusted to generate photons with a specific energy $h\nu$ (plus higher harmonics) and with a specific light polarization (vertical linear, horizontal linear, left or right circular). Unwanted radiation is stopped by the pinhole and the transmitted beam is demagnified by a toroidal mirror before it enters the monochromator. The angle of the plain mirror and the grating can be adjusted to reflect a nearly monochromatic beam with the wanted photon energy onto the exit slit. The width of the exit slit determines the final energy resolution. The refocusing mirrors finally produce a small beam spot on the specimen.

two *gratings*: 200 lines/mm for the energy range 50 to 250 eV and 400 lines/mm for the energy range 200 to 1000 eV. This total energy range belongs to the *soft X-ray spectrum*. Finally, the flux of the monochromatized radiation is an important argument for high-brilliant synchrotron sources and depends on the used photon energy, the monochromator and the exit slit width. The maximum value for this beamline is approx. $1.8 \cdot 10^{13}$ *ph/s* at an energy of $h\nu = 145$ eV and drops to $1 \cdot 10^{11}$ *ph/s* at 1000 eV [LBC⁺03, Loc].

Since the electron energy in the storage ring of *PETRA-III* is higher, the yield of *hard x-rays* is higher according to Eq. (3.13). The monochromator covers an energy-range between 2.7 and 50 keV with an RP between 7700 and 35000. Variable linear and circular polarized light is available by means of a diamond phase retarder [FSR⁺13] in the energy range between 3.3 and 8.5 keV. The incident photon flux within the 10^{-4} energy bandpass of the Si(111) primary monochromator is about $2 \cdot 10^{13}$ s^{-1} . The measured *beam spot diameter* during our beamtime in the last hutch of the *P09 beamline* were determined by fitting a Gaussian distribution to an intensity profile of the beam (see Fig. 8.6). The FWHM of the distribution in vertical (horizontal) direction is 270 μm (311 μm).

bandwidth of $\Delta(h\nu) = 33.3$ meV

3.3. Conclusions

An energy-filtered photoemission electron microscope (like the *NanoESCA*) consists of many different elements, as it is shown in Fig. 3.2. The function of each element needs to be understood to avoid instrumental artifacts or to be able to identify and correct them in a measurement. At the same time a lot of variations in the experimental setup are possible. This includes the possibility to switch between imaging and momentum mode, but also to adjust the magnification, the energy resolution and the spatial resolution in a wide range. The improvement of the resolutions always comes along with a decrease of the transmission of a microscope. Highly intense light sources are therefore a good choice to reduce the necessary exposure time for taking data sets with high resolutions. Especially synchrotron sources offer this high intensities in combination with a good energy resolution, a wide and continuously adjustable energy range, the possibility to adjust the light polarization and a natural time-structure in the ps-range, which can be used for time resolved studies.

This chapter gave an overview over the important instrumental details which are needed to operate the experiment. Further details will be studied in the subsequent chapters of this thesis which includes the objective lens (Ch. 5), the energy analyzer (Ch. 6) and the detection system (Sec. 7.1).

4. Evaluation methods

Like discussed before, a spectral image stack, as it is acquired by an energy-filtered microscope, can be seen as a huge amount of single spectra, namely one for each pixel in the image. For each image a circular area with 560 px in diameter is exposed. The final image spectrum therefore will consist of $N = \pi \cdot 280^2 = 246301$ single spectra. If a 2x2 - binning is performed which averages four adjacent pixel into one, the amount of spectra can be reduced to $N = 61575$, while the spatial resolution is also reduced by a factor four. To gain the biggest amount of information possible from a data set, it is in some cases useful to evaluate each single spectrum. Because of the huge amount of spectra this can economically only be performed in an automatized process. Depending on the complexity of the evaluation for each spectrum (e.g. fit) the whole process can take long computing times so that sometimes a compromise between quality and velocity of a fit procedure has to be found. Luckily this kind of evaluation task can be parallelized because the single spectra can usually be treated independent from each other. By using multi-core CPUs or even the huge amount of computing cores provided by today's graphic cards the evaluation time can be heavily reduced. Finally the evaluation procedure has to be robust enough to handle all different kinds of spectra (or even measurement errors) inside a data set. A quality check for each single fit (e.g. via a goodness of fit (GOF) value) is obligatory.

The second issue is that within an image spectrum acquired from a certain sample there will be regions, which have an equal spectroscopic fingerprint. If we imagine a structured sample which mainly consists of two different metals, we would expect only two different types of spectra among the thousands of single spectra. In such a case, statistical methods like the *principal component analysis* (PCA) can be used to extract the fundamental information from a data set and measurement errors like noise can be filtered out.

An automatized *work function analysis* which can be used to create a spatially resolved work function map of a sample is used for a variety of evaluations throughout this thesis. Beside a work function mapping of a structured sample (Sec. 8.2) these include the non-isochromaticity analysis of the energy filter (Ch. 6) and the

calibration of the detected momentum space (Sec. 7.2.1). The work function analysis is therefore introduced in some detail in the subsequent section.

4.1. Work function analysis

A spatial resolved *work function map* of a sample gives insights into the surface characteristic of the material under investigation, its crystallographic orientation (in the case of single crystals) and a possible coverage with adsorbates (see Sec. 2.4). Especially inhomogeneities of these characteristics can be discovered since they cause a work function difference $\Delta\Phi$ between the inhomogeneous regions of interest. This $\Delta\Phi$ can be detected much more precisely in energy than one would expect from the energy resolution of the energy filter¹. How a *work function shift* is detected in the energy filter of the *NanoESCA* is schematically shown in Fig. 4.1.

To create a work function map, an full image spectrum of the sample region of interest has to be acquired. The spectrum has to cover a few eV around the work function edge. Since the edge is a sharp feature the energy step size needs to be small for a precise fit. Each single spectrum in the image spectrum has to be evaluated to find the individual work function value at the corresponding spatial coordinates of the image. Depending on the resolution of the map this includes some ten thousand spectra, which have to be evaluated in an automatized procedure. The fitting function needs to be robust and fast. The latter requires to reduce the model to a small amount of free fit-parameters.

4.1.1. About the nature of the work function edge

A robust work function analysis needs a procedure to find a reliable value for the work function in a photoemission spectrum independently from eventual instrumental settings, measurement artifacts, noise or element specific changes to the shape of the work function edge. Therefore it is worth to list some issues which have influence on the appearance of this edge in the spectrum. Like it is shown in Fig. 2.2 and explained in Sec. 2.1.4, the *work function edge* is appended to the photoemission spectrum when the electrons have to overcome the surface potential. Photoelectrons with kinetic energies too small to overcome this barrier are cut off. This cut depends on the shape of the *surface potential* but is relatively sharp. Nevertheless it will

¹The work function analysis performed in Sec. 6.1 shows that work function differences smaller than 10 meV can be clearly distinguished, although the energy filter resolution was set to $\Delta E = 400$ meV.

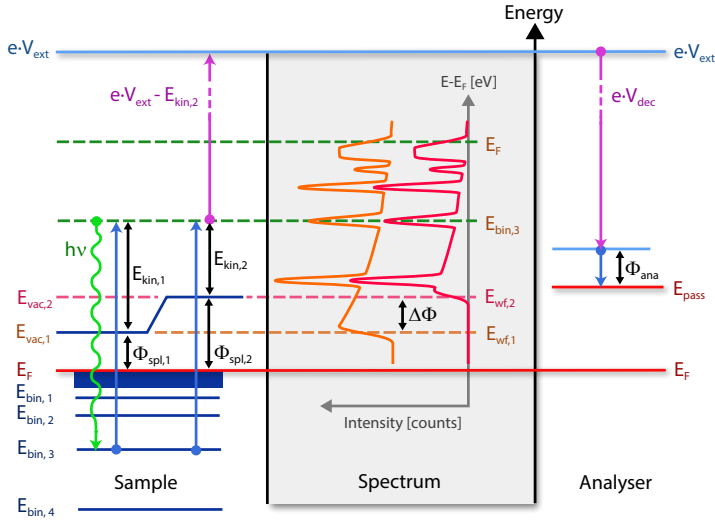


Figure 4.1.: Scheme of a work function difference detection in a photoemission experiment using the energy filter of the *NanoESCA*. The kinetic energy E_{kin} of the emitted photoelectrons from a specific core level (e.g. $E_{bin,3}$) changes with the work function of the sample. The core level is nevertheless detected at the same energy by the analyzer with reference to the Fermi level of the sample. Only the work function edge E_{wf} shifts to higher energies inside the spectrum with an increasing work function shift $\Delta\Phi$. For the work function analysis based on a fit-procedure it will make a difference if the work function edge appears in the secondary background ($E_{wf,1}$) of the photoemission spectrum or close to (or inside) a core level ($E_{wf,2}$) or valence band structure.

make some difference to the shape of the edge, how the spectrum looks like at the energetic position, where the cut happens. In the case of a high energetic photon excitation (e.g. synchrotron light) the cut will most likely appear in the *secondary electron background*, like it is shown in Fig. 4.1, if not, by chance, in a core level peak. The secondary backgrounds of different materials will differ in the intensity, but not so much in their shape. Furthermore they will be independent of the *energy resolution of the excitation source*, since the inelastically scattered secondary electrons have completely forgotten their initial energy [BLC⁺06]. In contrast, the photoelectron excitation with a low energetic light source (e.g. laser, Hg-lamp) will most probably lead to a work function edge cutting somewhere in the valence band. The shape of the valence band is very material dependent and also influenced by the energy resolution of the light source.

Instrumental aspects will additionally influence the shape of the measured work function edge. According to Eq. (2.17) the position of the work function edge in the measured spectrum depends on the direction in which the detected electrons leave the surface (see Fig. 7.9 (a)). This leads to the *photoemission horizon* shown in Fig. 7.7 (c). Only electrons which leave the sample perpendicular to its surface can be used for a direct work function determination according to Eq. (2.2). As shown in Fig. 5.5 the angular acceptance of the microscope in the real space imaging mode depends on the chosen *contrast aperture*. If a bigger CA is chosen, the work function edge for this partly angular integrated spectrum will become broader, like it is demonstrated in Fig. 7.13 (a). This broadening does not appear symmetrical around the actual work function edge but shifts to higher kinetic energies.

Finally, the photoemission spectrum is smeared out by the *resolution limit of the energy analyzer*, which broadens the measured work function edge. In contrast to the *photoemission horizon* effect, this broadening is applied symmetrically around the underlying spectrum. In most cases, the energy filter broadening will even be the dominant factor in the width of the measured work function edge. Anyway it is not straight forward to determine the energy resolution from it if the shape of the surface potential and the *photoemission horizon* effect is not taken into account.

4.1.2. Fit model for the work function edge

A procedure to find the work function value will be based on a fit-function. The method described in [BLC⁺06], for example, uses a straight line which is fitted to the work function edge. Its crossing with the baseline of the spectrum plus the energy resolution of the analyzer is regarded to give the true value of Φ . This line fit is

shown in Fig. 4.2(a, violet line), where it is applied to a photoemission spectrum of an uncleaned 100 nm Au-film (on Si), excited by a two-times frequency-doubled Nd:YAG laser ($h\nu = 4.66$ eV, $\Delta(h\nu) \approx 10$ meV). A contrast aperture of $30 \mu\text{m}$ was used for this experiment together with an energy resolution of approximately $\Delta E_{ana} \approx 100$ meV ($E_{pass} = 50$ eV, $d_{slit} = 0.5$ mm), which are the best settings possible with the *NanoESCA* for measuring a sharp work function edge. The spectrum was acquired in 25 meV steps. The line-fit cuts the baseline at $E - E_F = 4.17$ eV, which results in a measured work function of $\Phi = 4.27$ eV.

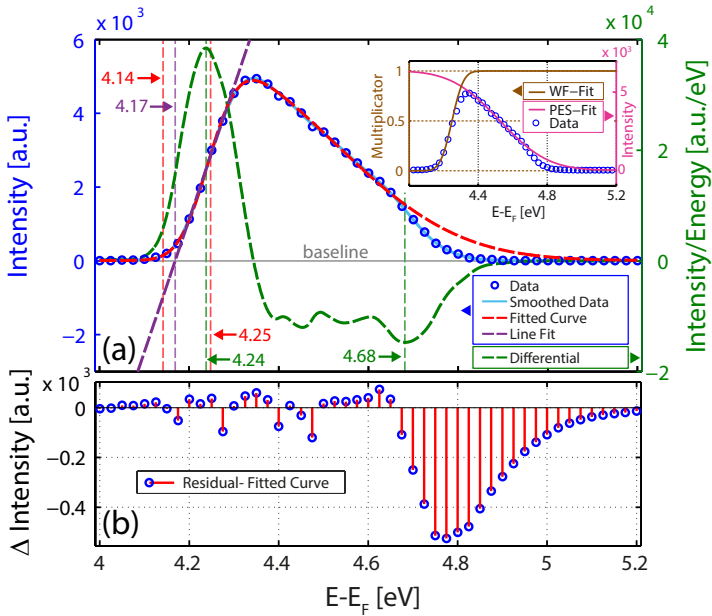


Figure 4.2.: (a) Example procedure of a work function fit on a Au photoemission spectrum excited by a 4.66 eV laser. To find the work function edge we calculate the differential of the smoothed data-curve and use the extrema (4.24 eV, 4.68 eV) as startpoints for the more precise fit-model presented in Eq (4.1). The residuals (b) of the fit show, that the model seems to represent the data very well, but the result of the edge fit (4.25 eV) also depends on the quality of the fit of the photoemission spectrum (see inset). Therefore, it is more reliable to derive Φ from the start of the edge (4.14 eV) according to Eq. (4.2).

The line-fit procedure is an adequate method for fitting a work function edge by hand, since the few data-points on the nearly straight flank of the edge, which should be taken into account for the fit, can be easily identified manually. For the automatized evaluation it is nevertheless desirable to have a more robust fit-function,

which takes more data-points into account. It has to be less dependent on exact start-values and less sensitive on a low signal-to-noise ratio. Therefore I developed a fit-model which describes the complete measured spectrum physically more correctly. It consists of two components, which is firstly a rough description of the shape of the measured photoemission spectrum (*PES-model*) and secondly the work function edge, which can be modeled by a step-function convoluted with a Gaussian function. This convolution is described by an error-function (see Sec. A.1). In many cases it was sufficient to also model the *PES-model* with a descending error-function. The overall fit-model for the photoemission intensity $I(\xi)$ as a function of the energy above Fermi level $\xi = E - E_F$ therefore can be written as

$$I(\xi) = \underbrace{\frac{1}{2} \cdot \left(1 + \operatorname{erf} \left(\frac{\xi - c_{wf}}{\sqrt{2} \cdot \sigma_{wf}} \right) \right)}_{\text{workfunction-edge}} \cdot \underbrace{\frac{I_0}{2} \cdot \left(1 - \operatorname{erf} \left(\frac{\xi - c_{pes}}{\sqrt{2} \cdot \sigma_{pes}} \right) \right)}_{\text{PES-model}} + I_{Bg} \quad (4.1)$$

and is shown as red, dashed line in Fig. 4.2 (a). The *PES-model* includes the (guessed) maximum intensity I_0 of the spectrum and the values defining the shape of the descending error-function (center c_{pes} , standard deviation σ_{pes}). This *PES-model* is cut-off at low energies by multiplying the ascending error-function representing the work function cut-off (center c_{wf} , standard deviation σ_{wf}). The model fits quite well to the data around the work function edge, which can be seen in the residuals of the fit shown in Fig. 4.2(b). The divergent part in this fit belongs to the Fermi edge. It could be included in the PES-model, but would cause longer evaluation times without gaining more accuracy for the work function fit.

The two components of the fit-model are shown separately in the inset of Fig. 4.2(a). It is obvious that the quality of the work function edge fit also depends on the applicability of the PES-model. Therefore the PES-model in Eq. (4.1) might be replaced, if another model is more reasonable. The FWHM of the work function fit can be used as a rough measure for the experimental energy resolution, if a small CA is used. For the edge in Fig. 4.2 a value of $\Delta E = 2\sqrt{\ln(2)} \cdot 2 \cdot \sigma_{wf} = 124 \pm 3$ meV is determined, which is indeed in the order of the expected analyzer resolution. To become fully independent from instrumental and especially material dependent influences for the measured work function edge, it is nevertheless recommended to not use the center $c_{wf} = 4.25$ eV of the fitted edge but rather a edge-width corrected value like

$$\Phi = c_{wf} - 2 \cdot \sigma_{wf} + \Delta E_{ana} = 4.242 \pm 0.003 \text{ eV}, \quad (4.2)$$

where the subtraction of approximately the half width ($2 \cdot \sigma_{wf}$) of the fitted edge from the center c_{wf} finds the start of the work function edge. This is comparable

with the line-fit method, although the gained values differ by 30 meV. To achieve the realistic value for Φ , the energy-filter resolution ΔE_{ana} has to be added again². However, usually only the work function difference $\Delta\Phi$ between different sample regions is of interest and the correction of the analyzer resolution is not necessary.

4.1.3. The fitting procedure

When applying the fit model in Eq. (4.1) in an automatized process to thousands of single spectra with potentially different work function values³, a pre-characterization of the work function spectrum is necessary to find appropriate start-values for the fit. Therefore, I differentiate the measured data after smoothing it (green curve in Fig. 4.2(a)). The absolute maximum of the differential marks the strongest ascending slope of the data and is a good guess for the center of the work function edge. In the same way the absolute minimum will indicate the position of the Fermi-edge, if the descending slope of the Fermi-edge is stronger than any descending slope of the measured band structure (which is usually true for the valence band). These values can be used as start values for c_{wf} and c_{pes} in the fit model. For σ_{wf} an approximate standard deviation of the analyzer energy resolution can be used and finally some value $\sigma_{pes} > \sigma_{wf}$ for the slope of the *PES-model*. A start value for the intensity I_0 can be the maximum value of the measured spectrum.

Since noise in the data set leads to heavy perturbations in the differential we have to smooth the data in an appropriate way before differentiating it. This is done by fitting a *smoothing spline* with an appropriate *smoothing parameter* to the data. The smoothing parameter defines the strength of the smoothing and should be chosen in a way that all noise is smoothed out but that the real slopes in the photoemission spectrum are preserved. Besides a standard nearest neighbors smoothing procedure, also a principal component analysis (PCA) could be used for a preliminary noise reduction, if a huge amount of in general similar spectra are available to calculate a generalized curve [HTWF08].

4.1.4. Applicability and robustness of the procedure

The described procedure proved a high robustness in several evaluations throughout this thesis. An example is the non-isochromaticity analysis shown in Fig. 6.2. A sample with a checkerboard structure made from two different elements (Au, Si) was

²The calculated value for the energy analyzer was used here. A more correct value is gained from a calibration measurement at the Fermi edge with an adequate single crystal, see Sec. 7.2.2

³work functions can have values between $\Phi = 2..6$ eV[Mic77]

analyzed over a field of view of 30 μm . After a correction of instrumental artifacts a very precise work function map could be extracted from the measurement. The Au pattern could be clearly separated from the Si substrate, although the work function difference was only around $\Delta\Phi \approx 10$ meV. Equal elements were detected with the same work function values in the complete field of view.

The same is true for the work function maps in Fig. 8.4, which show a sample with four different element compositions. The fit procedure gives the same results for equal elements. This works for an UV excitation as well as for an excitation with high energetic synchrotron radiation. Besides the work function map, also maps of the fitted edge-width and maps of the *goodness of fits* are shown for the two evaluations. The latter is an important tool to control, if the fit procedure worked for the whole data stack. A failed fit would have a small R^2 value and could be easily detected in the map. The examples nevertheless show that the fit procedure presented in this section lead to very homogenous results.

4.2. Principal Component Analysis

The *principal component analysis* (PCA) is a powerful statistical method to analyze the most significant components in e.g. a set of spectra. An image spectrum usually consists of a few different types of spectra (belonging to different chemical components) which appear in different areas on the sample. The absolute number of measured spectra for each of the different types will be huge (one spectrum at each image pixel). A statistical method like PCA therefore seems to be the perfect evaluation treatment.

A measured spectrum in our case is an array of n bins, each for one certain energy range ΔE . Each bin in this array was filled with a certain amount of electrons during the measurement. The result is an intensity distribution over a total energy range of size $n \cdot \Delta E$. The main trick to utilize PCA for a set of spectra is to see each spectrum as a vector \vec{s} in a n -dimensional vector space. Each spectrum is then a linear combination of n basis vectors, each representing one energy bin. Spectrum i

can be written in the form

$$\vec{s}_i = \begin{pmatrix} s_{1i} \\ s_{2i} \\ s_{3i} \\ \dots \\ s_{ni} \end{pmatrix} = s_{1i} \cdot \begin{pmatrix} 1 \\ 0 \\ 0 \\ \dots \\ 0 \end{pmatrix} + s_{2i} \cdot \begin{pmatrix} 0 \\ 1 \\ 0 \\ \dots \\ 0 \end{pmatrix} + s_{3i} \cdot \begin{pmatrix} 0 \\ 0 \\ 1 \\ \dots \\ 0 \end{pmatrix} + \dots + s_{ni} \cdot \begin{pmatrix} 0 \\ 0 \\ 0 \\ \dots \\ 1 \end{pmatrix} \quad (4.3)$$

where s_{ji} are the amount of electrons (the intensity) for each energy bin. If we imagine now that there are actually only two different chemical components (a and b) in our sample, each measured spectrum could actually only be a linear combination of two different basis vectors (\vec{a} and \vec{b}), each one representing the clean spectrum of a single component, plus some vectors \vec{v}_k representing perturbations in the spectra, which do not belong to the chemical components (e.g. background, noise, instrumental artefacts etc.). We can then write Eq. (4.3) as

$$\vec{s}_i = \begin{pmatrix} s_{1i} \\ s_{2i} \\ s_{3i} \\ \dots \\ s_{ni} \end{pmatrix} = c_{1i} \cdot \begin{pmatrix} a_1 \\ a_2 \\ a_3 \\ \dots \\ a_n \end{pmatrix} + c_{2i} \cdot \begin{pmatrix} b_1 \\ b_2 \\ b_3 \\ \dots \\ b_n \end{pmatrix} + c_{3i} \cdot \begin{pmatrix} v_{11} \\ v_{21} \\ v_{31} \\ \dots \\ v_{n1} \end{pmatrix} + \dots + c_{ni} \cdot \begin{pmatrix} v_{1(n-2)} \\ v_{2(n-2)} \\ v_{3(n-2)} \\ \dots \\ v_{n(n-2)} \end{pmatrix} \quad (4.4)$$

where c_{ji} are the coefficients of the new basis vectors. All new basis vectors still need to be orthogonal to each other in the n -dimensional vector space. The goal of PCA is exactly to identify these new basis vectors (called *principal components*) in the full set of experimentally acquired spectra and to sort them by the frequency of their appearance. While the two vectors \vec{a} and \vec{b} in our example will appear in every measured spectrum \vec{s}_i , the perturbations \vec{v}_k will appear much more randomly. The most important *principal components* therefore can be easily identified. A drawback nevertheless is that the *principal components* are identified in such a way that the most significant components account for the biggest amount of measured spectra \vec{s}_i . Therefore, the resulting basis vectors in general do not represent a decomposition into the real single spectra of the separate chemical components but rather *abstract factors*.

The set of new abstract basis vectors and their coefficients in Eq. 4.4 still include the full set of measured data. If we can really identify all other principal components as not physical (noise etc.), it is possible to neglect them and to reconstruct each spectrum \vec{s}_i' only from the relevant principal components. This is a direct noise

canceling method for the spectra and also reduces the amount of data which has to be saved.

In energy filtered photoemission microscopy PCA as a consequence can be first of all useful to separate real spectral information from noise [HTWF08]. This is necessary to gain information from image-spectra which have a low statistic due to limited electron count rates like it is the case in the field of hard X-ray photoemission microscopy (see Cha. 8). Nevertheless, the procedure can only work properly if continuous energy shifts like they are, for example, introduced by the *non-isochromaticity* of the energy-filter of the *NanoESCA* are eliminated (see Cha.6).

4.3. Conclusions

The huge amount of data which is generated by an energy-filtered photoemission microscope needs advanced automatized evaluation algorithms, for which the work function analysis presented in this chapter is one example. Also statistical methods like the *principal component analysis* are useful to extract the important information out of the measurements and to reduce the amount of data which needs to be stored.

5. Objective lens calculations

The first module of a photoemission microscope which electrons have to pass after their excitation is the one with the biggest influence on the microscopes resolution and transmission characteristics: the *immersion objective lens*. The accepted phase space of the electrons, which is, for example, influenced by the microscope's extractor potential V_{ext} , its sample potential V_{spl} (used for the energy-filtering) and the contrast aperture (CA) have fundamental impacts on the final image (e.g. resolution, magnification) in the real-space mode as well as in the momentum mode. In this chapter I show basic electron-optical calculations of the objective lens system, which will help to understand these impacts on the measurements performed with the *NanoESCA*. In contrast to the existent literature (e.g. [RG89]), this work has a special focus on the results for high *kinetic electron energies*, as they are used in the new *HAXPEEM* approach (see Cha. 8). The typical assumption that the electron kinetic energy is small against the extractor voltage ($V_0 \ll V_{ext}$) is in general no longer valid.

5.1. Basic calculations

For exact simulations of particle trajectories in electron-optical systems nowadays computer programs like *Simion* [Dah00] iteratively solve the *Laplace* equation for the electrode configurations involved to calculate the electrostatic potentials in space. Subsequently, the particle trajectories are simulated by evaluating the gradients of the potentials at each point in space and their impact on the particles with respect to their current position in the phase space (e.g. direction and momentum). Figure 5.1 shows a realistic diagram of the potentials and electron-trajectories inside a tetropole objective lens like the one of the *NanoESCA*, consisting of the sample and an extractor, focus and column electrode.

The goal of this section is to describe the characteristics of the NanoESCA objective lens by algebraic functions, although we have to introduce some simplifications. The dominant simplification will be the treatment of the three electrodes shown in

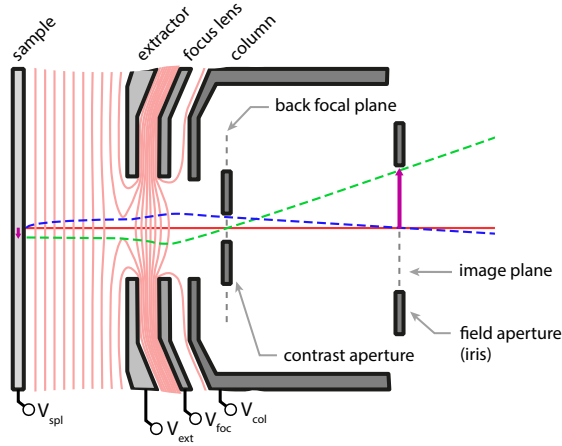


Figure 5.1.: Diagram of an immersion objective lens with equipotential lines (light red) and two different electron trajectories passing through these potentials. In general, the potential V_{ext} is high compared to V_{spl} and V_{col} . The focusing potential V_{foc} is slightly higher than V_{col} . The trajectory starting parallel to the optical axis (green) crosses the optical axis in the back focal plane. The blue trajectory starts from the optical axis with an angle and crosses the optical axis again in the image plane. The magnification of the lens depends on values of the indicated potentials. The contrast aperture and the iris have a fixed position in the microscope column. Usually the lens potentials are adjusted such that the back focal plane of the objective lens appears at the position of the contrast aperture.

Fig. 5.1 (extractor, focus lens, column) as a single, thin lens with a magnification M . The calculations then become analog to those of a thin lens in classical optics. The geometrical construction of the lens behavior and the relation to the real electron trajectories between the sample and the extractor-anode are shown in Fig. 5.2. We will discuss the various aspects of this construction piecewise, starting with the calculation of the electron-trajectories between the sample and the extractor.

5.1.1. Electron kinetics between sample and extractor

Our first calculation handles a photoelectron leaving the sample with a kinetic start-energy

$$E_{kin} = \frac{1}{2} \cdot m_e \cdot v_0^2 = e \cdot V_0. \quad (5.1)$$

The last part of this equation is of technical nature because it suggests that the electron gained its kinetic energy from an electric acceleration field rather than from a photon. Although the latter is true, the former leads to a more handy notation and

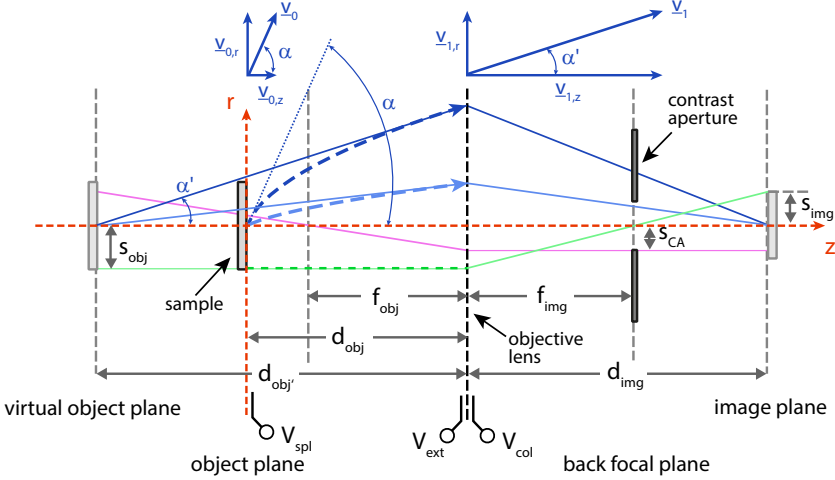


Figure 5.2.: The graphic combines a sketch of the simplified microscope objective lens, the calculated electron trajectories between the sample and the extractor anode and the geometrical optics construction which are used for the calculations in this chapter. See text for details.

is therefore used in the following. The electron is then accelerated in the electric field between the sample potential V_{spl} and the extractor potential V_{ext} . It is important to note that the filter-energy of the microscope is tuned by V_{spl} , which therefore can not be treated as a fixed value. While in the non-energy filtered PEEM mode of the *NanoESCA* the sample voltage is set to ground potential ($V_{spl} = 0$ V), it is set to the kinetic energy of the photoelectrons ($V_{spl} = V_0$) in the energy-filtered mode. The photoelectrons which should pass the hemispherical energy analyzer therefore will reach the extractor with a specified kinetic energy

$$E_{kin,ext} = e \cdot (V_0 + (V_{ext} - V_{spl})) = e \cdot V_{ext}. \quad (5.2)$$

That will be used later for some simplifications of the equations in this chapter.

To calculate the electron trajectories we use the cylinder symmetric coordinate system shown in Fig. 5.2 where z is the distance along the optical axis of the microscope (starting in the sample/object plane) and r the distance perpendicular to this axis. As an approximation we treat the electric field between the sample and the extractor as homogenous so that we can calculate with a constant force

$$F = m_e \cdot a_z = e \cdot \frac{(V_{ext} - V_{spl})}{d_{obj}} \quad (5.3)$$

which accelerates the electrons in z-direction towards the extractor. The equation of motion of an electron with constant velocity along the r - direction as a function of time is then

$$r(t) = \underbrace{v_0 \cdot \sin(\alpha)}_{=v_{0,r}} \cdot t \quad (5.4)$$

and for the acceleration in z-direction we get

$$z(t) = \underbrace{v_0 \cdot \cos(\alpha)}_{=v_{0,z}} \cdot t + \frac{1}{2} \cdot a_z \cdot t^2. \quad (5.5)$$

Combining the two equations and eliminating the time t results into the quadratic equation and its solution

$$A \cdot r^2 + B \cdot r - z = 0 \quad \text{and} \quad r_{1,2} = \frac{-B \pm \sqrt{B^2 + 4 \cdot A \cdot z}}{2 \cdot A} \quad (5.6)$$

with

$$A = \frac{1}{2} \cdot \frac{a_z}{v_{0,r}^2} = \frac{1}{4} \cdot \frac{(V_{ext} - V_{spl})}{V_0 \cdot d_{obj}} \cdot \frac{1}{\sin(\alpha)^2} \quad \text{and} \quad B = \frac{v_{0,z}}{v_{0,r}} = \frac{1}{\tan(\alpha)} \quad (5.7)$$

The complete algebraic expression for the electron trajectories is therefore finally

$$r_{1,2}(z) = \pm \frac{2 V_0 d_{obj} \sin(\alpha)}{V_{ext} - V_{spl}} \cdot \left(\sqrt{\frac{\cos^2(\alpha) V_0 d_{obj} + (V_{ext} - V_{spl}) z}{V_0 d_{obj} \sin^2(\alpha)}} \cdot \sin(\alpha) \mp \cos(\alpha) \right). \quad (5.8)$$

With this equation we can calculate the electron trajectories between the sample and the extractor as a function of the microscope settings. Some typical trajectories and relations are shown in Fig. 5.3. The most obvious results of these simulations are

- The distance $\Delta r(z = d_{obj})$ between electron trajectories with equidistant start-angles $\Delta \alpha$ in the extractor plane becomes smaller for bigger start angles (see Fig. 5.3(a,d)): $d^2 r(z = d_{obj}) / d\alpha^2 < 0$.
- For a smaller acceleration potential $(V_{ext} - V_{spl})$ or higher electron start energies $e \cdot V_0$ photoelectrons starting on the optical axis under some angle will reach the extractor with a bigger distance from the optical axis (b,c,e,f). Electrons which are too far outside will not enter the microscope anymore, which results in smaller accepted start angles and a lower transmission. In the energy-filtered mode, both happens at the same time.

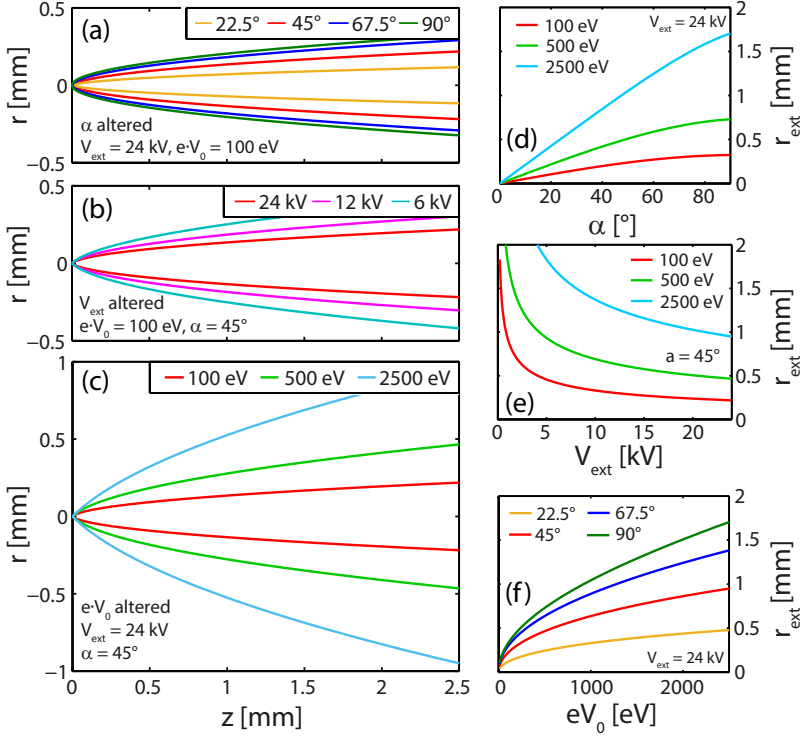


Figure 5.3.: The graphs (a)-(c) show electron trajectories between the sample surface ($z = 0 \text{ mm}$) and the extractor ($z = 2.5 \text{ mm}$) calculated with Eq. 5.8 as a function of (a) the electron emission angle α , (b) the extractor voltage V_{ext} and (c) the electron's kinetic start energy $e \cdot V_0$. All not altered parameters are kept on constant values ($e \cdot V_0 = 100 \text{ eV}$, $V_{ext} = 24 \text{ kV}$, $\alpha = 45^\circ$, $d_{obj} = 2.5 \text{ mm}$). The red line in each graph marks the trajectory with these standard parameters. Like in the energy filtered operation mode, V_{spl} was set equal V_0 . To understand the influence of the potentials we calculate the distances r_{ext} of the trajectories from the optical axis which the electrons have when they reach the extractor anode. These distances are shown in graphs (d)-(e) as a function of (d) the emission angle α , (e) the extractor voltage V_{ext} and the kinetic photoelectron start energy $e \cdot V_0$.

5.1.2. Conversion from the electron emission angle α to the microscope entrance angle α'

Due to the strong electric field between the sample-plane and the extractor the electron trajectories leaving the sample are bent towards the extractor. The emission angle α has converged to α' when it reaches the extractor. The microscope sees the electron entering under this new angle α' and with the new velocity v_1 . As it is shown in Fig. 5.2 we can construct this situation in geometrical optics using a virtual object and straight electron trajectories. While we are using α' for the geometrical calculations in Sec. 5.2, it is necessary to subsequently convert it back to the original electron emission angle α .

The dark blue dashed line in Fig. 5.2 indicates an electron trajectory with the start-angle $\alpha = 45^\circ$. The value of this angle along the trajectory $\alpha''(z)$ can be calculated by the first derivative in each point. Using equation 5.8 we get:

$$\tan(\alpha''_{1,2}(z)) = \frac{dr_{1,2}(z)}{dz} = \pm \left(\frac{1}{\tan^2(\alpha)} + \frac{(V_{ext} - V_{spl}) \cdot z}{V_0 d_{obj} \sin^2(\alpha)} \right)^{-1/2} \quad (5.9)$$

In the following we just use the first solution (valid for positive emission angles). The entrance angle into the microscope we gather from the previous equation by evaluating it as $\alpha' = \alpha''(z = d_{obj})$ and get

$$\tan(\alpha') = \tan(\alpha) \cdot \left(1 + \frac{V_{ext} - V_{spl}}{V_0 \cdot \cos^2(\alpha)} \right)^{-1/2} \quad (5.10)$$

$$\underset{V_{spl}=V_0}{\approx} \sin(\alpha) \cdot \sqrt{\frac{V_0}{V_{ext}}}. \quad (5.11)$$

The last approximation is valid for the energy filtered case $V_{spl} = V_0$ and small angles α . More useful for our aforementioned converting purpose is the inverse function of Eq. 5.10, which converts the microscope entrance angle α' into the electron start angle α between 0° and 90° :

$$\tan(\alpha) = \left(\frac{V_0}{V_0 + V_{ext} - V_{spl}} \cdot \left(1 + \frac{1}{\tan^2(\alpha')} \right) - 1 \right)^{-1/2} \quad (5.12)$$

$$\underset{V_{spl}=V_0}{=} \left(\frac{V_0}{V_{ext}} \cdot \left(1 + \frac{1}{\tan^2(\alpha')} \right) - 1 \right)^{-1/2}. \quad (5.13)$$

The last expression is again true for the energy-filtered mode. Below I will continue to calculate with the full set of relevant potentials ($V_0, V_{ext}, V_{spl}, V_{col}$) and additionally show the simpler solutions for the energy-filtered mode. Both Eq. 5.10 and Eq. 5.12 are plotted in Fig. 5.4 for different kinetic electron start energies eV_0 .

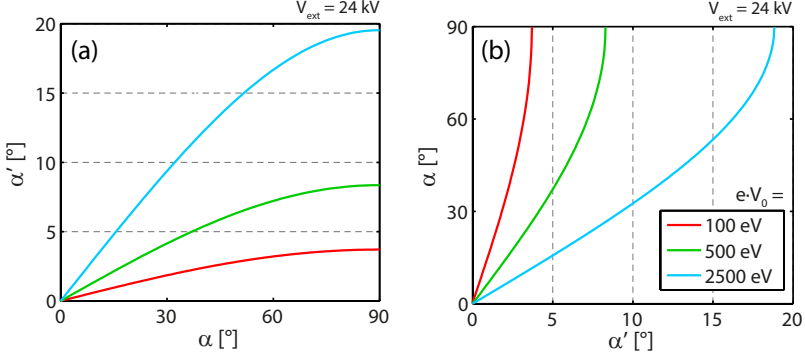


Figure 5.4.: (a) The figure shows, how the electron emission angles α are converted to the microscope's entrance angles α' . The results are strongly dependent on the photoelectron start energies $e \cdot V_0$. The related inverse functions are plotted in (b). The graphs were calculated for an extractor voltage of $V_{ext} = 24$ kV.

Note that the same result as in Eq. (5.12) can be achieved by an energy conservation approach, if the velocity vectors parallel and antiparallel to the optical axis of the emitted electron and the accelerated electron are compared to each other. This leads to a simpler expression

$$\sin(\alpha) = \sin(\alpha') \cdot \left(\frac{V_0 + V_{ext} - V_{spl}}{V_0} \right)^{1/2}. \quad (5.14)$$

Eq. (5.12) and Eq. (5.14) are identical, which is shown in Sec. B.1. Although Eq. (5.12) has a more complicated form, it is much more useful in the upcoming calculations, because most of the time we will need $\tan(\alpha)$ instead of $\sin(\alpha)$.

5.1.3. Estimation of relativistic corrections

Due to the high acceleration of the electrons inside the *NanoESCA* immersion lens with its extractor potential of up to $V_{ext} = 24$ kV we have to analyze how far *relativistic corrections* may become necessary in our calculations above. Therefore we will compare the final electron-velocities at the extractor plane according to a relativistic (index *r*) and a non-relativistic (index *nr*) calculation. In the latter case we expect that the potential energy of the acceleration-field between the sample and the extractor is converted into the kinetic energy of the electron

$$E_{kin} = \frac{1}{2} \cdot m_e \cdot v_{ext,nr}^2 = e \cdot V_0 + e \cdot (V_{ext} - V_{spl}) \quad (5.15)$$

The final electron-velocity is therefore

$$v_{ext,nr} = \sqrt{\frac{2 e (V_0 + V_{ext} - V_{spl})}{m_e}} = 9.188 \cdot 10^7 \frac{m}{s} = 0.305 \cdot c \quad (5.16)$$

for the energy-filtered mode ($V_{spl} = V_0$) and an extractor potential of $V_{ext} = 24 \text{ kV}$. The electrons would reach approximately 30% of the light velocity which makes relativistic corrections reasonable. In the relativistic case, some of the acceleration energy will go to the increase of the relativistic electron mass $m(v_{ext,r})$ which is described by

$$\frac{m(v_{ext,r})}{m_0} = \frac{1}{\sqrt{1 - \left(\frac{v_{ext,r}}{c}\right)^2}} \quad (5.17)$$

where $m_0 = m_e$ is the rest mass of the electron [Dem10]. With the electron rest energy $E_0 = m_0 \cdot c^2$ we can write the conservation of energy as

$$E_{total} = E_{kin} + m_0 c^2 = m(v_{ext,r}) c^2 \quad (5.18)$$

$$\Rightarrow E_{kin} = (m(v_{ext,r}) - m_0) \cdot c^2 = e \cdot (V_0 + V_{ext} - V_{spl}) \quad (5.19)$$

The velocity of the electron at the extractor-plane can be achieved by inserting Eq. 5.17 into Eq. 5.19 which gives

$$v_{ext,r} = c \cdot \sqrt{1 - \left(\frac{e \cdot (V_0 + V_{ext} - V_{spl})}{m_0 \cdot c^2} + 1\right)^{-2}} = 8.878 \cdot 10^7 \frac{m}{s} = 0.296 \cdot c. \quad (5.20)$$

for the energy-filtered mode ($V_{spl} = V_0$) and an extractor potential of $V_{ext} = 24 \text{ kV}$. The quotient of the relativistic and non-relativistic calculations of the velocities is

$$\frac{v_{ext,r}}{v_{ext,nr}} = 0.966. \quad (5.21)$$

That means that by not using the relativistic calculation we expect an error of 3.4 % on the electron velocity. Because our calculations anyway include several approximation this is still acceptable. I will go on with non-relativistic calculations for the sake of clearness and to avoid too complex formula. For exact calculations, relativistic effects have to be taken into account. The same is true for even higher extractor voltages.

5.2. Acceptance angle of the objective lens

The goal of this paragraph is to calculate the maximal *accepted electron emission angle* α which can enter the microscope. As we will see, α strongly depends on the

radius s_{CA} of the *contrast aperture* used and on the kinetic electron start energy. The electrons entering the microscope pass through the objective lens shown in Fig. 5.1. Electrons starting on the sample parallel to the optical axis will be focused in the back focal plane and form an image with the *magnification* M in the first image plane. At the same time the electrons are retarded by the potential difference between the extractor and the column (typical settings are $V_{ext} = 24.0 \text{ kV}$, $V_{foc} = 2.4 \text{ kV}$ and $V_{col} = 2.0 \text{ kV}$). The contrast aperture is placed in the back focal plane and reduces the angular distribution entering the microscope column. This reduction improves the spatial resolution (see Sec. 5.4) of the image, but at the same time lowers the transmission (see 5.3). In general, a compromise between lateral resolution and necessary exposure time has to be found. The following relations are based on the geometric construction shown in Fig. 5.2. Note, that the objective lens is simplified by a thin lens.

The maximal accepted entrance angle α'_{max} allowed by the contrast aperture can be constructed with the help of the violet line in Fig. 5.2. On the image side of the lens we draw a line parallel and with the distance s_{CA} (aperture radius) to the optical axis. This line is bend by the objective lens and crosses the optical axis at the focal length of the object side f_{obj} . Therefore we can write

$$\tan(\alpha'_{max}) = \frac{s_{CA}}{f_{obj}} \quad (5.22)$$

The ratio of (f_{obj}) and the focal length on the image side (f_{img}) of the lens is equal to the ratio of the square roots of the potentials on each side of the lens, which is a general property of all immersion lenses and analogous to the ratio of the *refractive indices* n_x of immersion lenses in light optics $f_{obj}/f_{img} = n_{obj}/n_{img}$ [Lie10].

$$\frac{f_{obj}}{f_{img}} = \sqrt{\frac{V_{ext} - V_{spl} + V_0}{V_{col}}} \stackrel{V_{spl}=V_0}{=} \sqrt{\frac{V_{ext}}{V_{col}}} \quad (5.23)$$

The focal length on the image side f_{img} we calculate by making use of the intercept theorem (using the green line in Fig.5.2) and connecting the result with the objective lens magnification M , which is defined by the relation between the size of the object s_{obj} and its image s_{img} .

$$M = -\frac{s_{img}}{s_{obj}} = -\frac{d_{img} - f_{img}}{f_{img}} \quad (5.24)$$

Together with the last two relations we can write Eq. 5.22 as

$$\tan(\alpha'_{max}) = |M| \cdot \sqrt{\frac{V_{col}}{V_{ext} - V_{spl} + V_0}} \cdot \underbrace{\frac{s_{CA}}{d_{img} - f_{img}}}_{=\tan(\beta_{max})} \quad (5.25)$$

where β_{max} is the maximum angle of the electron trajectories behind the objective lens, which can pass the CA. Note that $\beta_{max} > \alpha'_{max}$ in our microscope because $|M| \cdot \sqrt{V_{col}/V_{ext}} > 1$. Using Eq. 5.12 we can finally calculate the maximal electron emission angle α_{max} which can pass the contrast aperture

$$\tan(\alpha_{max}) = \left(\frac{V_0 \cdot (d_{img} - f_{img})^2}{s_{CA}^2 V_{col} M^2} - \frac{V_{ext} - V_0}{V_{ext} - V_{spl} + V_0} \right)^{-1/2} \quad (5.26)$$

$$\underset{V_{spl}=V_0}{=} \left(\frac{V_0 \cdot (d_{img} - f_{img})^2}{s_{CA}^2 V_{col} M^2} + \frac{V_0}{V_{ext}} - 1 \right)^{-1/2}. \quad (5.27)$$

Under ideal conditions the distance between the focal point of the objective lens and its first image plane ($d_{img} - f_{img}$) as well as the focal length f_{img} itself are fixed quantities for the NanoESCA so that the focal plane of the lens is positioned in the plane of the contrast aperture and the image plane sits in the plane of the iris (see Fig. 5.1). Depending on the chosen ratio of the extractor voltage and the column voltage V_{ext}/V_{col} as well as of the kinetic energy of the photoelectrons $e \cdot V_0$, the focus anode potential V_{foc} is adjusted to meet these conditions. The NanoESCA is constructed such that this works exactly only for the ratio $V_{ext}/V_{col} = 12$ (e.g. for our standard setting with $V_{ext} = 24 \text{ kV}$ and $V_{spl} = 2 \text{ kV}$). Realistic values for the objective magnification M_{obj} of the NanoESCA were gathered from simulations. Fig. 5.5(a) shows these simulated magnifications M_{obj} as a function of V_0 and for different V_{ext} , keeping $V_{ext}/V_{col} = 12$ on the optimal value. With this information we can calculate the maximal accepted angles of the microscope as a function of V_0 and for all available contrast-aperture diameters. They are shown in Fig. 5.5(b). In Sec. 7.2.3 the calculated acceptance angles are compared with measurements. It is shown that the approach presented here leads to reasonable results.

5.2.1. Relation between contrast aperture and energy analyzer entrance slit

The radius s_{CA} of the *contrast aperture* defines the maximum angle β_{max} (see Eq. (5.25) and Fig. 5.2) for paraxial electron trajectories in the first image plane. The second aperture which can further reduce the angular phase space in the microscope is the *entrance aperture* of the energy analyzer (see Sec. 3.1.3). For an interpretation of effects in the energy analyzer (see Ch. 6) which are related to the angular phase space it is necessary to know by which of the two apertures the phase space is defined. The maximum accepted angle $\alpha_{0,max}$ of electron trajectories in the intermediate image plane in front of the analyzer (see Fig. 6.4) can be calculated for an analyzer entrance

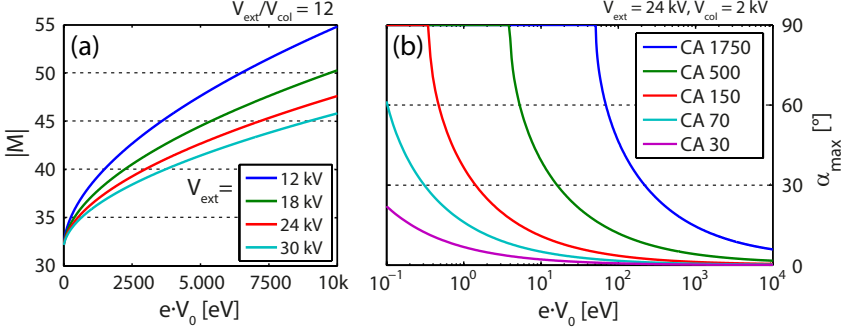


Figure 5.5.: (a) Objective lens magnification M_{obj} and (b) calculated maximal accepted electron emission angle α_{max} as a function of the kinetic photoelectron start energy eV_0 . The magnification $M_{obj}(V_0, V_{ext})$ was simulated for the realistic objective lens configuration of the NanoESCA and is used in Eq. 5.12 to calculate the $\alpha_{max}(V_0, s_{CA})$ shown in (b). The given CA-numbers in the legend specify the diameters of the used contrast apertures in μm .

slit of radius r_{entr} with Eq. (6.4). This angle has to be compared with the value of β_{max} in the same intermediate image plane in front of the analyzer.

The transformation of angles β_i between two image planes can be calculated with the *law of Helmholtz and Lagrange*, which can be expressed for conjugate planes by

$$\sqrt{eV_1} \cdot \sin \beta_1 = M \cdot \sqrt{eV_2} \cdot \sin \beta_2, \quad (5.28)$$

where eV_i are the kinetic electron energies in either plane and M is the magnification between both planes [KS67]. To transform β_{max} from the first image plane to the intermediate image plane in front of the analyzer, we have to take into account a retardation from the column potential V_{col} to the pass energy potential $V_{pass} = E_{pass}/e$ and a weak magnification M_{proj} in the projection lenses which leads to a maximum angle in the intermediate image plane of

$$\underbrace{\sin(\alpha_{0,max})}_{=\beta'_{max}} = \sqrt{\frac{V_{col}}{V_{pass}}} \cdot \frac{1}{M_{proj}} \cdot \sin \left(\arctan \left(\underbrace{\frac{s_{ca}}{d_{img} - f_{img}}}_{\beta_{max}} \right) \right) \quad (5.29)$$

Which aperture is dominantly reducing the angular space strongly depends on the radius s_{ca} of the contrast aperture, the radius r_{entr} of the analyzer entrance slit (see Eq. (6.4)) and its pass energy E_{pass} . Figure 5.6 shows the effect of these parameters on the maximal angle $\alpha_{0,max}$ which will enter the energy analyzer. The red lines mark the angular minimum as it is defined by the entrance slit while the dashed lines

mark the angular minimum as it is defined by the CA (shown for several E_{pass}). For most of the standard settings in the real space mode of the instrument, the CA dominates the angular phase space. Only if big CAs are used together with small entrance slits and small pass energies the situation is contrary¹.

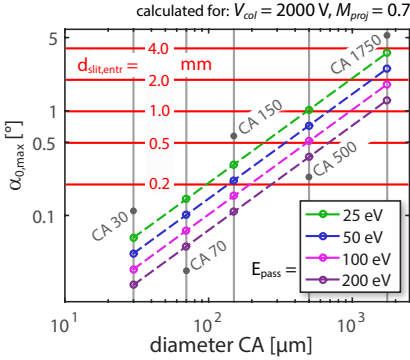


Figure 5.6: The graph shows, if either the entrance slit d_{slit} of the analyzer or the contrast aperture CA in the objective lens determines the maximum angle $\alpha_{0,max}$ which enters the analyzer. How the angle reduction of the CA is transferred to the analyzer entrance plane also depends on the pass energy E_{pass} (see text). E.g., for a typical analyzer setting ($E_{pass} = 100$ eV, $d_{slit} = 1$ mm) $\alpha_{0,max}$ is determined by the CA for $d_{ca} = 500$ μm but determined by the entrance slit for $d_{ca} = 1750$ μm .

5.3. Transmission of the objective lens

A reduced *acceptance angle* (see Sec. 5.2) consequently leads to a reduced *transmission* of the microscope and to longer exposure times to reach adequate statistics. To analyze this, we calculate the relative transmission T of the microscope as the ratio of an angle-dependent photoelectron intensity distribution $I(\alpha, \varphi)$ integrated over the accepted solid angle $\Omega_{max}(s_{CA})$ and the overall photoelectron intensity I_0 emitted into the full half space in front of the sample Ω_{full} . For the latter we can write

$$I_0 = \int_{\Omega_{full}} I(\alpha, \varphi) d\Omega = \int_0^{2\pi} \int_0^{\pi/2} I(\alpha, \varphi) \sin(\alpha) d\varphi d\alpha. \quad (5.30)$$

and the transmission as a function of the maximum acceptance angle α_{max} becomes

$$T(\alpha_{max}) = \frac{1}{I_0} \cdot \int_{\Omega_{max}} I(\alpha, \varphi) d\Omega = \frac{1}{I_0} \cdot \int_0^{2\pi} \int_0^{\alpha_{max}} I(\alpha, \varphi) \sin(\alpha) d\varphi d\alpha \quad (5.31)$$

In general the angular photoelectron distribution $I(\alpha, \varphi)$ which is emitted from the sample depends on the sample under investigation. To get anyway an idea of the

¹This is e.g. the case for *momentum microscopy* with high energy resolution (see Sec. 7.2)

microscope's transmission we will discuss two cases. The simplest case neglects any angular dependencies (model 1 in Fig. 5.7):

$$I_1(\alpha, \varphi) = \frac{I_0}{2\pi}. \quad (5.32)$$

The scaling was chosen in such a way that it fulfills Eq. 5.30. This is probably the best approach to describe the microscope's transmission, because it ignores any influence of a sample system. It rather describes a model system in which the same amount of photoelectrons is emitted in any direction of the half space in front of the sample (like a point source on the surface).

Nevertheless we get a more realistic model, when we take into account that most samples under investigation have a certain thickness. The aforementioned model describes well the emission characteristic of the surface layer, but electrons excited in a deeper layer with a distance z to the surface have a certain scatter probability on their way to the surface. While the way is shortest for an electron traveling perpendicular to the surface, it increases like $1/\cos(\alpha)$ with increasing emission angle α and therefore the scattering probability increases, too. The ratio for the non-scattered electrons reaching the surface from a specific location in the sample can be described with the inelastic mean free path $\lambda(E_{kin})$ of the electron² as follows [Hüf03, p. 12]:

$$\frac{I(z, \alpha)}{I_0} = e^{-\frac{z}{\lambda \cdot \cos(\alpha)}} \quad (5.33)$$

Assuming a sample of thickness t we can integrate over z and get the emission-angle-dependent intensity ratio for the whole sample

$$\frac{I(\alpha)}{I_0} = \int_0^t e^{-\frac{z}{\lambda \cdot \cos(\alpha)}} dz = \lambda \cdot \cos(\alpha) \cdot \left(1 - e^{-\frac{t}{\lambda \cdot \cos(\alpha)}}\right) \quad (5.34)$$

For samples with $t \gg \lambda$ we therefore use the photoelectron distribution

$$I_2(\alpha, \varphi) = \frac{I_0}{\pi} \cdot \cos(\alpha) \quad (5.35)$$

as a model system (model 2 in Fig. 5.7) to calculate a more realistic transmission characteristics. The scaling again fulfills Eq. 5.30. The two models discussed here mark the extrema of a real photoemission experiment with either a sample of zero thickness or a sample of infinite thickness. Real-world samples will lie somewhere in between.

²The inelastic mean free path λ of an electron (see Sec. 2.1.3) depends on its kinetic electron energy E_{kin} and the material of the layer it passes. The following calculation with a constant λ is therefore valid for an energy filtered measurement. For a non-energy-filtered measurement, the energy dependency of λ has to be taken into account.

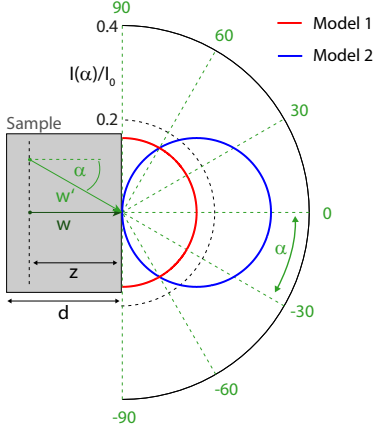


Figure 5.7: Left side: Photoelectrons originating from a depth z travel a longer distance $w' = w/\cos(\alpha)$ through the material, if the emission angle $\alpha > 0$. This leads to a higher scattering rate for this photoelectron. Different experiment setups (depending on the sample thickness t and the inelastic mean free path λ of the photoelectron) have therefore different angle-dependent emission characteristics. On the left we show the polar plots of the two emission characteristics discussed in the text: the angle-independent distribution (red) and the $\cos(\alpha)$ -distribution (blue).

On this basis we calculate the transmissions for the two models with Eq. 5.31 and subsequently use Eq. 5.26 to convert the maximum allowed acceptance angle $\alpha_{max}(sca)$ into the objective lens parameters. For our first model described in Eq. 5.32 we obtain the transmission

$$T_1(\alpha_{max}) = \int_0^{\alpha_{max}} \sin(\alpha) d\alpha = 1 - \cos(\alpha_{max}) \quad (5.36)$$

$$= 1 - \left(\left(\frac{V_0}{V_{col}} \left(\frac{d_{obj} - f_{obj}}{sca M} \right)^2 - \frac{V_{ext} - V_0}{V_{ext} - V_{spl} + V_0} \right)^{-1} + 1 \right)^{-1/2} \quad (5.37)$$

using the relation $\cos(\arctan(\xi)) = (\xi^2 + 1)^{-1/2}$. For our second model described in Eq. 5.35 we get:

$$T_2(\alpha_{max}) = 2 \cdot \int_0^{\alpha_{max}} \cos(\alpha) \cdot \sin(\alpha) d\alpha = \sin^2(\alpha_{max}) \quad (5.38)$$

$$= \left(\frac{V_0}{V_{col}} \left(\frac{d_{img} - f_{img}}{sca M} \right)^2 - \frac{V_{ext} - V_0}{V_{ext} - V_{spl} + V_0} + 1 \right)^{-1} \quad (5.39)$$

$$=_{V_{spl}=V_0} \left(\frac{V_0}{V_{col}} \left(\frac{d_{img} - f_{img}}{sca M} \right)^2 + \frac{V_0}{V_{ext}} \right)^{-1} \quad (5.40)$$

$$\approx \frac{V_{col}}{V_0} \cdot \left(\frac{sca M}{d_{img} - f_{img}} \right)^2 \quad (5.41)$$

Here we used the relation $\sin(\arctan(\xi)) = (\xi^2 + 1)^{-1/2}$. In the last approximation the second term was neglected, because it is usually very small compared with the first term for the *NanoESCA* objective lens. We can therefore expect that the microscope's transmission will be approximately inversely proportional to the kinetic

electron energy $E_{kin} = eV_0$. However, we also have to take into account that the magnification M is a function of V_0 (see Fig. 5.5). In Fig. 5.8 we show the calculated transmission as a function of the electron's kinetic start energy $e \cdot V_0$ and for the available contrast apertures for both models described above. The inset in Fig. 5.8 compares the calculated transmission for both models with each other by showing their ratio T_2/T_1 . For big contrast apertures and small kinetic electron energies all photoelectrons are entering the microscope and the start-angle-distribution does not matter $T_2/T_1 = 1$. For a CA 1750 this is for example true up to $E_{kin} = 51$ eV. For small contrast apertures and high kinetic electron energies, only small start-angles are transmitted into the microscope and the ratio of the transmissions converges to the ratio of the intensities of the start-angle distributions at $\alpha = 0$:

$$\lim_{V_0 \rightarrow \infty} \frac{T_2}{T_1} = \frac{I_2(\alpha = 0)}{I_1} = 2. \quad (5.42)$$

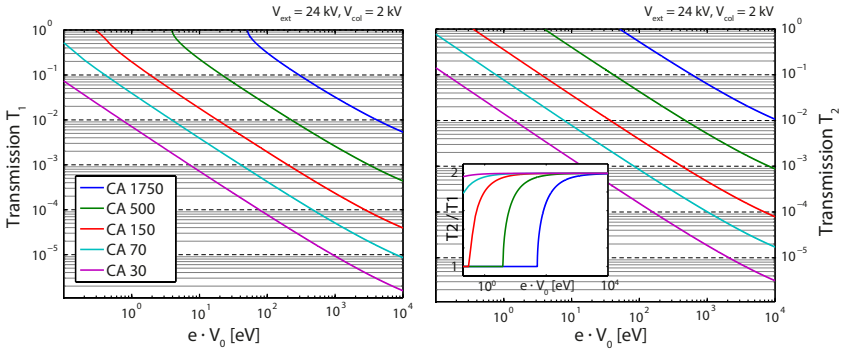


Figure 5.8.: The microscope's objective lens transmission $T(V_0, s_{CA})$ as a function of the electron's kinetic start-energy $e \cdot V_0$ and for all available contrast apertures, (a) calculated with Eq. 5.37 for a uniform start-angle distribution and (b) calculated with Eq. 5.40 for a $\cos(\alpha)$ -distribution (see text). In all simulations an extractor potential $V_{ext} = 24$ kV and a column potential $V_{col} = 2$ kV were used. A transmission of $T = 1$ means, that all photoelectrons leaving the sample can enter the microscope. For the biggest contrast aperture CA 1750 with $s_{CA} = 0.875$ mm that is true for kinetic electron energies up to 51.1 eV. The inset shows the ratio of the two used models.

5.4. Spatial resolution of the objective lens

The *spatial* and *momentum resolution* of a microscope is influenced by several factors. Some can be optimized by correct instrumental settings, others are intrinsic to the

used lenses, such as *spherical* or *chromatic aberrations*. With the knowledge of the aberration parameters, the latter can be corrected, for example, with electron mirrors [THE⁺10, THW⁺13]. Too high electron densities e.g. in crossing points of electron trajectories lead to space charge effects, which also disturb an image (see Sec. 8.3). Finally, also the topography of the sample under investigation or local charging can lead to field distortions on the sample surface and degrade the spatial resolution [NSS⁺00, SS02].

The total aberration of an electrostatic lens can be generally calculated by the square root of the quadratic sum of the spherical aberration disk δ_s , the chromatic aberration disc δ_c and the diffraction disc δ_d [SS02, Ege07] as

$$\delta_{total} = \sqrt{\delta_s + \delta_c + \delta_d}, \quad (5.43)$$

$$\text{with } \delta_s = C_s \cdot \alpha'^3, \quad (5.44)$$

$$\delta_c = C_c \cdot \frac{\Delta E_{kin}}{E_{kin}} \cdot \alpha', \quad (5.45)$$

$$\delta_d = 0.61 \frac{\lambda}{\beta_{max}} = 0.61 \frac{h}{\sqrt{2} m_e E_{kin}} \frac{1}{\beta_{max}}. \quad (5.46)$$

The last term describes the deterioration of the resolution by diffraction, which becomes important for small contrast apertures. C_s and C_c are the spherical and chromatic aberration coefficients of the lens³, λ the wavelength of the electron, α' the entrance angle of the electron into the lens and β_{max} the half angle of the pencil beam passing the contrast aperture. The equations above are approximations for small angles, where $\tan(\alpha') \approx \alpha'$ is valid. They are based on geometrical optics and are therefore valid for both, electrostatic and magnetic lenses.

As shown in previous chapters many of the microscope characteristics are defined by its immersion objective lens. In this section I will therefore calculate the spatial resolution on the basis of objective lens calculations in Sec. 5.1. The objective lens has three parts in which resolution limiting effects occur: the acceleration field, the lens itself and the contrast aperture. The task will be to calculate the spatial resolution as a function of the kinetic electron energy E_{kin} and the contrast aperture CA.

³The aberration coefficients strongly depend on the geometrical shape of the lenses and have to be measured. For magnetic lenses the range of C_s for a lens varies approximately between the focus-length f for weak lenses and $f/4$ for strong lenses. The range of C_c varies approximately between f for a weak lens and $f/2$ for a strong lens. The coefficients for electrostatic lenses are worse than that [Ege07].

5.4.1. Spherical aberration of the accelerating field

The strong accelerating field of the *immersion objective lens* adds its own aberrations to the system, which are a function of the accepted angles, the acceleration field and the start energy of the electrons. Earlier calculations for the NanoESCA described these dependencies under the assumption of small electron energies compared to V_{ext} [RG89, EWRB10]. That is not exactly true anymore for our HAXPEEM approach (see Cha. 8), therefore I performed the calculations without this kind of approximations.

The source of the *spherical* and *chromatic aberrations* of the acceleration field $\delta_{s,acc}$ and $\delta_{c,acc}$ is the fact, that the distance d'_{obj} between the objective lens and the virtual object plane (see Fig. 5.2) depends on the emission angle α and the kinetic start energy $E_{kin} = e \cdot V_0$ of the electrons, respectively. This distance d'_{obj} can be calculated for electrons starting on the optical axis. Fig. 5.9 shows exemplary trajectories for monochromatic electrons ($V_0 = 4$ kV) with two different starting angles ($\alpha_1 = 90^\circ$ and $\alpha_2 = 0.43 \cdot \alpha_1$). The tangent rays for the different electron trajectories cut the optical axis at different d'_{obj} .

The tangent to an electron trajectory in the lens plane ($z = d_{obj}$) follows the relation

$$r(z) = \tan(\alpha') \cdot (z - d_{obj}) + r_{ext}(\alpha), \quad (5.47)$$

where $r_{ext}(\alpha) = r(z = d_{obj}, \alpha)$ is the distance of the electron trajectory from the optical axis (\rightarrow Eq.(5.8)) and α' the angle of the trajectory in the lens plane (\rightarrow Eq.(5.10)). It cuts the optical axis at the position of the virtual object plane in the distance d'_{obj} from the objective lens:

$$d'_{obj} = \frac{r_{ext}(\alpha)}{\tan(\alpha')} \quad (5.48)$$

$$= \frac{2 d_{obj}}{\left(\frac{V_{ext}}{V_0} - 1\right)} \cdot \left(\frac{V_{ext}}{V_0} - \sin^2(\alpha) - \sqrt{\frac{V_{ext}}{V_0} - \sin^2(\alpha)} \cdot \cos(\alpha) \right), \quad (5.49)$$

for the energy-filtered mode ($V_{spl} = V_0$). In the case of small α we can ignore the $\sin^2(\alpha)$ terms and for $V_{ext} \gg V_0$ we can approximate Eq. (5.49) to

$$d'_{obj} \approx 2 \cdot d_{obj} \cdot \left(1 - \sqrt{\frac{V_0}{V_{ext}}} \cdot \cos(\alpha) \right), \quad (5.50)$$

which corresponds with the result in [RG89]. From Eq. (5.49) we see, that electrons leaving the sample with $\alpha = 90^\circ$ will have their virtual image plane at a distance

$$d'_{obj,max} = 2 \cdot d_{obj} \quad (5.51)$$

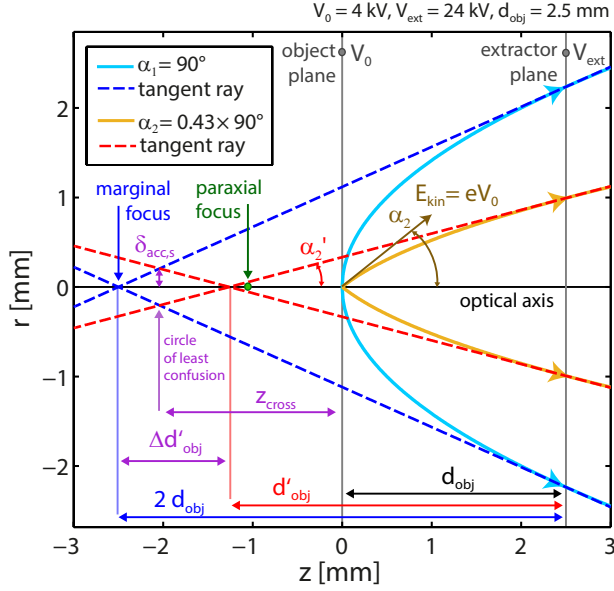


Figure 5.9.: Calculation of the spherical aberration of the accelerating field of the immersion lens. The resolution limit is defined as the radius of the *circle of least confusion* (see text). The graph shows the calculated trajectories for mono-energetic electrons ($V_0 = 4$ kV) in an accelerating field ($(V_{ext} - V_0) = 20$ kV) and two different start angles ($\alpha_1 = 90^\circ$ and $\alpha_2 = 0.43 \cdot \alpha_1$). The resolution limit in this case would be $\delta_{acc,s} = 0.21$ mm. In reality, the contrast aperture heavily reduces the maximum entrance angle into the microscope, which leads to a much smaller aberration.

in the *marginal focus*, whereas electrons with small emission angles have it near the *paraxial focus* which we calculate with Eq. (5.49) and $\alpha = 0^\circ$:

$$d'_{obj,0} = 2 d_{obj} \cdot \frac{1 - \sqrt{\frac{V_0}{V_{ext}}}}{1 - \frac{V_0}{V_{ext}}}. \quad (5.52)$$

The tangents to the electron trajectories for all other start angles α will cross the optical axis between these two points. The longitudinal spherical aberration is defined as the difference $\Delta d'_{obj}$ between the maximal and minimal crossing points. With the contrast aperture we can reduce the maximum accepted angle, so that the spatial aberration will be the difference between the maximal crossing point as a function of the CA and the paraxial focus:

$$\Delta d'_{obj} = d'_{obj}(V_0, V_{ext}, \alpha_{max}) - d'_{obj,0}(V_0, V_{ext}) \quad (5.53)$$

$$= \frac{2 d_{obj}}{\frac{V_{ext}}{V_0} - 1} \cdot \left(\sqrt{\frac{V_{ext}}{V_0}} + \cos^2(\alpha_{max}) - 1 - \sqrt{\frac{V_{ext}}{V_0} - \sin^2(\alpha_{max})} \cdot \cos(\alpha_{max}) \right) \quad (5.54)$$

$$\approx 2 d_{obj} \cdot \sqrt{\frac{V_0}{V_{ext}}} \cdot (1 - \cos(\alpha_{max})), \quad \text{for } V_{ext} \gg V_0 \text{ and } \alpha_{max} \text{ small} \quad (5.55)$$

where α_{max} can be calculated by Eq. (5.26) and is itself a function of V_0 , V_{ext} and the CA diameter.

As a measure of the spatial resolution which can be reached according to a given aberration the radius of the *circle of least confusion* can be calculated. For a given maximum acceptance angle α_{max} and all smaller angles $0 \leq \alpha_{test} < \alpha_{max}$ the circle of least confusion is the smallest area through which all of the virtual tangent rays pass. The position of the circle of least confusion along the z-direction for two rays can be calculated by the crossing point at

$$z_{cross} = d_{obj} - \frac{r(z = d_{obj}, \alpha_{max}) + r(z = d_{obj}, \alpha_{test})}{\tan(\alpha'_{max}) + \tan(\alpha'_{test})} \quad (5.56)$$

$$\approx d_{obj} - \frac{2 d_{obj}}{1 - \frac{V_0}{V_{ext}}} \cdot \left(1 - \frac{1}{2} \sqrt{\frac{V_0}{V_{ext}}} \cdot \frac{\sin(2 \alpha_{max}) + \sin(2 \alpha_{test})}{\sin(\alpha_{max}) + \sin(\alpha_{test})} \right) \quad (5.57)$$

of two tangent rays (with opposite gradient) by using the linear equation (5.47). The latter term is an approximation for small electron start angles ($\sin^2(\alpha) \approx 0$, $\cos^2(\alpha) \approx 1$). Using that result again with Eq. (5.47) and the maximum accepted angle α_{max} finally gives the radius of the *circle of least confusion* for the spatial aberration of the accelerating field

$$\delta_{acc,s} = r(z = d_{obj}, \alpha_{max}) - \frac{r(z = d_{obj}, \alpha_{max}) + r(z = d_{obj}, \alpha_{test})}{\tan(\alpha'_{max}) + \tan(\alpha'_{test})} \cdot \tan(\alpha'_{max}) \quad (5.58)$$

$$\approx \frac{2 d_{obj} \sin(\alpha_{max})}{\frac{V_{ext}}{V_0} - 1} \cdot \left(\frac{1}{2} \frac{\sin(2 \alpha_{max}) + \sin(2 \alpha_{test})}{\sin(\alpha_{max}) + \sin(\alpha_{test})} - \cos(\alpha_{max}) \right). \quad (5.59)$$

The latter term is again valid for small angles α and uses the same approximation as Eq. (5.57). When we use a contrast aperture in the *NanoESCA*, α_{max} is defined by Eq. (5.26), whereas α_{test} stands for all smaller angles $0 \leq \alpha_{test} < \alpha_{max}$. We have to find the α_{test} which gives the maximum value for $\delta_{acc,s}$ to have a measure for the resolution limit. This maximum can be determined numerically and appears at $\alpha_{test} = \gamma \cdot \alpha_{max}$ with $\gamma \approx 0.5$ for small α_{max} (see Fig. 5.10(a)).

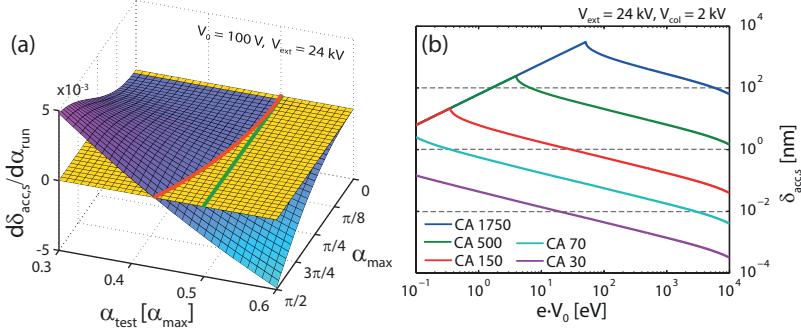


Figure 5.10.: (a) The derivative of Eq. (5.58) with respect to α_{run} was calculated for $\alpha_{max} = 0.. \pi/2$ and $\alpha_{test} = \gamma \cdot \alpha_{max}$. The cut of the derivative-plane with the zero plane (red line) shows, for which values of α_{test} Eq. (5.58) has its maxima. For small α_{max} the value γ becomes approx. 0.5 whereas it is approx. 0.43 for a full angle acceptance $\alpha_{max} = \pi/2$. (b) Calculated spherical aberration of the acceleration field of the immersion lens as a function of kinetic electron energy $e \cdot V_0$ and for all available contrast apertures. The calculation were performed according to Eq. (5.58). The maximum acceptance angle α_{max} was determined with Eq. (5.26). The standard objective potentials ($V_{ext} = 24$ kV, $V_{col} = 2$ kV) were used.

With Eq. (5.58) we are able to determine the spatial aberration of the accelerating field $\delta_{acc,s}$, which is increasing nearly linear as a function of the kinetic electron energy $e \cdot V_0$ as long as the contrast apertures are not limiting the maximum acceptance angle α_{max} . The results are shown in Fig. 5.10(b). As soon as α_{max} (calculated with (5.26)) is decreasing due to the CAs, the aberration is heavily reduced with higher kinetic electron energies.

5.4.2. Chromatic aberration of the acceleration field

The *chromatic aberration* of the accelerating field arises from the dependence of d'_{obj} on the kinetic electron start energy $e \cdot V_0$ [RG89]. The same calculations as for the spherical aberration calculation can be used, only that the energy difference ΔV_0 between two different electron start energies (eV_0 and $e(V_0 + \Delta V_0)$) is analyzed instead of different start angles. The calculations are always performed for a fixed emission angle α_{test} . For the given parameter set V_0 and ΔV_0 one angle $0 \leq \alpha_{test} \leq \alpha_{max}$ exists, for which the chromatic aberration is maximal. This maximum is evaluated numerically in our simulation, the maximal acceptance angle α_{max} is again defined by the contrast aperture via Eq. (5.26). The radius of the *circle of least confusion* for the chromatic aberration can be expressed as

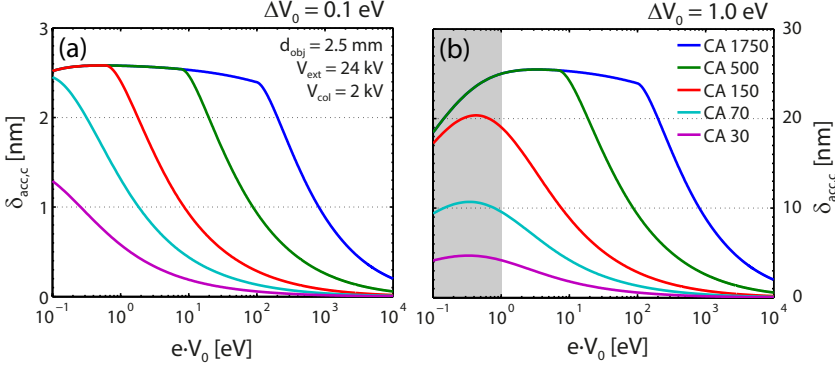


Figure 5.11.: Chromatic aberration of the accelerating field of the NanoESCA, calculated according to Eq. (5.60) for two different energy resolutions (a) $\Delta V_0 = 0.1$ eV and (b) $\Delta V_0 = 1.0$ eV. The chromatic aberration is weakly energy-dependent and scales linearly with ΔV_0 until the reduction of the maximum acceptance angle α_{max} due to the contrast aperture plays a role. The gray area in (b) is just shown for completeness. Probing kinetic energies smaller than the resolution limit is general not feasible.

$$\delta_{acc,c} = r_{ext}(\alpha_{test}, V_0) - \frac{r_{ext}(\alpha_{test}, V_0) + r_{ext}(\alpha_{test}, V_0 + \Delta V_0)}{\tan(\alpha'_{test}(V_0)) + \tan(\alpha'_{test}(V_0 + \Delta V_0))} \cdot \tan(\alpha'_{test}(V_0)) \quad (5.60)$$

$$\approx d_{obj} \sin(\alpha_{test}) \cdot \left(\frac{\sqrt{V_0 V_{ext}} - V_0 \cos(\alpha_{test})}{V_{ext} - V_0} - \frac{\sqrt{V_0 V_{ext}} - \sqrt{V_0 (V_0 + \Delta V_0)} \cos(\alpha_{test})}{V_{ext} - (V_0 + \Delta V_0)} \right), \quad (5.61)$$

with $r_{ext}(\dots) = r(z = d_{obj}, \dots)$. The approximation is valid for small angles α_{test} . Figure 5.11 shows the simulated results of Eq. (5.60) as a function of the kinetic electron energy $e V_0$ and the available contrast apertures. Two practicable energy resolutions $\Delta(e V_0) = 0.1$ eV and $\Delta(e V_0) = 1.0$ eV were chosen. The curves scale nearly linearly with ΔV_0 .

5.4.3. Aberrations of the objective lens

The aberrations of the objective lens like for all electrostatic einzellenses depends very much on the lens geometry [Lie10]. Approximate dependencies on the electron start angle α , its kinetic start energy $e V_0$ and the objective potentials can be estimated if lens specific constants are introduced, C_S for the spherical and C_C for the chromatic

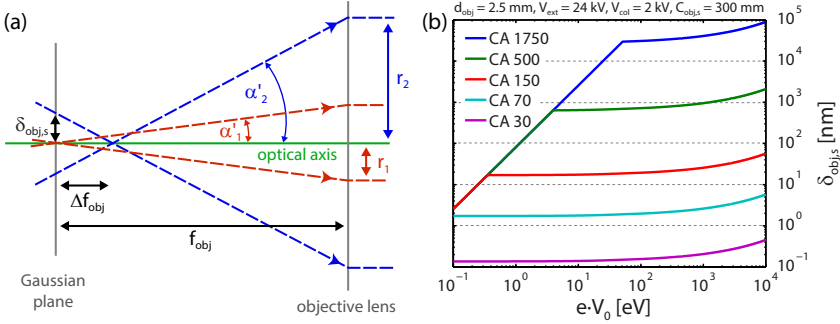


Figure 5.12.: Calculating the resolution disc $\delta_{\text{obj},s}$ of the spherical aberration of the objective lens. (a) Sketch of the geometrical construction for the calculations. (b) The simulated resolutions discs as a function of the kinetic electron energy $e V_0$ and for all available contrast apertures. The resolution disc is rapidly increasing with V_0 until the contrast apertures start to limit the accepted electron start angles α .

aberration. Following [Ege07] the spherical aberration of a lens can be estimated according to the sketch shown in Fig. 5.12(a).

While rays parallel and close to the optical axis (paraxial) are focused onto the Gaussian plane in the distance f to the lens, the focal point of axis-parallel rays with a distance r from the optical axis fall shorter with a distance Δf to the gaussian plane. This Δf , which characterizes the *spherical aberration*, is approximated by a power series with even powers

$$\Delta_s f = c_2 \cdot r^2 + c_4 \cdot r^4 + \dots \quad (5.62)$$

from which we only use the first term in the following. Geometrically, the relation between the shifted focus point $f - \Delta_s f$ and r can be expressed by

$$r = (f - \Delta_s f) \cdot \tan(\alpha') \approx f \cdot \tan(\alpha'). \quad (5.63)$$

The latter approximation is valid for $\Delta_s f \ll f$, which is in general true for the lenses in use. With this approximation we can simply express the focus shift by

$$\Delta_s f = \underbrace{c_2 f^2}_{\equiv C_{\text{obj},s}} \cdot \tan^2(\alpha'). \quad (5.64)$$

Finally, the disc of confusion is defined by the radial displacement of the non-paraxial

rays on the Gaussian plane with the radius

$$\delta_{obj,s} = \Delta_s f \cdot \tan(\alpha') \approx C_{obj,s} \cdot \tan^3(\alpha') \quad (5.65)$$

$$\approx C_{obj,s} \cdot \left(\frac{V_0}{V_{ext}} \right)^{3/2} \cdot \sin^3(\alpha). \quad (5.66)$$

In the last term the objective entrance angle α' was converted into the electron start angle via Eq. (5.10) (using the small angle approximation). The lens specific constant $C_{lens,s} = 300$ mm for the objective lens of the NanoESCA was published in [EWRB10]. The use of the non-approximated term in Eq. (5.63) leads to a quadratic equation in $\Delta_s f$ and a more complicated solution for $\delta_{obj,s}$, where a lens constant $C_{lens,s}$ could not easily be defined.

The chromatic resolution disc of the objective lens is similarly calculated, if we define the shift of the focus point due to the chromatic aberration by

$$\Delta_c f = C_{obj,c} \cdot \frac{\Delta V_0}{V_{ext}} \quad (5.67)$$

according to [RG89]. It is therefore characterized by the energy resolution $e \Delta V_0$ relative to the kinetic energy of the electrons at the extractor plane $e V_{ext}$ and a lens specific constant $C_{lens,c} = 130$ mm which was also published in [EWRB10]. The chromatic resolution disc is then

$$\delta_{obj,c} = \Delta_c f \cdot \tan(\alpha') \approx C_{obj,c} \cdot \frac{\Delta V_0}{V_{ext}} \cdot \tan(\alpha') \quad (5.68)$$

$$\approx C_{obj,c} \cdot \left(\frac{V_0}{V_{ext}} \right)^{3/2} \cdot \frac{\Delta V_0}{V_0} \sin(\alpha). \quad (5.69)$$

In Fig. 5.13 the simulated resolution discs of the objective lens are shown as a function of the kinetic electron energy and for the available contrast apertures.

5.4.4. Diffraction at the contrast aperture

The conclusion of the previous chapters is that a reduction of the maximum electron beam angles is the method of choice to reduce all kinds of aberration in the microscope and to improve the spatial resolution. This is achieved by the reduction of the *contrast aperture* (CA) in diameter. Closing the CA has on the one hand the disadvantage of a heavily decreased transmission (see Fig. 5.8) and on the other hand, *diffraction* of the electrons at the contrast aperture will play a dominant role and limit the achievable spatial resolution.

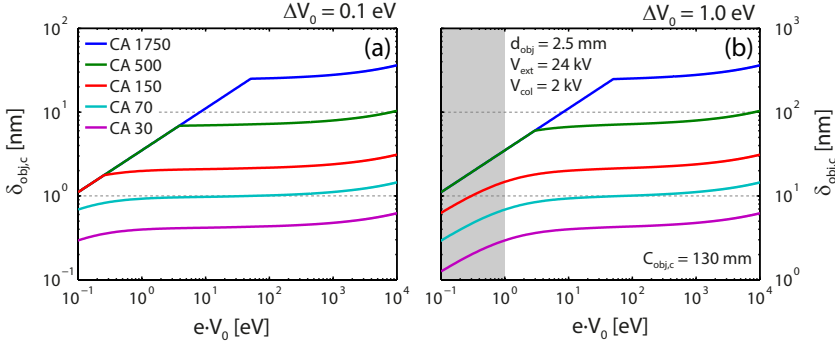


Figure 5.13.: Resolution disc $\delta_{obj,c}$ caused by the chromatic aberration of the objective lens, simulated with Eq. (5.68) for two different energy resolutions $e \Delta V_0$ with (a) $\Delta V_0 = 0.1$ eV and (b) $\Delta V_0 = 1.0$ eV .

Figure 5.14(a) schematically shows this effect for the immersion lens of the *NanoESCA*: The electrons starting from one point of the sample will not reach the image plane in one point, but will show a diffraction pattern in the image plane, which depends on the form and size of the CA and on the *de Broglie* wavelength $\lambda_{e,CA}$ of the electrons when they cross the CA. In the case of circular CAs, the diffraction pattern on the image-plane will show an *Airy disc* with the intensity distribution [Dem09]

$$I(\theta) = I_0 \cdot \left(\frac{2 J_1(\xi)}{\xi} \right)^2, \quad \text{with } \xi = \frac{2 \pi s_{CA}}{\lambda_{e,CA}} \cdot \sin(\theta), \quad (5.70)$$

where $J_1(\xi)$ is the first order *Bessel function* and s_{CA} the radius of the CA. According to the *Rayleigh criterion*, two *Airy discs* can be separated from each other, if their centers are not closer to each other than the distance ρ_{min} between the center of the *Airy disc* and its first minimum. This first minimum is at $\sin(\theta) = 0.61 \lambda_{e,CA}/s_{CA}$ and therefore the minimal distance between two discs on the image plane with a distance $d_{img} - f_{img}$ to the CA is

$$\rho_{min} = \tan(\theta) \cdot (d_{img} - f_{img}) \approx 0.61 \frac{\lambda_{e,CA}}{s_{CA}} \cdot (d_{img} - f_{img}). \quad (5.71)$$

Because θ is usually very small, the approximation $\tan(\theta) \approx \sin(\theta)$ can be used. This minimal distance ρ_{min} on the image plane has to be projected back onto the object plane to find the real resolution limit. Knowing the magnification M of the objective lens the minimal distance δ_D on the object plane can be calculated as

$$\delta_{Diff} = M^{-1} \rho_{min} = 0.61 \lambda_{e,CA} \cdot \frac{d_{img} - f_{img}}{M \cdot s_{CA}} = \frac{0.61 \cdot \lambda_{e,CA}}{\tan(\alpha'_{max})} \cdot \sqrt{\frac{V_{col}}{V_{ext}}}. \quad (5.72)$$

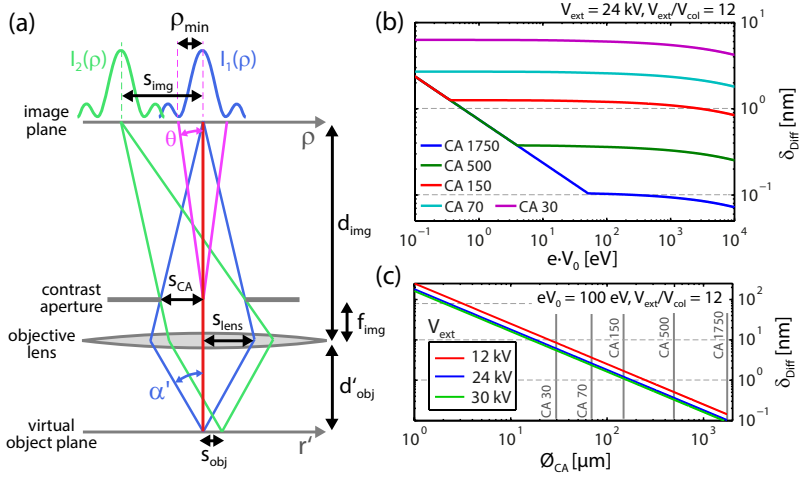


Figure 5.14.: (a) Sketch to construct the diffraction at the contrast aperture of the objective lens. Two electron point-sources will not be imaged into points on the image plane, but will show a diffraction pattern. Two different point sources are still distinguishable, if their diffraction patterns are not closer to each other than the distance ρ_{min} between the center and the first minimum of the pattern. (b) The resolution limit δ_{Diff} of the *NanoESCA* due to diffraction as a function of the electron start energy $e V_0$ and for all available CA diameters. (c) The resolution limit δ_{Diff} as a function of the CA diameter ($\varnothing_{CA} = 2 \cdot s_{CA}$) for a kinetic electron energy $e V_0 = 100$ eV and for different extractor voltages V_{ext} .

The last term is obtained by comparing the second term with Eq. (5.25). By using Eq. (5.10) we can convert the expression for α' into an expression for the electron starting angle α . For the calculation of the *de Broglie* wavelength $\lambda_{e,CA}$ it was assumed, that the electrons have the kinetic energy $e V_{col}$ when passing the CA. We get

$$\delta_{Diff} = 0.61 \underbrace{\frac{h}{\sqrt{2} m_e e \sqrt{V_{col}}}}_{=\lambda_{e,CA}} \cdot \underbrace{\frac{1}{\sin(\alpha_{max})} \sqrt{\frac{V_{ext}}{V_0}}}_{\approx \tan^{-1}(\alpha'_{max})} \cdot \sqrt{\frac{V_{col}}{V_{ext}}} = \frac{0.748 \cdot 10^{-9} [m\sqrt{V}]}{\sin(\alpha_{max}) \cdot \sqrt{V_0}}, \quad (5.73)$$

which is the same result as published in [RG89], if we use the approximation for small angles α . Note that in Eq. (5.73) the value of the maximum acceptance angle as given by Eq. (5.26) has to be used. The calculated resolution limit δ_{Diff} is shown in Fig. 5.14(a) as a function of the kinetic electron start energy $e V_0$ for the available CA diameters and in (b) as a function of the CA diameters for different extractor voltages V_{ext} . As soon as the contrast aperture comes into play the resolution limit is relatively independent of V_0 , because the diffraction mainly depends on the kinetic electron energy $e \cdot V_{col}$ at the contrast aperture, which is constant for a chosen setting. The remaining dependence on V_0 is due to the fact that the lens magnification M varies with V_0 .

The smallest CA of the *NanoESCA* having 30 μm in diameter is close to the limit where the diffraction starts to play a dominant role in the resolution limit. A further reduction of the CA would be counterproductive.

5.4.5. The total aberration of the objective

Having analyzed the influences of the separate parts of the objective on the resolution of the NanoESCA the *total resolution* can be approximated by combining the separate resolution discs. According to [RG89, SS02] we can calculate the total resolution limit of the objective as

$$\delta_s = \delta_{acc,s} + \delta_{obj,s} \quad (5.74)$$

$$\delta_c = \delta_{acc,c} + \delta_{obj,c} \quad (5.75)$$

$$\delta_{total} = \sqrt{\delta_s^2 + \delta_c^2 + \delta_d^2}. \quad (5.76)$$

This total resolution limit is shown in Fig. 5.15(a) for typical instrument settings ($V_{ext} = 24$ kV, $V_{col} = 2$ kV, $\Delta(e V_0) = 500$ meV) as a function of the CA diameter \mathcal{O}_{CA} and the kinetic electron start energy $e V_0$. The resolution limit depends much

more on \mathcal{O}_{CA} than on eV_0 . According to the calculations, the best resolution can be reached with a CA between 35 and 45 μm . The exact value depends on eV_0 (see Fig. 5.16).

Which of the resolution limiting effects plays the dominant role for the total resolution limit δ_{total} depends on the size of the CA and the kinetic electron start energy eV_0 . Figures 5.15 (b-f) show the separate resolution limiting components as a function of eV_0 for all available CAs including the total limit calculated according to Eq. (5.76). For big CAs the spherical aberrations of the objective lens and the accelerating field determine the total resolution limit. For smaller CAs, the chromatic aberrations play a more important role. They scale linearly with the energy spread accepted by the energy filter so that they could be significantly decreased with energy-filter resolutions better than the 500 meV assumed for the calculations. As mentioned earlier, the diffraction at the CA starts to limit the resolution below a CA diameter of 45 μm .

5.5. Conclusions

The objective of a photoemission microscope has a high impact on the size of the phase space acquired in a measurement. The phase space which passes through the microscope determines the crucial characteristics of the experiment like spatial and momentum resolution, the field of view, which can be acquired in either mode, and the transmission. Although simulations are more accurate, analytic calculations allow a better understanding on the dependencies of these characteristics and the experimental conditions. The calculations in this chapter were performed to understand the peculiarities of using an energy filtered photoemission microscope with high kinetic electrons, excited by hard x-rays. Therefore, the aberration calculations were performed without the usual approximations that the ratio between kinetic electron energy and acceleration field of the objective lens is very small.

The main results are the fast drop of the acceptance angle acquired by the microscope for high energies which directly leads to very low transmissions in the hard X-ray regime. This effect adds to other count-rate reducing issues like the decreasing photo-ionization cross-section in the hard X-ray regime and needs to be instrumentally improved.

Finally, the calculations of the objective lens aberration show that the spatial resolution does not dramatically increase at higher kinetic electron energies. If an

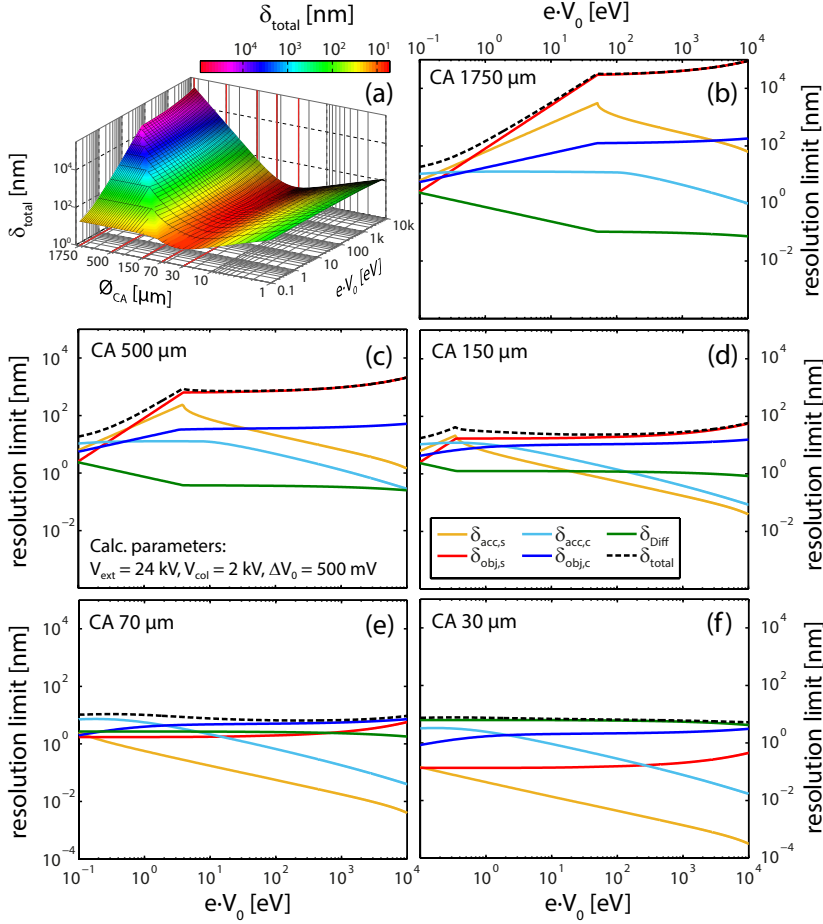


Figure 5.15.: Calculated resolution limits of the *NanoESCA* objective for typical instrument parameters ($V_{ext} = 24 \text{ kV}$, $V_{col} = 2 \text{ kV}$, $\Delta(e V_0) = 500 \text{ meV}$). (a) Total resolution limit δ_{total} calculated with Eq. (5.76) as a function of the CA diameter ϕ_{CA} and the kinetic electron start-energy $e V_0$. The global minimum δ_{min} can be reached with a CA between 35 and 45 μm (see inset). The graphs (b-f) show, which kind of aberration dominate the total resolution limit for each CA setting. For big CAs (b-d), the spherical resolution discs of the objective lens $\delta_{obj,s}$ and of the accelerating field $\delta_{acc,s}$ are predominant. For the smallest CAs (e-f) the chromatic aberrations and the diffraction determine the resolution limit. Note that the chromatic aberrations scale with the energy spread $\Delta(e V_0)$ and can be more or less dominant according to the set energy resolution.

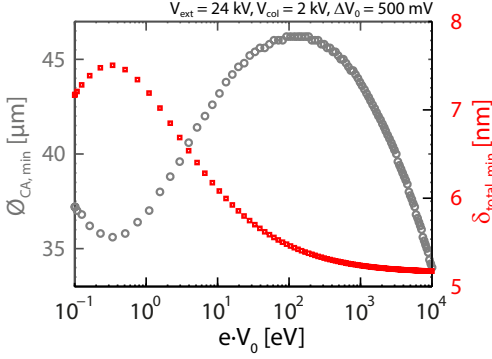


Figure 5.16: The global resolution limit minimum $\delta_{\text{total},\text{min}}$ and the related CA diameter $\mathcal{O}_{\text{CA},\text{min}}$ as a function of the kinetic electron start energy eV_0 , calculated with Eq. (5.76). The minimal resolution limit of the objective is below 10 nm with optimal CAs between 35 and 45 μm .

energy filter is used, which automatically reduces all chromatic aberrations, the spherical aberrations of the objective lens limit the resolution whether big or medium contrast apertures are used. The resolution improves for smaller contrast apertures until the diffraction limit, which depends on the kinetic electron energy and appears for contrast aperture diameters between 35 and 45 μm (in the energy range between $10^{-1} \dots 10^4 \text{ eV}$).

6. Non-Isochromaticity of the Imaging Energy Filter

The most prominent characteristic feature of the *NanoESCA* is without doubt its double-hemispherical imaging *energy filter*¹. The tandem configuration of two hemispheres ensures a cancellation of the α^2 aberration term which would otherwise deteriorate the *image resolution* [EWM⁺05, EWRB10]. Nevertheless the energy-filter introduces a significant *non-isochromaticity* into an energy-filtered PEEM-image, which means that different points in the image represent photoelectrons with different kinetic energies. Due to the construction of the energy-filter, the dominant *energy shift* appears along the dispersive plane of the analyzer. A closer analysis nevertheless unveiled that the *non-isochromaticity* in general has to be regarded as a two-dimensional effect in a PEEM-image. Depending on the microscope setting, the energy shift within one image can range from several ten milli-electron-volts to above one electron-volt. In many cases it will be mandatory to take these shifts into account for a precise data analysis. Especially in regard to measurements with a low count-rate like *HAXPEEM* (see Sec. 8) the pass-energy of the analyzer is raised to reach a higher transmission, which at the same time increases the *non-isochromaticity*. A correction of the energy shifts is, for example, necessary for data post-processing methods like PCA (see Sec. 4.2). But also in experiments which rely on a defined electron energy output behind the energy filter like, e.g., an imaging spin filter [TEU⁺11] the knowledge of the *non-isochromaticity* of the filter is necessary for a comprehensive understanding of the measured data.

In this section I present a reliable procedure based on a *work function analysis* (see Sec. 4.1) to determine the energy shifts in a PEEM image for an individual microscope setting and to subsequently correct the image spectra measured with this setting. To understand the technical details of the *non-isochromaticity* I will present first-order calculations of the electron trajectories passing the analyzer. Based on these calculations, the transport of a full energy filtered PEEM-image can be simu-

¹see Sec. 3.1 for a general description

lated. Subsequently, a set of calibrated measurements will show, in how far the model calculations represent the reality and which additional effects have to be taken into account. These insights can be used to formulate a generalized fit model for the *non-isochromaticity* in a PEEM image, which can help to correct it without any time-consuming calibration measurements.

6.1. Non-Isochromaticity analysis and correction

A first technical description of the effect was mentioned in [EWRB10] noting that the energy-shift ΔE relative to the set filter energy E_{kin} is a function of the distance Δx of measured image points from the optical axis of the microscope and can be calculated as

$$\Delta E = E_{Pass} \cdot \left(\frac{M_1 \cdot \Delta x}{f_{FL}} \right)^2 \quad (6.1)$$

where E_{Pass} is the energy-filter's pass-energy, M_1 is the microscope's magnification in the intermediate image plane at the coupling lens entrance before the energy-filter and f_{FL} is the *focal length* of the entrance lens. The implications of this *non-isochromaticity* in energy-filtered imaging were e.g. mentioned in [LPBZ⁺10]. In an energy-filtered PEEM image the spatial energy shift causes a change in intensity, since the image points represent different energetic positions of a spectrum. With a detailed understanding of the non-isochromaticity of the instrument it is possible to reduce the effect and to correct it in the post evaluation of the measured data-sets. In this section I demonstrate the influence of the non-isochromaticity on a real-space measurement and a method to correct it.

6.1.1. Impact of the energy shift on the intensity distribution of a photoemission image

A *checkerboard patterned test-sample*² (see sketch in Fig. 6.1) is well suited to probe the non-isochromaticity effect. A pattern of 100 nm thick gold squares (1x1 μm) is arranged on a SiO₂/Si template to a 10x10 μm checkerboard structure. This 10x10 μm square is again repeated in a checkerboard structure to a 100x100 μm square. The biggest squares on this sample finally have a 1x1 mm dimension. The use of the different materials gives a strong chemical contrast in photoemission microscopy but also a detectable *work function contrast* (see Sec. 2.4) which is used in

²commercially available from *Plano GmbH* [Pla14]

this section. The pattern allows one to check for correct microscope settings (spatial and chromatic aberration, focus, lens settings, astigmatism, distortion etc.) for a large variety of microscope magnifications. Furthermore it allows one to calibrate the field of view of the sample, which is projected on the MCP of the detector. The spatial resolution of the sample-pattern is better than 300 nm, as it was shown with a line-profile evaluation of a PEEM image (see Sec. 7.1.3).

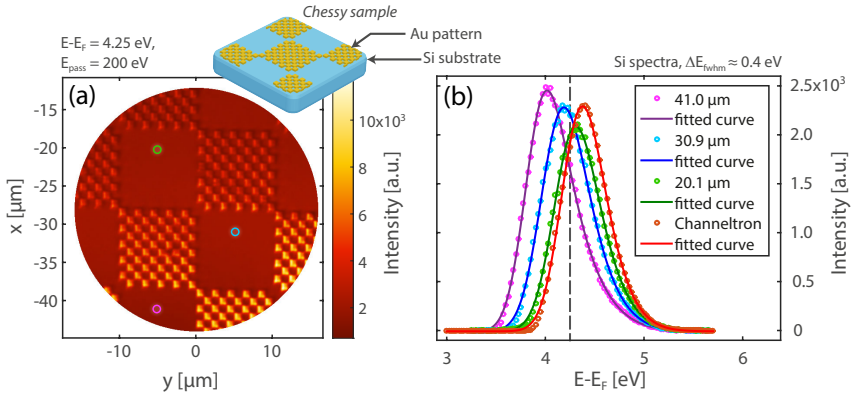


Figure 6.1.: (a) Energy-filtered PEEM-image ($E - E_F = 4.25$ eV) of the used specimen, consisting of a Au checkerboard pattern on a Si-wafer. The colored circles are the region of interests from which the spectra in (b) were extracted. The extracted spectra show a significant shift in energy, although they were acquired on the same material (Si). The filter-energy which was used for the PEEM image in (a) is marked in (b) with a grey line. Additionally a spectrum of the Si-film was acquired in the channeltron mode with a closed iris around a Si-field (microspectroscopy). This channeltron spectrum has a slightly different shape and is shifted to even higher energies.

The energy-filtered PEEM image in Fig. 6.1(a) was taken at $E - E_F = 4.25$ eV as part of an image spectrum over the full photoelectron yield which can be excited by a *mercury lamp*. The mercury lamp ensures a relatively homogenous illumination over the full field of view. The visible field of view has a size of approx. 30 μm. The energy filter was set to a pass energy of $E_{pass} = 200$ eV with an entrance/exit slit width of 0.5 mm, which results in an energy resolution of approximately $\Delta E \approx 0.4$ eV. A *flat field correction* according to Eq. 7.1 was performed prior to all further analysis, nevertheless the photoelectron intensity is not homogenous due to the non-isochromaticity of the energy filter. Spectra which were extracted from the image spectrum at the regions of interest marked in Fig. 6.1(a) are shown in (b). Although all spectra were acquired from the same Si substrate, their energetic

positions are shifting as a function of the distance along the x-axis. Additionally a *micro-spectrum* from a pure Si region (defined by the closed *field aperture*) was acquired with the *channeltron* for comparison. It is shifted to even higher energies and has a slightly different line shape than the spectra extracted from the image spectrum. The different line shape appears, because the channeltron is integrating the incoming photoemission signal over a larger field of view. The larger field of view converts due to the Fourier lens into a bigger angular space entering the analyzer (see Sec. 3.1.3), which changes the spectral line shape and shifts it to slightly higher energies [IAK76]. The energy shift of the channeltron spectrum in this case nevertheless has another reason as will be explained later in this chapter.

6.1.2. Determination of the energy shift by a work function analysis

The measured image stack can be used to perform a *work function analysis* as it is described in Sec. 4.1. The spectra in Fig. 6.1 (b) were fitted with the model given in Eq. (4.1) to analyze the position of the work function edge with Eq. (4.2). If this procedure is performed for each pixel in the image spectrum, a work function map can be compiled, like it is shown in Fig. 6.2 (a). Here the shift of the work function along the x-direction of the image becomes clearly visible. If the same image spectrum is acquired on a pure Si region without the checkerboard pattern, the same procedure results in the work function map shown in (b). A line profile of the work function map along the x-direction unveils the nature of the energy shift as is shown in (d): it can be fitted with a parabolic function. The zenith x_c of the parabola was set as origin of the x-axis in all images. There we can expect the real center of the image (on the optical axis of the microscope) as will be explained later. Furthermore, the work function value extrapolated at the zenith of the parabola is the real measured work function value $\Delta\Phi_0 = 4.210 \pm 0.001$ eV for the Si substrate. All work function values along the x-axis differing from that value are shifted, because of the non-isochromaticity of the energy filter. If we set ΔE_0 as new origin of the energy axis the work function map in (b) therefore directly becomes an energy shift map. Because of small spatial work function variations on the Si substrate this energy shift map needs to be smoothed and can then be used to correct the work function map of the checkerboard patterned region in (a) by a simple subtraction. The result is shown in (c). This corrected work function map shows in general the same work function values for equal materials in the pattern, which proves that the correction worked correctly for the whole field of view. The mean work function of the Au pattern is approx. 15 meV higher than that for Si. Local work function variations

can be much more precisely detected after the energy shift correction (Fig. 6.2 (c) compared to (a)).

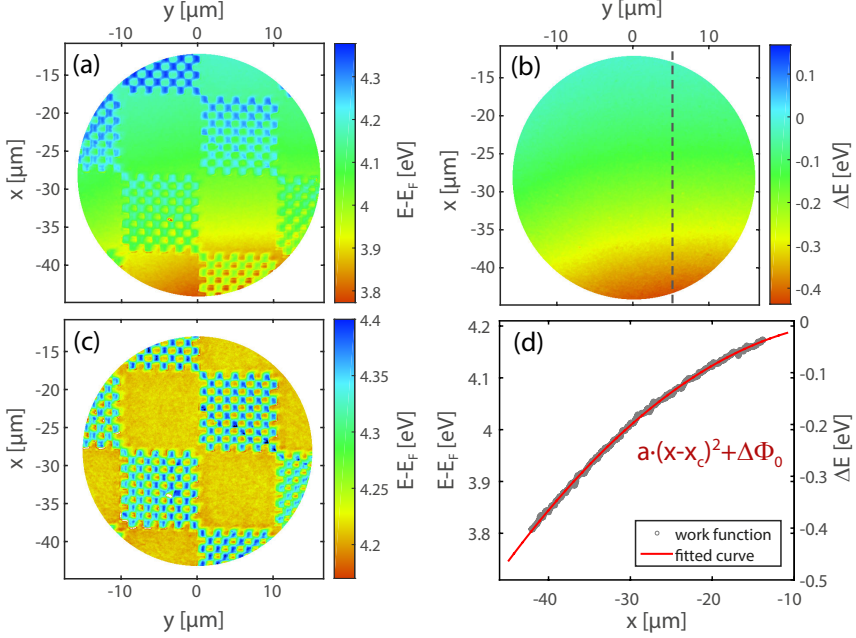


Figure 6.2.: (a) Work function mapping of the Chessy sample. The Au pattern has a higher work function than the Si substrate which gives a visible contrast. Nevertheless, the work function shift due to the non-isochromaticity of the instrument is clearly visible. (b) If the same work function scan is repeated on a pure Si area, the absolute energy shift ΔE can be gained. After smoothing this measurement, it can be used to correct the work function scan of the patterned sample (c). Smaller work function differences can be detected now. (d) A profile along the energy shift (dotted line in (b)) is shown in (d). The energy shift as a function of the distance in the dispersive x-direction can be modeled by a parabola.

Three additional remarks should be made:

- The fitted work function of the channeltron measurement in Fig. 6.1 (b) is $\Delta\Phi_0 = 4.217 \pm 0.007$ eV and within the errors equal to the work function values extrapolated from the parabola fit in Fig. 6.2 (d). Consequently, although spectra extracted somewhere from an image spectrum may be shifted in energy, the channeltron measurement can give an exact reference value.
- In Fig. 6.2 (b) we can see that the non-isochromaticity not only happens in the x-direction but also in the y-direction. It is a two dimensional effect and a

full 2D energy-shift map is needed for a complete energy-shift correction. Nevertheless the effect in the y-direction is considerably smaller compared to the x-direction (see Tab. 6.2) and a one-dimensional correction with the parabola shown in Fig. 6.2 (d) may already give reasonable results. The advantage of a one-dimensional correction is simply the faster evaluation of the correction curve.

- Although the shown measurement was performed with a comparable low energy resolution of $\Delta E = 400$ meV, the precision of the evaluated work function differences on the sample is around $\Delta\Phi = 10$ meV. Consequently, the effective energy resolution of the instrument for the work function analysis is much higher than one would expect from the settings of the energy analyzer.

6.1.3. Energy shift correction of the image spectrum

The knowledge of the 2D energy shift distribution in Fig. 6.2 (b) can also be used to correct the full image spectrum. A cut through the originally measured energy-filtered image stack is shown in Fig. 6.3 (a). The energy shift can be clearly seen in the energy-x-direction plane. Spectra which were extracted from the region of interest marked in Fig. 6.1 (a) are again shown in Fig. 6.3 (c). After the correction of the full image spectrum (b) also the intensity distribution along one constant energy cut (top x-y-plane) becomes homogenous. Extracted micro spectra from the same regions of interest as before now perfectly fit together in terms of the line shape. The remaining differences of the maximal intensity of the spectra might be due to a variation of the light intensity of the excitation source or also to the microscope. An energy shift corrected intensity map of the Si measurement for a constant energy of $E - E_F = 4.43$ eV (maximum intensity in the spectra) is shown in (e). The shape of the intensity inhomogeneity differs from the work function map in Fig. 6.2 (b). Detector-artifacts can be excluded after the aforementioned flat field correction. Most probably, a remaining intensity-inhomogeneity of the light source is visible here. This measured inhomogeneity map can be used for an intensity correction by dividing it from, e.g., a measurement of the checkerboard pattern (f). The color in (f) was reduced to see effects on the pure Si part, the brighter Au pattern is cut off (black color). The Si intensity is now homogenous and shadowing effects of the Au pattern can be studied. Like the shadows suggest, the light excitation is positioned at the bottom left of the sample with a 65° angle to the surface normal.

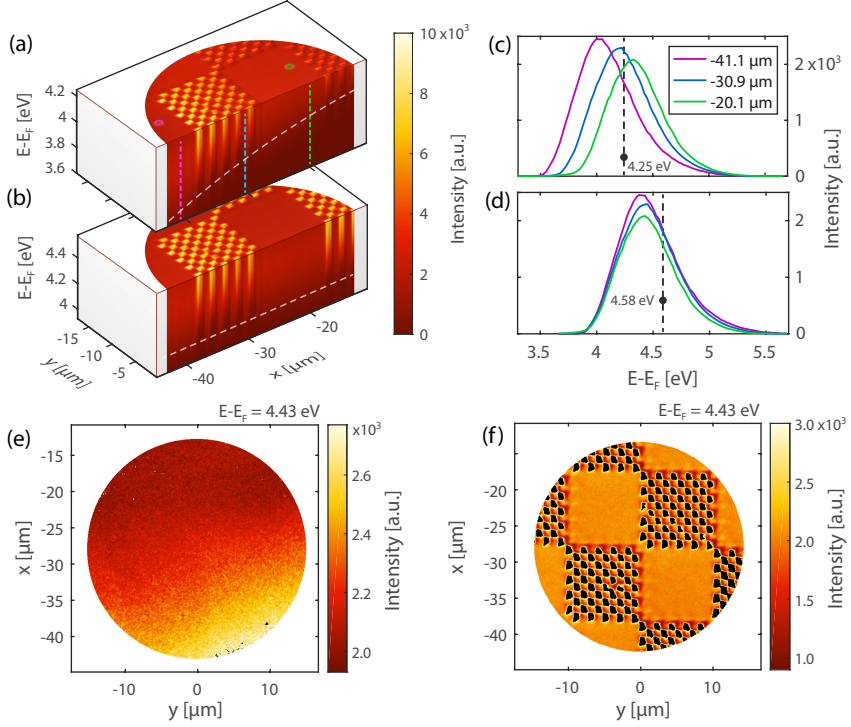


Figure 6.3.: The use of the energy-shift map deduced from the work function analysis in Fig. 6.2(b) can be used to correct a whole image spectrum. The original measurement is shown as image spectrum in (a) and as exemplary local spectra extracted from the regions of interest marked in Fig. 6.1(a). The white line in (a) marks the parabolic energy shift along the x -direction of the image. After the correction (b) the extracted spectra (d) have the same position in energy. Consequently, the corrected constant energy cut at $E - E_F = 4.58$ eV (top x - y -plane) in (b) shows a much more homogenous intensity distribution compared to the uncorrected case. The maximal intensities of the spectra in (d) still suggests that the spatial intensity distribution is still not completely homogenous for on material, which is supported by the Si-intensity map in (e). The energy filtered PEEM image in (f) was finally intensity corrected with the map in (e). The color scale was reduced to the intensity spectrum of the Si substrate, so that shadow effects from the chessy pattern can be made visible. The black spots simply mark intensities above 3000.

6.2. Energy filter calculations

The goal of this section is to get a more theoretical understanding of the non-isochromaticity, which was described in the previous section. I programmed a simulation, which is based on the analyzer description presented in Sec. 3.1.3. In the first part of this section, the path of the electron trajectories through the analyzer is calculated for different start conditions. The main reason for the non-isochromaticity becomes visible. On the basis of these trajectory calculations it is then possible to simulate, how a complete photoelectron image is transferred through the analyzer.

6.2.1. The set of transfer functions to calculate the electron trajectories

An intermediate image (see Fig. 6.4) which is formed in the deflector plane in front of the analyzer is transferred into the round analyzer entrance aperture with diameter $w_{entr,1}$ by a *Fourier lens* according to the transfer function given in Eq. (3.5) (all values are relative to the optical z-axis, red line in Fig. 6.4). The Fourier lens interchanges spatial and angular coordinates. The focal length of the lens is $f_{FL} = 29$ mm [EWRB10]. The transfer through the first HSA is described by Eq. (3.1) and Eq. (3.2). According to the HSA's medium radius $r_0 = 125$ mm, the direct distance from its entrance to its exit is $\pi \cdot r_0 = 392.7$ mm. The *exit slit* of the HSA has the same width³ $w_{exit,1} = w_{entr,1}$ as the *entrance aperture* diameter. A *transfer lens* system transfers the exit coordinates of the first HSA into the entrance of the second HSA. Because the field direction of the second HSA is reversed compared to the first HSA, the transfer system needs to perform a sign change in the electron trajectory's position and angle (see Eq. (3.7)). In the simulation that is performed by a combination of two Fourier lenses according to

$$\begin{pmatrix} x_{out} \\ \alpha_{out} \end{pmatrix} = \begin{pmatrix} 0 & f \\ -1/f & 0 \end{pmatrix} \cdot \begin{pmatrix} 0 & f \\ -1/f & 0 \end{pmatrix} \cdot \begin{pmatrix} x_{in} \\ \alpha_{in} \end{pmatrix} = \begin{pmatrix} -1 & 0 \\ 0 & -1 \end{pmatrix} \cdot \begin{pmatrix} x_{in} \\ \alpha_{in} \end{pmatrix}. \quad (6.2)$$

The direction change of the second HSA also requires a change of the transfer function given in Eq. (3.2) to

$$x_{exit} = -x_{entr} - 2 \cdot r_0 \cdot (\varepsilon - \alpha^2). \quad (6.3)$$

The entrance and exit slit widths of the second HSA ($w_{exit,2}$ and $w_{entr,2}$) are much bigger than the one of the first HSA. They should in general be opened as wide as

³Only the slit width in the dispersive x-direction is limited to $w_{exit,1}$, the slit width in the non dispersive y-direction is a few times larger.

possible, because they have no energy filter function. Finally, a last Fourier lens behind the second HSA interchanges the spatial and angular information again and forms an energy filtered image.

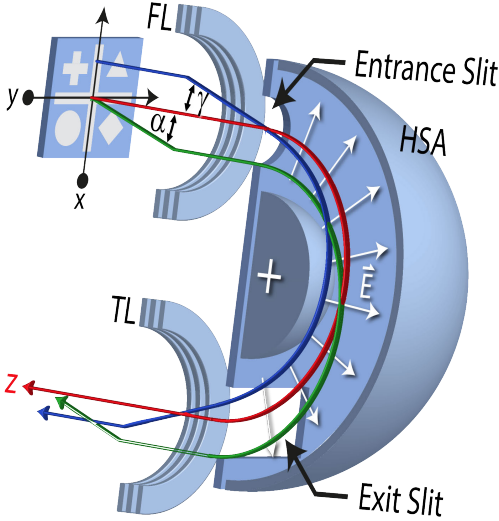


Figure 6.4: Sketch of the first half of the *NanoESCA* energy filter system, which shows, how an image is transferred through a Fourier lens (FL), the hemispherical sector analyzer (HSA) and a transfer lens (TL). The red line marks the (partly bent) optical axis which is shown as (straight) z -direction in the simulations. The same parts have to be added to the shown setup (in reversed order) to give the complete filter system. In this sketch the trajectories of mono energetic electrons (optimal pass energy) are shown.

6.2.2. Calculating the electron trajectories passing the filter

To understand the transfer of an image through the double hemispherical analyzer, we have to follow the electron trajectories which form an image in front of the analyzer to its exit. I use a Cartesian coordinate system like it is shown in Fig. 6.4, where x is the distance and α the angle of a trajectory to the optical axis along the dispersive direction of the analyzer and y is the distance and β the angle of a trajectory to the optical axis in the non dispersive direction. The coordinate z follows the (partly bent) optical axis. Finally, each electron trajectory is defined by a certain kinetic energy with an energy difference ΔE compared to the filter's pass energy E_{pass} . The calculation should show the trajectories which pass the energy filter and form the intermediate image behind the filter and which of them are cut off by the apertures or slits in the system.

Firstly, the influence of the *entrance aperture* on the transmitted phase-space should be analyzed. Electron trajectories in the image plane can have a maximum start angle $\alpha_{0,max}$ to pass the entrance aperture (green line in Fig. 6.4). This angle

depends on the radius $r_{entr,1}$ of the entrance aperture and can be calculated as

$$\tan(\alpha_{0,max}) = \frac{r_{entr,1}}{f_{FL}}. \quad (6.4)$$

The same is true for the y -direction and the angle β . Note that Eq. (6.4) describes only an effective maximum angle, if the angular space is not already more limited earlier in the microscope. As it is shown in Fig. 5.6, for most of the standard settings the angular space is indeed more limited by the contrast aperture in the objective lens (see Sec. 5.2.1) and the entrance slit of the analyzer doesn't play any role in real-space microscopy.

The maximum angle $\alpha_{entr,1,max}$ which enters the energy filter (labeled as γ in Fig. 6.4) only depends on the distance r_{img} of the electron trajectory in the image plane according to Eq. 3.5. A general assumption is that the angle term in Eq. (3.4) should be smaller than the slit term [KS67] to avoid a too asymmetric energy distribution passing the HSA. For the subsequent calculations I define therefore

$$\alpha_{entr,1,max} = \sqrt{\frac{d}{r_0}}, \quad \text{with } d = \frac{w_{entr,1} + w_{exit,1}}{2}. \quad (6.5)$$

A limited $\alpha_{entr,1,max}$ means that the radius of the intermediate image which is transferred through the energy filter is also limited to

$$r_{img} = f_{FL} \cdot \tan(\alpha_{entr,1,max}) \quad (6.6)$$

and that the *field of view* on the sample which is acquired should not be bigger than

$$FOV \leq \frac{2 \cdot r_{img}}{M_{obj} \cdot M_{proj}} = \frac{2 \cdot f_{FL} \cdot \tan(\sqrt{d/r_0})}{M_{obj} \cdot M_{proj}}, \quad (6.7)$$

where M_{obj} is the magnification of the objective lens and M_{proj} is the magnification of the projective lenses in front of the energy filter.

How the electrons which have passed the entrance slit are transferred through the double hemispherical analyzer is shown in Fig. 6.5 according to the transfer functions described above. Note, that the shown path of the trajectories inside the HSAs are not covered by the transfer functions. They were calculated by a cubic interpolation between the trajectory vectors at the entrance and the exit of the HSA⁴ and are shown here for illustrative purpose only.

⁴The simulation relies on the transfer functions described above, which just give a relation between the entrance and exit vectors of a HSA. For a perfect HSA the equation of motion of the electrons inside the HSA can be given in an analytical form and an analytic relation between entrance and exit vectors can be deduced from it [IAK76]. The used transfer functions are nevertheless an approximation [Ton90]. If the entrance and exit vectors are known, it is logical in such a

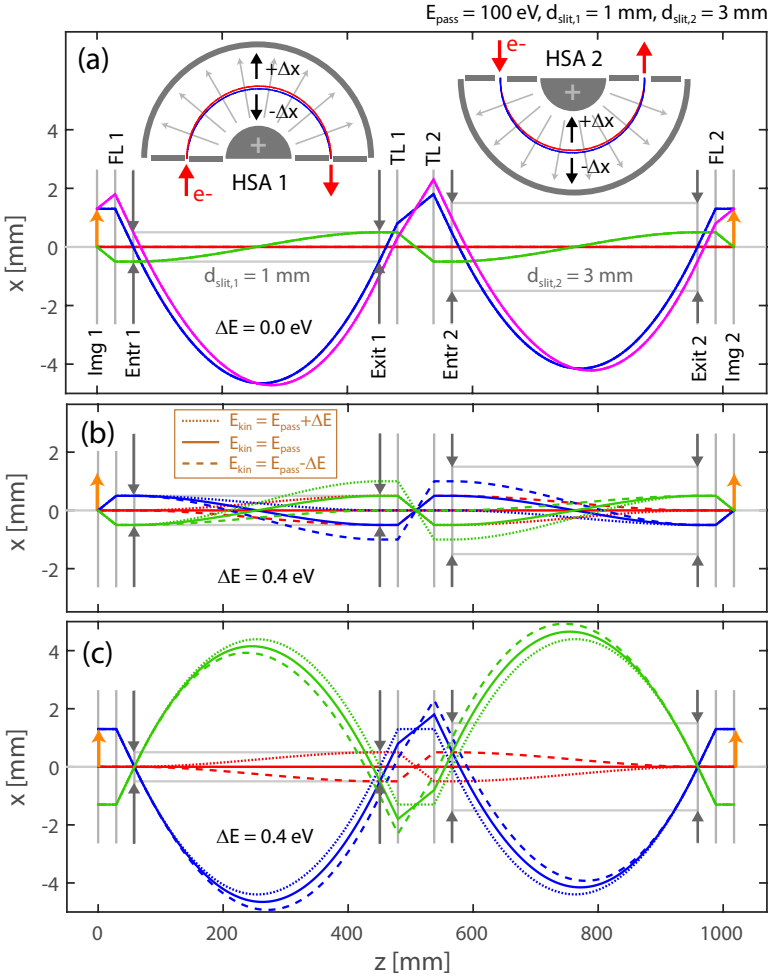


Figure 6.5.: The simulations show the electron trajectories between the intermediate image in front of and behind the double hemispherical analyzer of the *NanoESCA*. The semicircular optical axis inside the HSA (red line) is shown straight in the simulation. One has to keep in mind, that the field direction and the deviation in the second HSA is reversed compared to the deviation in the first one. The separate simulations show (a) the transfer of an image of monochromatic electrons ($E_{\text{kin}} = E_{\text{pass}}$) through the analyzer, (b) the transfer of one point on the optical axis with the maximal angle spread and three different start energies and (c) the transfer of three points of the image plane along the x -direction, also with three different start energies.

6.2.3. Analysis of the calculated trajectories

In Fig. 6.5 (a) the transfer of monochromatic electrons which exactly have the correct pass energy $E_{pass} = 100$ eV are shown. The transferred image has a size of $x_{img} = 1.3$ mm, which is half of the allowed size according to Eq. 6.6 for an entrance aperture diameter and an exit slit width of 1 mm. While all trajectories starting from the optical axis pass the exit slit of the first HSA, for trajectories starting in the image point $x = x_{img}$ that is true only for those parallel to the optical axis (blue line). Bigger start angles (violet line) are cut off. The slits of the second HSA don't play a role, because they are big enough to not block the electrons.

In the calculations shown in Fig. 6.5(b) and (c) also electrons are included, which differ from the ideal pass energy by

$$\Delta E = E_{pass} \cdot \frac{d}{2 \cdot r_0} \quad (6.8)$$

according to the energy resolution formula Eq. (3.4). We see, that electrons with different kinetic energies are separated by the first HSA and joined by the second HSA so that they end up at the correct position in the final image. Note, that these calculations are simplified in so far as no aberrations of the lenses are taken into account. These of course would have some effect on the final image like a reduction of the spatial resolution (see Sec. 5.4). In (b) we see that electrons traveling along the optical axis pass the exit slit exactly with the kinetic energy spread $E_{pass} \pm \Delta E$. For an image point starting from the optical axis with the maximal negative start angle $-\alpha_{0,max}$ only electrons with kinetic energies up to $2 \cdot \Delta E$ lower than E_{pass} can pass. The opposite is true for positive start angles where the transmitted energy distribution is shifted to higher kinetic energies by up to $2 \cdot \Delta E$. If there is no anisotropy in the α_0 distribution, this angle depended energy distribution is symmetric around E_{pass} .

In (c) the shown trajectories are starting parallel to the optical axis but with a distance $x_{img} = \pm 1.3$ mm to it. These trajectories enter the HSA with relatively big angles $\alpha_{entr,1}$ which results in a shift towards the center of the analyzer ($-x$ - direction) according to Eq.(3.2) for positive and negative x_{img} . As a consequence, the energy distribution which can pass the exit slit is shifted to higher kinetic energies.

high symmetrical configuration like the HSA that the connection between them is the shortest continuously differentiable path possible. If the bent coordinate system is transformed to a straight coordinate system, this shortest continuously differentiable path between two vectors can be found by a cubic interpolation. The shown paths inside the HSA are therefore deduced from the simulation, but are not part of it.

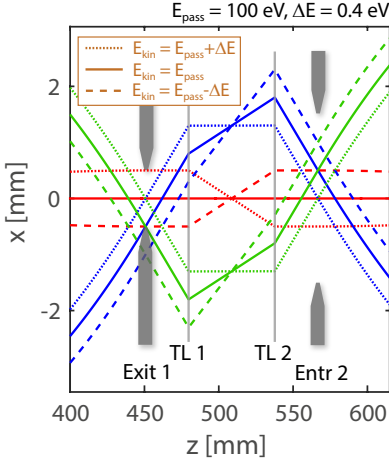


Figure 6.6: Zoom into Fig.6.5(c), showing the electron trajectories in the exit slit of the first hemisphere. Trajectories starting at off-axis positions in the image plane (blue, green) are shifted in the exit slit plane compared to trajectories starting at the optical axis (red). As a consequence, lower energy tails are cut off by the exit slit and higher energetic electrons will pass. In average that causes an energy shift for off axis electrons to higher energies.

This *energy shift* E_{shift} increases with an increasing absolute value of the entrance angle $\alpha_{entr,1}$ and is the reason for the asymmetric tail towards higher energies in the energy distribution of a HSA like it is described in [IAK76]. The obvious explanation is that E_{shift} has to fully compensate the α^2 term in Eq. (3.2) which is true for

$$E_{shift} = E_{pass} \cdot \alpha_{entr,1}^2 \quad (6.9)$$

$$= E_{pass} \cdot \arctan^2\left(\frac{x_{img}}{f_{FL}}\right) = E_{pass} \cdot \arctan^2\left(\frac{M_{obj} \cdot M_{proj} \cdot x_{spl}}{f_{FL}}\right). \quad (6.10)$$

The second equation uses Eq. (6.6) to connect $\alpha_{entr,1}$ with a point x_{img} in the intermediate image in front of the analyzer respectively a point x_{spl} on the sample, if the magnifications of the microscope are known. This solution corresponds to Eq. (6.1) given in [EWRB10]. The result is a non-isochromaticity along the x -direction of an energy-filtered PEEM image where the image center has passed the filter with the kinetic energy distribution

$$E_{kin} = E_{pass} \pm \Delta E \quad (6.11)$$

and the image-points with a distance $\pm x_{spl}$ to the center has passed the filter with a kinetic energy distribution which is shifted to higher energies:

$$E_{kin}(x_{spl}) = E_{pass} + E_{shift}(x_{spl}) \pm \Delta E. \quad (6.12)$$

Because the analyzer entrance angles $\alpha_{entr,1}$ which would usually lead to an asymmetrical energy-distribution (tail to higher energies) [IAK76] are separated along the x -axis of the image, micro-spectra taken out of an image spectrum are shifted in energy according to Eq. (6.10) but the energy-distribution itself is symmetrical for each

point in the image. For completeness, exemplary trajectories of electrons passing the

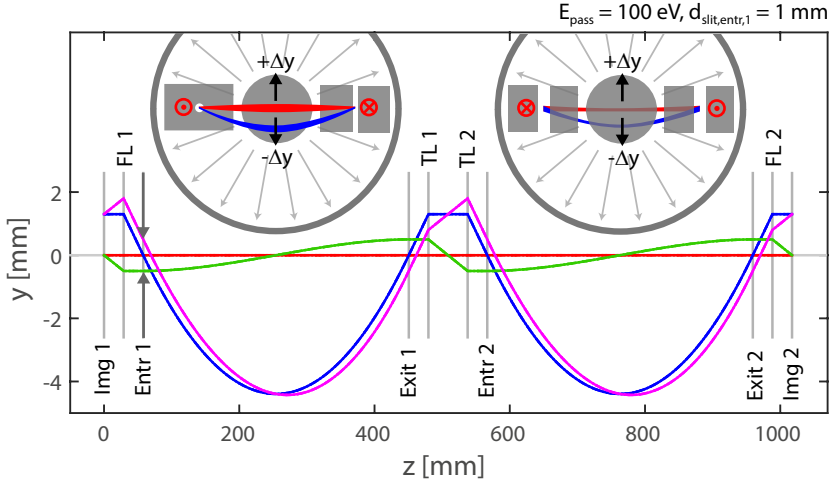


Figure 6.7.: The graph shows, how electron trajectories of an image plane which start in the y - z -plane in front of the analyzer (see Fig. 6.4) are transferred to the image plane behind the analyzer. All slits except the entrance aperture are open in the y -direction so that they don't block the electrons.

analyzer in the y -direction (angle β) are shown in Fig. 6.7. To first order they pass the HSA only with a sign-change in the position and the angle relative to the optical axis. Except for the *entrance aperture* of the first HSA all other slits can be regarded as fully open. Therefore, the above statements concerning the entrance aperture and the x - z -plane are also valid for the y - z -plane. The other effects appear exclusively in the dispersive x -direction of the analyzer.

6.2.4. Simulation of energy-filtered PEEM images

With the formula deduced in the previous section I can simulate how a full PEEM image is transmitted through the energy filter. The image pattern shown in Fig. 6.4 was used as an intermediate image in front of the analyzer. The intermediate image for the simulation only consists of two different start intensities: $I_{start,0} = 100$ in the bright areas of the pattern, $I_{start,0} = 0$ in the dark ones. A pass energy of $E_{pass} = 100$ eV and slit widths of $d_{slit,1} = 1$ mm and $d_{slit,2} = 3$ mm were chosen for the two hemispheres, which is the same as for the trajectory calculations in the previous section. The maximal size of the image was set to $x_{img} = \pm 2.6$ mm

according to Eq. (6.6). For the simulation it was assumed that each intermediate image point (x,y) in front of the analyzer is formed by trajectories of different start angles (α,β) and different kinetic energies E_{kin} . For each possible start trajectory the transmission through the analyzer has to be calculated. The final image behind the analyzer is the sum of the trajectories, which could reach the detector without being blocked by any aperture. The limits of the start angles, which have to be taken into account, are given by Eq. (6.4). The lower limit of the energy-difference ΔE to the pass energy is given by Eq. (6.11) and the upper limit by Eq. (6.12). Sufficient step-sizes had to be chosen for each parameter. The α -parameter was calculated in more than 50 steps between its lower and upper limit. Since the resulting image was found to be insensitive to β , only 9 steps were calculated here. The energy range was calculated in 0.1 eVsteps. For a more realistic intensity distribution in the intermediate image, the angular dependance of the start intensity was taken into account as $I_{start}(\alpha_0, \beta_0) = I_{start,0} \cdot \cos(\alpha_0) \cdot \cos(\beta_0)$, where (α_0, β_0) are the start angles of the electrons on the sample.

Two exemplary results of this simulation are shown in Fig. 6.8, which differ by the CA diameter in use. For large *contrast apertures* (a), the maximum angle of the image plane in front of the analyzer is determined by the *entrance aperture* of the analyzer (like in Fig. 6.5), but usually (b) it will be determined by the CA (see Fig. 5.6). A smaller *angle acceptance*, e.g. due to the smaller CA, results in a reduced smear-out of the intensity distributions along the dispersive x-direction in the images. The image series in (a) and (b) show, how monochromatic electron images with different energies $E_{kin} = E_{pass} + \Delta E_{kin}$ around the real pass energy would be transferred through the filter. The experimental equivalent is to use energetically pre-filtered electron images. The results of the simulation is that the center of the transferred full image is indeed formed by electrons with the correct kinetic energies around E_{pass} . In contrast, image parts with a higher distance from the center along the x-axis are formed by electrons with higher kinetic energies. The non-isochromaticity of the energy filter becomes directly visible here, although the calculations, which the simulation is based on, only describes a one-dimensional effect.

6.2.5. The footprint of the non-isochromaticity in energy-filtered images

In reality, all electrons with different kinetic energies around E_{pass} enter the analyzer together at the same time. By combining the energy separated results of the simu-

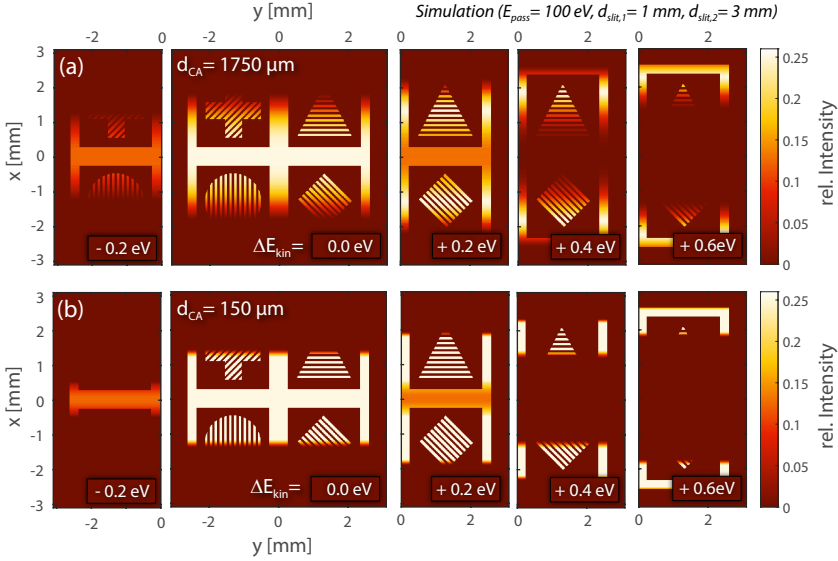


Figure 6.8.: The simulation shows, how an image of monochromatic electrons at the entrance of the analyzer is transferred through the hemispheres ($E_{pass} = 100 \text{ eV}$, $d_{slit,1} = 1 \text{ mm}$, $d_{slit,2} = 3 \text{ mm}$). The kinetic energy of the monochromatic images is varied around the pass energy: $E_{kin} = E_{pass} + \Delta E_{kin}$. The intensity distribution of the image behind the analyzer is given relative to the absolute transmitted intensity ($\sum_i I(E_{kin,i})$). An energy dependent effect is only visible in the dispersive x-direction. While the center of the final image is dominated by electrons with $E_{kin} = E_{pass}$, the outer borders of the image consists of electrons with higher kinetic energies. This energy-shift appears symmetrical around $x = 0 \text{ mm}$. The calculation is shown for two different contrast apertures. With an open contrast aperture $d_{ca} = 1.75 \text{ mm}$ the transmitted angles are limited by the entrance slit (a). A small CA of $d_{ca} = 0.15 \text{ mm}$ nevertheless limits the angle space much more (b).

lation one can deduce, how a more realistic measurement would look like. Averaging all energy-values ΔE by weighting them with the intensity distribution $I_{xy}(\Delta E)$ for each simulated image according to

$$\Delta E_{xy} = \frac{\sum_{\Delta E} I_{xy}(\Delta E) \cdot \Delta E}{\sum_{\Delta E} I_{xy}(\Delta E)} \quad (6.13)$$

results in the map in Fig. 6.9 (a). It shows the simulated mean energy shift at each point of a complete energy-filtered image. Since the effect in the simulation is one-dimensional, the energy-shift can be analyzed with a profile along the x-axis like it is shown in Fig. 6.9 (b). Additional profiles are shown for comparison, which were simulated for different E_{pass} . The results of a parabolic fit to these profiles are perfectly consistent with Eq. (6.10).

This energy shift map in principal is exactly what can be measured with the work function analysis shown in Fig. 6.2(b) and (d). The obvious difference is the opening direction of the parabola. The energy shift in the analyzer increases to higher energies as a function of the distance to the optical axis. In a work function scan this has the consequence that the work function edge for these image points is reached already for a smaller filter energy according to Eq. (3.11). The measured work function shift therefore in general needs to be multiplied by (-1) to describe the energy shift in the analyzer. The measurements furthermore show a two dimensional effect. Thus, the non-isochromaticity is not fully explained by the model. This difference will be systematically examined in Sec. 6.4.

With the help of the simulated energy-shift map it can be calculated, how an energy filtered photoemission image from, e.g., a core level peak would look like. The simple sum $\sum_{\Delta E} I_{xy}(\Delta E)$ over the intensity distributions for all energies in Fig. 6.8 results in an homogenous intensity distribution. This is not the case in reality, since the photoelectron intensity from a core level is very energy dependent. Thus, each monochromatic image $I_{xy}(\Delta E)$ in the simulation has to be weighted with the photoelectron intensity for each kinetic electron energy represented by ΔE . The sum over all weighted monochromatic images then will not result in a homogenous intensity distribution. For example, if we measure a PEEM image on a core level peak, we get a strong signal from the peak in the center of the image. At the top and the bottom of the image the electrons which pass the filter are less intense off-peak electrons. These photoelectrons have higher kinetic energies compared to the peak electrons and therefore had smaller binding energies E_{bin} in the material.

To simulate such a photoemission image, I use a *Voigt profile* to describe the

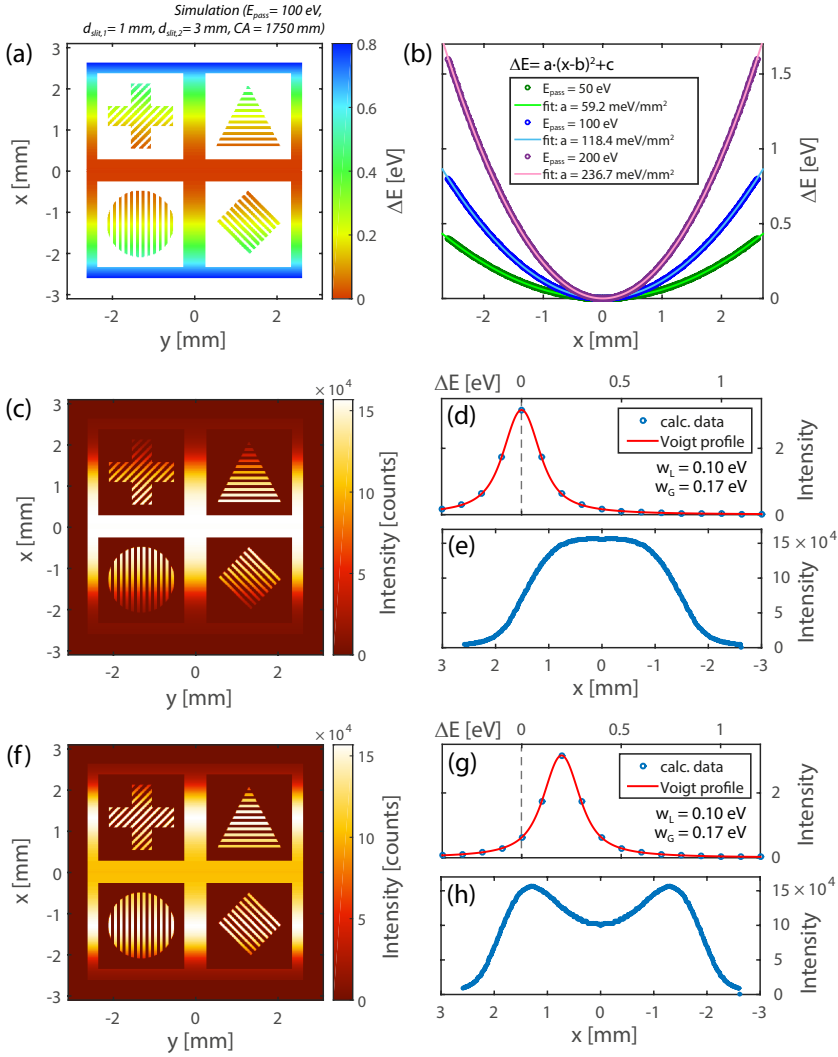


Figure 6.9.: From the simulation in Fig. 6.8 we can (a) deduce the mean energy difference from E_{pass} across the image. The energy-shift effect only appears along the x-direction and increases for increasing E_{pass} as is shown in (b). The energy-shift effects the intensity distribution in a final image (c), if the photoelectron intensity distribution as a function of the measured energy is not homogenous, but e.g. a Voigt profile (d). That is true for a core level measured by an analyzer with a limited energy resolution. The profile along the x-axis is shown in (e). If E_{pass} is set on a 0.2 eV lower kinetic energy than the core level (g), the final image would look like shown in (f,h).

energy dependent intensity distribution of a *core level peak* which can be written as

$$I(\Delta E_{kin}) = V(\Delta E_{kin}, w_L, w_G) = \int G(\varepsilon, w_G) \cdot L(\Delta E_{kin} - \varepsilon, w_L) d\varepsilon, \quad (6.14)$$

and is a convolution of a *Lorentzian profile* $L(\varepsilon)$ with scale parameter w_L and a *Gaussian profile* $G(\varepsilon)$ with standard deviation w_G . Such a Voigt profile is shown in Fig. 6.9(d) for the complete kinetic energy range which can pass the filter according to the side conditions of the simulation (see Sec. 6.2.4). Figure 6.9(c) shows the final simulated image and its profile along the x-axis (e) if the filter energy is set to the peak of the energy profile in (d).

Since the simulated kinetic energy shift $\Delta E_{kin}(x)$ along the x-axis is fully described by Eq. (6.10), it can be directly used in Eq. (6.14) to get a formula which describes the intensity profile in (e) as a function of the x-position with

$$I(x) \propto V(\underbrace{E_{pass} \cdot \arctan^2\left(\frac{x}{f_{FL}}\right)}_{=E_{shift}} - \varepsilon_c, w_L, w_G). \quad (6.15)$$

The energy filter does not necessarily have to be set on the peak of a core level, but can be adjusted with a energetic distance ε_c to it. If the filter energy, for example, is set to lower kinetic energies⁵ (see Fig. 6.9(g)), the intensity distribution in the photoemission image (f) and the profile along the x-axis (h) also change. A generalized fit model for this intensity profile can be given in Sec. 6.5 after performing an experimental characterization of the energy filter in the next section.

6.3. Calibration of the intermediate image plane

The calculations in the previous section explain the non-isochromaticity along the dispersive direction of the hemispheres. To characterize the deviations between these calculations and experiment, a series of test measurements needs to be performed (see Sec. 6.4). In Eq. (6.10), the energy shift caused by the analyzer is a function of the electron position in the intermediate image in front of the analyzer⁶. To be able to compare the measured and calculated non-isochromaticities, the experimental data needs to be related to the same intermediate image plane. In this section I study, how this can be done. The results will be used in the subsequent sections.

⁵which means to higher binding energies in the photoemission spectrum

⁶This intermediate image is positioned in the deflector plane in front of the Fourier lens, see Fig. 3.2 and Fig. 3.5.

6.3.1. Magnification of the intermediate image plane

If the non-isochromaticity measured by a work function analysis (see Fig. 6.2(b)) should be compared with the calculated energy shift in Eq. (6.10), the scaling of the intermediate image in front of the analyzer needs to be estimated as exactly as possible. The best way to do this is to place an aperture of known size into the image plane. Since such an aperture is not available in our instrument the calibration of the image plane has to be estimated from the *magnification* steps of the microscope before and after the image plane.

With a *checkerboard patterned sample* it is possible to calibrate the field of view on the sample and relate it to the magnified PEEM image which is mapped on the imaging detector. The visible area of the detector has a diameter of 19.1 mm which corresponds to 562 px on the CCD camera⁷. With those values the total magnification of the microscope M_{total} can be determined if the measured size of a checkerboard square on the CCD w_{px} (in pixel) is compared to the known real size of the square $w_{\mu m}$ as

$$M_{total} = \frac{w_{px}}{w_{\mu m}} \cdot \frac{19100 \mu m}{562 \text{ px}} = M_{obj} \cdot M_{P12} \cdot \underbrace{M_{rf} \cdot M_{rb}}_{=M_{res}} \cdot M_{P34}. \quad (6.16)$$

The total magnification is the product of the magnifications of several separate microscope elements (see Sec. 3.1). These are the magnifications of the objective lens M_{obj} and the projective lens M_{P12} in front of the analyzer as well as the projective lens M_{P34} in the back of the analyzer. The values of these magnifications can be simulated for each lens as a function of different lens settings and used in Eq. (6.16). Nevertheless, a possible residual magnification always M_{res} needs to be taken into account, because especially the objective lens magnification (see Fig. 5.5(a)) very much depends on insufficiently calibrated factors like the distance between the sample and the extractor. To find a calibration for the intermediate image in front of the analyzer it is useful to split M_{res} up into a part in front of it (M_{rf}) and behind it (M_{rb}). The analyzer itself is assumed to not add any magnification to the transferred image.

A test measurement of M_{total} as a function of M_{P12} and, independently, M_{P34} is shown in Fig. 6.10. Simulated values were used for M_{P12} , M_{P34} and M_{obj} , while M_{total} was determined with the checkerboard pattern as mentioned above. By fitting the measurement and correcting the fit-values with the known magnifications

⁷The camera diameter physically has the double size but works in a 2x2 binning mode, see Sec. 3.1.4

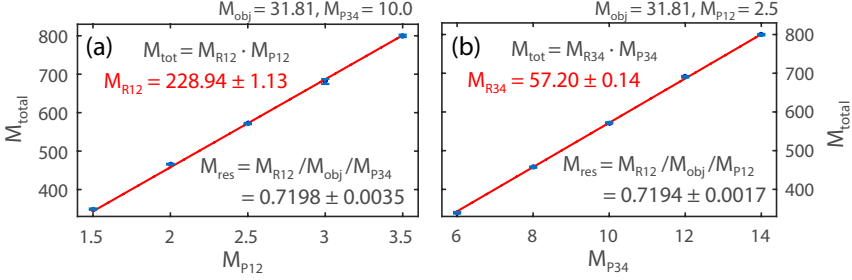


Figure 6.10.: The total microscope magnification is measured as a function of the magnification of the projective P_{12} (a) and of the magnification of the projective P_{34} (b). All other lens settings were kept on constant values. The fitted rest magnifications M_{R12} , M_{R34} are a product of the respective remaining magnification steps of the microscope. If the fitted residual magnifications are divided by the known magnifications, a total residual magnification of $M_{\text{rest}} \approx 0.72$ remains.

according to Eq. (6.16) a residual magnification of $M_{\text{res}} \approx 0.72$ remains. Since it is still not possible to determine how this residual magnification splits into M_{rf} and M_{rb} , I need to calibrate the intermediate image plane from both sides of the microscope and to compare the results.

The first calibration factor κ_{im1} is therefore derived from the calibration of the detector diameter $\kappa_{det} = 19.1 \text{ mm}/562 \text{ px}$. It needs to be divided by the magnification steps behind the intermediate image as

$$\kappa_{im1} = \frac{\kappa_{det}}{M_{P34} \cdot M_{rb}}. \quad (6.17)$$

The second calibration factor is derived from an image of the checkerboard sample. This calibration $\kappa_{spl} = w_{\mu\text{m}}/w_{\text{px}}$ needs to be multiplied with the magnification steps in front of the intermediate image as

$$\kappa_{im2} = \kappa_{spl} \cdot M_{obj} \cdot M_{P12} \cdot M_{rf}. \quad (6.18)$$

Both calibrations have to result into the same scale of the intermediate image. By measuring an effect which is related to the scale of the intermediate image (like the energy shift in the analyzer) it is possible to disentangle the unknown magnifications M_{rb} and M_{rf} . This is used in the next section.

6.3.2. Non-Isochromaticity dependence on the projective magnification

If the energy shift only depends on the scale of the intermediate image in front of the analyzer (as it is supposed by Eq. (6.10)), the profile of the energy shift which

is mapped onto the detector should stay the same, if all microscope settings behind the intermediate image plane remain unchanged. A change of the *projective lenses* in front of the intermediate image plane only influences the field of view of the sample, which is mapped onto the detector. Precisely this experiment is shown in Fig. 6.11. A work function analysis was made on a checkerboard sample with two different magnifications $M_{P12} = 2$ (a) and $M_{P12} = 3$ (b) of the projective lens in front of the intermediate image plane. The change of the magnification by a factor of 1,5 is visible on the checkerboard pattern. The FoV in (a) is approximately $53 \mu\text{m}$ and in (b) approximately $35 \mu\text{m}$. The scaling of the axes are already related to the intermediate image plane by using Eq. (6.17) and setting the unknown factor (arbitrarily) to $M_{rb} = 1$. Furthermore, the intermediate image is inverted in the x and y direction compared to the image on the detector, because the chosen projective lens P_{34} setting generates only one cross-over of the electron trajectories which point-mirrors the image.

Indeed, the non-isochromaticities in both work function maps in Fig. 6.11 (a,b) are of a comparable magnitude, but not completely equal. The analysis of the obvious differences lead to some important insights. As already recognized in Sec. 6.1, the non-isochromaticity is in contrast to the calculations not entirely one dimensional. The *iso-energy-shift-lines* (iso-esl) in the work function maps, which denote the same energy shift ΔE , are bent upwards in (a) and (b). The reason for this effect is an additional parabolic energy-shift along the y -direction, which can be measured with a profile scan along the y -axis of the map (not shown here).

This additional energy shift parabola has the opposite sign compared to the energy shift parabola ascribed to the energy-filter. The work function shift increases with the distance from the optical axis. This effect scales with the magnification of the P_{12} lenses, as can be seen from the shape of the *iso-esls* in (a) and (b). The additional non-isochromaticity effect therefore depends on the settings of the microscope modules in front of the analyzer. Because all modules in the microscope (except the octupole stigmator/deflector elements) are cylinder-symmetric it is very reasonable to assume that this additional non-isochromaticity has a cylinder-symmetric component in contrast to the one-dimensional effect of the analyzer. Since both energy shifts have opposite signs they counter-act each other along the x -axis.

To disentangle both non-isochromaticities, I assume that the negative *work function shift* along the x -axis has a profile according to Eq.(6.10). The remaining positive

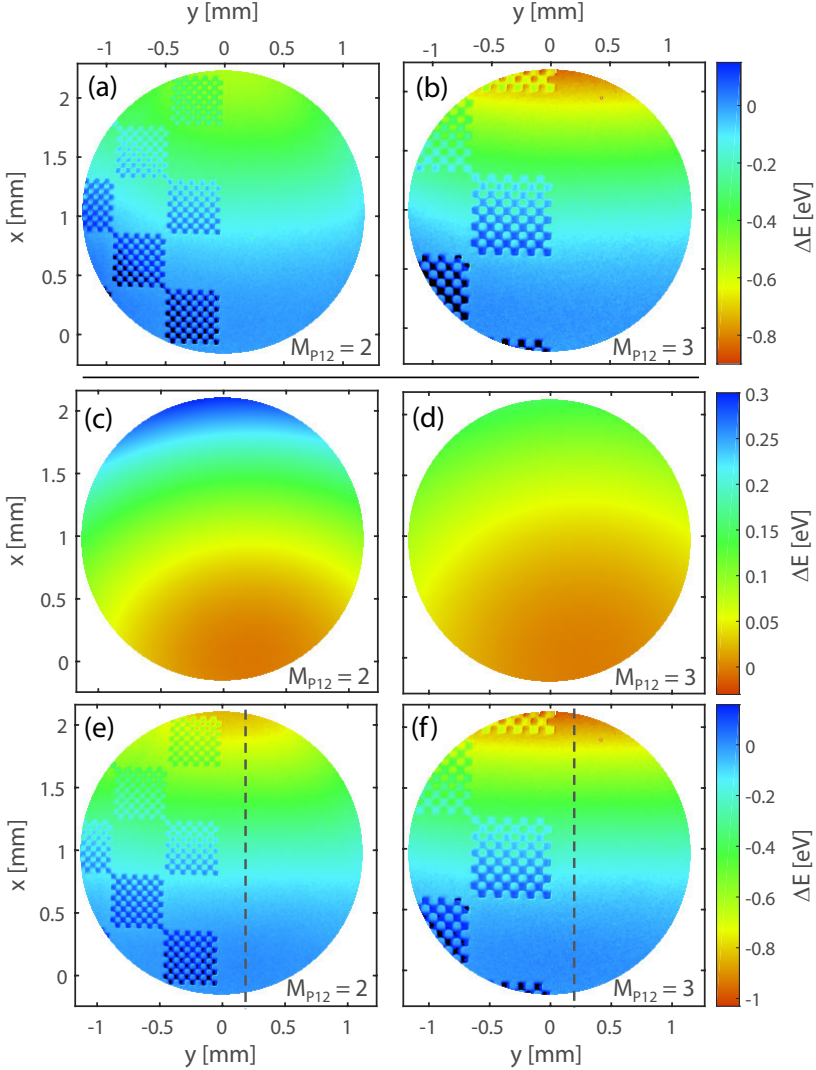


Figure 6.11.: Work function maps were measured for two different projective lens P_{12} magnifications: (a) $M_{P_{12}} = 2$ and (b) $M_{P_{12}} = 3$. The axis - scaling was calculated backwards from the detector to the image plane in front of the analyzer, assuming $M_{r_b} = 1$. The detected energy shift is different for both P_{12} magnifications, because an additional non-isochromaticity from the microscope (c,d) has to be taken into account, which scales with the magnification of P_{12} . After subtracting the additional non-isochromaticities (c,d) from the original work function maps (a,b), the remaining non-isochromaticity maps (e,f) are related to the analyzer, showing an only one dimensional effect along the dispersive direction of the analyzer.

work function shift can be fitted by the two dimensional parabolic model

$$\Delta E(x, y) = \underbrace{a_{cyl} \cdot ((x - c_x)^2 + (y - c_y)^2)}_{\text{cylinder symmetric}} + \underbrace{a_{1dim} \cdot (x - c_x)^2}_{\text{one dimensional}} + \Delta E_0 \quad (6.19)$$

with the coordinates (c_x, c_y) of the center of the parabola. The model consists of a cylinder-symmetric term with the coefficient a_{cyl} , which represents instrument parts which have a cylinder symmetry⁸, but also a term with coefficient a_{1dim} , which describes additional one-dimensional effects along the x-axis. These are either corrections to the calculated energy-shift described by Eq.(6.10) or additional energy-shifts caused by other components in the instrument. The fit results according to Eq. (6.19) are shown in in Fig. 6.11(c,d) for both P_{12} magnifications. If the aforementioned interpretation of the parabola is correct, its center can be identified with the position of the *optical axis* in the PEEM image.

By subtracting the fitted (positive directed) energy-shifts in Fig. 6.11(c,d) from the original measurements (a,b), the energy shift maps shown in (e,f) are achieved. Indeed, both maps show a nearly equal, in first order one-dimensional energy-shift which is independent of the P_{12} magnification. Profiles along the x-directions of both maps (gray lines) are shown in Fig. 6.12. Up to a distance of $x \approx 1.32 \mu\text{m}$ ($M_{P_{12}} = 2$) or $x \approx 1.40 \mu\text{m}$ ($M_{P_{12}} = 3$), respectively, both extracted energy shifts can be described by the parabolic function

$$\Delta E = -E_{pass} \cdot \left(\arctan \left(\mu_{rx} \cdot \frac{x - c_x}{f_{FL}} \right) \right)^2 + \Delta E_0 \quad (6.20)$$

$$\text{with } \mu_{rf} = M_{rf} \text{ or } \mu_{rb} = \frac{1}{M_{rb}} \quad (6.21)$$

which is equal to Eq. (6.10) except for two points:

- As explained in Sec. 6.2.5, the sign of the measured energy-shift parabola in a work function scan is reversed to the real energy shift of the electron energies passing the analyzer. This is represented by the minus sign in Eq. (6.20).
- Because of the unknown exact magnification of the intermediate image, the scaling factor μ is introduced in the equation. It directly relates to the magnification corrections in Eq. (6.17) and Eq. (6.18). If the scaling of the intermediate image is calculated backwards from the detector, we can write $\mu = 1/M_{rb}$. If the scaling is calculated from the dimensions on the sample, we can write $\mu = M_{rf}$.

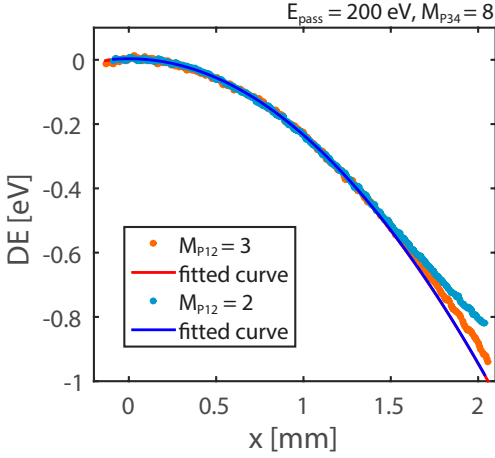


Figure 6.12: Profiles along the non-isochromaticity maps in Fig.6.11(e,f) (gray lines), which were corrected for the non-isochromaticity of the microscope in front of the analyzer. Both profiles have the same shape close to the optical axis and can be fitted with the energy-shift parabola in Eq.(6.20). Only data points far away from the optical axis differ from that model (see text).

Because the fit-parameters E_{pass} and μ in Eq. (6.20) cannot be disentangled, the pass energy was set to the fixed value of $E_{pass} = 200$ eV which was used during the measurement. An energy-shift profile along the x-axis was evaluated for both P_{12} magnifications and with the two different scaling methods starting from the front or from the back of the NanoESCA. The results of these fits are compiled in Tab. 6.1.

While M_{res} was calculated with Eq. (6.16) by comparing the scaling of the sample with the scaling of the detector screen and dividing by the known magnifications, M_{rf} and M_{rb} were fitted independently with the model in Eq. (6.20). The product of the two fit results is also shown in Tab. 6.1. It agrees with the total residual magnification M_{res} as it was defined in Eq. (6.16). The splitting of M_{res} in parts before and after the intermediate image plane is thereby found and the scaling of the intermediate image can be calculated. It is used in Fig. 6.11(c-f) and Fig. 6.12. The initially used scaling in Fig. 6.11(a,b) assuming $M_{rb} = 1$ was already correct. The

⁸Cylinder-symmetrical parts are: objective, projective lens, Fourier lens, round entrance aperture, transfer lens

M_{P12}	M_{res}	M_{rf}	M_{rb}	$M_{rf} \cdot M_{rb}$
2	0.712 ± 0.004	0.672 ± 0.002	1.060 ± 0.003	0.712 ± 0.003
3	0.717 ± 0.006	0.697 ± 0.003	1.028 ± 0.004	0.717 ± 0.004

Table 6.1.: Evaluation of the energy shift profiles (Fig. 6.12) for both P_{12} magnifications using Eq. (6.20).

values for M_{rf} on the other hand differ significantly from unity. Since the origin of this deviation is not clear yet, the calibration of the intermediate image plane should be performed according to Eq. (6.17) from the detector side of the instrument.

The fact that the data in Fig. 6.12 start to differ from the parabolic model for distances above 1.4 mm could be explained by the assumption in Eq. (6.6) for a limited intermediate image radius $r_{img,max}$, which should be used for a certain analyzer slit-width d_{slit} . For the slit-width of $d_{slit} = 0.5$ mm used in this measurement that would be $r_{img,max} = 1.837$ mm. On the other hand, those deviations become less significant with a higher P_{12} magnifications. This indicates that not only the slit but also the projective lens has an influence on this behavior.

6.4. Experimental characterization of the Non-isochromaticity

After the energy-shift measurements of different P_{12} magnifications helped to disentangle different non-isochromaticities in the *NanoESCA*, the goal of this section is to study how the change of the energy filter settings (namely pass-energy and slit-width) affects the energy-shift. As mentioned in the previous section, it is adequate to calculate the scaling of the intermediate image plane in front of the analyzer according to Eq. (6.17) using $M_{rb} = 1$. In this case we can unify the fit models in Eq. (6.19) and Eq. (6.20) to a model, which can be directly applied to a measured work function map:

$$\Delta E = \underbrace{-E_{pass} \cdot \arctan^2\left(\frac{x - c_x}{f_{FL}}\right)}_{\text{one dimensional I}} + \underbrace{a_{1dim} \cdot (x - c_x)^2}_{\text{one dimensional II}} + \underbrace{a_{cyl} \cdot ((x - c_x)^2 + (y - c_y)^2)}_{\text{cylinder symmetry}} + \Delta E_0. \quad (6.22)$$

An example of this fit is shown in Fig. 6.13. The two different one dimensional parts in Eq.(6.22) can only be disentangled, if the parameter E_{pass} is already set as a fixed value in the fit-function according to the experimental setting. The interesting fit-parameters are then the coefficients a_{1dim} and a_{cyl} of the additional non-isochromaticities, which describe the deviation of the real measured non-isochromaticity from the model presented in Sec. 6.2. Also the probable position of the *optical axis* (c_x, c_y) is a direct result of the fit and is used as image center in all figures. In the following I will study those fit parameters as a function of different analyzer settings.

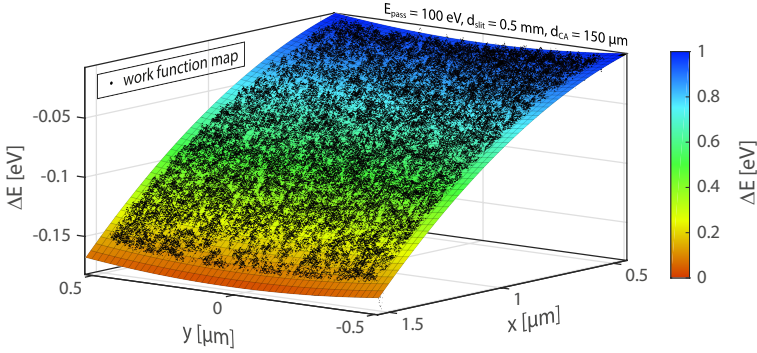


Figure 6.13.: Exemplary 3D fit of a work function map according to Eq. (6.22)

6.4.1. Effects of the analyzer pass-energy and slit configuration

The *pass energy* E_{pass} is the only parameter defining the strength of the non-isochromaticity in Eq. (6.10). Therefore it is reasonable to first analyze the deviations from this equation as a function of E_{pass} . This measurement is shown in Fig. 6.14. The first row (a-c) shows the original measured work function maps for three different pass energies. The second row (d-f) shows the cylinder-symmetric part of the fit model in Eq. (6.22). The third row (g-i) shows the sum of the cylinder-symmetric and the one-dimensional deviation. Subtracting the entire deviation in the third row from the original measurement in the first row results in the map in the fourth row (j-l). Like in Fig. 6.11 (e,f) it then mainly shows the dominant non-isochromaticity effect described by Eq. (6.10).

The range of the color scales in each row scale is proportional to the pass energy represented in each column. Despite the fact that the image center is slightly different in each measurement, it is visible that the measurements look qualitatively very similar. All energy shift effects seem to scale proportional to the pass energy. Profiles along the gray lines indicated in (j-l) are shown in Fig. 6.15 (a). They were fitted with Eq. (6.20). The free parameter M_{rb} which allows a correction of the scaling of the intermediate image plane varies only slightly between 1.01 and 1.02 which proves that the fitting procedure worked as expected. The measured results correspond with the calculations for different pass energies shown in Fig. 6.9(b).

If I keep $E_{pass} = 50$ eV constant and vary the width of the exit slits instead, the profiles of the work function maps (after subtracting the additional energy-shifts)

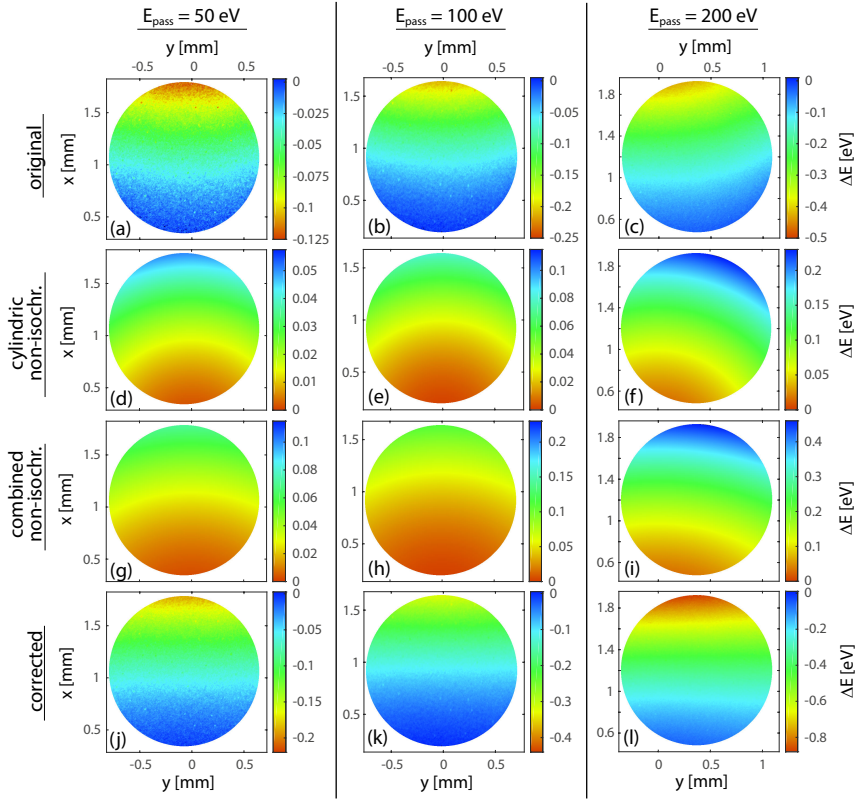


Figure 6.14.: Disentangling the non-isochromaticity effects for different pass energies.

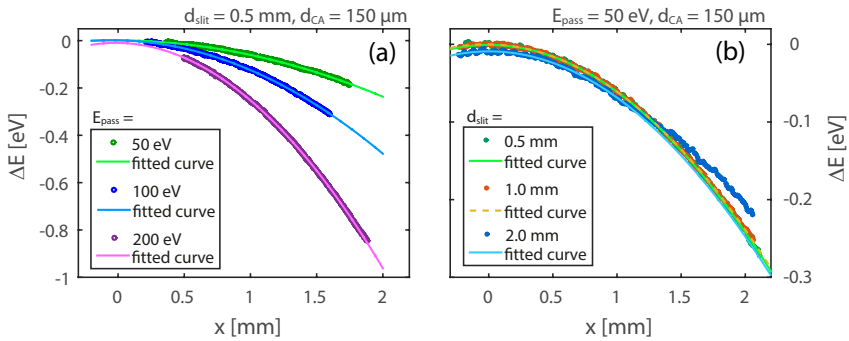


Figure 6.15.: Fits to the corrected work function maps in Fig. 6.14.

are nearly equal, as shown in Fig. 6.15 (b) . Only for the biggest slit width and higher image distances from the optical axis the measurement deviates from the parabolic model, like it was already observed for the P_{12} magnification scan in Fig. 6.1. The fitted additional non-isochromaticity maps of this measurements are shown in Fig. 6.16(a-c). A significant energy-shift dependency from the slit-width is visible in the cylinder symmetrical non-isochromaticity represented by the coefficient a_{cyl} . It becomes smaller with increasing slit-width. Interestingly, the additional one dimensional energy shift (represented by a_{1dim}) increases and nearly compensates the coefficient a_{cyl} along the x-axis so that the sum of both energy shifts (d-f) is equal for all slit-widths.

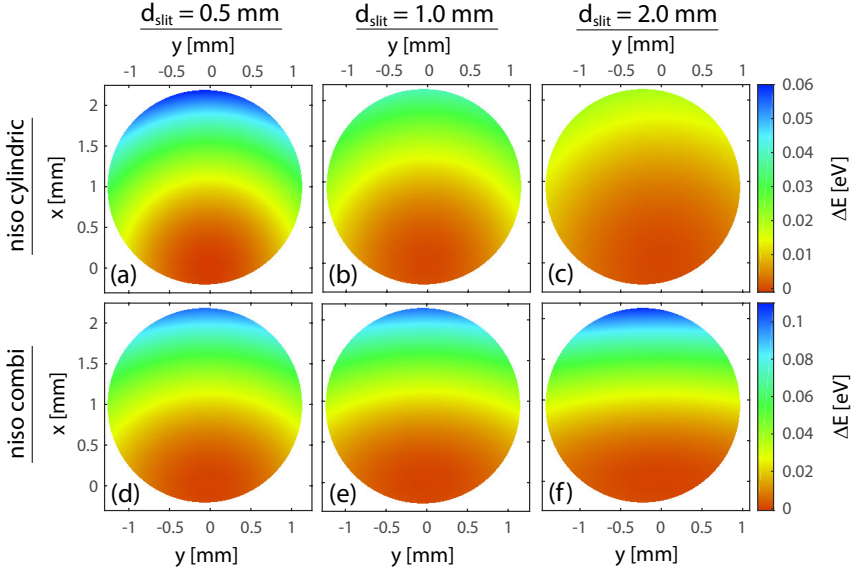


Figure 6.16.: Additional non-isochromaticity effects as a function of the slit width.

An overview of all analyzed microscope settings is compiled in Tab. 6.2. Besides the mentioned pass energy and slit width dependencies, also a series of measurements was performed with alternating contrast aperture diameters. The differences are hardly visible in the work function maps because mainly the a_{1dim} fit parameter is affected. Therefore they are not shown here. The table also lists the parameters of the P_{12} magnification series in Sec. 6.3.2.

#	$\frac{E_{pass}}{\text{eV}}$	$\frac{d_{slit}}{\text{mm}}$	$\frac{d_{CA}}{\mu\text{m}}$	M_{P12}	M_{P34}	$\frac{E_{pass}/\text{meV}}{(29 \text{ mm})^2}$	$a_{cyl}/\frac{\text{meV}}{\text{mm}^2}$	$a_{1dim}/\frac{\text{meV}}{\text{mm}^2}$
01	200	0.5	150	2	8	237.81	-44.9 ± 0.3	-50.9 ± 0.6
02	200	0.5	150	3	8	237.81	-24.5 ± 0.3	-15.7 ± 0.7
03	50	0.5	150	2	13.25	59.45	-15.8 ± 0.1	-6.5 ± 0.2
04	100	0.5	150	2	13.25	118.91	-29.7 ± 0.1	-12.0 ± 0.2
05	200	0.5	150	2	13.25	237.81	-59.2 ± 0.3	-63.6 ± 0.3
06	50	0.5	150	2	8	59.45	-13.5 ± 0.1	-7.6 ± 0.1
07	50	1.0	150	2	8	59.45	-8.7 ± 0.1	-13.3 ± 0.1
08	50	2.0	150	2	8	59.45	-4.5 ± 0.2	-19.5 ± 0.4
09	50	0.5	30	2	8	59.45	-13.8 ± 0.2	-3.0 ± 0.2
10	50	0.5	70	2	8	59.45	-15.3 ± 0.1	-3.8 ± 0.1
11	50	0.5	150	2	8	59.45	-13.5 ± 0.1	-7.6 ± 0.1
12	50	0.5	500	2	8	59.45	-14.0 ± 0.1	-9.4 ± 0.2

Table 6.2.: Overview over the fit parameters measured in this chapter. The energy shift according to Eq.(6.10) is compiled in the third last column. It is normalized so that its size can be directly compared to the coefficients a_{cyl} and a_{1dim} . The grey column-background color mark the parameters which were changed in one series. The measurements marked with either green or yellow color belong to different series, but represent a comparable parameter set, as explained in the text. Line (11) shows the results of the same measurement as line (6) and was just repeated for clarity.

6.4.2. An interpretation of the energy-shift dependencies

In general it is not straight-forward to associate the non-isochromaticity effects represented by the fitted parameters compiled in Tab. 6.2 with a specific lens or module in the *NanoESCA*, because the action of one element in the machine has a direct influence on following elements. For example, the measurements with $E_{pass} = 200$ eV in line (1) and line (5) are comparable except for the magnification of the second projective P_{34} . A higher magnification obviously leads to higher coefficients a_{cyl} and a_{1dim} . That is also true for a_{cyl} in line (3) ($E_{pass} = 50$ eV) if we compare it with line (6). A possible reason is that energy shifts applied by the energy analyzer leads to chromatic aberration effects in the subsequent lenses. These are the transfer lenses behind the first hemisphere, the Fourier lens behind the second hemisphere and finally also the projective lenses P_{34} . The fit parameters a_{cyl} and a_{1dim} are plotted in Fig. 6.17(a-c) as a function of the pass energy, the slit widths of the first hemisphere and the used contrast aperture diameter. For those independent parameters only a small number of variations is available in the instrument (e.g. fix amount of aperture diameters). Nevertheless, some trends can be identified from this limited data set.

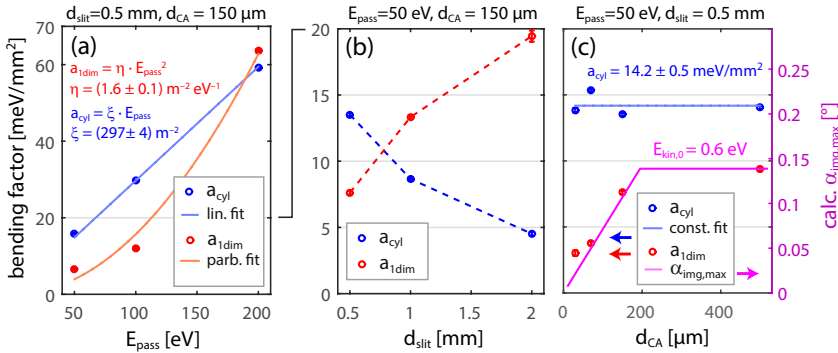


Figure 6.17.: Graphical representation of the fit parameters listed in Tab. 6.2 (in absolute values).

A parameter which is comparatively easy to interpret is the diameter of the contrast aperture. A smaller CA mainly reduces the maximal angle space in the microscope. The maximal start angle $\alpha_{spl,max}$ on the sample⁹ can be calculated with Eq. (5.26). Using the *law of Helmholtz and Lagrange* (similar to Eq. (5.29)) this $\alpha_{0,max}$ can be transferred to the maximal angle in the intermediate image plane

⁹as a function of the kinetic electron energy eV_0 and the diameter of the contrast aperture

$\alpha_{img,max}$ in front of the analyzer as

$$\alpha_{img,max} = \arcsin \left(\sqrt{\frac{e \cdot V_0}{E_{pass}}} \cdot \frac{1}{M_{obj} \cdot M_{P12} \cdot M_{rf}} \cdot \sin(\alpha_{spl,max}) \right). \quad (6.23)$$

The value for the residual magnification M_{rf} is taken from Tab. 6.1. The calculated angle $\alpha_{img,max}$ is plotted in Fig. 6.17(c) and very well fits to the behavior of the a_{1dim} fit parameter. The curve depends on the kinetic start energy $E_{kin} = e \cdot V_0$ of the electrons and fits best for $e \cdot V_0 = 0.6$ eV. This value is still in the emitted electron spectrum (compare Fig. 6.3(d)), but a little bit higher than expected from the work function analysis. The kink at $d_{CA} = 196$ μm marks the contrast aperture diameter, for which all electrons leaving the sample with this specific kinetic energy can pass the contrast aperture without being cut off (compare with Fig. 5.5(b)). While the a_{1dim} fit parameter is a function of the maximum angle in the intermediate image, a_{cyl} is not. It doesn't show a significant dependance on the contrast aperture diameter. To understand how the maximum trajectory angle $\alpha_{img,max}$ in the image plane influences the non-isochromaticity, a trajectory calculation is shown in Fig. 6.18. It focuses on off-axis electrons with non-zero start angles in the image plane and considers the energy-shift. In contrast to the calculation in Fig. 6.5, off-axis electrons are directly calculated for higher kinetic energies according to Eq. (6.10). Consequently, the lateral shift of the trajectories in the exit slit plane, which could be seen in Fig. 6.6, disappears. Instead, a general asymmetry for the starting angles becomes visible: The low energy tail of positive starting angles (violet) is cut off by the exit slit of the first hemisphere, which means that there will be an angle dependent shift to higher energies for those electron trajectories. The opposite is true for all negative starting angles. They will shift to lower energies. For a homogenous start angle distribution, this angular asymmetry will not be visible in the final image behind the analyzer, because low- and high- energy shifts cancel each other out in the sum. As it is visible in Fig. 6.18(b) the angular asymmetry leads nevertheless to a big spatial and energetic spread in the transfer lens system between the hemispheres, which will result in spatial and chromatic aberration effects.

Both fit parameters as a function of E_{pass} are shown in Fig. 6.17(a). For the cylinder symmetric parameter a_{cyl} it is possible to fit a line with a slope of $\xi = 297 \pm 4 \frac{1}{m^2}$ to the data, which goes through the origin. This linear behavior supports the previous assumption that a_{cyl} is independent of the angular space in the microscope, which would approximately scale with $1/\sqrt{E_{pass}}$ according to Eq. (6.23). Also the entrance aperture does not have an influence, because the maximum radius x_{entr} of

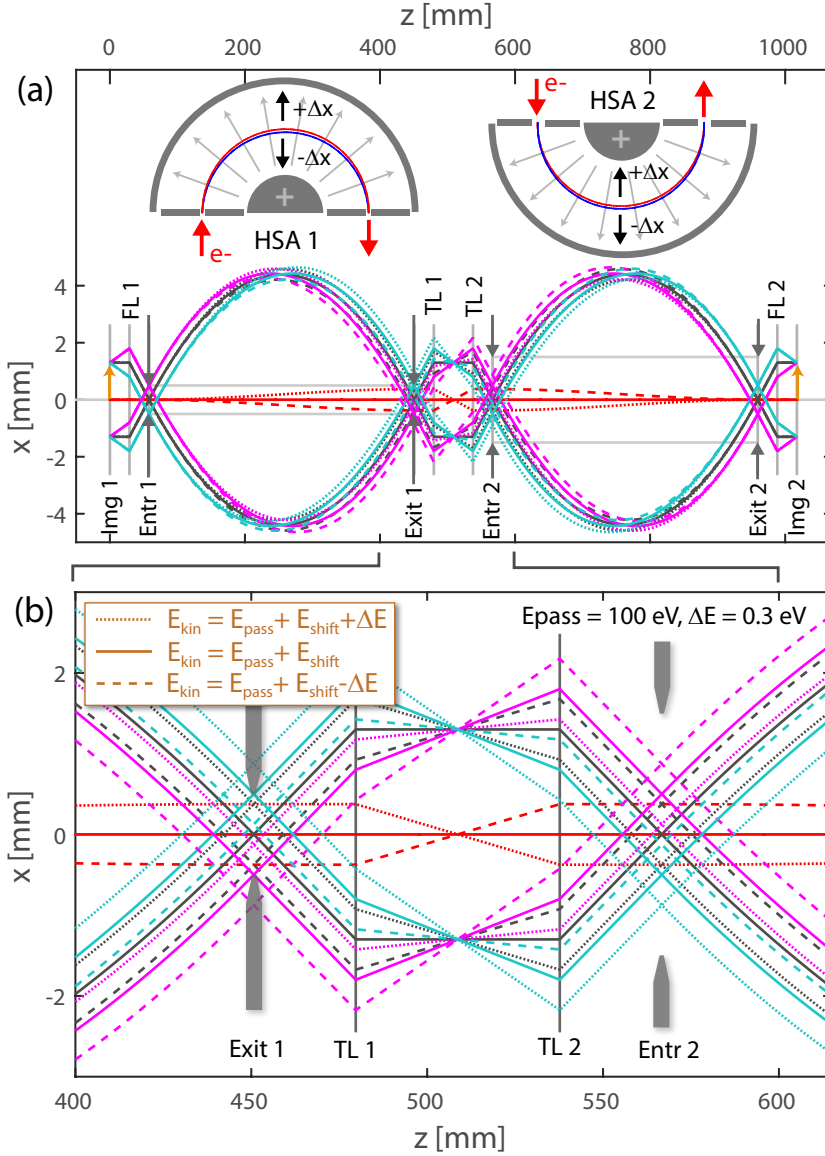


Figure 6.18.: Calculated electron trajectories passing the double hemispherical energy analyzer. In (a) the complete path from the intermediate image in front of the analyzer to the energy filtered image behind the analyzer is shown, whereas (b) focuses on the important region around the exit slit of the first hemisphere and the entrance of the second hemisphere. The calculations were performed like it is described in Sec. 6.2 with taking into account the x dependent energy shift according to Eq. (6.10).

the trajectory disk entering the analyzer was smaller than the radius of the used contrast aperture (see Fig. 5.6). The a_{cyl} parameter is therefore most probably influenced by the transfer optics, consisting of two Fourier lenses and an additional transfer lens in between them¹⁰. All potentials of the transfer optics scale linearly with the pass energy of the surrounding hemispheres, which fits to the measured behavior of the a_{cyl} parameter. The a_{1dim} parameter instead is rather a quadratic function of the pass energy and can be fitted with a parabola starting in the origin of the coordinate system. It can be interpreted as a correction to the calculated energy shift in Eq. (6.10). Most likely an (angle-dependent) deviation, which was applied to the electron trajectories by the first hemisphere of the analyzer, cannot be perfectly transferred through the transfer lens system due to aberrations. This deviation is then multiplied in the second hemisphere and results in a quadratic E_{pass} dependency.

A significant dependency of the fit parameters also exists on the width of the entrance and exit slit of the first HSA as shown in Fig. 6.17(b). Of these two apertures, only the entrance slit is cylindrical symmetric and can have an influence on the a_{cyl} parameter. The a_{cyl} non-isochromaticity is increasing for smaller slits. This might be due to inhomogeneities of the electric field near the edge of the aperture. The a_{1dim} parameter increases with bigger slits. This means that the non-isochromaticity effect becomes smaller than predicted, because a larger angular phase space seems to counter-act the energy-shift described by Eq. (6.10). The reason are probably angle-dependent higher order terms in Eq. (3.2) which lead to higher deviations for the larger angular phase space.

Finally, the results for the two different projective P_{12} settings in Sec. 6.3.2 can be explained consistently with the preliminary observations. According to Eq. (6.23) the maximal angle in the intermediate image in front of the analyzer is inversely proportional to the projective magnification $\alpha_{img,max} \propto \alpha_{spl,max}/M_{P12}$ so that it will be 1.5 times bigger for the $M_{P12} = 2$ magnification than for the $M_{P12} = 3$ magnification. The factor between the related a_{1dim} parameters is $50.9/15.7 \approx 3.24 \approx (1.5)^3$ and between the a_{cyl} parameters $44.9/24.5 \approx 1.83 \approx (1.5)^1$. This supports the idea that the a_{1dim} parameter is related to spherical aberrations in the transfer lens system, which are proportional to α^3 (see Eq. (5.44)) and therefore strongly depends on the angle $\alpha_{img,max}$. As shown in Fig. 6.17(c), the a_{cyl} parameter should be independent of $\alpha_{img,max}$. The reason for this dependency on the projective lens magnification

¹⁰The additional transfer lens is implemented in the real *NanoESCA* for technical reasons but not used in the calculation model in Sec. 6.2

might have its origin already in lens aberrations in front of the analyzer.

6.5. A generalized fit model for the intensity shift

In energy filtered photoemission microscopy often, because of low count rates, a single image takes a long exposure time to achieve the necessary statistics. An example is the EAL determination in Sec. 8.5.1 with the *HAXPEEM* approach. Just one energy-filtered image of a Au core-level peak is needed. To acquire a full image spectrum to perform the energy-shift correction presented in Sec. 6.1 is not economic. In this case, the variation of the intensity of the core level signal along the sample (see the simulation in Fig. 6.9(c,f)) can be reproduced faster: If the correct peak shape of the core level is known (which only requires the much faster channeltron measurement of a spectrum) and the energy shift map for the microscope setting is available (deduced from a work-function scan), the intensity variation can be calculated according to Eq.(6.14).

With a simplified analytical form of Eq.(6.15) we can even generate a handy fit-model to analyze and correct the intensity shift caused by the non-isochromaticity. In the following, I use a Gauss profile instead of a Voigt profile¹¹, which is often an adequate approximation for a core level peak

$$I(\varepsilon) = \frac{I_0}{\sigma \cdot \sqrt{2} \pi} \cdot \exp\left(-\left(\frac{\varepsilon - \varepsilon_c}{\sqrt{2} \cdot \sigma}\right)^2\right). \quad (6.24)$$

The model for the energy-shift parabola in Eq. (6.10) has to be supplemented with a correction term based on the analysis in Sec. 6.4 and can be written as

$$\varepsilon(x) = E_{pass} \cdot \left(\mu \cdot \frac{x - x_c}{f_{FL}}\right)^2 \quad \text{with} \quad \mu = \underbrace{\frac{19.1 \text{ mm}}{562 \text{ px}}}_{=c_{scr}} \cdot \frac{\mu_c}{M_{P34}} \quad (6.25)$$

where μ is a calibration factor which transfers the mm/px relation¹² c_{scr} from the screen-image to the intermediate image plane in front of the analyzer. The magnification M_{P34} of the projective behind the analyzer needs to be known and the correction-factor μ_c should not differ much from 1. Together both equations can be

¹¹Since no analytic form of the Voigt profile exists, a simple Gaussian profile is used here for the sake of a simpler expression. The literature also knows a pseudo Voigt profile, which is a linear combination of a Gaussian and a Lorentz curve and could be used as a more precise approximation of the Voigt profile.

¹²The relation was calibrated for the used microscope and might differ for other instruments

combined to a fit-model which can directly be applied on an energy-filtered image:

$$I(x) = \frac{I_0}{\sigma \cdot \sqrt{2} \pi} \cdot \exp \left(- \underbrace{\left(\frac{\left(E_{pass} \cdot \left(\frac{c_{scr} \cdot \mu_c}{M_{P34}} \cdot \frac{x-x_c}{f_{FL}} \right)^2 \right) - \varepsilon_c}{\sqrt{2} \cdot \sigma} \right)^2}_{\equiv C_{niso}(x)} \right). \quad (6.26)$$

The standard deviation σ describes the energy resolution of the analyzer. The lateral shift x_c of the energy-shift parabola from the optical axis depends on the microscope and it's settings and should be zero in the ideal case. The parameter ε_c describes the energetic distance of the filter energy from the core level peak position for which the image was acquired.

6.6. Conclusions

The non-isochromaticity analysis in this chapter leads to a better understanding of the instrumental artifacts which appear in each energy filtered measurement performed with the *NanoESCA* analyzer or similar filters performing with hemispherical analyzers and an energy separating aperture. The artifacts are systematic and strongly depend on the instrument settings. Because of the complexity of the microscope it is difficult to precisely predict the correct shift mathematically for a given setting, but the most influential parameters could be identified in this section. The dominant energy shift in an energy-filtered image is caused by the first HSA, is one-dimensional along the dispersive plane of the analyzer and only depends on the pass energy of the filter according to Eq. (6.10). The energy shift is positive, which means that faster electrons are passing the analyzer if they start further away from the optical axis in the intermediate image plane in front of the analyzer. Two additional negative energy-shifts could be identified. A one-dimensional shift characterized by the parameter a_{1dim} directly counter-acts the positive shift in Eq. (6.10) and can be seen as the realistic correction to the calculated shift values. A bigger absolute value of the a_{1dim} parameter, which increases with a higher angular phase space in front of the analyzer, is actually desirable, since it more strongly compensates the energy-shift of the first HSA.

The origin of the cylinder symmetric energy-shift is hard to identify. The *entrance aperture* of the first hemisphere seems to have an impact, but also the transfer lens between the hemispheres and the projective lenses around them. It should be tuned as small as possible, because it adds a two-dimensional energy shift to an energy-filtered PEEM image, which is more complicated to correct for.

A good instrumental setting with a low non-isochromaticity can be deduced from the experimental results:

- The pass energy should be as low as possible
- If the required energy resolution allows, the slit - widths of the first hemisphere should be increased, because it reduces the cylinder-symmetric shifts and increases the a_{1dim} parameter.
- A contrast aperture of 150 μm seems to be a good choice, since it offers a good spatial resolution and an increased a_{1dim} parameter.

For a very precise analysis of the non-isochromaticity of a certain instrumental setting, a work function scan should be acquired. It can be used to deduce an energy shift map, as shown in Sec. 6.1 which is then used to correct a whole image spectrum pixel by pixel. In many cases it is sufficient to correct the one-dimensional non-isochromaticity which can be determined by fitting the model in Eq. (6.26).

Since the energy shift can be determined very precisely via a work-function evaluation (better than 10 meV), the non-isochromaticity could be also used for high energy-resolution experiments. If a sample material is homogenous inside a certain field of view, the non-isochromaticity allows one to study its energy dependance with a very high energy resolution far beyond the usual possibilities of the analyzer. The field of view examined on the sample and the energy shift distribution of the analyzer can be adjusted independently from each other (see Fig.6.11) within a certain range. The energy spread between the upper and lower image point shown in Fig. 6.14(a), for example, is around 100 meV over a distance of 562 px. This would mean a theoretical energy step of 0.18 meV per pixel. This lower resolution limit will not be reached due to noise and other instrumental inaccuracies, but an energy precision between 1 and 10 meV is expectable. By the use of the non-isochromaticity at least one dimension of spatial resolution is lost, but compared to conventional photo-emission spectrometer the region from where the information is acquired is only of a few micrometer size and therefore comparably precisely determined. Of course, light sources with a suitable small energetic band widths are needed for the photoelectron excitation (e.g. laser or discharge lamps).

7. Instrumental characterization measurements

To study the characteristics of the *NanoESCA* instrument in combination with a synchrotron light source, several performance tests were realized at the synchrotron *Elettra* (see Sec. 3.2.2), to determine the possible spatial resolution, the momentum resolution and the energy resolution. Suitable analysis methods are presented for each measurement. The results are compared to the calculations and evaluations presented in the preceding chapters 5 and 6.

The form of the measured photoemission distribution in either mode¹ (including all resolution issues but also instrumental artifacts) depends on the microscope column, which can be mainly characterized by the *objective lens* (see Cha. 5), the *energy filter* (see Cha. 6) and the *detection system*. The latter therefore should be discussed first in this chapter before spatial and momentum resolved measurements on particularly suitable sample systems are presented. A special attention is given to the new *single event counting* detection which offers some statistical and resolution advantages compared to the analogue imaging mode.

7.1. Detection of the photoelectrons

The *analogue* imaging mode (see Sec. 3.1.4) is the most often used detection mode so far in photoemission electron microscope systems. For proper subsequent data analysis, it is necessary to eliminate some artifacts connected with this mode which are explained in the following section. The *single event counting* approach overcomes these problems, but is limited to low count rates.

¹*real-space microscopy* or *momentum microscopy*, see Fig. 2.1

7.1.1. Flat field, Dark field and Image-Correction in the analogue imaging mode

The use of the analogue detection mode superimposes the measured photoelectron image with textures (hexagonal structure of the MCP, blind spots on the scintillator screen, dirt on the UHV-window) or adds some backgrounds (dark field of the CCD Camera, after-glow of the scintillator screen). Most of these instrumental artifacts have to be corrected before further data analysis. To make the inhomogeneities of the detection system visible, one can find a microscope setting which illuminates the MCP with a homogenous photoelectron distribution². The image which is then acquired only contains the undesired patterns of the detection system. This so called *flat field* image should be measured with sufficiently long exposure times to reach a good counting statistics and therefore a low noise-level. If the *flat field* is measured behind the energy filter, flat field images should be measured and summed up over a certain energy range, to avoid an intensity profile (see Fig. 6.9 (e,h)) which is due to the *non-isochromaticity* of the analyzer. An exemplary flat field is shown in Fig. 7.1. It was acquired 200 times with an exposure time of 5 s. The intensity-level was normalized to its mean value ($I_{mean} = 7375.2$) for the sake of the later image-processing³.

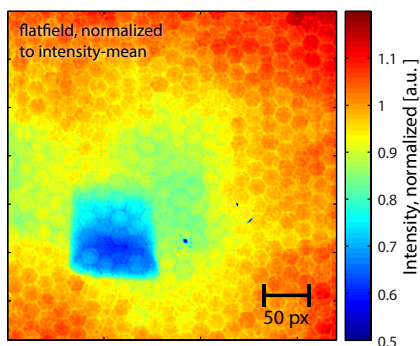


Figure 7.1: A typical flat field measurement with the NanoESCA, which shows the inhomogeneity of the detection system (MCP, scintillator screen, camera). The dark field of the camera was subtracted and the image was divided by its mean value. The pattern shown here will be reflected in each measurement performed with this detection system and should be corrected.

The flat field image clearly shows the hexagonal structure of the stacked single-

²It is promising to use a structureless sample (e.g. single crystal) and to slightly de-focus the microscope in the real-space imaging mode. One should also use an unfocused light-source (e.g. Hg-lamp) to avoid a spatial distribution of the excitation intensity. Since the energy-filter causes a spatial intensity shift (see Sec. 6.5), the measurement should be performed over a sufficient energy range.

³If an image is divided by the flat-field, the normalization of the flat field ensures, that the mean intensity level of the original image is not changed.

fiber arrays of the MCP [LW79], but also a huge rectangular and several small dark areas, where a too high local photoemission signal in the past lowered the detection sensitivity of the scintillator screen. To correct PEEM images, it is usually sufficient to divide the measured image I_{meas} by the flat field I_{ff}

$$I_{corr}(x, y) = \frac{I_{meas}(x, y) - I_{df}}{I_{ff}(x, y) - I_{df}}. \quad (7.1)$$

Especially for measurements I_{meas} with low signal intensities, it is mandatory to subtract the *dark field* level of the camera I_{df} from the measurement as well as from the flat field. The dark field mainly arises from the dark current of the camera's CCD sensor. It can be determined by acquiring a camera image without any light. The level of the dark field is a function of the exposure time, so that it has to be determined for different exposure times separately. Fig. 7.2(a) shows such a dark field, which was measured 100 times with an exposure time of 500 ms. The background level has a value of 99.2 intensity steps and a small standard deviation of the intensity distribution of 0.6. Nevertheless, the dark field is inhomogeneous and the count rate is significantly lower at the top-part of the image. If the exposure time is increased to 50 s, the background level is not changing very much, but the standard deviation increases to 7.5 intensity steps. The dark field looks much more grainy (b). In (c) an evaluation of the dark field intensity and its standard deviations as a function of the camera exposure time is shown. The histogram of the intensity distribution in the blue ROI shown in (b) was fitted with a Gaussian distribution (compare with Fig. 7.3). The aforementioned observation is supported: The standard deviation is strongly increasing with the exposure time (double-logarithmic plot), whereas the mean intensity level is only slightly changing. The camera exposure time therefore should not exceed 5 s to keep the background noise level below one intensity step. If a high statistics is needed, it is preferable to increase the number of measurements and lower the camera exposure time.

7.1.2. Image intensity and its dependency on the MCP voltage

The 14 bit *CCD sensor* can distinguish $n = 2^{14} = 16384$ intensity steps. The MCP amplification and the CCD exposure time has to be adjusted such, that the CCD chip doesn't get more photons than it can bear, otherwise the PEEM image will be overexposed and information will be lost. Also the electron flux on the MCP and on the scintillator-screen should not exceed certain limits to guarantee a proper functionality and a long component life-time. A favorable rate is, for example, 2000

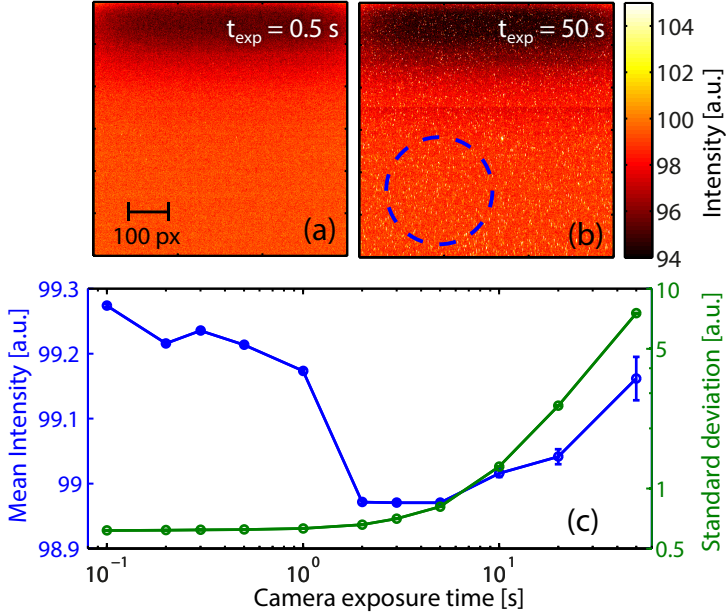


Figure 7.2.: The dark field is the background signal, which is created by the dark current of the CCD, even if not light shines on it. It has to be subtracted from each measured photo emission image. The dark field changes with the exposure time of the camera. The full $600 \times 600 \text{ px}^2$ screen is shown in (a) for 500 ms exposure time and in (b) for 50 s. The dark field intensity level and the standard deviation of the Gaussian intensity distribution as a function of the exposure time are shown in (c).

counts/s/px on the CCD screen. With an exposure time of 5 s one would fill the CCD channel with 10000 counts, which is still far away from the overexposure limit. The electron flux onto the scintillator screen can be adjusted by the MCP voltage V_{MCP} . The amplification increases, inside certain limits, exponentially with V_{MCP} . If the amplification behavior is known, measurements acquired with different MCP settings can be compared with each other.

To determine the MCP characteristic, a test series with different MCP settings was performed on a *Chessy* sample. Fig. 7.3 (a) shows an energy-filtered PEEM image with $V_{MCP} = 1720 \text{ V}$. The intensity distribution on the Au pattern and on the Si pattern was evaluated separately, to check, if the measured intensity as a function of V_{MCP} behaves equally for different photoelectron fluxes. A Hg-lamp was used as excitation source, the energy filter was set to $E - E_F = 4.65 \text{ eV}$. The histogram of the intensity distribution of the Au pattern (b) was fitted with a Gaussian profile (see

Eq. (A.2)) while the histogram of the Si intensity distribution was asymmetric. I chose a *generalized extreme value function* for a fit. Probably scattered light from the much brighter Au-areas causes the shoulder to higher intensities in the Si-histogram.

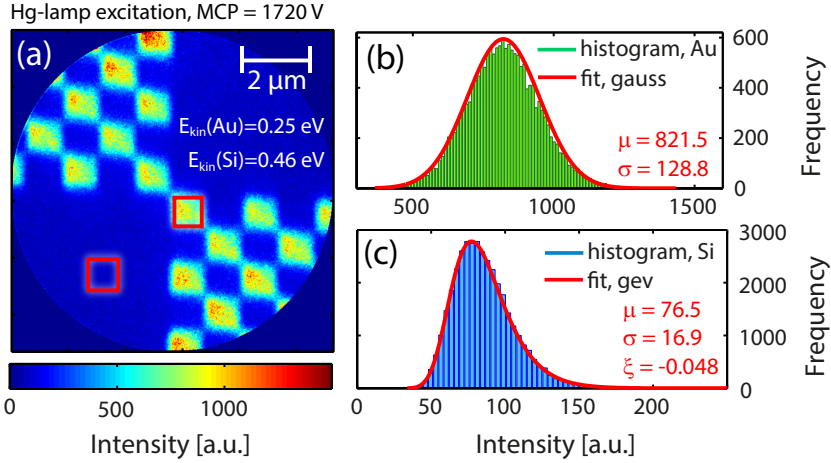


Figure 7.3.: (a) A *Chexsy* sample was measured with a high magnification and subsequently flat field and dark field corrected according to Eq. (7.1). The intensity distribution for the Au structure was plotted as a histogram (b) and fitted with a Gaussian function. The intensity distribution of Si is not symmetric and was fitted with a *generalized extreme value function*.

The extreme values of the intensity distributions are shifting to smaller values, if V_{MCP} is decreased. The logarithm of the determined intensity maxima as a function of V_{MCP} is shown in Fig. 7.4 (a). Inside certain limits, this curve can be fitted by a line

$$\ln(I(V_{MCP})) = a \cdot V_{MCP} + b \Rightarrow I(V_{MCP}) = e^b \cdot e^{a \cdot V_{MCP}}. \quad (7.2)$$

The limits of the line-fit can be clearly seen in the residuals of the fit (b). At the lower limit, the amplification was not strong enough to allow a proper analysis of the photoemission signal. Naturally, that happens earlier for the weaker Si-signal than for the Au signal. The lower limit for the Au line-fit was set to $V_{MCP,min} = 1510$ V. The upper limit is $V_{MCP,max} = 1720$ V. Above this limit, the amplification of the MCP is not strictly exponential anymore, because a gain saturation is caused by *space-charge* effects within the micro channels [SH66].

The fit-results for the line fits are compiled in Tab. 7.1. The exponents p_1 are very similar for the Au and the Si. Because of the higher statistics and the

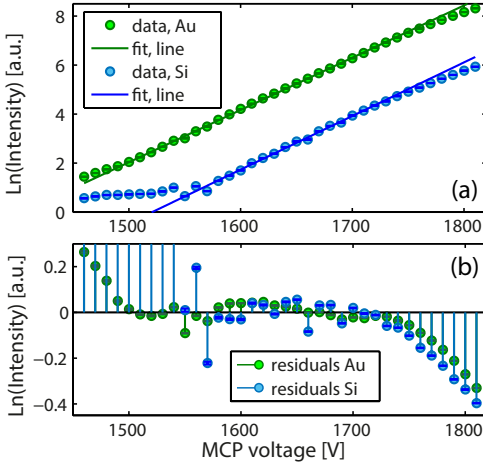


Figure 7.4: The amplification of the MCP increases exponentially with the applied MCP voltage. The exponent is determined by fitting a line to the logarithm of the intensity increase as a function of the MCP voltage (a). To identify the limits of the exponential behavior, the residuals of the data to the line-fit are plotted in (b). The lower divergence is due to a too low count rate, the upper limit of the MCP is at $V_{MCP} = 1720$, where the amplification characteristic of the MCP runs into a saturation.

Gaussian intensity distribution, the Au-value can be seen as reference, while the Si evaluation proves that all aspects discussed are equal for Au and Si and are therefore characteristic of the MCP.

As a conclusion, the MCP should not be used above $V_{MCP} = 1720$ V because the amplification goes into saturation. All image intensities I_j which were acquired with an MCP-voltage $V_{MCP,j}$ up to this limit can be subsequently normalized and compared with other image-intensities I_k , which were acquired with different MCP-voltages $V_{MCP,k}$ with

$$\frac{I_j}{I_k} = \frac{\exp(a \cdot V_{MCP,j})}{\exp(a \cdot V_{MCP,k})}, \quad (7.3)$$

using the $a(\text{Au})$ parameter from Tab. 7.1. The determination of this value was performed for the built-in MCP of the NanoESCA Mark III instrument and should be individually repeated for each MCP.

	a	b
Au	$21.33 \cdot 10^{-3} \pm 0.12 \cdot 10^{-3}$	-29.96 ± 0.19
Si	$21.88 \cdot 10^{-3} \pm 0.39 \cdot 10^{-3}$	-33.27 ± 0.63

Table 7.1.: Fit-results of the line-fits shown in Fig. 7.4.

7.1.3. Single Event Counting

In the case of low count rates up to 700000 counts/s, or 2.84 counts/s/px⁴, it is possible to use a more accurate procedure to count the photoelectron events which reach the detector, called *single event counting* (SEC). The assumption is that each light signal produced on the scintillator-screen (see Fig. 3.4) is related to one single photoelectron. Because of the low event-density, the light signals can be separated by the event counting algorithm and counted as single events at specific screen coordinates. This mode effectively emulates a two-dimensional *multichannel analyzer* by software.

This counting procedure is more precise than the analogue imaging, because it is able to achieve a true Poisson statistic as is commonly the case for a channeltron electron multiplier driven counting system. Artifacts, like the cross-talk of intensities or the image inhomogeneities, which arise in the detector system, are suppressed. The signal-to-noise ratio is improved.

The procedure works best with a high camera frame rate so that two events do not happen in the same or close-by camera pixel in the same frame and are not counted as only one event. As mentioned earlier, the highest possible frame-rate with the *PCO.1600* for a continuous measurement is 53.4 fps, which divides into a 18607 ns exposure time for each frame and an 120 ns inter-framing time [PCO14]. The decay-time of the YAG:Ce screen is with 70 ns even shorter so that we can calculate that 99.36% of the events are really acquired within the exposure time of one frame. The above-mentioned maximal count-rate of 700000 counts/s corresponds to 13024.9 captured events on a single frame or an event-density of 5.29% in one frame. A fast computation algorithm with the appropriate hardware is used, to analyze the events in real time.

With a higher frame-rate camera, the maximum count-rate for the single event counting procedure can be increased. If the count rate is anyway low because of a weak photoelectron signal, the event counting is preferable because of the quantitative character of the measurement and the superior signal-to-noise ratio. It was, for example, necessary for the EAL determination in the hard x-ray imaging 8.5.1.

To compare the SEC mode with the analogue imaging mode, an energy-filtered PEEM image of the *Chessy* sample was taken with both methods under equal conditions. An Hg-lamp was used as excitation source. To reach the low count rate necessary for the SEC mode, the energy-filter was set to $E - E_F = 5.3$ eV which is on the tail of the Fermi edge. Both images are shown in Fig. 7.5(a). Because of the

⁴the maximum rate in the analogue imaging mode is 2000 counts/s/px

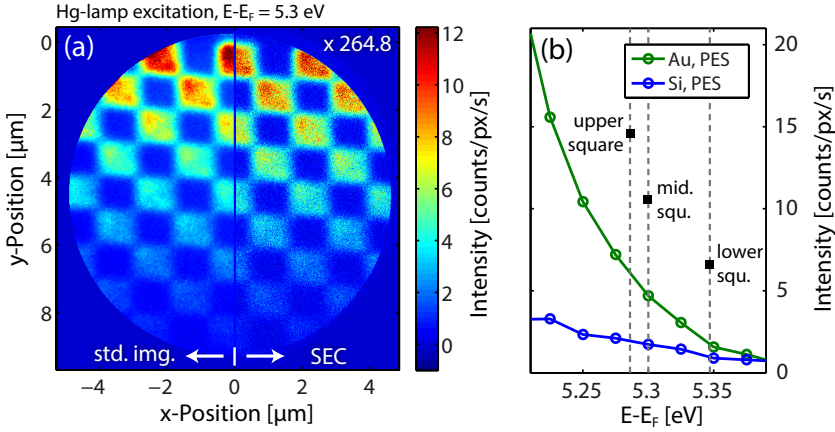


Figure 7.5.: Comparison between a high resolution image of the Chessy sample, measured with the analogue imaging mode (left) and the single event counting (right). Both measurements were acquired with the same exposure-time of 900 s. The vertical intensity drop is due to the effect of the non-isochromaticity of the energy filter. The spectral region which is accessed from the upper Au square to the lower Au square is indicated in (b). For a better comparison, the counts of the SEC measurement were multiplied by a factor of 264.8.

non-isochromaticity of the energy-filter (see Cha. 6), the real filter energy between the upper Au-square and the lower Au-square differs by 61.4 meV, which translates into a strong intensity drop along the vertical axis of the image. Photoemission spectra of the Au and Si regions in this sample around $E - E_F = 5.3$ eV are shown in (b). Also the spectral region covered by the image is indicated. While the density of states for Si are relatively flat around the Fermi edge, the Au signal is strongly rising. Note that the sample was not cleaned for this measurement.

The analogue PEEM measurement (left in Fig. 7.5(a)) was flat field and dark field corrected, the region outside the measurement circle was set to zero. The SEC measurement is shown as measured, only the counts were multiplied by a factor of 264.8 to be comparable with the analogue PEEM measurement. Although the count-rate-level in the SEC mode is smaller by such a factor, the image shows a better contrast between the Au and Si squares and appears sharper in general. Furthermore, less details are lost compared to the standard imaging mode in the low intensity regime at the bottom of the image.

To have a closer look on the differences between the two imaging modes, I analyzed the line-profile along the vertical axis of both images shown in Fig. 7.5(a)

at $x=0$. These profiles are plotted in Fig. 7.6 (a) and were fitted with a sum of Gauss/Step-profiles according to Eq. (A.6). The model fits very well to the SEC measurement (blue dots). For that reason, the non-isochromaticity correction function $C_{niso}(x)$ (Eq. (6.26)) was kept equal for the fit of the analogue image profile (green dots). This fit could not match the alternating intensity steps between Au and Si squares as well as the one for the SEC measurement.

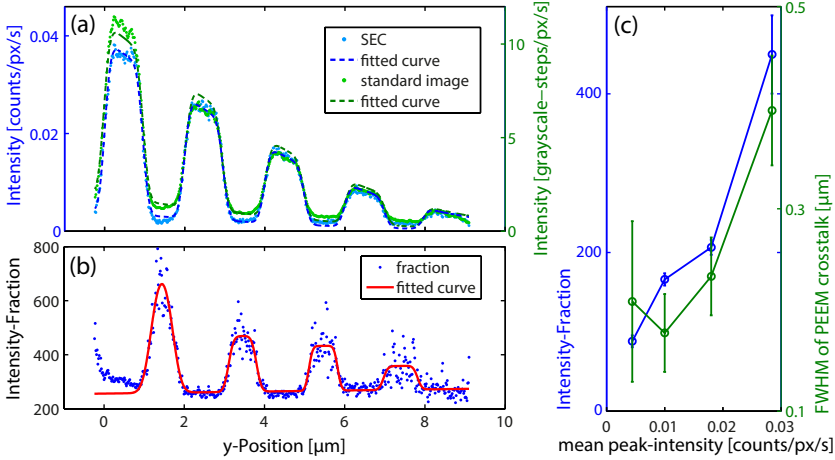


Figure 7.6.: (a) Line profiles along the y -direction of the *Chessy* sample (see Fig. 7.5) for the single event counting mode and the standard imaging. (b) The fraction of the two line profiles was fitted, to find a systematic in the increasing difference of the Si signal between SEC and standard imaging. The results, namely the fraction factor and the sharpness of the fraction, are plotted against the mean intensity level of the surrounding Au signal in (c).

To make the difference of both profiles in (a) more clearly visible, the analogue image profile was divided by the SEC profile. The result is shown in (b). The factor between the intensity levels of the Au-pads are equal except for the one at position $y=0.5 \mu\text{m}$ (which is probably due to a not successful flatfield correction at the image border). A constant factor means that for the high intensity parts of the profile the signal increase between both profiles is qualitatively equal. This is not true for the low intensity Si regions between the Au pads. The factor between both profiles is increasing with the increasing signal intensity of the surrounding Au pads.

A multi *Gauss/step-function* was fitted to the profiles in (b) (like Eq. (A.6), but with individual parameters for the height and the edge-width of each peak). The resulting fit-parameters for the width and the height of the low-intensity profile

differences are shown in Fig. (c).

Both values are increasing with the increasing Au pad intensity. The explanation is a cross talk of the high intensity areas in a standard PEEM image, which raises the intensity level of areas with a lower intensity in its neighborhood. These detector artifacts are significantly suppressed in the SEC mode. The cross-talk also influences the spatial resolution evaluated for the profiles in (a). The resolution for the SEC measurement is $FWHM_{SEC} = 277.6 \pm 4.7$ nm while it is $FWHM_{std} = 306.6 \pm 9.2$ eV for the analogue imaging mode.

7.2. Momentum microscopy and k-Calibration

As it was described in the beginning of Sec. 2, the *real space microscopy mode* and the *momentum microscopy mode* are first of all different ways to map the same photoelectron distribution excited in a certain region of interest on the sample. This is obvious from the lens settings and electron trajectories as shown in Fig. 3.5(b,c) for the telescopic real space mode and the momentum mode: up to the field aperture the trajectories are identical. Only the settings of the two subsequent projective lenses determine, if a real image of the sample is mapped onto the detector (integrated over all accepted angles) or if the momentum/angular distribution is mapped onto the detector (integrated over the illuminated area on the sample). The accepted angular space can be restricted by the *contrast aperture* and the region of the sample from where electrons are detected can be restricted by the *field aperture*. Whichever operation mode is used for the final measurement, it is useful to check the phase-space restriction accessible by the other mode. Therefore, in this section the general nature of the momentum detection in the *NanoESCA* is discussed using a clean Ag(001) single crystal as example. In this case it is reasonable to assume that there is no difference in the momentum distribution of electrons emitted from different regions of the sample. Samples which for example do not have long range ordering like small single crystals (e.g. graphene flakes of limited size) will lead to a completely smeared out momentum image, since a superposition of differently orientated momentum distributions would be mapped onto the detector screen.

The plot in Fig. 7.7(a) shows a complete data stack of an energy and momentum resolved photoemission measurement, covering approximately the first *Brillouin zone* in the k_{\parallel} momentum directions parallel to the Ag(001) surface and the energy-range between the Fermi edge E_F ($E_{bin} = 0$ eV) and the work function cut-off Φ ($E_{bin} = 61.095$ eV) (compare with Fig. 2.2). The photoelectrons were excited

with monochromatic linear p-polarized synchrotron radiation with an energy of $h\nu = 65.42$ eV and an energy bandwidth of $\Delta(h\nu) = 34$ meV (according to Eq. (3.15)). The energy-filter was set to $\Delta E_{ana} \approx 200$ meV ($E_{pass} = 50$ eV, $w_{slit} = 1$ mm). The Ag(001) surface was cleaned by Ar⁺-sputtering (1 keV for 20 min.) and annealed (400° C for 20 min.) before measuring. The first interesting part of this data stack is in the region of low kinetic electron energies, where the parabolic photoemission horizon can be used to correctly calibrate the k_{\parallel} axis of the measurement (see Sec. 7.2.1). A magnification of this region is shown in Fig. 7.7(c). The most important part in this measurement is nevertheless the region below the Fermi level including the valence band (Fig. 7.7(b)), since the electronic band-structure of the crystal can be examined here.

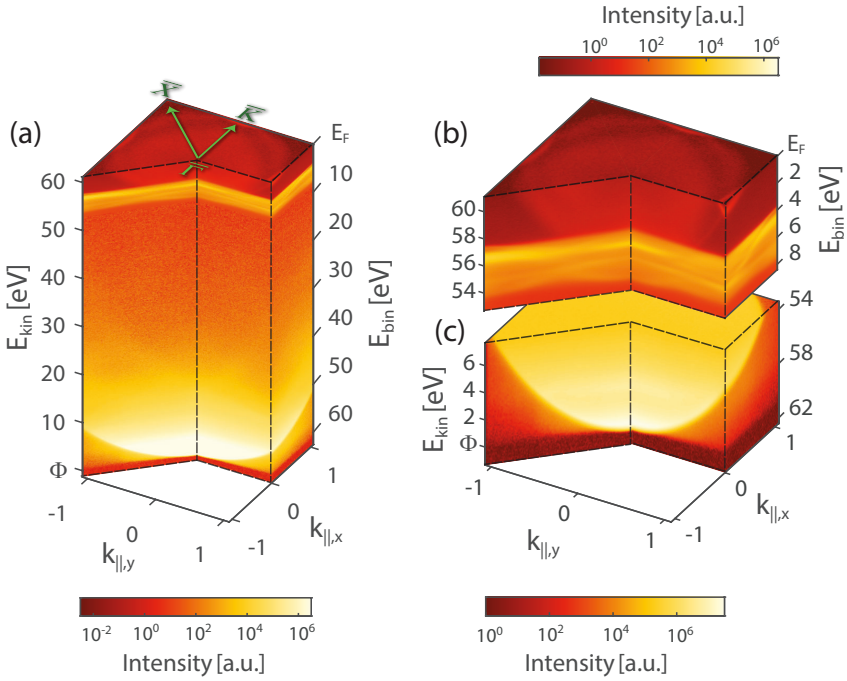


Figure 7.7.: A full data set of energy filtered momentum distributions of a Ag(001) crystal was measured from from the Fermi edge E_F down to the work function cut off Φ . The most interesting energy-range covers the energies from the Fermi level and the valence band (b) where real electron bands can be imaged. The parabolic photoemission horizon in (c) can be used for a correct calibration of imaged k_{\parallel} distances.

The momentum microscope uses the fact that the wave vector of a photoelectron parallel to the surface $\vec{k}_{\parallel} = \vec{p}_{\parallel}/\hbar$ is conserved while crossing the surface potential barrier and in the subsequent acceleration process in the extractor field of the immersion lens of the microscope [KKO⁺03], as shown in Fig. 2.7. A given parallel momentum of a photo-electron is mapped to an angle α' in the extractor plane according to

$$\sin(\alpha') = \frac{p_{\parallel}}{\sqrt{p_{\parallel}^2 + p_{\perp}^2}} = \frac{p_{\parallel}}{\sqrt{p_{\parallel}^2 + 2 m_e \cdot e \cdot V_{ext}}}, \quad (7.4)$$

since the final perpendicular momentum $p_{\perp} = \sqrt{2 m_e \cdot e \cdot V_{ext}}$ is kept constant due to the energy-filter scheme of the *NanoESCA* (see Fig. 3.3). The different parallel momenta are encoded in the angles α' of the electron trajectories in the extractor plane and are then projected into the back focal plane of the objective lens where one position in the plane represents one specific momentum independent of the starting position of the electron (see Fig.3.5(c)). This momentum distribution is then projected onto the image plane in front of the energy filter (including the deceleration to the analyzer pass energy E_{pass}) and after the energy filtering finally onto the detector screen.

As described in Sec. 2.2, momentum microscopy measures the distribution of the parallel momentum components $k_{f,\parallel}$ of the electron final state inside the crystal. Related to the constant energy distribution at the Fermi-energy E_F , this is a spherical cut through the 3D Brillouin zone as shown in Fig. 7.8(a). The radius $\sqrt{k_{\perp}^2 + k_{\parallel}^2}$ of this spherical cut depends on the kinetic electron energy of the electrons. One needs to solve Eq. (2.18) to determine the position of the cutting plane along k_{\parallel} . The photoelectrons in the experiment shown in Fig. 7.7 were excited with a photon energy of $h\nu = 65.42$ eV and the *work function edge* was measured as $\Phi = 4.33$ eV. The kinetic electron energy for electrons excited at the Fermi-level is therefore $E_{kin} = h\nu - \Phi = 61.1$ eV. The value for the *inner potential* for Ag was taken from [Gos82] and was determined via electron diffraction (*Yamagui method* [Gos80]) as $V_{iP} = 17.8 \pm 1.1$ eV. Solving Eq. (2.18) with these values gives $k_{\perp} = 4.547 \text{ \AA}^{-1}$ at $k_{\parallel} = 0 \text{ \AA}^{-1}$. The size of the Brillouin zone of the fcc crystal along the [001] direction (*reciprocal lattice vector*) is given by $|\vec{G}| = 4\pi/a = 3.072 \text{ \AA}^{-1}$ [KH06, p. 44] for Ag with the *lattice constant* $a = 4.09 \text{ \AA}$. The final state of the electrons from the Fermi level in our measurement is therefore positioned at the top of the second Brillouin zone (in [001] direction) (see Fig. 7.8(a)) and very close to the neck between the second and the third one. Photoemission momentum images addressing exactly this cutting surface in momentum space are shown in Fig. 7.8 (b,c) for two different microscope

extractor voltages. Doubling the extractor voltage leads to an increase in *angular acceptance* by a factor of $\sqrt{2}$ according to Eq. (5.14). The borders of the central Brillouin zone with its fourfold symmetry are marked in (b). The projections of the two *high symmetry directions* $\Gamma - X$ and $\Gamma - K$ from the [001] *emission plane* onto the cutting surface are indicated as $\bar{\Gamma} - \bar{X}$ and $\bar{\Gamma} - \bar{K}$. The *NanoESCA* also images the adjacent Brillouin zones, where the cutting surface rather cuts through the central region of the zones. Consequently, the photoelectron distributions look different compared to the central Brillouin zone. By changing the excitation energy of the synchrotron light, any cut through the Brillouin zone can be obtained.

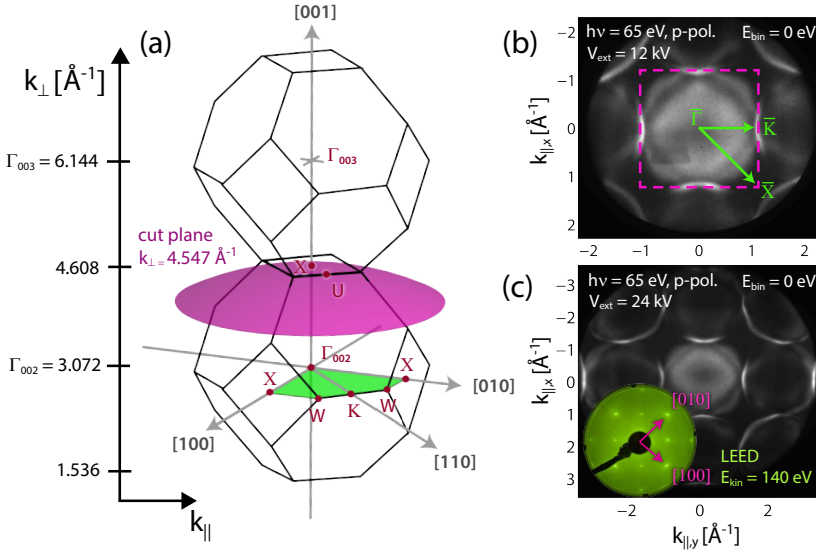


Figure 7.8.: (a) Sketch of the second and the third *Brillouin zones* along the [001] direction of the Ag fcc crystal structure. The violet spherical plane indicates the final state wave vector of photoelectrons excited from the Fermi edge with a photon energy of $h\nu = 65.42$ eV. The momentum images in (b,c) show the electron distribution along this plane for two different magnifications. The violet square in (b) indicates the borders of the Brillouin zone. The inset in (c) shows the LEED pattern of the Ag (001) surface for electrons with 140 eV kinetic energy. The typical fourfold symmetry is also visible in the momentum map of the Fermi edge.

The cuts through the data stack shown in Fig. 7.7 unveil the band-structure along the two high symmetry directions $\bar{\Gamma} - \bar{X}$ and $\bar{\Gamma} - \bar{K}$ as far as the transitions are allowed by the dipole selection rules. Fig. 7.9 shows spectra extracted from selected $k_{\parallel,y}$ along the $\bar{\Gamma} - \bar{K}$ direction (from the Brillouin zone center to its border). As mentioned earlier, the visible work function edge is shifting to higher energies

because of the different photoemission horizons (see Sec. 7.2.1). This effect influences the shape of the work function edge in the real space microscopy mode, if different microscopy settings (CA diameter, extractor voltage) are used. The extreme increase in intensity in the low energetic part of the spectrum is not only due the secondary electron background. The relation between the start angles α of the photoelectrons and their parallel momentum k_{\parallel} changes with the kinetic energy. The full solid angle of emitted electrons will convert into a small test-range Δk_{\parallel} around $k_{\parallel} = 0 \text{ \AA}^{-1}$ if the kinetic electron energy E_{kin} is small enough. For higher kinetic energies less start angles will fit into this test-range. The derivation of this effect is the same for the objective lens transmission in Sec. 5.3. Since the momentum distribution is projected in the plane of the contrast aperture, the test-range Δk_{\parallel} is equivalent with an appropriately small contrast aperture in Eq. (5.40). Hence, this background in the spectra is to a first approximation inversely proportional to the kinetic electron energy.

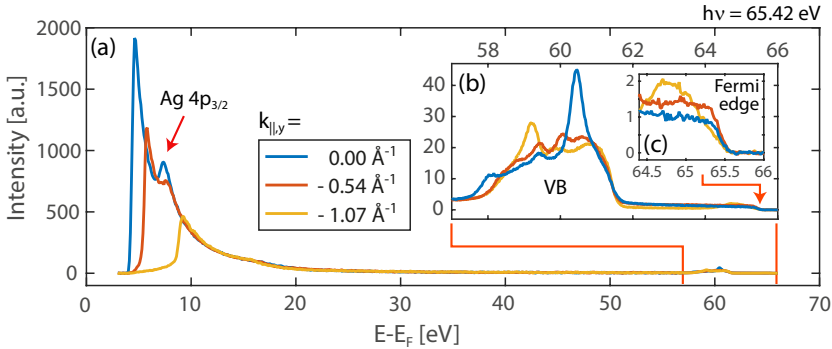


Figure 7.9.: (a) Complete spectra extracted from the image stack in Fig. 7.7 for different k_{\parallel} from the center to the border of the Brillouin zone. (b) Zoom on the valence band spectra. (c) Zoom on the Fermi edges.

On the opposite side of the spectrum, the intensity distribution in the valence band is extremely k_{\parallel} -dependent because of the diversified band structure of Ag. At the Fermi-edges it is noticeable that the edge measured at the border of the Brillouin zone is significantly broader than the others.

7.2.1. Calibration of the k_{\parallel} scale with the photoemission horizon

As it is shown in Fig. 7.8 (b,c), the range of the momentum space, which is projected onto the detector, varies with the extractor voltage V_{ext} . It also depends on the magnification settings of the projection lenses. It is therefore an important issue to find the calibration between the pixel-distance on the screen and the distance in the momentum space in units of [\AA^{-1}]. For this purpose, the parabolic *photoemission horizon* shown in Fig.7.7(c) can be used. It arises, because for a given kinetic electron energy E_{kin} and a given start angle α of an electron leaving the surface, the component perpendicular to the surface has to be big enough to overcome the work function barrier. With an increasing component of E_{kin} parallel to the surface, the absolute value of E_{kin} has to increase. This *photoemission horizon* is described by Eq. (2.17) if the K_{\perp} component is exactly equal to zero. As a fit-model related to the energy above the Fermi level ($E - E_F$) we can write:

$$E - E_F = \frac{\hbar^2}{2 m_e} \cdot (\kappa \cdot K_{\parallel}(px))^2 + \Phi \quad \text{with} \quad \frac{\hbar^2}{2 m_e} \approx 3.810 \text{ eV } \text{\AA}^2 \quad (7.5)$$

where κ is the conversion factor between the pixel scale and the momentum scale and has the unit [κ] = $\text{\AA}^{-1}/\text{eV}$. To extract the exact position of the photoemission horizon from the measurement shown in Fig.7.7(c), the work function analysis described in Sec. 4.1 can be used, since it can find the cut of edges which are shifting in energy as a function of K_{\parallel} (see Fig. 7.9). The slight intensity rise in front of the edges for bigger K_{\parallel} comes from the cross-talk of the neighboring spectra in the detector, if the analogue mode is used (see Sec. 7.1) and can be ignored in the photoemission horizon analysis procedure.

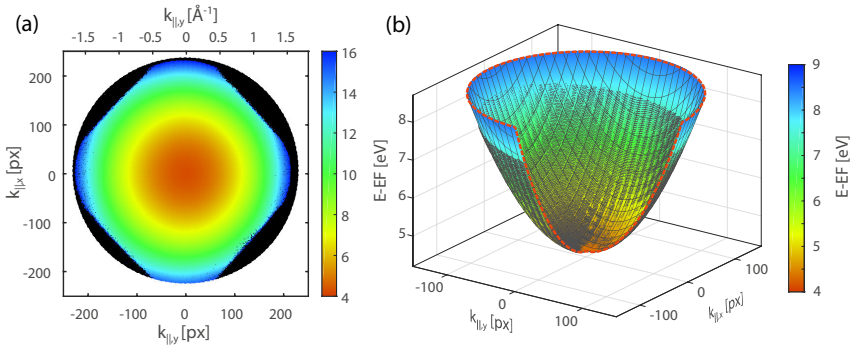


Figure 7.10.: (a) Work function analysis of the photoemission horizon. (b) Parabolic fit of the photoemission horizon to find the scaling of k_{\parallel} .

	κ_x [$\text{\AA}^{-1}/\text{px}$]	κ_y [$\text{\AA}^{-1}/\text{px}$]	Φ [eV]
3D-Fit	$(7.114 \pm 0.0004) \cdot 10^{-3}$	$(7.284 \pm 0.0004) \cdot 10^{-3}$	4.325 ± 0.0002

Table 7.2.: Fit values from the parabolic fit shown in Fig. 7.11(b).

The resulting extracted *photoemission horizon* is shown in Fig. 7.11(a). The data can be fitted with a three-dimensional parabolic fit based on Eq. 7.5, like it is shown in (b). The fit-results for both axis are compiled in Tab.7.2. The axis in Fig. 7.7 were calibrated with these values.

7.2.2. Energy resolution

The *Fermi edge* of a cleaned Ag crystal lends itself for determining the energy resolution of a photoemission setup. As shown in Fig. 7.9(b), the valence band structure of d characteristic is approximately 4 eV away from the Fermi edge where only flat s-like bands are dominating the spectrum. Thus, the Fermi edge shows a transition between two well defined intensity levels, which can be evaluated. The shape of the Fermi edge is described by the *Fermi-Dirac function*

$$F(x, T) = \frac{1}{\exp\left(\frac{x-E_F}{k_B \cdot T}\right) + 1} \quad (7.6)$$

with the energy position of the Fermi edge E_F for the temperature $T = 0$ K, and the Boltzmann constant k_B . For higher Temperatures T , the Fermi edge is not a sharp step, but smeared out because electrons at the Fermi level are thermally excited to higher energies. This energy spread is characterized by $\Delta E = 4 k_B \cdot T$. If this Fermi edge is measured by an energy filtered photoemission setup, the width of this edge is convoluted by a Gaussian distribution, which includes the bandwidth $\Delta(h\nu)$ of the excitation source and the energy resolution ΔE_{ana} of the analyzer. If two of these values are known, the third one can be determined by a fit of the measured Fermi edge.

Two ways of fitting the Fermi edge are common. Firstly, it can be fitted with Eq. (7.6) assuming an effective temperature T_{eff} which is subsequently deconvolved according to the formula

$$(4 \cdot k_B \cdot T_{eff})^2 = (4 k_B T_{real})^2 + (\Delta(h\nu))^2 + (\Delta E_{ana})^2. \quad (7.7)$$

The more correct approach is to fit the convolution of the Fermi distribution in Eq. (7.6) including the real temperature of the experimental setup with a Gaussian

distribution, which has the full width have maximum of

$$FWHM_{gauss}^2 = (2 \cdot \sqrt{2 \cdot \ln(2)} \cdot \sigma_{gauss})^2 = (\Delta(h\nu))^2 + (\Delta E_{ana})^2. \quad (7.8)$$

The convolution

$$F_g(x, \sigma, T) = \int_{-\infty}^{\infty} F(t, T) \cdot G(x - t, \sigma) dt \quad (7.9)$$

has no analytic solution and has to be used in its integral form as a fit function (see also appendix A.15). To determine the energy resolution of the *NanoESCA* setup, a spectrum integrated over a circular ROI with radius $\Delta K_{\parallel} = 0.072 \text{ \AA}^{-1}$ around the center of the Brillouin zone was extracted from the image spectrum shown in Fig.7.7. The spectrum was divided by a fitted $1/E_{kin}$ function (see Sec.7.2.1) to get a flat profile at smaller $E - E_F$ values. The fit of the Fermi/Gauss convolution as well as the Gaussian part of the convolution is shown in Fig. 7.11(a).

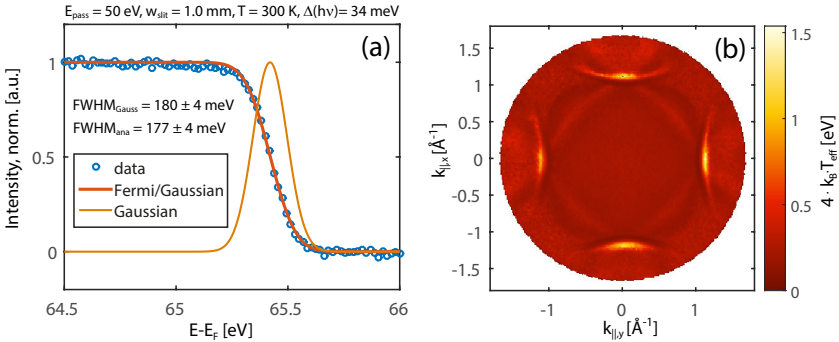


Figure 7.11.: (a) Fit of a Fermi/Gauss convolution at the Fermi edge of Ag(001). The data was extracted from the image stack in Fig. 7.7 from the center of the Brillouin zone. (b) Map of the Fermi edge width for the complete momentum distribution. While the center is homogenous, especially the borders between the Brillouin zones show extremely width edges, like it was also seen in Fig. 7.9(c).

The FWHM of the Gaussian was determined to $FWHM_{gauss} = 180 \pm 4 \text{ meV}$. Since the bandwidth of the synchrotron light was calculated to be $\Delta(h\nu) = 34 \text{ meV}$, the energy resolution of the analyzer can be determined to $\Delta E_{ana} = 177 \pm 4 \text{ meV}$, which is significantly better than the value estimated by Eq. (3.4) to $\Delta E_{ana} = 200 \text{ meV}$ for the given analyzer setup ($E_{pass} = 50 \text{ eV}$, $w_{slit} = 1 \text{ mm}$).

In the spectra shown in Fig.7.9(c) the Fermi edge at the border of the Brillouin zone looks different to the ones closer to the center. An automatized fit-procedure

using the model in Eq. (7.6) with an effective temperature T_{eff} was used to generate a map of the Fermi edge width over the full momentum distribution. The result is shown in Fig. 7.11(b). While the widths are homogenous in the Brillouin zone center, they become significantly broader at transition areas to adjacent Brillouin zones.

7.2.3. Relation between the contrast aperture and the momentum space

It was described above that the first momentum image is formed in the back focal plane of the objective lens. At this position, also the different *contrast apertures* can be placed, which cut out a certain part of the momentum image. With a calibrated momentum distribution, the size of the contrast aperture can be related to a distance in K_{\parallel} and with Eq.(7.5), the kinetic energy can be calculated, up to which all emitted electrons would pass the CA, and above which, part of the electron distribution is cut off. This cut-off energy can then be compared to the cut-off energy in the theoretical model for the acceptance angle Eq. (5.26) for the correspondent CA. If the model were to be perfect, both results should be identical.

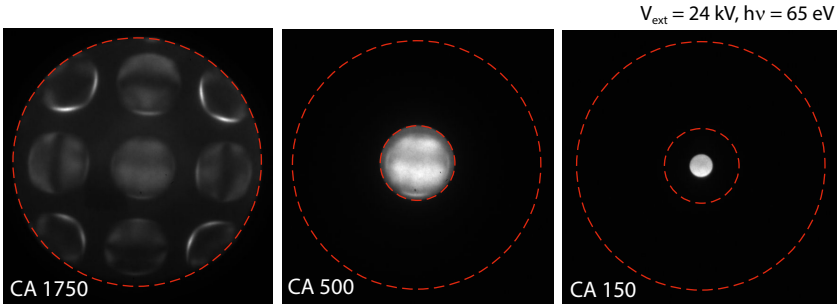


Figure 7.12.: A calibrated momentum distribution imaged with different contrast aperture diameters. The accepted momentum space can be determined as a function of the CA.

An exemplary measurement series with different CA diameters is shown in Fig. 7.12. A second measurement series was performed with a different extractor voltage $V_{ext} = 12$ kV. The results of the measurements and the calculated values for the same setup are compiled in Tab. 7.3. For the two smaller CAs, the agreement between measurement and calculation is good. For the CA 1750 it seems like not the CA is limiting the visible momentum range, but other parts of the microscope. Therefore the measured value is just a lower limit and it is not surprising that the calculated

dia. CA [μm]	V_{ext} [kV]	V_{col} kV	$2 \cdot K_{\parallel}$ [\AA^{-1}]	E_{kin} [eV]	calc. E_{kin} [eV]
1750	24	2	6.248	37.14	46.67
500	24	2	1.849	3.252	3.679
150	24	2	0.5733	0.3127	0.3195
1750	12	1	4.235	17.07	23.63
500	12	1	1.435	1.960	1.764
150	12	1	0.4524	0.1947	0.1583

Table 7.3.: The cut-off energies for different contrast apertures and extractor voltages are compared with the correspondent results of Eq. (5.26).

values are bigger. Additionally, the measurements at $V_{ext} = 12$ kV were not as sharp as those for $V_{ext} = 24$ kV. Within the limitations of this test, I conclude that the algebraic model in Eq. (5.26) gives reasonable results.

As a consequence, the formula for the dependency of the objective lens transmission Eq. (5.40) can be used, to divide the $1/E_{kin}$ -background in the spectra shown in Fig. 7.9. It is also possible to calculate the radius which corresponds to a certain CA and extract a spectrum from the image stack in Fig. 7.7 by integrating over this radius. The resulting spectra are shown in Fig. 7.13 for the most interesting regions around the work function edge (a) and the valence band (b). In both cases, no significant difference is visible between the smallest CAs with 30 and 70 μm . For the CA 150, the work function edge already becomes broader, because more of the parabolic *photoemission horizon* is included in the integrated spectrum. Also the shape of the valence bands changes, because the integration covers a bigger part of the band-structure. For CA 500 finally, the changes are serious. Up to $E_{kin} = 3.25$ eV ($E - E_F = 7.58$ eV) the spectrum includes all emitted electrons excited from the sample. The influence of the photoemission horizon is very pronounced. Beyond this energy, a part of the electrons is cut off and the $1/E_{kin}$ dependency dominates the shape of the spectrum.

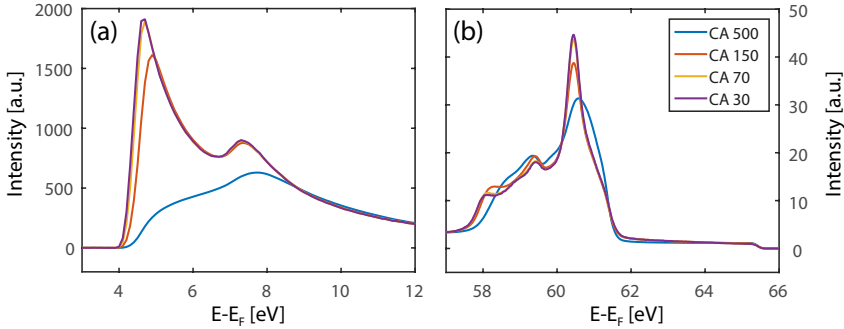


Figure 7.13.: Spectra were extracted from the image stack in Fig. 7.7 by integrating over different radii in k_{\parallel} . The radii were calculated such that they correspond with the available CA diameter.

7.3. Spatial resolution in spectro-microscopy

7.3.1. A test sample for spatial resolution

The test of the *spatial resolution* of the microscope was performed with a specifically designed sample.

A 9 nm thick Au film was grown via *molecular beam epitaxy* (MBE) on a Si wafer (b) with a 1 nm Cr buffer layer to ensure adhesion. Before the film deposition, the oxidized surface of the Si wafer was cleaned by dipping in HF (2% HF, 60 s)[EHC91], quickly transferred into the MBE chamber and annealed at 250°C for 2 h. During the MBE the sample was cooled down to -197°C to achieve a film growth with small crystallites. A pattern with 320 nm wide and 2 μm long stripes, but with decreasing spacing between the stripes from 900 nm down to 30 nm were milled into the Au

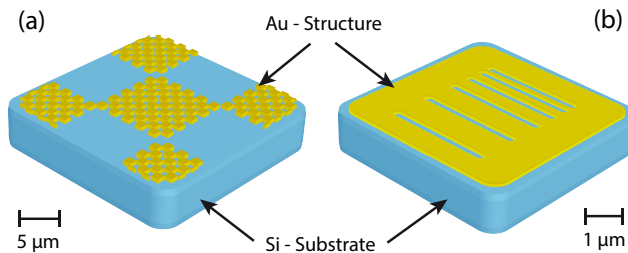


Figure 7.14.: Testsamples used for calibration purposes of the microscope: (a) commercially available checkerboard patterned sample, (b) FIB patterned sample for high-resolution tests.

film via *focused ion beam* (FIB), using 30 keV Ga-ions. The micro-crystallinity of the Au film should facilitate the formation of sharp edges. An SEM⁵-image and a fitted line profile along the pattern of this sample are shown in Fig. 7.15(a). The pattern is reasonably sharp and even the 30 nm wide line can be clearly identified. The line profile was fitted with a series of *Gauss-/Step-Functions* (see also appendix A.1) which can be expressed as

$$I(x) = I_0 \cdot \left(- \sum_{i=0}^6 \Gamma(x_i) + \sum_{i=7}^{12} \Gamma(x_i) \right) + I_{bg} \quad (7.10)$$

$$\text{with } \Gamma(x_i) = \frac{1}{2} \cdot \text{erf} \left(\frac{x - x_i}{\sqrt{2}\sigma} \right) \quad (7.11)$$

where the x_i mark the edge-positions along the profile with raising or falling steps, I_0 the maximal photoemission intensity and I_{bg} the photoemission background. Since we expect equal resolution at each edge, the standard deviation σ which describes the sharpness of the edge is chosen to be just one single fit parameter throughout the whole fit-function. As a measure for the resolution⁶, the *full width at half maximum* (FWHM) is in use in the literature, which for a *Gauss*-profile can be calculated from σ as

$$FWHM = 2 \cdot \sqrt{\ln(2)} \cdot 2 \cdot \sigma \approx 2.3548 \cdot \sigma. \quad (7.12)$$

The edge resolution determined from the fit of the SEM measurement is 19.9 ± 1.1 nm which is reasonably sharp for a resolution test.

To test the spatial resolution performance of the energy-filtered imaging mode of the *NanoESCA*, the pattern was imaged with the energy filter set on two different core levels: Au $4f_{7/2}$ ($E_{bin} = 84.00$ eV) and Si $2p$ ($E_{bin} = 103.10$ eV as Si^{4+} in a fully oxidized state). The flat-field corrected measurements are shown in Fig. 7.15(d,e). Clearly visible is the change in the *chemical contrast* between the two energy filter settings because different elements are probed.

The photon energy was chosen to be $h\nu = 200$ eV. The *photo-ionization cross sections* for Au $4f$ and Si $2p$ are very similar for this energy (see Fig. 2.3). The

⁵scanning electron microscope

⁶Throughout this thesis, the FWHM of the Gaussian profile convoluted with a Heaviside function is used to specify a resolution. For the model in Eq. (7.11) this FWHM equals the distance between the point where the height of the step reaches 12% of its total height and the point where it reaches 88%. In literature also the width between 16% and 84% of a profile height is in use, to describe the edge resolution. This width equals $2 \cdot \sigma$ in our model. The two measures for the resolution therefore differ by a factor 1.18 which should be taken into account, if they are compared with each other.

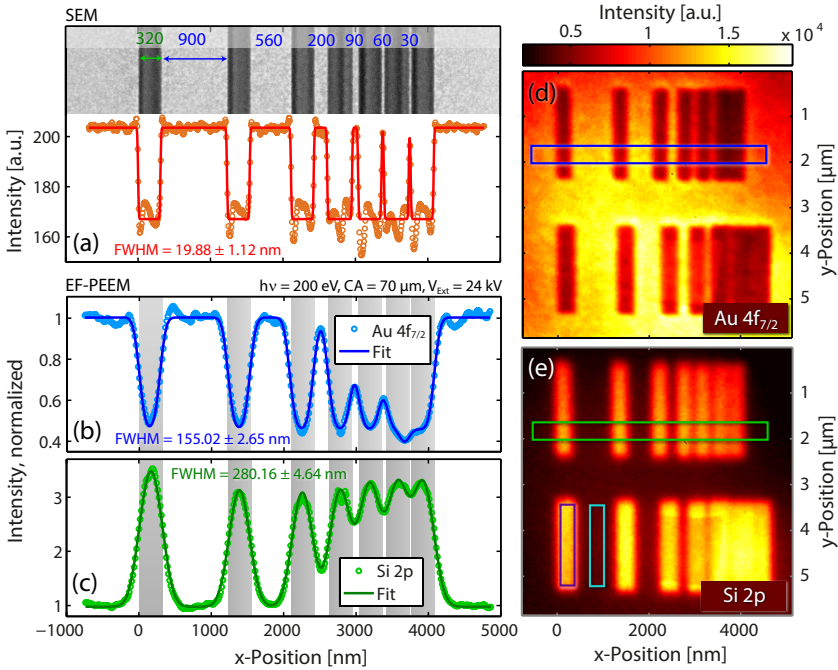


Figure 7.15.: A FIB-patterned sample was measured with SEM to prove, that the structure has a spatial resolution of better than 20 nm . Energy filtered PEEM was then proceeded with synchrotron excitation.

inelastic mean free paths (IMFP) of the excited photoelectrons depend on their kinetic energy inside the solid $E_{kin} = h\nu - E_{bin}$ and the element of the material they are travelling through (see Fig. 2.6). All relevant values are compiled in Tab.7.4. The calculated cross sections and IMFPs are quite comparable for the chosen core levels. The small IMFPs imply a high *surface sensitivity* of the measurement. Especially for Au the absolute minimum of the energy dependent IMFP curve was chosen.

The thin Au film and the surface sensitive experimental settings should provide the best requirements for a high spatial resolution, since the flat topography of the pattern makes only minor disturbances to the acceleration field of the immersion lens [NSS⁺00] and the short electron path to the surface reduces the probability of elastic scattering, which could smear out sharp features. A contrast aperture of CA=70 μ m was chosen, which is the best compromise between microscope transmission (see Fig. 5.8) and spatial resolution (see Fig. 5.15). Both values are a function of the contrast

$h\nu$ [eV]	Level	E_{bin} [eV]	Cross sec. [Mbarn]	E_{kin} [eV]	IMFP, Si [nm]	IMFP, Au [nm]
200	Au 4f_{7/2}	84	2.27	116	0.57	0.44
200	Si 2p	103.1	2.86	96.9	0.52	0.43
180	Au 4f_{7/2}	84	1.40	96.0	0.52	0.43
180	Si 2p	103.1	3.49	76.9	0.47	0.45

Table 7.4.: Calculated cross sections and IMFPs for the presented experiments.

aperture and the kinetic electron energy outside the solid. For the latter one, the *work function* has to be subtracted from the values for E_{kin} given in Tab. 7.4. Values for the work functions for this sample system should be comparable with the sample analyzed in Ch. 8. The work function analysis shown in Fig. 8.4 was also done for a Au pattern grown on Si. Since both samples were exposed to air, typical adsorbates (carbon, oxygen) stick to the surface and change the tabulated work function for clean element surfaces (see Sec. 2.4). For the Au film on our sample, I assume therefore a work function of $\Phi = 4.24$ eV and for the Si substrate a work function of $\Phi = 4.16$ eV as it was measured in the aforementioned analysis.

The calculated resolution limit for the objective lens (see Sec. 5.4) for a CA of 70 μm and a kinetic electron energy outside the solid of 111.76 eV is 6.6 nm if an energy filter resolution of maximal 500 meV limits the chromatic aberrations. The measured spatial resolution of 155.02 ± 2.65 nm verifies the results shown in [EWRB10] achieved under similar conditions, but exceeds the calculated prediction by far (see Fig. 7.15(b)). Although the calculations are an approximation, it is to be expected that much better values can be reached with this setup and it is worthwhile to analyze the reason for this discrepancy. Possible vibrations at the instrument were already suppressed as far as possible (e.g. expendable pumps off). Also to find the perfect focusing of the objective lens is problematic, especially at low count rates, when an adequate image cannot be recorded within short time scales. An instrumental source of inaccuracy is the cross-talk in the detection system, as discussed in Sec. 7.1, which might be improved by the single-event counting approach. Especially the use of the analyzer raises another question: Since spatial information is converted into an angular distribution inside the analyzer, the associated trajectories undergo stronger spherical aberrations in the transfer lens system between the hemispheres, which additionally vary with the lateral position on the sample, from where they are coming (see Fig. 6.18). Improved settings for the transfer optic system might

also yield an improvement in spatial resolution. Finally, also a limit for the electron flux passing the microscope exists: space charge effects cause perturbations in the electron distribution if the electron density in crossovers becomes too high (see Sec. 8.3).

Finally, another example of a virtually decreased resolution is shown in Fig. 7.15(c). The fit of the profile along the Si 2p signal suggest a spatial resolution of only 280.16 ± 4.64 nm for the same pattern and similar core level. A closer look on the profile shows that in principal all stripes (even the 30 nm one) can be identified. Nevertheless, the base-width of the fitted Si profiles is bigger than for the Au profile. A considerable electron-signal from the Si layer seems to penetrate the Au layer especially at the edges of the pattern, which may distort the edge-fits of the profile. This is supported by the micro-spectra in the following section.

7.3.2. Microspectroscopy and chemical analysis

The two different regions in the sample, which are the Au covered silicon substrate and the focused ion milled stripes, can be spectroscopically analyzed. For this purpose, a spatially resolved image spectrum of the sample region shown in Fig. 7.15(d,e) was acquired for the full spectrum from the Au 4f to the Si 2p core level with a step width of 200 meV. The energy resolution of the analyzer was set to $\Delta E_{ana} \approx 400$ meV ($E_{pass} = 100$ eV, $w_{slit} = 1$ mm) and a CA of 150 μm was used. The photon energy was $h\nu = 180$ eV. This slight change has a significant effect on the cross section so that the new values are also compiled in Tab. 7.4. Spectra were extracted from the ion milled stripes and from Au covered regions as indicated in Fig. 7.15(e). Both spectra show a dominant secondary background which was fitted with the flank of a Gaussian peak and subtracted. The resulting photoemission spectra from the nanometer-scale regions are plotted in Fig. 7.16.

For a better comparison both spectra were normalized to the peak height of the Si 2p peak. The Au $4f_{7/2}$ peak was set to $E_{bin} = 84$ eV, which is a usual binding energy calibration in XPS. The base lines in the plot are shifted by 0.5 arbitrary intensity units. The spectrum from the Au covered region shows an intense signal from the spin-orbit split Au 4f doublet. The Si 2p peak is broad and slightly asymmetric. Although the signal from the Si has to pass 10 nm cover layer (which equals approximately 22 times the calculated IMFP), the intensity (as integral under the peak) is comparable to that of the Au peaks. The focused ion milled stripes on the other hand show very weak Au signals compared to the Si peak. Obviously, the

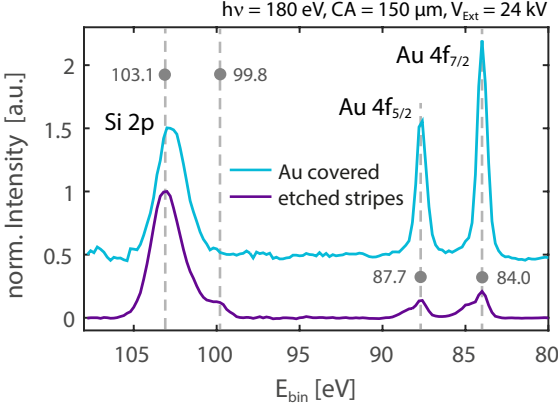


Figure 7.16: Microspectra taken from etched and Au covered regions of the sample. Exemplary ROIs are shown in Fig.7.15(e). To get a better statistics, the signal of several stripes regions (Au covered regions, respectively) were averaged.

Au was not completely removed by the FIB procedure and small particles remained. This spectrum shows a very interesting structure with additional shoulders not visible in the spectrum from the Au covered region.

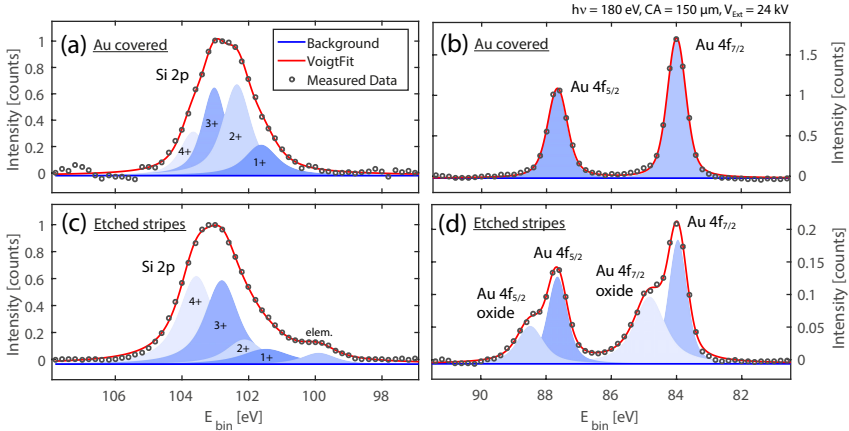


Figure 7.17.: Spectral analysis of the microspectra

For a more quantitative chemical analysis, all spectra were fitted with a reasonable number of *Voigt* profiles. A *Voigt* profile is a convolution of a *Lorentz* profile $L(\xi, \gamma)$, which describes the natural line shape of a spectral line emitted by an atom, and a *Gaussian* profile $G((\xi, \sigma)$, which describes additional broadenings (bandwidth of the photon source, instrumental broadening by the energy analyzer). For the Voigt profile no analytic form exists so that its integral form had to be used (see appendix

A.3). The fit model for i different *Voigt* profiles was

$$I(E_{bin}) = \sum_i \left(A_i \cdot \int_{-\infty}^{\infty} L(t, \gamma_i) \cdot G((E_{bin} - E_{peak,i}) - t, \sigma) dt \right) + I_{bg} \quad (7.13)$$

where i is the peak-index, A_i the area beneath a peak and I_{bg} a remaining background which was not subtracted by the procedure described above. The best way to start the analysis was the Au 4f doublet shown in Fig. 7.17(b) because it has only two symmetrical peaks, as it is expected from pure Au. Two *Voigt* peaks were fitted. Thereby only one σ parameter (Gaussian width of the profile) was allowed for both peaks, whereas the γ was fitted individually for each peak. The reason is the same as for the fit of the spatial resolution: the peak broadening described by σ comes from effects which influence all peaks in the same way. The result of the profile fits was $\sigma = 233 \pm 11$ meV or a full width half max of the Gaussian part of $\text{FWHM}_G = 525 \pm 25$ meV. The latter value describes the resolution of the experimental setting consisting of the instrumental resolution of the energy filter ΔE_{ana} and the bandwidth of the excitation source $\Delta(h\nu)$. Since the resolution of the analyzer is approximately known (400 ± 10 meV), the bandwidth of the excitation source can be calculated as $\Delta(h\nu) = \sqrt{\text{FWHM}_G^2 - E_{ana}^2} = 340 \pm 40$ meV. The exit slit of the beamline monochromator was opened very far to reach a higher flux.

The instrumental resolution of the experiment could be identified, because the clear line shape of the Au 4f doublet allows a precise disentanglement of the Gaussian and the Lorentzian part of the peak profile. All other measured spectra are more complicated and need more peaks to fit, which makes the separate fits less accurate. Since all spectra are from the same image spectrum, the parameter σ is the same for each spectrum and can be set as a fixed value in all fits, which makes the fit results for the separate peaks more reliable.

The residual fit values for the Au 4f doublet are compiled in Tab. 7.5, namely the fitted peak center which describes the binding energy E_{bin} of the core level, the FWHM of the Lorentzian part of the profile $w_L = 2 * \gamma$, and the area beneath the peak (relative to the total area of the peak doublet), which describes the intensity measured from each separate core level.

The fit values for the Au 4f spectra from the Au cover agree well with literature values [Man94] concerning the peak position and the area beneath the peaks. The Lorentzian w_L parameter is slightly bigger for the Au 4f_{5/2} peak than for the Au 4f_{7/2}. It represents the time, which an excited 4f^{m-h} state needs to recombine into the ground state 4f^m, and therefore the intrinsic lifetime of the core hole. The parameter

Au 4f	Au covered			etched stripe		
	$E_{bin}[eV]$	$w_L [eV]$	% Area	$E_{bin}[eV]$	$w_L [eV]$	% Area
7/2	83.99 ± 0.00	0.27 ± 0.03	58.94	83.97 ± 0.01	0.27 ± 0.03	30.30
<i>ox.</i>	—	—	—	84.84 ± 0.03	0.89 ± 0.07	31.83
5/2	87.66 ± 0.01	0.33 ± 0.03	41.06	87.66 ± 0.01	0.34 ± 0.04	23.26
<i>ox.</i>	—	—	—	88.49 ± 0.04	0.66 ± 0.11	14.61

Table 7.5.: Fit values for the Au 4f spectra shown in Fig.7.17(b,d)

n denotes the available number of electron states of the 4f shell and h the number of holes created by the photoemission process. The width w_L increases proportional to the number h of unoccupied 4f orbitals in the excited state [Hir75, CCW+76].

The Au 4f spectrum of the focus-ion beamed stripes shows additional peaks to the 4f doublet. The peak fitting of this spectrum gives nearly identical results for the 4f core levels in all fit-parameters compared to signal from the Au film, which shows the reliability of the fit-procedure. The additional peaks are shifted by $\Delta E_{bin} = 0.87 \pm 0.03$ eV (Au 4f_{7/2}) and $\Delta E_{bin} = 0.83 \pm 0.04$ eV (Au 4f_{5/2}) to higher binding energies, which is the same within the fit-errors. The intrinsic life-time of the additional peaks is smaller than for the core-levels of the pure Au.

The additional peaks depict a *chemical shift* in the photoemission spectrum of the measured Au particles in the FIB-stripes. The discovered shift probably belongs to an oxidized state of the small Au nanoparticles which were produced during the ion beam etching. Au atoms then give valence electrons nearly completely to the more electronegative oxygen atoms (charge-transfer). The missing electrons lead to a reduced *screening* of the Au core and the binding energies of the core levels increase. Although Au is actually the most noble of all metals due to its lack of reactivity [HN95], the appearance of different Au-oxides in Au nanoparticles have been detected [TMZ+15], the most common of which is Au_2O_3 which corresponds to Au^{3+} and O^{2-} oxidation states. This oxide nevertheless shows a shift of $\Delta E_{bin} = 1.5$ eV [THP+03], which is nearly twice as high as the one detected in our experiment. The shifted 4f states possibly belong to a sub-oxide state of Au formed in the presence of the Cr wetting layer; however, the existence of sub-oxides of Au is so far undocumented in the literature.

In the same way as the Au 4f peak, also the Si 2p peak can be analyzed. While Au is chemical inert and oxidation states only appear under special conditions, Si is known to have a variety of oxidation states between the elemental Si^0 and Si^{4+} ,

<i>Si 2p</i>	Au covered			etched stripe		
	E_{bin} [eV]	w_L [eV]	% Area	E_{bin} [eV]	w_L [eV]	% Area
<i>el.</i>	–	–	–	99.90 ± 0.19	1.0 ± 1.0	5.00
1+	101.62 ± 0.62	0.9 ± 1.1	14.72	101.48 ± 4.55	1.6 ± 4.8	9.98
2+	102.35 ± 0.23	0.7 ± 1.5	37.03	102.12 ± 1.44	1.1 ± 11.8	11.26
3+	103.03 ± 0.17	0.5 ± 1.3	29.81	102.80 ± 0.46	1.0 ± 2.3	35.01
4+	103.66 ± 0.33	0.6 ± 0.5	16.52	103.57 ± 0.19	1.0 ± 0.3	38.75

Table 7.6.: Fit values for the Si 2p spectra shown in Fig.7.17(a,c)

which are all present in the Si spectrum acquired from the FIB-stripe (see Fig.7.17 (c)). The associated fit-parameters are listed in Tab. 7.6. A fit of several peaks is less exact, therefore the approximate peak positions were taken from [LPBZ⁺10] and used as start values for the fit. Except for the Au particles discovered above, the Si area is uncapped and was exposed to air so that a high degree of oxidation is expected at the surface which decreases in deeper layers [LPBZ⁺10]. Although the bulk is dominated by elemental Si⁰, the bulk contribution to the photoemission is very low because of the low IMFP of the electrons at the chosen excitation energy. The use of hard x-rays (see Ch. 8) allows to study predominantly the bulk states.

As mentioned earlier, the Si 2p spectrum for the Au capped Si has a different shape. The signal of the elemental Si⁰ can be hardly detected through the capping layer because of the low IMFP, but also the distribution of the oxidation states is different. Since the oxidized Si was etched away by the HF dip prior to growing the capping layer a very low amount of oxidized Si was expected. It is still possible that oxygen from air could diffuse through the thin Au film, especially since a growth of small crystallites was stimulated by the deposition conditions during the MBE process.

7.4. Conclusions

Each setting of the microscope has an important influence on the measured data set. When measuring in the analogue mode, it is important to acquire bright- and dark-field images, to make a proper image correction. The single event counting is more reliable from its counting statistics, its suppression of detector artifacts and its sharpness, but is at the moment only working for very low count rates. Cameras with faster frame-rates are needed, to make it applicable for higher count-rates.

The momentum mode was discussed with an eye on its meaning for microscopy. On the Ag sample it was easy to study the influence of different CA diameters on a spectrum. The same effects have to be taken into account, if different CAs are used in microscopy. But also the momentum mode itself gives important insights into the electronic structure of materials, if highly ordered samples are investigated. Especially in connection with a continuously tunable light-source like a synchrotron with undulator beamline, any position of the final states in the 3D Brillouin zone can be addressed.

For the microscopic part it was shown that very localized spectroscopy with a good compromise of lateral and energy resolution is possible. Evidence of Au nanoparticle oxide peaks could be identified in the spectral analysis.

The analysis of the cut-off energies as a function of the CA diameter showed, that the calculations for the acceptance angles in Ch.5 give useful results. This supports the reliability of the results which are derived from these calculations like those for the transmission or the aberration of the microscope.

8. Bulk sensitive hard x-ray photoemission electron microscopy

The spectromicroscopy discussion in Sec. 7.3 showed that a spatially resolved chemical analysis of a sample system is possible with a high accuracy. Nevertheless, the method is very surface sensitive. As explained in the introduction of this thesis (1), a *bulk-like* analysis is also needed to understand bulk related phenomena in more complicated layer systems or for devices, which need a top-electrode for their functionality. The *information depth* of photoemission spectroscopy can be increased by using higher kinetic electron energies which leads to significantly larger IMFPs (see Sec. 2.1.3). The higher kinetic electron energies are reached by exciting the photoelectrons with photons in the hard x-ray regime (see Sec. 3.2.2). This method is called *hard x-ray photoemission spectroscopy* (HAXPES) and an overview is given in [Fad10]. We combined this method with the microscopic approach of the *NanoESCA* and proved its feasibility. Consequently, the method was named *hard x-ray photoemission electron microscopy* (HAXPEEM). Most of the results discussed in this chapter were published in [PWW⁺14] and will be recapitulated in the context of this thesis. All measurements with hard x-ray excitation were performed at the P09 undulator beamline at *PETRA-III* in Hamburg, Germany (see Sec. 3.2.2).

8.1. Preliminary aspects of HAXPEEM experiments

In this section the experimental peculiarities of the *HAXPEEM* method will be explained and a specially designed sample will be presented, with which the method can be evaluated with respect to the possible spatial resolution and the information depth.

8.1.1. Experimental peculiarities

The working principal of the *HAXPEEM* instrument is in general the same as explained for the standard design of the *NanoESCA* (see Sec. 3.1.6). The use of high

kinetic electrons nevertheless has some electron-optical consequences. Since the energy filtering is controlled via the sample voltage V_{spl} , the electrical isolation of the sample stage has to be improved to enable bias voltages of up to 10 kV. For example the sample potential has to be approximately set on $V_{spl} = 10$ kV, if electrons from the Fermi level are excited with hard x-rays having photon energies of $h\nu = 10$ keV. At the same time, threshold photoemission at very low kinetic energies has to be possible for a fast imaging and for work function scans. The power supply has to provide a high voltage resolution over the whole range.

Crucial for the functionality of the immersion objective lens of the microscope is the ratio between the kinetic energy $E_{kin} = e \cdot V_0$ of the photoelectrons leaving the specimen and the electrical *accelerating field* $(V_{ext} - V_{spl})/d$, where d is the distance between the sample and the extractor. This can be nicely seen from the calculated trajectories in Fig. 5.3(a-c). Photoelectrons with higher kinetic energies leaving the sample under an angle to the surface-normal are more resistant to the bending of their trajectories by the extractor field so that the electrons might not enter the microscope column (c). A reduction of the acceleration field leads to the same effect (b). Due to the energy filtering concept of the *NanoESCA* (see Sec. 3.1.3), both effects happen at the same time, if the analyzer is set to filter for higher kinetic electron energies. This leads to a reduced *angular acceptance* (see Fig. 5.5) and a reduced *transmission* (see Fig. 5.8) of the microscope, which combined with the low *photo-ionization cross sections* for hard x-rays (see Sec. 2.1.1) leads us to expect a low count-rate for core level imaging.

To improve this situation, the HAXPEEM works with an increased extractor voltage ($V_{ext} = 24$ kV) together with an accordingly raised column potential ($V_{col} = 2$ kV). The distance between the sample and the extractor was increased to $d = 2.5$ mm to avoid too high fields at the sample surface, which could cause flash-arcs (depending on the sample surface). Typical settings for the HAXPEEM experiment are shown in Fig. 8.1(a). A consequence of changing V_{spl} during an energy scan is that the *objective lens magnification* increases since the virtual object plane (see Fig. 5.2) shifts towards the objective lens. This behavior was studied with a series of energy filtered PEEM images of the *checkerboard sample* (see Fig. 7.14) for various kinetic electron energies. A selection of these images is shown in Fig. 8.1(b). The sample bias V_{spl} was set to the correct filter energy and the focus of the objective lens V_{foc} was adjusted, all other microscope settings were fixed. The change in the magnification was evaluated according to Eq. (A.6) and compared to simulated

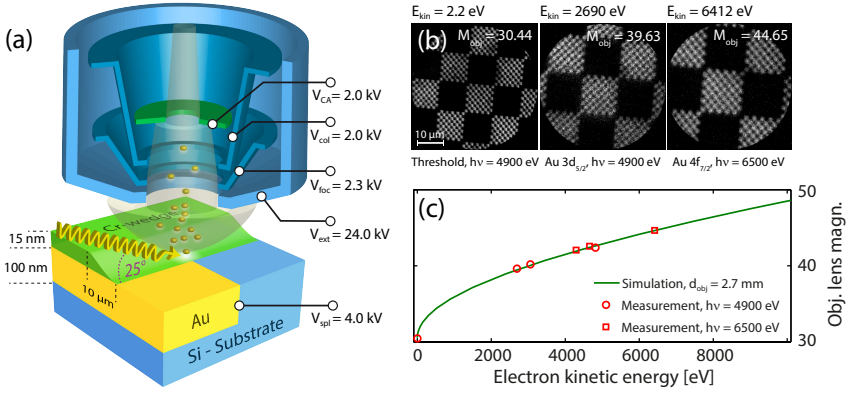


Figure 8.1.: (a) Schematic setup of the HAXPEEM experiment including typical potential settings for the objective lens in the high kinetic energy operation mode. Also the design of the wedge sample is shown, which was used to study the microscopic performance. To analyze the behavior of the objective lens for high kinetic electrons, energy filtered PEEP images of a checkerboard patterned sample were taken for several core levels (Au $4f_{7/2}$, Si $1s$, Au $3d_{5/2}$) and for the threshold photoelectrons. Two different photon energies in the hard X-ray regime ($h\nu = 4900$ eV and $h\nu = 6500$ eV) were used. The magnification is a function of the kinetic energy of the electrons. Selected energy-filtered PEEP images are shown in (b). The experimental results were acquired with a sample distance of $d_{obj} = 2.7$ mm, an extractor voltage $V_{ext} = 18$ kV, and a column potential of $V_{col} = 1.5$ kV and are shown as dots in (c). They very well fit to the simulated values (solid line) for these settings. Adapted from [PWW⁺14]

results (c). The simulation fits to the experimental data, therefore it can be used to automatically correct V_{foc} during an energy-scan. These simulated data were also used in the objective lens calculations in Ch. 5 (see Fig. 5.5(a)).

8.1.2. Sample design

A special test sample was designed to address the aspects of information depth and lateral resolution in hard X-ray imaging. The manufacturing process is shown in Fig. 8.2. *Optical lithography* and *reactive ion beam etching* (RIBE) were used to mill approx. $17 \mu\text{m}$ wide and 130 nm deep channels into a Si wafer and subsequently fill them with Au via *molecular beam epitaxy* (MBE). The surface was then treated with *chemical mechanical polishing* (CMP) to mill down the overlying Au. The result is a flattened surface with two chemically different materials and a sharp boundary. The thickness of the Au layer (ca. 100 nm) had to be much bigger than the expected

inelastic mean free (IMFP) path of Au for electrons excited with hard X-ray experiments so that it can be considered as nearly infinite for a photoemission experiment. Finally, the Cr-overlayer was evaporated perpendicular to the Au-stripe via MBE. To implement a thickness gradient, a knife edge was positioned 0.5 mm away from the sample, covering half of it. The maximum cover-layer thickness was chosen to be 15 nm, which is in the regime of twice the expected IMFP. This way, the wedge thickness increases from 0 nm to 15 nm over a length of approximately 10 μm . This dimension is optimal to analyze the structure via *atomic force microscopy* (AFM) and *HAXPEEM* at the same time (see Fig. 8.12).

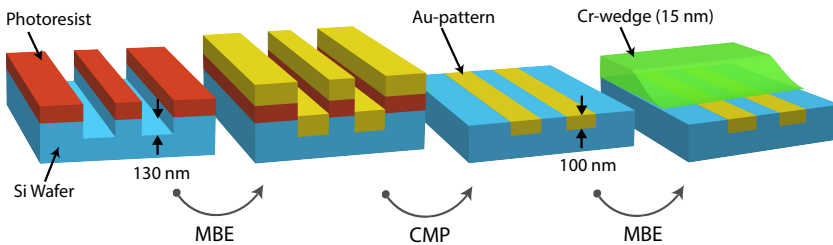


Figure 8.2.: Sketch of the manufacturing steps for the HAXPEEM test sample as explained in the text.

Cr was chosen as wedge-material, because it has no photoemission peak in the range of Au or Si. All photoemission signals can be clearly separated from each other in the experiment. This is shown in Fig. 8.3 where an overview spectrum from the whole sample structure was acquired in the *channeltron mode* of the *NanoESCA*, using an excitation energy of $h\nu = 6549$ eV. Only peaks from the expected elements (Au, Cr, Si) could be identified. The spectrum is shown as measured. Due to the decreasing acceptance angle of the microscope as a function of kinetic electron energy, higher binding energies have a higher transmission. This can be corrected by dividing by a calculated transmission curve (see Fig. 5.8).

8.2. Work function analysis with high kinetic photoelectrons

A first examination of the HAXPEEM test sample was performed with the work function analysis presented in Sec. 4.1. Energy-filtered image-stacks were acquired with the *NanoESCA* instrument, covering the energy range around the low energy

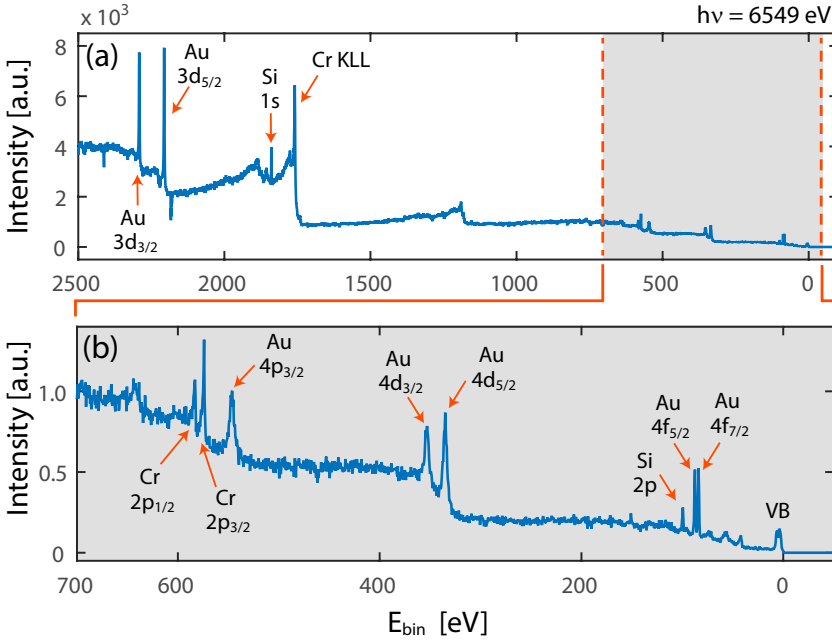


Figure 8.3.: Spectral analysis of the HAXPEEM test sample in a wide spectral range (a) and zoomed in into the typical range of a soft x-ray experiment (b). The core level signals from the expected elements of the test sample (Au, Si, Cr) can be identified.

secondary photo electrons and the *work function cut-off*. The instrument settings were kept equal in both measurements ($U_{ext} = 24$ kV, $E_{Pass} = 100$ eV, $slit = 1$ mm). The calculated instrumental energy resolution for these settings is approx. $\Delta E = 400$ meV. We used a rather large field of view of $260 \mu\text{m}$ to gather information about all element combinations predominant on the sample. The measurements were performed with two different *light sources* which will be compared in this chapter. One is a *high pressure mercury plasma arc-discharge lamp* with a photon energy of $h\nu = 4.98$ eV and an energy-resolution of $\Delta(h\nu) \leq 100$ meV, the other is a *hard X-ray synchrotron source* with its Si(111) monochromator set to a photon energy of $h\nu = 6550$ eV with an energy-resolution of $\Delta(h\nu) \approx 800$ meV. The sample itself was not sputtered before the measurements to not destroy the sample structure and is therefore covered with a naturally adsorbed carbon and oxygen layer.

Fit-results of the *work function analysis* for both light sources are shown as color-maps in Fig. 8.4. Their non-isochromaticity was corrected as explained in Sec. 6.1. The work function values (a,d) were calculated according to Eq. (4.2).

The work function edge widths w_{wf} (b,e) were calculated from the fit as $w_{wf} = 2 \cdot \sqrt{2 \cdot \ln(2)} \cdot \sigma_{wf}$ which can be roughly seen as a measure for the energy resolution of the experiment. To overview the quality of each spectral fit of the work function analysis, each *goodness of fit* (R^2) is plotted as a map (c,e).

Photoelectron spectra for the two light sources and for the four different material compositions marked in Fig. 8.4(d) are plotted in Fig. 8.5, all fitted with the model in Eq. 4.1.

The PES measured with the mercury lamp shows a much sharper work function edge compared to the hard X-ray measurements. This is due to the higher energy-resolution of the mercury lamp relative to the microscope's analyzer resolution. The measured resolution of the edge is therefore comparable to the analyzer resolution. The broadening of the work function edge of the hard X-ray PES on the other hand is dominated by the energy resolution of the synchrotron light.

I have to note that the model in Eq. (4.1) is not fitting each spectrum with the same goodness, which can be seen in Fig. 8.5(a). For a correct positioning of the work function edge fit, the I_0 - parameter was not fitted, but set to the maximum value of the spectrum. This issue has not a big influence on the evaluated work function position, but the value for σ_{wf} becomes less reliable for Si and Cr, because the fit does not match perfectly the profile shapes as it can be seen in Fig. 8.5(a). This also explains the differences for the *goodness of fits* in Fig. 8.4(c).

If the work function edge broadening in the UV measurement was completely due to the analyzer, the edge width map (Fig. 8.4(b)) should homogeneously show one value representing the analyzer resolution. The differences we still see depend on how good the model Eq. (4.1) can be applied to the spectra of the different materials. As discussed above, it works best for the Au spectra, which is also supported by the goodness of fits in Fig. 8.4(c). To find a value for the *analyzer resolution* I therefore averaged the resolution results of the Au region and found $\Delta E_{ana} = 351$ meV. For the same region on the hard X-ray resolution map I measured an average of $\Delta E_{wf} = 914$ meV, which is significantly broader. The resolution is obviously dominated by the resolution of the synchrotron light. By deconvolving the two resolutions we can approximate the resolution of the synchrotron light source to

$$\Delta(h\nu) = \sqrt{\Delta E_{wf}^2 - \Delta E_{ana}^2} = 844 \text{ meV}. \quad (8.1)$$

Very eye-catching in the hard X-ray work function edge width map is, that there are big differences between the uncovered Au and all other material combinations.

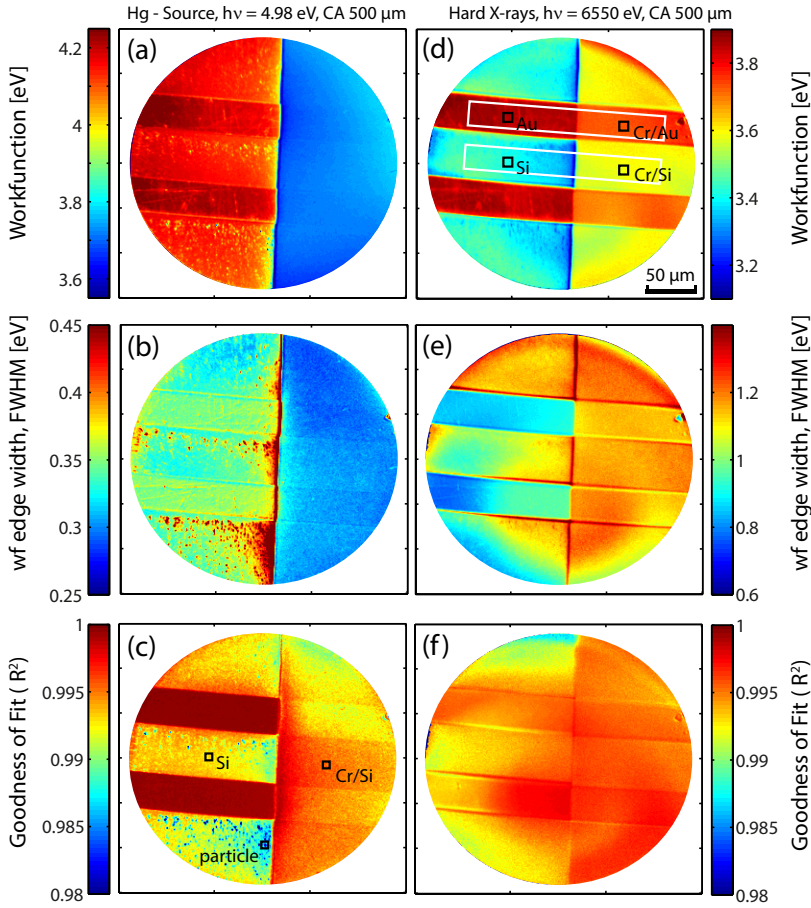


Figure 8.4.: The fit with the model function Eq. 4.1 (as shown in Fig. 8.5 for the ROIs marked in (d)) was performed for each pixel of the energy-filtered PEEM-image stacks, which provides a spatially resolved mapping of the work functions (a,d), the fitted width of the work function edge (b,e) and the overall goodnesses of the fit (c,f) for the measurements performed with the Hg-light-source (a-c) and the hard X-ray synchrotron light-source (d-f).

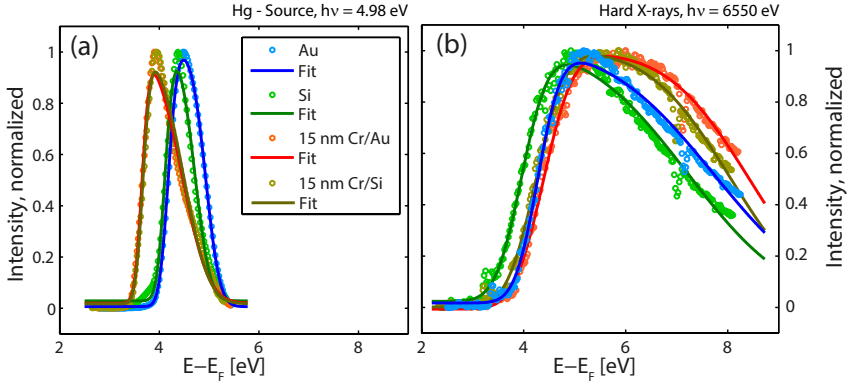


Figure 8.5.: Photoemission spectra for the four different material compositions present on the sample, taken from the region of interest marked in Fig. 8.4. With the model function in Eq. 4.1 the position and the FWHM of the work-function edges can be determined. The FWHM of the edges is a good quantity for the energy resolution of the experimental setup. The measurements on the same parts of the sample were performed with (a) a Hg light source and (b) hard X-ray synchrotron light with a photon energy of $h\nu = 6550$ eV and equal instrument settings. The difference in energy resolution is due to the different energy resolutions of the light sources.

In contrast to the UV measurements that is not only due to different fit-qualities, which are actually quite homogenous according to Fig. 8.4(f). In the extracted spectra shown in Fig. 8.5(b) we can see, that the Au work function edge is significantly sharper than the work function edge of the other spectra. What is more, the resolution differs for the same material depending on the sample position.

The beam-spot on the sample has a FWHM of $270 \mu\text{m}$ in vertical direction and $311 \mu\text{m}$ in horizontal direction, as evaluated by fitting a Gaussian profile to intensity profiles of a PEEM image (see Fig. 8.6). The chosen FOV of $261 \mu\text{m}$ therefore covers already a big part of the beam-profile.

As it could already be seen in Fig. 8.5, the work functions for the different material combinations significantly differ from each other for the two different excitation sources (see Fig. 8.4(a,d)). Already in these work function maps a higher surface sensitivity for the UV measurement is obvious. The Au stripes in the images running from left to right are covered with 15 nm Cr on the right half. Nearly no effect of the Au stripes underneath the Cr layer is visible for the UV measurement. The work function is the same for all Cr covered regions. In the hard X-ray measurement the work function of the Cr covered Au stripes clearly differ from the one

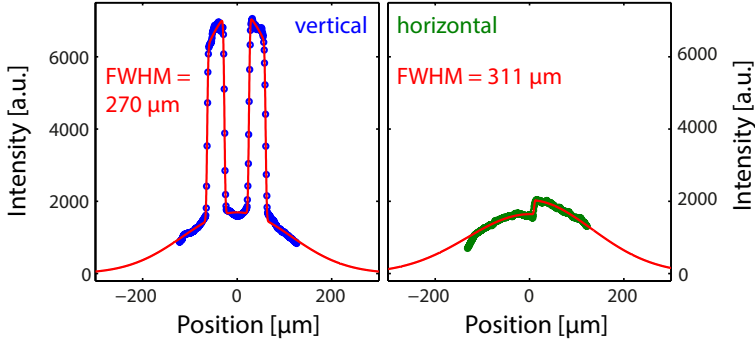


Figure 8.6.: From an intensity map of the spatially resolved photoelectron distribution at $E - E_F = 5.375$ eV (excited with $h\nu = 6550$ eV) the dimensions of the beam can be estimated. A vertical and a horizontal intensity line profile was fitted with a model for structure, modulated by a Gaussian which describes the beam profile on the sample.

of the Cr covered Si.

Another hint for the surface sensitivity of the UV measurement are the small speckles which occur on the uncovered side in all UV-maps in Fig. 8.4 and which do hardly appear in the hard X-ray maps. The origin of these speckles can be analyzed by comparing the original photoemission spectra on the positions indicated in Fig. 8.4(c). These spectra are shown in Fig. 8.7 (a). Beside a nearly pure Si spectrum and a nearly pure Cr spectrum, the spectrum of the speckle is a superposition of both. These speckles therefore consist of Cr which was scattered underneath the knife edge installed to grow the Cr wedge (see Sec. 8.1.2). A few amount of Cr traveled much higher distances underneath the shielding than the average $10 \mu\text{m}$ wedge-length, which was probably due to a tilted evaporation angle in the MBE combined with *surface diffusion* [AE07].

To investigate the influence of the Cr coverage on the work function for the hard X-rays, we analyzed the profile of the work function map along the Au stripe and in parallel along the Si stripe, averaged over the regions marked (white) in Fig. 8.4(d). The results are displayed in Fig. 8.7(b). The behavior along the Au stripe seems to be simple: The work function of the Au starts at a level of 3.85 eV and monotonically decreases at the boundary to the Cr coverage (over $10 \mu\text{m}$). With a constant Cr thickness of 15 nm the work function has decreased by 150 meV. On Si the work function drops monotonously over a distance of approximately $45 \mu\text{m}$ towards the edge of the Cr layer. That is probably due to the aforementioned small amount of scattered Cr sparkles reaching far into the actually Cr free half of the sample.

Approximately 50 μm away from the boundary it reaches a maximum plateau of 3.45 eV. Close to the boundary, where the Cr thickness rapidly increases, the work function drops to a minimum of 3.18 eV and then increases to a maximal level of 3.58 eV with a 15 nm Cr coverage. Such a behavior is well known and understood for adsorbed Cs as cover layer, describing the work function changes by a classical point-dipole model for a coverage significantly below one Cs atom per 30 \AA^2 and an orbital-overlap model for a more dense coverage [CVB⁺12]. Because of these electrostatic and orbital effects the work function decreases for low coverages and increases again to match the work function of the cover material, if the layer becomes thick enough to dominate the surface. The responsible dipole moment is governed by the difference between the electronegativities of the adsorbate and the substrate [CVB⁺12], which would explain a different behavior for Cr on Au and Cr on Si. Not compatible with this idea is, that Cr in general has the lowest work function of the three materials under investigation [Mic77]. The source of this behavior must be related to the high photon energies and the consequently high electron energies involved.

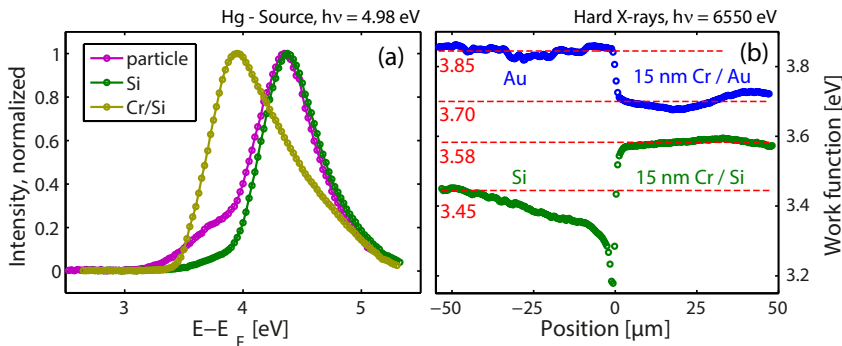


Figure 8.7.: (a) Comparison of the spectra marked in Fig. 8.4(c). The particles visible in the evaluation of the UV light measurement can be identified as Cr. The spectrum of the particle consists of the Si spectrum and low- kinetic energy shoulder belonging to Cr. (b) Profiles of the work function of the hard X-ray measurement along the Au stripe (Si stripe, respectively) marked in Fig. 8.4 (d). Beneath the 15 nm Cr layer the Au work function is lowered and the Si work function is raised.

8.3. Space-Charge influence on the spatial resolution

In photoemission electron microscopy a *space-charge effect* has to be taken into account, which limits the ratio of a possible spatial resolution to the number of photoelectrons passing through the microscope column. The reason is that very high electron densities can occur especially in the regions of the microscope where electron trajectories cross each other. In the standard real space mode, the most pronounced trajectory crossings lie for example in the first image plane and between the projection lenses (see Fig. 3.5(a)). High electron densities lead to Coulomb repulsion of the electrons, which decreases the lateral resolution of a microscope (repulsion in the image plane direction) and can also broaden the energy distribution (repulsion in the positive or negative direction of the electron momentum outside the crystal) [LMNB11, NJP⁺09]. As general law it was found (see [Pie49, p. 151] and [KS67]) that the maximal current I_{max} which can be passed through a volume defined by two apertures with diameter d which are separated by a distance l is given by

$$I_{max} = 38.5 \frac{\mu\text{A}}{\text{eV}} \cdot E_{kin}^{3/2} \cdot \left(\frac{d}{l}\right)^2. \quad (8.2)$$

High electron concentrations in low kinetic electron energy regions of the microscope (e.g. energy-filter) are more severe than in the regions where the electrons are highly accelerated (e.g. objective lens). The issue in case of the HAXPEEM approach with high kinetic electron energies is that powerful light sources with a high *photon flux* are essential to obtain adequate signal levels in core level imaging because of a lower *photo-ionization cross section* and a decreased *microscope transmission*. The higher electron kinetic energies at the same time create a cascade of low energy secondary electrons due to inelastic scattering processes (see Sec. 2.1.3) and therefore a huge secondary electron yield (see e.g. Fig.8.5(b)). In addition, the low energetic secondary electrons have a higher transmission in the objective lens (see Fig. 5.8). Since electrons are separated for their kinetic energy only in the analyzer, all electrons pass the microscope column together (except for differences in the time-of-flight between high and low kinetic electrons). Possible image deterioration due to space charge interaction between the high flux of low energy secondary electrons and high energy electrons used for core level imaging has to be excluded.

To answer this question, resolution tests with alternating amounts of photoelectrons entering the microscope column were performed. The results are shown in Fig. 8.8. Two different methods to alter the photoelectron flux are possible, (i) choosing a small contrast aperture to reduce the transmission of the objective lens (see Fig.

5.8) or (ii) reduce the photon flux from the beamline. Therefore, the beamline was set to the full flux ($\approx 10^{13}$ photons/s) and images from the Au stripe of the HAX-PEEM wedge sample (see Fig. 8.2) were acquired with different CA diameters (500, 150, 70 μm) and also for a CA diameter of 500 μm with a reduced photon flux (by approximately a factor 10). The photon flux was reduced by inserting Al filters into the beam. Exemplary measurements for energy filtered PEEM images in the secondary yield ($E_{kin} = 3.9$ eV) are shown in Fig. 8.8(a,b) comparing the two different light intensities. It is obvious that the image measured with full light intensity is blurred. To quantify this blur, the profile along the structure was evaluated with a model similar to Eq.(7.11)

$$I(x) = \left(\frac{I_0}{2} \cdot \left(\operatorname{erf} \left(\frac{x - x_1}{\sqrt{2} \cdot \sigma} \right) - \operatorname{erf} \left(\frac{x - x_2}{\sqrt{2} \cdot \sigma} \right) \right) + I_{bg} \right) \cdot C_{niso}(x). \quad (8.3)$$

but including the term C_{niso} which describes the intensity shift caused by the *non-isochromaticity* of the energy-filter from Eq. (6.26). The fitted profiles of the images in (a,b) are shown in (c). The spatial resolution of the setting is described by the full-width half-maximum ($FWHM = 2 * \sqrt{2 \ln 2} \cdot \sigma$) of the Gaussian. The results of the spatial resolution as a function of the calculated relative intensity of the electron flux is shown in (e). The spatial resolution improves dramatically by closing the CA or by reducing the photon intensity by an equivalent factor. Note that a decrease of the contrast aperture size itself would usually improve the resolution, but since a reduction of the photon flux with CA 500 has an equal impact on the spatial resolution like a reduction of the contrast aperture diameter to CA 70, it can be concluded that only the amount of electrons plays the dominant role in this measurement. The dependency of the spatial resolution ϱ_s on the photoelectron intensity I_{pe} seems to follow a quadratic law. The four data points could be fitted with $\varrho_s = a \cdot I_{pe}^2 + b$. This makes sense since the perturbation of the resolution due to space-charge in an electron trajectory crossing of the microscope would be mainly effected by the two dimensional electron density in a plane perpendicular to the mean drift-direction of the electrons.

After the space charge effect in the microscope was characterized, the same measurements were performed at high kinetic energies (Au 3d, $E_{kin} = 4344.4$ eV). The results for the spatial resolution is shown in Fig. 8.8(f). Even with the full photon flux and a CA of 500 μm a good resolution was achieved. Obviously, these electrons are not affected by any space charge from secondary electrons.

As one reason the *time-of-flight* differences in the microscope for electrons of

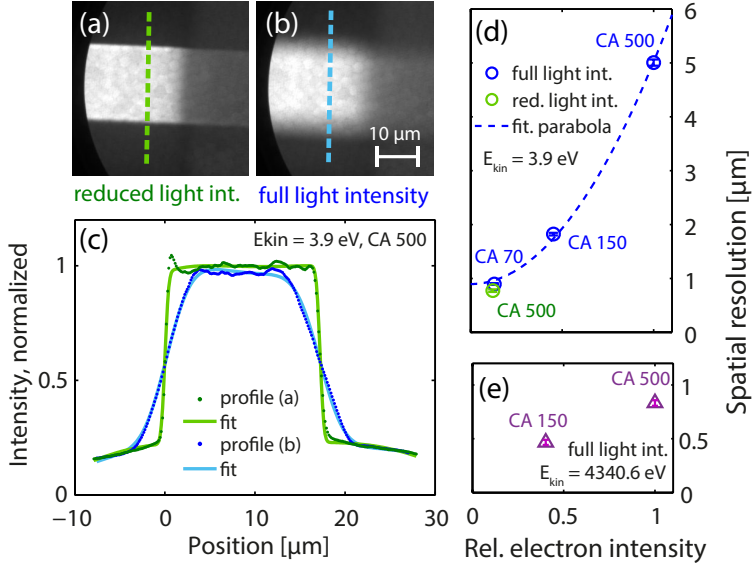


Figure 8.8.: Depending on the photoelectron current densities inside the microscope the spatial resolution varies significantly. Energy filtered PEEM images of a Au stripe structure were taken for different photon intensities (a,b) at the same photon energy $h\nu = 6550 \text{ eV}$ and the same contrast aperture $CA = 500 \mu\text{m}$ at the maximum secondary peak $E_{\text{kin}} = 3.9 \text{ eV}$. The line profiles of these measurements were fitted to estimate the resolution (c). Finally, the instrument's spatial resolution was evaluated for various experimental settings at the secondary peak (d). The resolution improves with smaller CA size or a reduction of the photon flux. This suggests that the degradation of lateral resolution is caused by space charge effects within the microscope. The data points could be fitted with a simple parabola $FWHM = a \cdot I^2 + b$. The resolution at high kinetic electron energies is still significantly better (e), because the disturbing secondary electrons are filtered out by the objective lens in this microscope setting (see text). Taken from [PWW⁺14]

different kinetic electron energy E_{kin} should be taken into account. An electron which is flying with a constant drift velocity v_d through a part of a microscope with length L_d needs a transit time of

$$\tau = \frac{L_d}{v_d} = \frac{L_d}{\sqrt{2 \cdot E_{kin}/m_e}}. \quad (8.4)$$

The differential drift time difference per kinetic drift energy is described by [SSZ⁺98]

$$\frac{d\tau}{dE_{kin}} = -\frac{L_d}{2} \cdot \sqrt{\frac{m_e}{2}} \cdot E_{kin}^{-3/2}. \quad (8.5)$$

From Eq. (8.5) the time difference $\Delta\tau$ for two electrons with a difference ΔE_{kin} in kinetic energy can be calculated with respect to the drift length L_d and the mean kinetic drift energy E_{kin} . A multiplication with the mean drift velocity v_d gives the spatial separation ΔL between the two electrons as

$$\Delta L = \underbrace{\frac{d\tau}{dE_{kin}} \cdot \Delta E_{kin}}_{=\Delta\tau} \cdot \underbrace{\sqrt{2 \cdot E_{kin}/m_e}}_{=v_d} = -\frac{L_d}{2} \cdot \frac{\Delta E_{kin}}{E_{kin}}. \quad (8.6)$$

As mentioned above, it is interesting to approximate the spatial electron separation in the regions with a strong crossing of electron trajectories, like it happens between the projective lenses. The drift length between the back focal plane and the center of the projective lenses¹ is approximately $L_d = 230$ mm. Over this length, the electrons have a kinetic drift energy of $E_{kin} = e V_{col} = 2000$ eV. Electrons with a difference in kinetic energy of $\Delta E = 1$ eV then have a time-of-flight difference $\Delta\tau = 2.17$ ps between the lenses and a spatial separation of $\Delta L = 50$ μm . Fast electrons are therefore sufficiently ahead of a low kinetic secondary yield in the trajectory crossings to be influenced by its space-charge. Figure 8.9 shows the results for this calculation for different drift energies E_{kin} . For the operation of a time-of-flight PEEM, which uses $\Delta\tau$ as an energy filter, long drift-tubes with low drift energies between 10 and 100 eV are used. This way, delays in the nanosecond-regime between the incoming electrons can be reached so that single electron events can be separated by the electron detector [SSZ⁺98].

The main reason for the non detectable influence of the secondary electrons on the fast electrons in our experiment is nevertheless that the objective lens with the settings shown in Fig.8.1 (a) works as a high-pass filter for the hard x-ray excited

¹The mean drift velocity in front of the back focal plane is high compared to the microscope column and the drift length is short so that a time-of-flight difference in this part can be neglected according to Eq. (8.5).

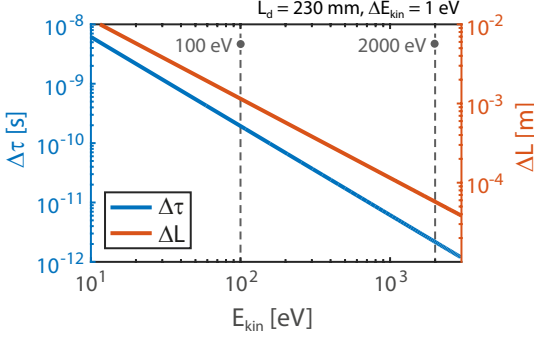


Figure 8.9: Time-of-flight differences $\Delta\tau$ and the spatial separation ΔL between electrons, which have a difference in kinetic electron energy of $\Delta E = 1$ eV after passing a drift length of $L_d = 230$ mm. The results are plotted for different kinetic drift energies E_{kin} .

electrons. Photoelectrons are accelerated between the sample and the extractor and gain a kinetic energy of $e \cdot (V_{ext} - V_{spl})$. Subsequently they are decelerated between the extractor and the column and lose a kinetic energy of $e \cdot (V_{col} - V_{ext})$. As a consequence, only photoelectrons with a minimal kinetic start energy of

$$E_{kin,min} \geq e \cdot (V_{spl} - V_{col}) \quad (8.7)$$

are able to pass this potential barrier. If the energy filter is for example set to 4 keV ($V_{spl} = 4.0$ V) and the column works at $V_{col} = 2.0$ kV, all photoelectrons with a kinetic energy less than $E_{kin} = 2.0$ keV are blocked. The massive secondary photoelectron yield produced with hard x-ray excitation will therefore not disturb the imaging of high kinetic photoelectrons. The excitation intensity and the microscope transmission can therefore be increased, which will be necessary in the future to shorten exposure times.

8.4. Bulk sensitive imaging and chemical imaging

The larger IMFP of photoelectrons excited by hard x-ray photons increases the bulk sensitivity of the measurement. This effect can be shown on the Si 2p peak of a Si surface which was exposed to air and exhibits a natural oxide layer with a decreasing oxidation level towards the bulk [LPBZ⁺10]. Spectra extracted from highly surface sensitive image-spectra acquired with a photon energy of $h\nu = 180$ eV were shown in Sec. 7.3.2. In this section, measurements performed on the *checkerboard sample* (see Fig. 7.14(a)) are discussed, which contains the same elements as the focused ion-beam patterned sample in Sec. 7.3.2.

Photoemission spectra from two different core levels of Si excited with three different photon energies are shown in Fig. 8.10. Both spectra of Si 2p are extracted

from image-spectra of the *checkerboard* sample so that they contain only the signal from Si which is not covered with Au. The instrumental energy resolution was set to 400 meV ($E_{pass} = 100$ eV, $w_{slit} = 1$ mm). In contrast, the Si 1s spectra were acquired in the *channeltron mode*, integrated over a large area which also included the Au checkerboard-pattern. The settings for the instrumental energy resolution was equal to the Si 2p measurements, but since an integration over a larger field of view leads to a reduced energy resolution because of the *non-isochromaticity* of the analyzer (see Cha. 6), the energy resolution in the channeltron mode was worse.

The spectra were measured on the same sample and with the same instrument and are therefore directly comparable. The experiment with $h\nu = 0.4$ keV was performed at the *Nanospectroscopy* soft x-ray undulator beam-line at the synchrotron *Elettra* (Italy), all other experiments at the *P09* hard x-ray undulator beamline at the synchrotron *DESY* (Germany). All energy scales are calibrated using the Au 4f_{7/2} ($E_{bin}=84$ eV) peak, which was measured together with the corresponding Si peaks. The instrumental energy spread (FWHM of the Gaussian part of the Voigt profile) was determined at the Au 4f peak in the case of the soft x-ray excitation (not shown here) and set to a fixed value for the Si 2p fit. In all other cases, the peaks were sharp enough to fit the Gaussian width as a free parameter in the Voigt-fit. The secondary background in all spectra was calculated with an *Active Shirley Background* method [HG12]. The fitted peak-positions and the ratios of the areas beneath the peak are compiled in Tab.8.1.

The Si 2p fit-results at $h\nu = 0.4$ keV qualitatively correspond to the measurement shown in Fig. 7.17 (c) for an oxidized Si surface only that the Si 2p⁴⁺ state from SiO₂ is even more pronounced, which is probably due to a thicker oxide layer. The peaks of the less oxidized Si states are less pronounced than the Si⁴⁺ state. An interpretation can be given on the basis of the five-layer model used in [LPBZ⁺10] in which each layer corresponds to a different chemical state of Si going from bulk silicon in the substrate to SiO₂ at the surface. Three sub-oxide layers (Si¹⁺, Si²⁺, Si³⁺) are placed between the SiO₂/Si interface and form an oxidation gradient. The sub-oxide layer thickness depends on the sample preparation and oxidation conditions [HMTI⁺88]. The layer thicknesses determined from photoemission experiments in [LPBZ⁺10] are around 1.2 nm for the Si⁴⁺ layer at the surface. The thickness of the sub-oxide layers are significantly smaller and are decreasing with the oxidation level. They reach from approximately 0.3 nm for Si³⁺ to a sub-monolayer of approximately 0.03 nm for Si¹⁺. The decreasing peak intensity for the less oxidized states in the photoemission spectra

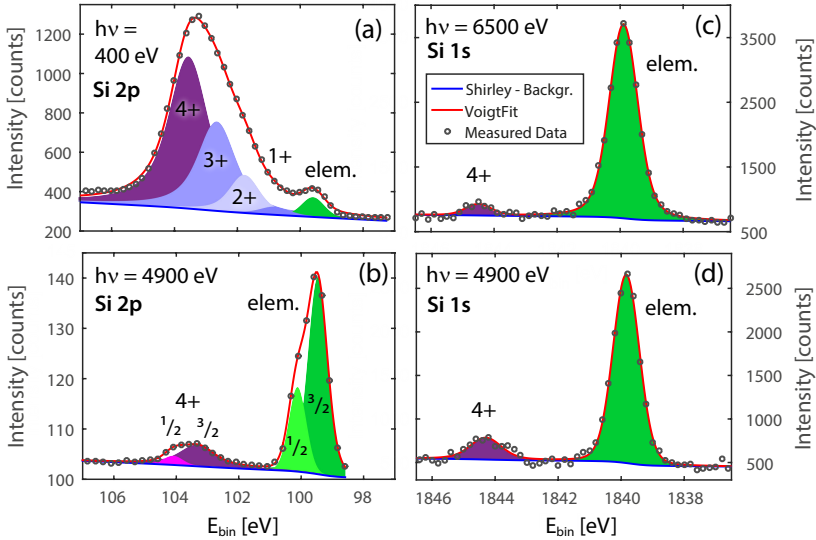


Figure 8.10.: (a) Si 2p spectral distributions obtained with soft x-ray excitation ($h\nu=400$ eV, acquired at the Elettra NanoESCA beamline [WPK⁺11]); (b) Si 2p spectra with hard x-ray excitation ($h\nu=4.9$ keV, taken at *PETRA III*, beamline P09); Both spectra were extracted from image spectra, taken with 100 eV pass energy and 1 mm slits, resulting in approx. 0.4 eV energy resolution. The Si 1s spectra were acquired in the channeltron mode using two different excitation energies: (c) $h\nu=6.5$ keV and (d) $h\nu=4.9$ keV.

(a) Si 2p spectral distributions obtained with hard x-ray excitation ($h\nu=4.9$ keV, taken at *PETRA III*, beamline P09); (b) Si 2p spectra with soft x-ray excitation ($h\nu=400$ eV, acquired at the Elettra NanoESCA beamline [WPK⁺11]); The inset shows the IMFP of Si as a function of the kinetic electron energy calculated according to [TPP11]. The energies used in the experiment are marked with red circles. (c) Atomic concentration images using the Si 2p and Au 4f core level peaks. The data have been evaluated with CasaXPS and principal component analysis (PCA) for noise reduction and separation of spectral contributions according to the oxidation state. Exposure time 8 min/image, energy step 0.25 eV, field of view 38 μm . All spectra were taken with 100 eV pass energy and 1 mm slits, resulting in approx. 0.4 eV energy resolution.)

	$h\nu = 0.4 \text{ keV}$		$h\nu = 4.9 \text{ keV}$	
	$\Delta E = 742 \text{ meV}$		$\Delta E = 650 \text{ meV}$	
	$E_{bin}[\text{eV}]$	% Area	$E_{bin}[\text{eV}]$	% Area
Si 2p el.	99.59 ± 0.06	3.3	3/2 99.47 ± 0.01	61.3
			1/2 100.12 ± 0.01	21.2
Si 2p¹⁺	100.79 ± 0.63	1.9		
Si 2p²⁺	101.75 ± 0.37	9.6		
Si 2p³⁺	$102.63 \pm NaN$	30.3		
Si 2p⁴⁺	103.53 ± 0.17	54.9	3/2 103.33 ± 0.06	14.9
			1/2 104.08 ± 0.07	2.5
	$h\nu = 6.5 \text{ keV}$		$h\nu = 4.9 \text{ keV}$	
	$\Delta E = 898 \text{ meV}$		$\Delta E = 925 \text{ meV}$	
	$E_{bin}[\text{eV}]$	% Area	$E_{bin}[\text{eV}]$	% Area
Si 1s el.	1839.89 ± 0.005	95.6	1839.84 ± 0.01	86.8
Si 1s⁴⁺	1844.50 ± 0.08	4.4	1844.30 ± 0.06	13.2

Table 8.1.: Fit-results of the spectral distributions of the Si 2p and Si 1s core levels excited with different photon energies as shown in Fig. 8.10.

is therefore due to a smaller volume and because the electrons have to overcome an increasing over-layer thickness. Only the elemental Si peak is comparatively strong, because it contains contributions from a much bigger volume as compared to the oxide species which are confined to the few layers near the surface.

If the same measurement is performed with a photon energy of $h\nu = 4.9 \text{ keV}$, the distribution of the measured peak intensities changes completely. The elemental Si peak now gives the strongest signal and only a weak signal of the relatively thick Si 2p⁴⁺ layer is visible. The intermediate oxidation state layers obviously have not enough volume to show a pronounced contribution in the spectrum. The energy resolution of this measurement is good enough to see a slight asymmetry in both peaks which is due to the spin-orbit split 2p level. The literature value for this splitting is $\Delta E_{SO} = 0.61 \text{ eV}$ [HMTI⁺88], which corresponds well with the fitted data at the elemental Si 2p peak ($\Delta E_{SO} = 0.65 \pm 0.06 \text{ eV}$). The *chemical shift* between the elemental and the oxidized Si can be determined as ($\Delta E_{CS}(Si_{2p}) = 3.86 \pm 0.06 \text{ eV}$). Within the given errors this is equal to the separation in the measurement with $h\nu = 0.4 \text{ keV}$ and fits with the value given in [HMTI⁺88].

The *chemical shift* of the oxidized Si can be also identified in the 1s level, where

	$h\nu$ [eV]	$h\nu - E_{bin}$ [eV]	$IMFP(Si)$ [nm]	I_{Si}/I_{SiO_2}
Si 2p	400	300.41	1.013	0.06
Si 2p	4900	4800.53	8.850	4.74
Si 1s	4900	3060.16	6.077	6.58
Si 1s	6500	4660.11	8.632	21.73

Table 8.2.: Comparison of the peak intensity ratio of Si an SiO₂ for different photon energies.

the energy difference is slightly larger than for the 2p level. For the measurement with $h\nu = 4.9$ keV a shift of $\Delta E_{CS}(Si_{1s}) = 4.46 \pm 0.06$ eV was determined and for $h\nu = 6.5$ keV a shift of $\Delta E_{CS}(Si_{1s}) = 4.61 \pm 0.08$ eV, which is significantly bigger than the value $\Delta E_{CS}(Si_{1s}) = 3.4$ eV given in [KBH⁺74]. The reduced *screening* of the Si nucleus in the SiO₂ causes a higher chemical shift for the 1s states than for the 2p states. That the chemical shift of oxidized states can be detected also in deeper core levels is advantageous for the HAXPEEM approach, since deeper core levels in general have a higher *photo-ionization cross section* for a photon excitation in the hard x-ray regime (see Fig. 8.3) and a higher count rate is necessary for imaging with a high statistics in an adequate exposure time. The goal will be to find the right excitation energy to have a good cross-section for the core level under investigation and at the same time high-energetic photoelectrons with long enough *IMFPs* to overcome a capping layer.

The impact of the cross section and the IMFP can be studied at the intensity-ratio of the Si⁴⁺ and the elemental Si peaks, which are compiled in Table 8.2. It compares the energy of the photons, the kinetic energy of the photoelectrons inside the solid ($h\nu - E_{bin}$) and the calculated IMFP for this kinetic energy for Si (see Eq.(2.12)) with the ratio of the peak-intensities. If the increase of the Si peak compared to the SiO₂ overlayer would only be due to an increased IMFP, the peak intensity ratio difference between Si 2p excited with $h\nu = 4900$ and Si 1s excited with $h\nu = 6500$ could not be explained, because their IMFPs are nearly equal. The measured intensity ratios therefore also depend on the cross-section of the materials and can be described by the equation [HMTI⁺88]

$$\frac{I_{SiO_2}}{I_{Si}} = \frac{n_{SiO_2} \sigma_{SiO_2} \lambda_{SiO_2}}{n_{Si} \sigma_{Si} \lambda_{Si}} \cdot \left(\exp\left(\frac{t}{\lambda_{SiO_2}}\right) - 1 \right) \quad (8.8)$$

with the bulk atom density n , the photo-ionization cross-section σ and the IMFP λ for a SiO₂ over-layer of thickness t .

8.5. Accessing buried interfaces

The sample presented in Sec. 8.1.2 was especially devised to test the spatial resolution, the information depth and the necessary acquisition time of the HAXPEEM method for a structure beneath a cover layer with continuously increasing thickness. Energy filtered photoemission images were acquired on the Au $3d_{5/2}$ core level ($E_{bin} = 2206.5$ eV) and the on Au $4f_{7/2}$ core level ($E_{bin} = 84.0$ eV), both excited with a photon energy of $h\nu = 6550$ eV with an energy resolution of $\Delta(h\nu) \approx 700$ meV.

As it was discussed in Sec. 8.4 for the example of silicon, the two different core levels have different photo-ionization cross-sections σ for this excitation energy (see Sec. 2.1.1) and their different kinetic electron energies $E_{kin,in} = h\nu - E_{bin}$ inside the material result in different IMFPs for travelling through the Au and the Cr-layer (see Fig. 2.6). Additionally, their different kinetic electron energies $E_{kin,vac} = h\nu - E_{bin} - \Phi$ outside the sample result in different angular phase-spaces entering the microscope with maximum *accepted start angles* α_{max} (see Fig. 5.5(b)) and as a consequence in different microscope transmissions (see Fig. 5.8). Finally, also the spatial resolution of the objective lens is a function of $E_{kin,vac}$ (see Fig. 5.15). Fig. 8.11 shows *channeltron spectra* for the two core levels which allow one to compare the initial intensity differences. They were acquired by spatially integrating over the illuminated sample area and mainly reflect the signal from the regions not covered with Cr, because the Au and Si signal from the Cr covered regions is significantly damped by the over-layer. The fit values of the photoemission peaks are compiled in Tab. 8.3. The FWHM of the Gaussian width of the Voigt fit was determined as $FWHM_{gauss} = 1.23$ eV in the Au 4f and Si 2p fit and was used as a fixed value for the Au 3d fit. It represents the *energy resolution* of the setup and corresponds with the values which could be found for the width of the work function edge in Fig. 8.4(e). The energy filter resolution was set to $\Delta E_{ana} = 800$ meV ($E_{pass} = 100$ eV, $w_{slit} = 2.0$ mm) which combined with the resolution of the light-source would lead to a calculated resolution of

$$\Delta E = \sqrt{\Delta(h\nu)^2 + \Delta E_{ana}^2} = 1063 \text{ meV}. \quad (8.9)$$

The reason for the slightly worse experimental value is the big field of view covered in the channeltron mode, which increases the α^2 term in Eq. (3.4).

The area beneath the Au $3d_{5/2}$ and the Au $4f_{7/2}$ peaks differ by a factor of 39.3, the full heights at the peak center by a factor of 15.9. Since the natural broadening w_L of the Au 3d level is bigger than the energy resolution of the setup, not the

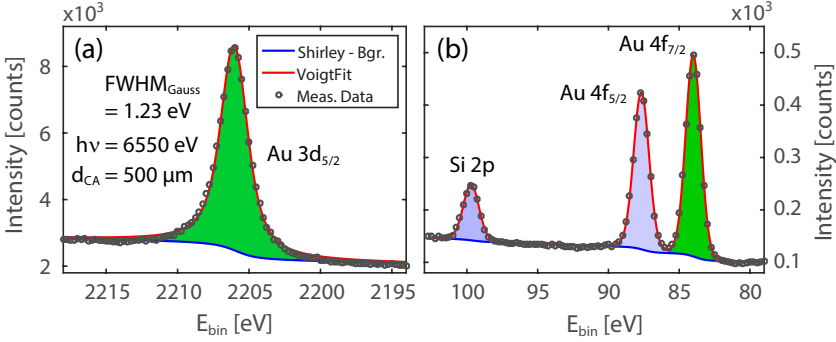


Figure 8.11.: Au $3d_{5/2}$ core level (a) and Au 4f and Si 2p core level spectra (b), excited with a photon energy of $E_{Ph} = 6550$ eV. The spectra were measured in the channeltron mode with different exposure times and normalized for better comparison. The amount of photoelectrons captured from the Au $3d_{5/2}$ is approximately 40 times higher compared to the Au 4f core level and the exposure time for the Au 4f core level has to be massively increased.

full intensity difference of the peaks will determine the count-rate difference in the imaging mode. Thus one needs at least 16 times longer exposure time for an image on the Au $4f_{7/2}$ to reach the same statistics as for the Au $3d_{5/2}$ peak. These values are valid for a contrast aperture diameter of $500 \mu\text{m}$, which was chosen to have a sufficiently high signal level for the imaging mode with a reasonable spatial resolution.

Energy filtered photoemission images on the HAXPEEM test sample are shown in Fig. 8.12 (c,e) as measured and in (d,f) as 3D reconstructions. The thickness of the Cr over-layer was measured with an *atomic force microscope* as shown in (a,b). In the HAXPEEM images it is clearly visible that the strongest signal is measured in the Cr free Au regions and decreases under the increasing cover-layer. Because of the *element-selectivity* of the experiment, the count rate from the Si part of the sample only consists of the *secondary photoemission background* and

	E_{bin} [eV]	w_L [eV]	Area [counts]
Au $4f_{7/2}$	84.00 ± 0.003	0.071 ± 0.019	531 ± 4
Au $4f_{5/2}$	87.67 ± 0.004	0.105 ± 0.020	423 ± 4
Si 2p	99.70 ± 0.01	0.143 ± 0.038	155 ± 3
Au $3d_{5/2}$	2206.04 ± 0.004	1.710 ± 0.013	20851 ± 88

Table 8.3.: Comparison of the peak intensity ratio of Au 4f and Au 3d.

is comparatively low. Because of the generally low count rate of the HAXPEEM approach (≈ 0.012 counts/px/s for the Au 3d measurement) it was possible to use the *single event counting detection* for the data acquisition, which has a more reliable counting statistics (see Sec. 7.1.3). The averaged maximal signal from the Au 3d_{5/2} level is $I_0 = 29.61$ counts/px after 50 min exposure time, the maximal signal from the Au 4f_{7/2} level is $I_0 = 8.21$ counts/px after an 150 min exposure. An 10.8 times longer exposure time would be needed for an image from the Au 4f_{7/2} level to reach a similar count statistic which is slightly less than expected from the channeltron spectra.

The spatially resolved measurements of the Cr wedge thickness dependent photoemission signal in Fig. 8.12 lend themselves to an analysis of both the *information depth* and the *spatial resolution* achievable at buried structures. These investigations will be the subject of the following sections.

8.5.1. EAL determination

As representation² of the *information depth* of the HAXPEEM method, the *effective attenuation length* λ (EAL) of photoelectrons passing through an over-layer of thickness t_{wedge} can be determined from the data shown in Fig. 8.12. Equation (2.11) is used as a fit model in the slightly revised form

$$I(t_{wedge}) = I_0 \cdot \exp\left(\frac{t_{wedge}}{\lambda \cdot \cos(\alpha)}\right) + I_{bg}, \quad (8.10)$$

where I_{bg} is the photoemission secondary background, I_0 the photoemission signal of the chosen core level from the uncovered part of the sample and α the start angle of the excited electron relative to the surface normal. Electrons with larger start angles would travel by a factor $\cos(\alpha)$ longer distances through the cover-layer. In the case of our photoemission microscope the accepted electron emission angles (outside the sample surface) are very low for high kinetic electron energies (see Fig. 5.5(b)). In view of the refraction of electrons at the sample surface, the start angles of the detected electrons inside the solid are even smaller (see Fig. 2.7). Therefore the α dependency in Eq. (8.10) and a variety of additional acceptance angle related effects on the measured photoelectron intensity [JEE87] can be neglected in my evaluation.

The exact height $t_{wedge}(x)$ of the Cr over-layer was determined with an atomic force microscope as shown in Fig. 8.12(a,b). A line profile along the wedge-gradient was measured from the AFM measurement as well as from the photoemission images

²see [JP99] for a definition of the terms connected with information depth in XPS

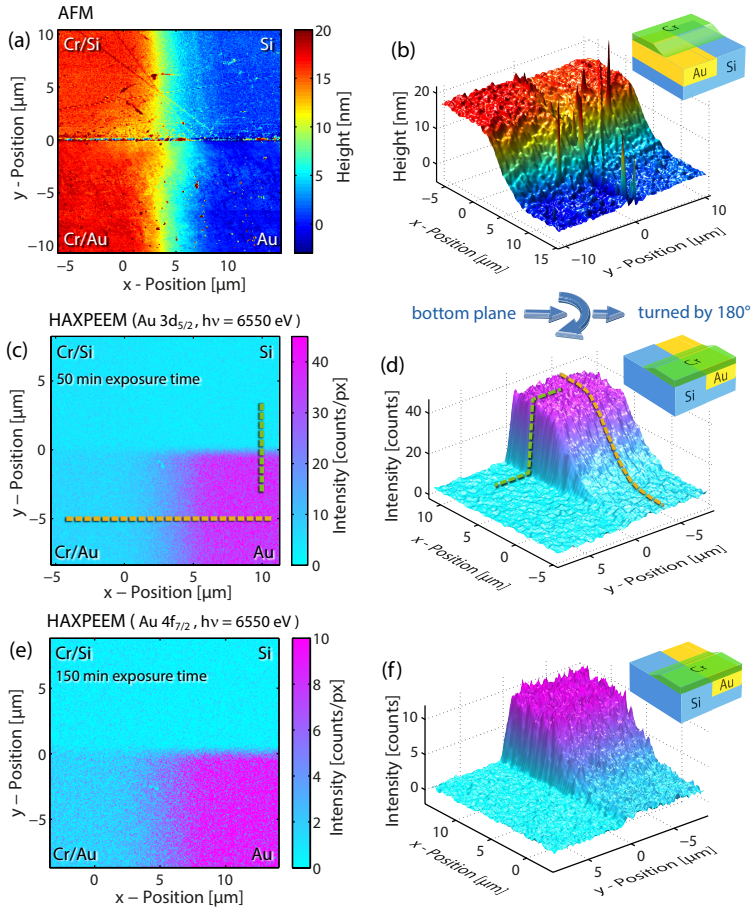


Figure 8.12.: (a) Atomic force microscopy relief of a manufactured wedge sample. The interface between the Au and the Si layer shows up as a thin fissure. Both materials are nearly on the same height level and are homogeneously covered by the Cr-wedge. (b) 3D reconstruction of the AFM data. The spikes indicate polluting particles, probably residuals of the CMP process. They are more prevalent on the Au layer. (c) HAXPEEM image of the wedge on the $Au\ 3d_{5/2}$ peak after 50 min exposure-time. The strong Au signal of the uncovered Au-stripe vanishes under the Cr-wedge. The Si-part gives no significant contribution. (d) 3D reconstruction of the HAXPEEM data. The dashed lines indicate the directions along which profiles were taken for the further evaluations. (e) HAXPEEM image of the wedge on the $Au\ 4f_{7/2}$ peak after 150 min exposure-time and (f) the related 3D reconstruction. The $Au\ 4f_{7/2}$ signal is significantly lower than the $Au\ 3d_{5/2}$ so that much longer exposure times are needed to reach similar statistics. Taken from [PWW⁺14]

(as indicated with the yellow line in Fig. 8.12(c,d)). For a better statistics, the AFM data was averaged over a 6.5 μm wide band and the photoemission data over a 9.7 μm wide band. The resulting profiles in Fig. 8.13a show, how the photoemission signals measured from both core-levels decrease with an increasing wedge thickness. Plotting the photoemission curves against the smoothed wedge height³ (green line in (a)) results in the exponential curves shown in (d). They can directly be fitted with the model in Eq.(8.10).

The challenge in this assignment is that the exact shape of the resulting exponential curve strongly depends on the correct alignment of the wedge-height profiles with the photoemission profiles. A *best fit criterion* was used to find the best alignment, assuming that Eq. 8.10 is indeed the best model for the signal decrease. Therefore the photoemission profiles were first manually aligned with the wedge height profile and the resulting exponential functions were fitted. The fit quality is given by the *root-mean-square error* (RMSE). Systematically shifting the photoemission profiles against the wedge profile along the x-direction leads to the curves shown in (b,c), where the exponential fit-results are plotted as a function of this shift. For both photoemission profiles the RMSE value appears to be a quadratic function of the shift and has a minimum. Additionally the value of the exponential fit-parameter λ is shown as a function of the shift. According to the aforementioned best fit criterion the minimum of the RMSE curve should indicate the best possible agreement of the alignment of the profiles and the exponential model in Eq. 8.10. The corresponding fit-parameter λ was then taken as a result for the EAL of the electrons traveling through the Cr over-layer. As described in Sec. 2.1.3 the EAL in contrast to the IMFP considers elastic scattering of photoelectrons inside the solid. Elastic scattering does not change the kinetic energy of the electrons traveling through the over-layer but increases the effective path-length they travel from their point of excitation to the surface. The measured EAL value is therefore usually smaller than the calculated IMFP value.

The EAL values determined in this way are compiled in Tab. 8.4, together with the corresponding kinetic electron energies inside and outside the solid, the calculated α_{max} -values according to Eq. (5.26), the calculated objective lens transmission according to Eq. (5.40). They are in good agreement with the inelastic mean free path (IMFP) calculated using the modified Bethe equation (2.12) for the related kinetic electron energies and the element specific parameters for Cr given in [TPP11].

³Obvious peaks in the AFM data were neglected in the smoothed curve.

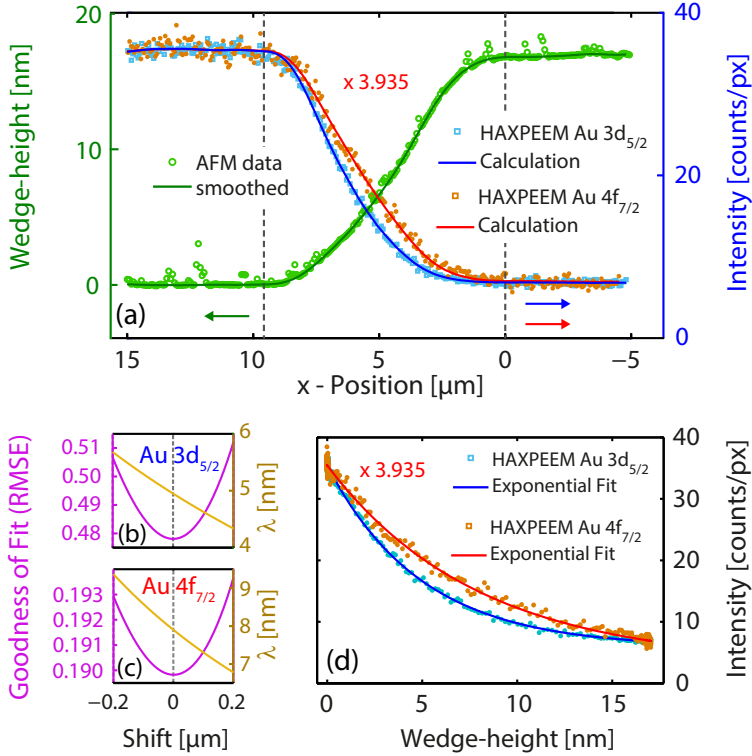


Figure 8.13.: (a) Comparison between the AFM (green dots) profile representing the Cr-wedge and the HAXPEEM (blue and red squares) data for photoelectrons filtered on two different kinetic electron energies. The photoelectron intensities from the $\text{Au } 4f_{7/2}$ core level were multiplied by a factor of 3.935 so that the signal of the not covered Au parts are on the same level for both core levels. The AFM profile was smoothed (green line). The HAXPEEM data at any wedge position was then assigned to the height of the Cr-wedge, resulting in the exponential curves (d). These curves were fitted with Eq. (8.10). Using the parameters of these exponential fits to simulate the HAXPEEM signal as a function of the Cr-wedge thickness, the red and blue solid lines in (a) are obtained, which very well fit to the original HAXPEEM data. In order to find the correct alignment between the AFM and HAXPEEM profiles in (a), they were shifted with respect to each other and the quality of the resulting exponential fit was judged by its RMSE, where the minimum marks the best fit (b,c). The orange curves show the EALs resulting from the exponential fits as a function of the alignment and reveals how sensitive the result of the EAL is on the correct alignment. Taken from [PWW⁺14]

	<i>Au 3d_{5/2}</i>	<i>Au 4f_{7/2}</i>
$E_{kin,in}$ [eV]	4344	6466
$E_{kin,out}$ [eV]	4340.3	6462.3
calc. $\alpha_{max}(E_{kin,out})$ [deg]	2.27	1.96
calc. transm. ($E_{kin,out}$)	$1.57 \cdot 10^{-3}$	$1.17 \cdot 10^{-3}$
I_0 [counts/px]	29.61 ± 0.07	8.21 ± 0.05
I_{bg} [counts/px]	5.84 ± 0.07	0.80 ± 0.06
λ [nm]	4.95 ± 0.05	7.90 ± 0.15
calc. IMFP($E_{kin,in}$) [nm]	5.28	7.35

Table 8.4.: Results of exponential fits shown in Fig. 8.13(d) and related calculations. The calculated α_{max} as well as the related objective lens transmission were calculated with Eq. (5.26) and (5.40), the IMFP was calculated according to [TPP11]. The kinetic electron energy outside the crystal was calculated as $E_{kin,out} = E_{kin,in} - \Phi$ with $\Phi = 3.7$ eV as it was determined in Sec. 8.2 for the Cr covered Au region.

With the fit-parameters in Tab. 8.4, the model in Eq.8.10 and the smoothed wedge profile in Fig. 8.13(a) (green line) it should be possible to reproduce the measured photoemission intensities along the wedge (red and blue squares). The profiles which were calculated in such a manner are plotted as (red and blue) lines into the same graph and indeed reproduce the measured data very well. This indicates that the profile alignment with the *best fit criterion* worked correctly.

This way of determining the EAL for a certain kinetic electron energy and a specific material is in literature commonly referred to as *overlayer film method*. The uncertainties of this method are discussed in [PJ99b] and include uncertainties in the film-growth and the measurement of the film-thickness, angular anisotropies in the electron transport, atomic reconstruction and intermixing at the substrate/overlayer interface, a lack of film uniformity, and effects of surface excitations. Some of those effects may be even a function of the film thickness [JEE86] under certain experimental geometries which as a consequence would lead to deviations from an exponential dependence of the photoemission intensity on the overlayer thickness [JE88]. By combining the hard x-ray photoemission microscopy approach with the thickness determination via AFM it is possible to analyze the photoemission signal as a function of a continuously increasing over-layer thickness. This at least ensures homogenous film growth and measurement conditions for the whole dataset, which would be hard to reach with conventional photoemission spectroscopy using a batch of samples with different film thicknesses. Note that the use of the *single event counting* approach

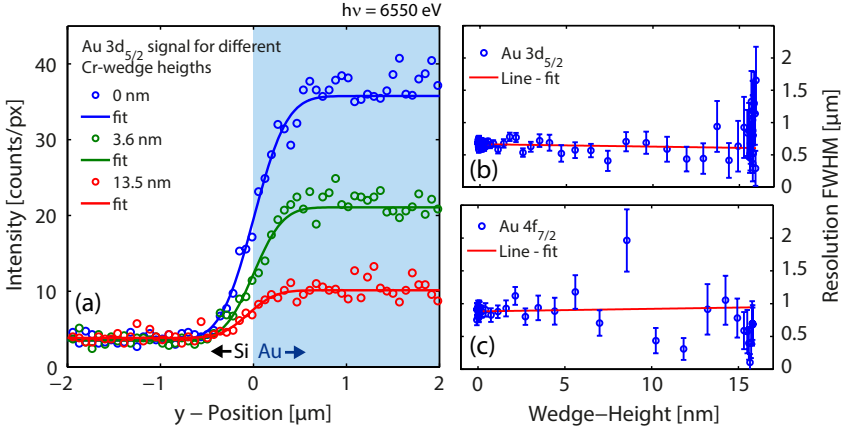


Figure 8.14: (a) Profiles extracted from the HAXPEEM data in Fig. 8.13(c) with different cover thicknesses are fitted to determine the resolution as a function of the cover layer thickness. The results for the $\text{Au } 3d_{5/2}$ core level are shown in (b) and for the $\text{Au } 4f_{7/2}$ core level in (c). The Au 4f measurements suffer from worse statistic. Nevertheless, both measurements do not show a clear dependence of the spatial resolution with the thickness of the cover layer. Taken from [PWW⁺14].

(see Sec. 7.1.3) is advantageous for this kind of evaluation, because of its more reliable electron counting statistic and because it avoids many instrumental artifacts which would affect the intensity distribution in the image.

8.5.2. Lateral Resolution and Probing Depth

After finding the correct alignment between the AFM measurement and the energy filtered photoemission images in the previous Sec. 8.5.1, it is possible to analyze the *spatial resolution* of the Au/Si interface as a function of the overlayer-thickness and for different kinetic electron energies. The calculations in Sec. 5.4 predict a slightly increasing resolution limit for higher kinetic electron energies which in the case of a CA with $500 \mu\text{m}$ diameter (see Fig. 5.15(c)) would lead to a better resolution for the Au $3d_{5/2}$ measurement ($E_{kin,out} = 4340 \text{ eV}$) compared to the Au $4f_{7/2}$ measurement ($E_{kin,out} = 6462 \text{ eV}$) by a factor of 0.85. On the other hand it was shown that thick metallic over-layers should not significantly smear out the spatial information carried by fast electrons from structures underneath, as long as not too many elastic scattering events with large scattering angles come into play [KIK⁺07].

The AFM measurement in Fig. 8.12(a,b) shows that the Au and Si layers of the

sample are on the same height. The small fissure between them was measured to have a width of FWHM=155 nm, which is far below the calculated resolution limits for a CA of 500 μm . Profiles of the photoemission data over the Au/Si interface (perpendicular to the wedge direction, green curve in Fig. 8.12(d)) were extracted from the HAXPEEM images for different wedge heights as shown in Fig. 8.14(a). Even beneath a Cr cover layer of 13.5 nm the signal-to-noise ratio is good enough to detect the chemical contrast between the Au and the Si layer. The extracted profiles were fitted with a Gauss/Step convolution (see appendix A.1) of the form

$$I(y) = \left(\frac{I_0}{2} \cdot \left(1 + \operatorname{erf} \left(\frac{y - y_1}{\sqrt{2} \cdot \sigma} \right) \right) + I_{bg} \right), \quad (8.11)$$

where $\text{FWHM}_{\text{gauss}} = 2 \sqrt{\ln(2)} \cdot \sigma$ is the lateral resolution determined from the profile (equal to Sec. 7.3.1).

The fitted spatial resolution as a function of the over-layer thickness for the photoelectrons excited from the Au $3d_{5/2}$ and the Au $4f_{7/2}$ core level is shown in Fig.8.14(b,c). To achieve a suitable signal-to-noise ratio for the fit, the profiles had to be integrated over a certain distance in the direction of the wedge gradient, which is noted in Tab. 8.5. This worked fine for the Au $3d_{5/2}$ measurement. Although the error-bars are increasing with an increasing over-layer thickness due to a worse signal-to-noise ratio, the fitted resolution value stays on one level. The fits of the Au $4f_{7/2}$ measurements were more problematic between a wedge thickness of 5 nm and 12 nm. The signal-integration along the strong slope of the wedge in combination with a worse initial signal-to-noise ratio restrained the accuracy of the fit-procedure. The results of the resolution fits ρ_s were again fitted with the linear model

$$\rho_s = a \cdot t_{\text{wedge}} + \rho_{\text{abs}} \quad (8.12)$$

and the data points were weighted according to their error σ with σ^2 . These fit results are also compiled in Tab.8.5. Indeed, the slope a of these fits is close to zero (within the fit-error) which means that no dependence of the spatial resolution from the over-layer thickness could be found in our experiment which fits to the conclusions provided in [KIK⁺07]. Nevertheless, the absolute resolution of the measurement, which is represented by the fit-parameter ρ_{abs} is not good enough to exclude any such effect. The issue should be revisited with an improved lateral resolution experiment, as soon as a higher light flux allows to measure with smaller contrast apertures in adequate time scales. The absolute resolution is better for the Au $3d_{5/2}$ measurement than for the Au $4f_{7/2}$, as it was expected from the calculations for the different kinetic electron energies involved.

	<i>Au 3d_{5/2}</i>	<i>Au 4f_{7/2}</i>
$E_{kin,out}$ [eV]	4340.3	6462.3
wedge-length [μm]	9.58	9.58
Integration-length [nm]	413	521
a	-4.39 ± 4.06	3.89 ± 14.98
ϱ_{abs} [nm]	673 ± 9	882 ± 19
calc. resolution limit [nm]	1433	1690

Table 8.5.: Results of line fits to the resolution measurements shown in Fig. 8.14

8.6. Conclusions

The feasibility of energy-filtered photoemission microscopy with high kinetic electron energies was explored in this chapter. It was shown that thanks to the larger IMFPs of the high kinetic electrons an investigation of chemically different regions is possible through a 15 nm thick cover layer. The measured spatial resolution for the high kinetic energies with a CA of 500 μm was even better than predicted by the calculations in Sec. 5.4 and is not influenced by the over-layer thickness. It is expected that a decrease of the contrast aperture diameter will further improve the spatial resolution until the same effects as noted in Sec. 7.3.1 come into play, which limit the spatial resolution in the energy-filtered imaging to a FWHM of 150 nm so far. The next smaller CA of 150 μm diameter at the same time decreases the transmission by a factor of 11. It would take an exposure time of 9 hours instead of 50 min to acquire the HAXPEEM image shown in Fig. 8.12(c) with this CA with the same count statistics. It is obvious from Fig. 8.14 that a count statistic below 10 - 20 counts/px (in the single event counting mode) is not desirable, if a chemical contrast between different elements should be identified. This already determines a lower limit for an exposure time for a chosen experimental setting.

An optimized count-rate therefore is a crucial issue for future HAXPEEM experiments and the investigations in this thesis point to a couple of departure points for improvement:

- The important parameters to increase the transmission of the objective lens are presented in Eq. (5.40). Besides a bigger *contrast aperture* (which at the same time worsens the spatial resolution) also an increased extractor voltage V_{ext} with an accordingly raised column potential V_{col} (keeping $V_{ext}/V_{col} = 12$) increases the *transmission*, since the transmission is directly proportional to

V_{col} . This way the immersion lens would be able to gather a higher angular phase space of high kinetic photoelectrons starting at the sample (see Fig. 5.3) without changing the angular phase space inside the microscope. The *spherical aberrations* of the microscope are not increased this way and the spatial resolution is not affected.

- A higher electron flux can be reached with a higher *photon flux* on the sample. The *beam-spot diameter* used at the P09 beamline at DESY was focused to a FWHM of approximately 300 μm (see Fig. 8.6). Since the flux increases inversely proportional to the square of the diameter, a stronger focusing would improve the electron yield massively. At the same time increased secondary electron flux does not disturb the imaging of high kinetic electrons as it was shown in Sec. 8.3.
- The photoelectron yield from a core level heavily depends on its *photo-ionization cross section*. It is worth to optimize the photon energy with respect to the cross-section of the core-level under investigation and with respect to the kinetic electron energy needed to have a high enough IMFP to pass e.g. an over-layer. Different stoichiometries of a compound can be detected via the *chemical shift* of a core level. In Sec. 8.4 it was shown on the example of SiO_2 that these shifts can also be detected in more strongly bound core levels, which usually have a higher cross section for hard x-ray radiation.

Nevertheless, the low angle-acceptance of the microscope is advantageous for the microscopic EAL determination. Angle-dependent effects can be neglected and mainly electrons which are crossing the cover layer parallel to the surface normal are detected. The measured results for the EAL of these electrons are in good agreement with the calculated IMFPs according to [TPP11]. This also proves the applicability of the method for reliable quantitative analysis in connection with the *single event counting* detection.

9. Outlook: Towards time-resolved device analysis

In the previous chapters it was shown that energy-filtered photoemission microscopy is a great tool for spatially resolved chemical analysis. In combination with hard x-ray excitation, it is even possible to access buried layers. This approach is perfectly suited for the analysis of future electronic devices, which work with an active layer covered by a metallic electrode. A typical system is, for example, SrTiO₃ (STO) which is investigated in the context of resistive non-volatile memory cells with a high storage density. By applying a voltage to this *perovskite oxide*, oxygen vacancies are introduced into the material which act as n-dopants. Such an oxygen vacancy creates two free electrons which are transferred to the Ti conduction band. The regions of the crystal where these oxygen vacancies are introduced therefore become more conductive. The Ti atoms in those regions change their valence state from Ti⁴⁺ to Ti³⁺.

While the change in resistivity can be probed by small voltage pulses, stronger applied fields can control the diffusion of the vacancies and thus switch the resistivity of material between a high and a low-resistive state. This *resistive switching* process is the basis for a memory cell. A typical metal-insulator-metal (MIM) structure of such a cell is shown in Fig. 9.1(b) consisting of two electrodes and the active resistive switching layer in between. Microscopic photoemission analysis with soft x-rays on such structures were so far successful on structures, where the top electrode was melted away during the forming process, so that the active layer could be analyzed by x-ray absorption microscopy [LPM⁺14]. Local changes in the Ti L₃ edge could be attributed to Ti³⁺ and Ti⁴⁺ states. Another approach is to mechanically remove the electrode after the switching process [LKS⁺15].

A comprehensive study nevertheless would also include the investigation of dynamic processes of such a switching element. This requires a *time-resolved in operando* measurement of an intact device, which would be in principal possible with the setup shown in Fig. 9.1(b).

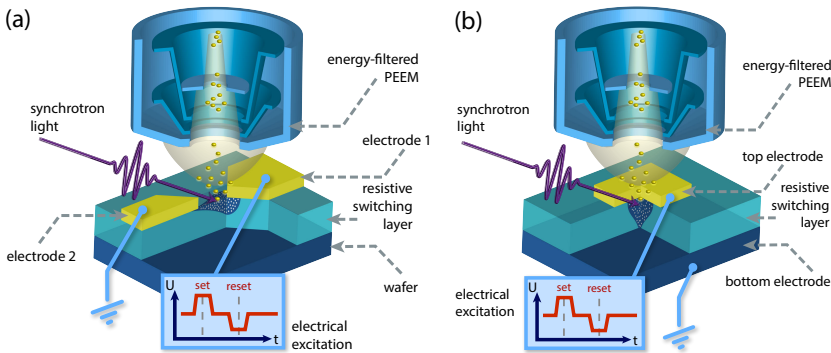


Figure 9.1.: Switching geometries for the time-resolved experiments. (a) in-plane geometry, (b) vertical geometry.

9.1. First HAXPEEM results on STO

Spectral fingerprints of switched Fe-doped STO cells could be identified with surface sensitive XAS measurements using a soft x-ray synchrotron excitation. Figure 9.2 shows the aforementioned example with changes in the Ti L_3 edge. Similar results were visible in the Fe L_3 edge. The same sample was then measured with the HAXPEEM approach. Due to a limited measurement time we were only able to acquire an image spectrum from a core level with a comparatively strong signal, which was the Sr $2p_{5/2}$ level. The results are shown in Fig. 9.3. The area with the red circle marks the needle scratch shown in the SEM image in Fig. 9.2(a), whereas the black circle marks the switching crater. These areas were compared with the STO region below the undestroyed electrode (blue) and the STO region outside the electrode (green).

Slight energy shifts are already visible in the corresponding spectra in Fig. 9.3(b). But for a reliable analysis which is comparable to the XAS measurements, HAXPEEM measurements with a higher magnification will have to be performed in the future. Also the Ti core levels will probably show bigger chemical shifts between the less and stronger oxidized states. All of this requires measurements with higher count-rates or longer exposure times. The studies in this thesis helped to understand, which parameters can be optimized for upcoming experiments. The first step will probably be to improve the focusing of the beamline to increase the photon flux. Also an increase of the extractor voltage will lead to a higher microscope transmission.

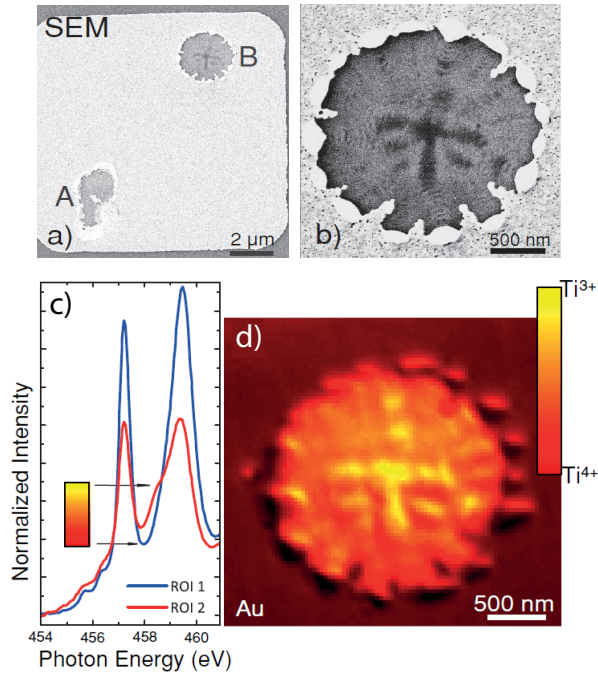


Figure 9.2.: (a) SEM image of the Au electrode of a switched STO-cell. The contact point of the needle is marked with (A), the forming crater is marked with (B). In (b) a higher magnified SEM image of the forming crater is shown. This crater was analyzed with x-ray absorption microscopy. Spectra of the crystal field split Ti L₃ edge are shown in (c) for two different region of interest, which is the dark cross structure in (b) as ROI 2 and the rim around it as ROI 1. In ROI 2 a shoulder is visible which belongs to Ti³⁺ instead of the expected Ti⁴⁺ in STO. It belongs to reduced sample regions, where oxygen vacancies were formed. After such a spectral fingerprint was identified, a map could be created (d), which shows in which sample regions the filament forming took place. Taken from [LPM⁺14]

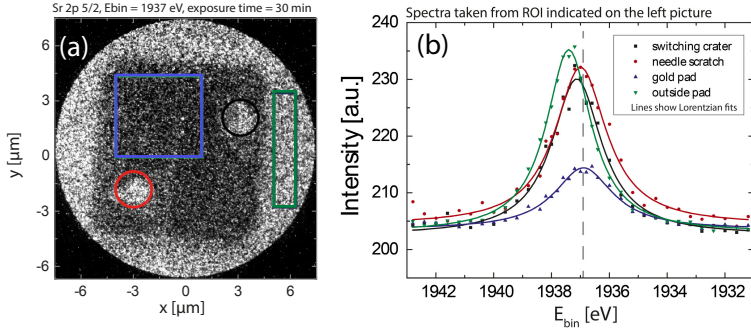


Figure 9.3.: Excited by the high photon energy, the Sr 2p core level electrons have a high kinetic energy of $h\nu = 4560$ eV which increases their IMFP and makes it possible to pass through the top electrode. Chemical changes which could be identified via XAS measurements (see Fig. 9.2) were also examined via HAXPEEM. Each image in the stack was measured for 30 min. In (a) the image on the peak of the Sr $2p_{5/2}$ level is shown. Extracted spectra for different regions of interest are shown in (b). The statistic and the spatial resolution will have to be increased in the future, to achieve a clear understanding of the chemical changes which happen in the bulk region of the sample.

9.2. Towards time resolved studies

The time structure of a synchrotron (see Sec. 3.2.2) allows time resolutions down to 10 ps [NGK⁺13] which may be short enough for a study of the rather slow vacancy movements. A voltage source must be synchronized with the probe pulse of the synchrotron and switches between a *set* and *reset* state forth and back. By shifting the time-delay between the *electrical pump* and the *optical probe* pulse, each time step of the switching process could be analyzed. Via *HAXPEEM*, the changes in the active layer could be imaged directly through the electrode. An alternative concept is an in-plane geometry as it is shown in Fig. 9.1(a), where the switching would take place along the surface of the active layer between two top-electrodes. This kind of structure could be also studied via soft x-rays, because no large IMFPs are needed this way.

The feasibility of time-resolved studies with the *NanoESCA* was already proven at the synchrotron *Elettra*. The schematic setup is shown in Fig. 9.5. Since the 2 ns gaps between the standard electron bunches in a synchrotron are too short, to analyze an adequate time-range, the 100 ns dark gaps between the pulse trains are filled with a single intense bunch. The photoelectrons excited by this single-

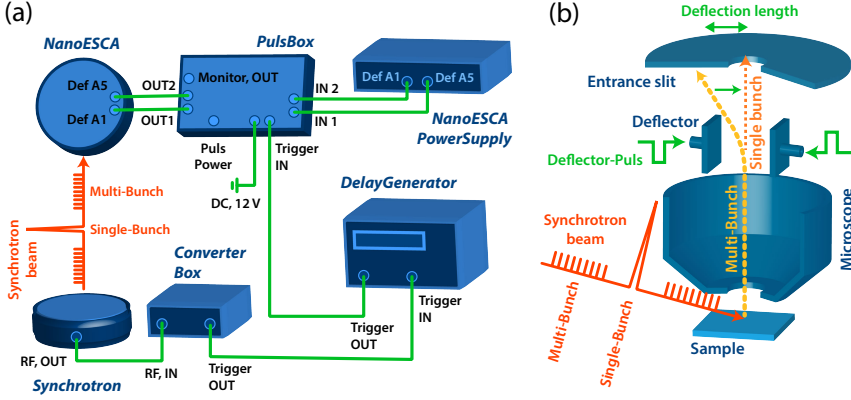


Figure 9.4.: The beam-pattern of the synchrotron consists of a light-intense multi-bunch and a dark-gap with a single bunch. The single bunch has a time resolution of several 100 ps. The synchrotron's trigger-signal of the single-bunch is transported to the PEEM via a complex electronic system including a delay-generator (a). This trigger is used to sort out photo-electrons excited by the multi-bunch by using the deflector inside the PEEM (b).

bunch are separated from the signals of the multi-bunches inside the *NanoESCA* with a deflector gating mechanism, as it is shown in (b). The deflector in front of the analyzer is set to a standard bias, which deflects the electrons away from the entrance slit. An electrical pulse is applied to the deflector only, if electrons from the single bunch are passing the deflector. The electrical pulse neutralizes the deflector bias and lets the electrons pass the entrance slit into the analyzer. This process can be made directly visible in the *NanoESCA*. The projective lenses behind the analyzer can be adjusted such that the analyzer entrance slit is projected onto the detector. In Fig. 9.5 (a), we can see the bright beam-spot excited by the multi-bunches, and the single-bunch, which is deflected away from the multi-bunch signal. The trace around the single bunch is due to the fact that the dark gap was not completely dark, but still filled with a low intensity of multi-bunches. By analyzing this trace as a function of delay time, the time structure in (b) could be deduced. One sees the single bunch inside a 100 ns wide (not really empty) dark-gap, and the intensity rise of the surrounding multi-bunches on both sides.

From the distance of the 2 ns separated multi-bunches, the deflection velocity of the gating was determined. The profile along the flight direction was then evaluated to estimate a light pulse duration of the single bunch of $\Delta t = 261.9$ ps, which should be rather seen as an upper limit. The real pulse width at Elettra is expected to be

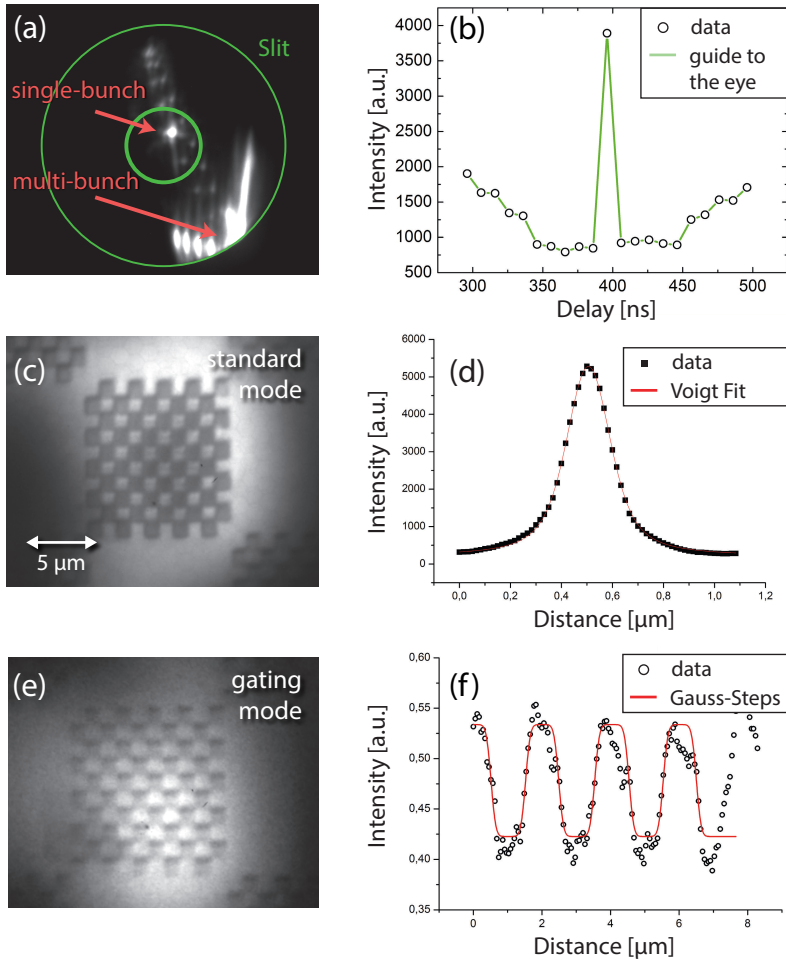


Figure 9.5.: On the image-plane of the analyzer entrance slit the single bunch can be separated from the multi-bunch (a). The bunch-pattern of the ring could be measured with a time-resolved experiment (b). An analysis of the velocity and broadening of the single bunch (d) leads to a time resolution of $\Delta t=261.9$ ps. An EF-PEEM image of a checkerboard-sample was taken without (c) and with (e) using the gating mechanism. The measured spatial resolution of the gated image (f) is FWHM=259 nm and only slightly bigger than for the non-gated image (233 nm).

below 100 ps. The most important test was finally, if the imaging would work with the gating mechanism. The deflector is set such, that only the deflected single bunch can pass the entrance slit. Therefore, the slit size was reduced compared to (a). Fig. (c) and (e) compare images of a Chessy patterned sample, measured with and without gating. A subsequent analysis of the resolution of the structure showed that the images measured with the deflection was only slightly blurred (FWHM=259 nm) as compared to the image without deflection (233 nm). This proves that the time-resolved deflection gating works well.

10. Summary

The scope of this thesis was to give a comprehensive analysis of the possibilities offered by a state-of-the-art photoemission microscope combined with an imaging energy-filter. The real-space as well as the momentum microscopy are powerful tools to study the chemical and electronic structure of material systems, compounds and complete devices. This information is needed, since the future of information technology will be dominated by more complicated physical and chemical effects than it is the case today.

One example for such material systems is strontium titanate (STO), which is used to build non-volatile resistive memory cells. These *memristors* are also potential candidates for improving actual microprocessors with “brain-like” abilities. This work showed, how such devices in general can be analyzed. First results could be achieved with a combination of photoemission microscopes and synchrotron radiation in spatially resolved absorption scans, showing that the reduced areas of the sample can be identified due to a change in Ti or Fe L edges. This reduction is exactly the fingerprint of the expected filaments build from oxygen vacancies, which cause the resistivity changes in a cell. An energy resolution of several 100 meV, which can be provided by the presented microscopes or beamlines, is sufficient for detecting such chemical shifts. A spatial resolution of below 100 nm, which will be needed to resolve single filaments, is more demanding. Dedicated tests showed that the *NanoESCA* instrument with its optimized energy filter in combination with soft x-ray beamlines reached at least 150 nm. According to the presented calculations of the objective lens system, taking into account aberration and diffraction effects, these microscopes nevertheless should reach resolutions better than 10 nm. In contrast, even the best results of instruments with involved aberration correctors did not exceed 34 nm at synchrotron beamlines. A general problem probably lies in space charge effects and upcoming studies will have to show, if this physical limit can be circumvented. In the case of the *NanoESCA* the origin of the actual resolution limit still needs to be found. The analysis of the double-hemispherical energy analyzer rises the question, if spatial resolution is not lost due to aberrations in the transfer-lens system between

the hemispheres.

The energy resolution increases with the reduction of the pass energy of the energy filter and its exit-slit width and even seems to be better than predicted by the calculations. Theoretically, the pass energy can be even reduced, until the increasing scale of the electron trajectories in the filter are disturbed by the inner rim of the analyzer. In addition the exit-slit diameter can be reduced as well as long as no diffraction effects come into play. The approximations of the electron trajectories in the energy filter are helpful for an understanding of these limits.

More problematic is the issue of non-isochromaticity, which is an inherent feature of the current analyzer design. It has a direct impact on the energy filtered imaging since different image pixels represent different filter-energies. The knowledge of these energy shifts is crucial if a spectral change for different regions of a specimen should be analyzed. Therefore, in general, each image-spectrum has to be corrected. The best way to do this is to measure a two-dimensional energy-shift map for each instrumental setting with a work function analysis and to use it for the correction of the complete image spectrum. Systematic measurements in combination with trajectory calculations in this thesis identified the main instrumental parameters which influence the energy shift. Even a simplified fit-model could be developed, which will in many cases be sufficient to analyze and correct the intensity shift in a single picture, caused by the non-isochromaticity.

While some corrections can be easily applied after a measurement, the situation is more complicated, if an experimental setup actually relies on a monochromatic energy image behind the analyzer. This is, for example, the case for an imaging spin filter. It is based on a spin-dependent reflectivity of suitable crystals (W, Au/Ir) at a specific, well-defined scatter energy. Energetic inhomogeneities in an image will cause inhomogeneities in the spin-analysis which are difficult to correct. In this case it is necessary to use instrumental settings with a minimized non-isochromaticity, which is most effectively reached with a low pass energy.

Low pass energies on the other hand reduce the transmission of the microscope and are not recommended, if the energy resolution of the light source is anyway limited and a high transmission is essential for an acceptable count-rate for imaging. This is the case for energy-filtered photoemission with hard x-ray excitation. Due to low photo-ionization cross-sections and a low acceptance angle of the objective lens for high kinetic electrons the transmission is heavily reduced. The instrumental settings have to be optimized for the best possible transmission - possibly by increasing the energy resolution of the beamline and of the energy filter. The latter leads to

higher non-isochromaticities.

Despite the transmission problem, the HAXPEEM approach is promising. The determined information depths through a Cr cover layer agreed with the predictions of theoretical IMFP calculations. An EAL of 7 nm was determined for electrons excited from an Au 3d core level by photons with an energy of $h\nu = 6500$ eV. This is enough to study materials through realistic electrodes of resistive switching devices. A spatial resolution of around 500 nm was reached with a large contrast aperture (CA) of 500 μm diameter, which is a better value than predicted by calculations. The use of a contrast aperture of 150 μm diameter should make resolutions in the 100 nm regime possible but reduces the transmission by a factor 10. In the future, it might be even economic to introduce a CA between 500 μm and 150 μm to reach the best compromise between spatial resolution and transmission for a HAXPEEM measurement. A higher count-rate can in general be reached with changes in the experimental setup. According to the calculations, an even higher extractor voltage is necessary to increase the acceptance angle of the objective lens for high kinetic electrons and therefore the transmission. A stronger focusing of the synchrotron beam onto the sample is a second possibility. Consequently, the transmission problem can be circumvented to some extent in the future.

The limit will be again defined by space charge effects. In our measurements we already experienced a high increase of secondary electrons caused by the longer IMFPs and the increased number on inelastic scattering events. These high electron densities already caused significant image blurs due to space charge effects. For imaging with such secondary electrons the detected space charge effects had to be reduced by a reduction of the light intensity as well as by closing the CA. Since both approaches influenced the image blur in the same way, the space charges can be related to trajectory crossings inside the microscope rather than to effects directly above the sample. However, the secondary electrons did not seem to influence high energetic electrons. This allows the prediction that the light intensity for HAXPEEM experiments can indeed be raised, until at some point the limiting space charge effect directly above the sample surface play a dominant role.

A. Often used equations

In this section I summarize some equations and functions, which are often used throughout this thesis. The general nature of the equations is explained here, special implementations are described inside the corresponding chapters.

A.1. Gauss/Step-Function

The function which is referred to as *Heaviside/Step-function* throughout this thesis describes a convolution of a sharp edge at a position $x = 0$, represented by a Heaviside step-function

$$H(x) = \begin{cases} 0 & \text{for } x < 0 \\ 1 & \text{for } x \geq 0 \end{cases} \quad (\text{A.1})$$

and a *Gaussian* function

$$G(x) = \frac{1}{\sqrt{2\pi}\sigma} \cdot \exp\left(-\frac{1}{2} \cdot \frac{x^2}{\sigma^2}\right) \quad (\text{A.2})$$

with the standard deviation σ , representing the (spatial or energy) resolution of the microscope. The convolution of a step (height I_0 at a position $x = b$) with a Gaussian function (standard deviation σ) can be calculated as

$$C(x) = I_0 \int_{-\infty}^{\infty} H(t - b) \cdot G(x - t) dt \quad (\text{A.3})$$

$$= \frac{I_0}{2} \left(\operatorname{erf}\left(\frac{x - b}{\sqrt{2}\sigma}\right) + 1 \right). \quad (\text{A.4})$$

The result is a special form of the *error* function. All three functions are plotted in Fig. A.1 for the exemplary case ($I_0 = 1, \sigma = 0.5, b = 5$).

A.2. Spatial Calibration

In microscopy it is often necessary to determine the calibration of an image. The data acquired by the fast acquisition camera (see Sec. 7.1) is saved in the dimension

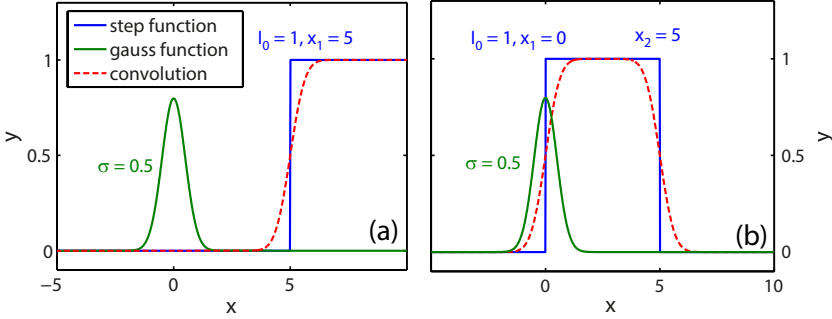


Figure A.1.: The convolution of a *Gaussian* profile and a *Heaviside* step-function results in a special *Error* function (see text), which can be used to analyze spatial- or energy resolved PEEM-data. The convolution works with a single step (a) or with multiple steps (b). The latter is often used to calibrate the spatial dimensions of a PEEM image with a known structure.

image-pixel without a reference to realistic dimensions (of spatial or momentum nature). The spatial calibration can be done with the help of a known test sample (see Fig. 7.3.1) with precisely structured patterns. Knowing the distance $d_{\mu m}$ between a start-point and an end-point of the structure, we take an image of this structure and extract a profile of the photoemission signal along this structure. The well-defined start-point ($x = b_1$) and end-point ($x = b_2$) of the structure can be described by Heaviside functions. If we convolve that with a Gaussian function we get equivalent to (A.4) the equation

$$I(x) = C_{niso}(x) \cdot \left(I_0 \int_{-\infty}^{\infty} (H(t - b_1) - H(t - b_2)) \cdot G(x - t) dt + I_{bg} \right) \quad (\text{A.5})$$

$$= C_{niso}(x) \cdot \left(\frac{I_0}{2} \left(\operatorname{erf} \left(\frac{x - b_1}{\sqrt{2} \sigma} \right) - \operatorname{erf} \left(\frac{x - b_2}{\sqrt{2} \sigma} \right) \right) + I_{bg} \right). \quad (\text{A.6})$$

An exemplary plot for this function is shown in Fig. A.1(b). Note, that we keep the same resolution σ for both edges. The fitted distance in image-pixel $d_{pix} = \operatorname{abs}(b_2 - b_1)$ together with the known structure dimension $d_{\mu m}$ let us calculate a calibration factor for the PEEM image

$$c_{calib} = \frac{d_{\mu m}}{d_{pix}}. \quad (\text{A.7})$$

The function $C_{niso}(x)$ in Eq. (A.6) describes a superimposition of the intensity-profiles by a broad Gaussian function, which can derive from the *isochromaticity* of the energy-filter, as it is described by Eq. (6.26). The intensity distribution of the beam-spot has also be taken into account, if the spot diameter is in the order of the microscope's field of view.

Finally, we can evaluate the spatial resolution of the actual microscope setting from an image-profile fitted with Eq. (A.6). As mentioned earlier, the resolution is described by the standard deviation σ of the Gaussian. Throughout this thesis, I use the full-width half-maximum (FWHM)

$$FWHM = 2 \sqrt{\ln(2)} \cdot 2 \cdot \sigma \approx 2.3548 \cdot \sigma \quad (\text{A.8})$$

of the Gaussian function to describe the spatial resolution.

A.3. Spectral fits with a Voigt profile

The *Voigt profile* is the convolution of the Gaussian profile in Eq. (A.2) and a *Lorentz profile*

$$L(x) = \frac{\gamma}{\pi \cdot (x^2 + \gamma^2)} \quad (\text{A.9})$$

where γ is the scale parameter of the profile and in spectroscopy is often associated with the life-time of an excited state. Due to the uncertainty principle, a state with a short life time will have a large uncertainty in its spectral emission (big γ) and vice versa. The FWHM of the profile is given by $2 \cdot \gamma$. Since no analytic form of the convolution exists, the integral form needs to be used in a fit.

$$V(x, \gamma, \sigma) = \int_{-\infty}^{\infty} L(t, \gamma) \cdot G(x - t, \sigma) dt \quad (\text{A.10})$$

$$= \frac{\gamma}{\sqrt{2} \pi^{3/2} \cdot \sigma} \cdot \int_{-\infty}^{\infty} \frac{\exp\left(-\frac{1}{2} \frac{(x-t)^2}{\sigma^2}\right)}{t^2 + \gamma^2} dt \quad (\text{A.11})$$

$$(\text{A.12})$$

If for some reason an analytic form is needed, a *Pseudo Voigt* profile can be used as an approximation, which is a linear combination of the Gauss- and Lorentz profile. The Voigt profile was used in all spectral fits in this thesis, see Fig. 8.11 for an example.

A.4. Energy resolution with a Fermi/Gauss convolution

The *Fermi* edge of a photoemission spectrum is described by the temperature dependent Fermi function convoluted with a Gaussian profile which describes additional broadenings (bandwidth of the excitation source, resolution of the energy analyzer).

Again, no analytic form exists and the integral form must be used in a fit. The Fermi function can be written as

$$F(x) = \frac{1}{\exp\left(\frac{x-E_F}{k_B \cdot T}\right) + 1} \quad (\text{A.13})$$

where T is the temperature, k_B the Boltzmann constant and E_F the Fermi energy level. The integral form of the convolution is

$$F_g(x, \sigma, T) = \int_{-\infty}^{\infty} F(t, \gamma) \cdot G(x - t, \sigma) dt \quad (\text{A.14})$$

$$= \frac{1}{\sqrt{2\pi} \cdot \sigma} \cdot \int_{-\infty}^{\infty} \frac{\exp\left(-\frac{1}{2} \cdot \frac{(x-t)^2}{\sigma^2}\right)}{\exp\left(\frac{t-E_F}{k_B \cdot T}\right) + 1} dt \quad (\text{A.15})$$

An example for the use of this function is shown in Fig. 7.11(a).

B. Complementary objective lens calculations

The results in section 5.1 are directly derived from the initial calculations of the photoelectron trajectories, which travel from the sample to the extractor lens. Nevertheless, alternative approaches are possible to calculate the relation between the electron start angle on the sample and the entrance angle into the microscope as well as the value of the immersion lens acceptance angle. For completeness, the alternative approaches are presented here, to support the results presented in section 5.1.

B.1. Conversion between start angle and entrance angle

As it is deduced in Sec. 5.1.2, the angle conversion from the photoelectron start angle α on the sample to its angle α' at the extractor entrance is given by Eq. (5.12) as

$$\tan(\alpha) = \left(\frac{V_0}{V_0 + V_{ext} - V_{spl}} \cdot \underbrace{\left(1 + \frac{1}{\tan^2(\alpha')} \right)}_{= \frac{1}{\sin^2(\alpha')}} - 1 \right)^{-1/2}. \quad (\text{B.1})$$

An alternative approach to calculate this conversion uses the fact that the velocity component of the photoelectron parallel to the sample remains unchanged during the acceleration in the extractor field of the immersion lens: $v_{0,r} = v_{1,r}$ (see Fig. 5.2) and thus we can write

$$\sin(\alpha) \cdot v_0 = \sin(\alpha') \cdot v_1, \quad (\text{B.2})$$

where v_0 is the norm of the velocity vector of the photoelectron leaving the sample

$$\frac{1}{2} m v_0^2 = e \cdot V_0 \quad (\text{B.3})$$

and v_1 is the norm of the velocity vector of the accelerated photoelectron when reaching the extractor entrance

$$\frac{1}{2} m v_1^2 = e \cdot V_0 + e \cdot (V_{ext} - V_{spl}). \quad (\text{B.4})$$

Combining the last three equations gives a simpler expression for the angle conversion than Eq. (B.1):

$$\sin(\alpha) = \sin(\alpha') \cdot \left(\frac{V_0 + V_{ext} - V_{spl}}{V_0} \right)^{1/2}. \quad (\text{B.5})$$

To show that both solutions are identical, we insert Eq. B.1 into the left side of Eq. B.5 and get:

$$\sin(\alpha) = \sin \left(\arctan \left(\left(\frac{A}{\sin^2(\alpha')} - 1 \right)^{-1/2} \right) \right) \text{ using } A = \frac{V_0}{V_0 + V_{ext} - V_{spl}} \quad (\text{B.6})$$

since $\sin(\arctan(\xi)) = \frac{\xi}{\sqrt{1+\xi^2}}$ we can write this as:

$$\sin(\alpha) = \frac{\sqrt{\left(\frac{A}{\sin^2(\alpha')} - 1 \right)^{-1}}}{\sqrt{1 + \left(\frac{A}{\sin^2(\alpha')} - 1 \right)^{-1}}} = \frac{1}{\sqrt{\frac{A}{\sin^2(\alpha')} - 1 + 1}} = A^{-1/2} \cdot \sin(\alpha') \quad (\text{B.7})$$

This proves that Eq. B.1 and Eq. B.5 can be used equivalently and furthermore underlines the correctness of the trajectory calculations in Sec. 5.1.

B.2. Maximum accepted emission angle

Also the result for the maximum accepted emission angle $\alpha_{0,max}$ in Eq. (5.26) can be compared with an alternative phase space conservation approach. The result deduced in this thesis is

$$\tan(\alpha_{max}) = \left(\frac{V_0}{V_{col}} \cdot \left(\frac{d_{img} - f_{img}}{s_{ca} \cdot M} \right)^2 + \frac{V_0}{V_{ext}} - 1 \right)^{-1/2} \quad (\text{B.8})$$

and with $\sin(\arctan(\xi)) = \frac{\xi}{\sqrt{1+\xi^2}}$ I can convert this to

$$\sin(\alpha_{max}) = \left(\frac{V_0}{V_{col}} \cdot \frac{1}{M^2} \cdot \left(\frac{d_{img} - f_{img}}{s_{ca}} \right)^2 + \frac{V_0}{V_{ext}} \right)^{-1/2} \quad (\text{B.9})$$

The alternative calculation uses the *phase space conservation* between the sample and the first image plane

$$\sqrt{U_0} \cdot r_0 \cdot \sin(\alpha_0) = \sqrt{U_{col}} \cdot r_i \cdot \sin(\alpha_i) \quad (\text{B.10})$$

where r_0 is the distance of the image point from the optical axis in the sample plane and r_i the distance from the optical axis in the image plane. Furthermore we know the magnification M as

$$M = \frac{r_i}{r_0} \quad (\text{B.11})$$

and from the geometrical construction we get

$$\tan(\alpha_i) = \frac{s_{ca}}{d_{img} - f_{img}} \quad (\text{B.12})$$

with these formula and $\sin(\arctan(\xi)) = \frac{\xi}{\sqrt{1+\xi^2}}$ we can write Eq. B.10 as

$$\sin(\alpha_{0,max}) = \sqrt{\frac{V_{col}}{V_0}} \cdot M \cdot \sin\left(\arctan\left(\frac{s_{ca}}{d_{img} - f_{img}}\right)\right) \quad (\text{B.13})$$

$$= \left(\frac{V_0}{V_{col}} \cdot \frac{1}{M^2} \cdot \left(\left(\frac{d_{img} - f_{img}}{s_{ca}}\right)^2 + 1\right)\right)^{-1/2}. \quad (\text{B.14})$$

If we use a typical relation for immersion lenses [Lie10]

$$M = \sqrt{\frac{V_{ext}}{V_{col}}} \cdot \frac{d_{img}}{d_{obj}} \quad (\text{B.15})$$

we can finally write

$$\sin(\alpha_{0,max}) = \left(\frac{V_0}{V_{col}} \cdot \frac{1}{M^2} \cdot \left(\frac{d_{img} - f_{img}}{s_{ca}}\right)^2 + \frac{V_0}{V_{ext}} \cdot \left(\frac{d_{obj}}{d_{img}}\right)^2\right)^{-1/2}. \quad (\text{B.16})$$

Now it is easy to see, that Eq. B.9 and Eq. B.16 are nearly the same except of the second summand, which has the factor d_{obj}/d_{img} for the phase space approach. This factor becomes small for big magnifications and my then be neglected.

Although there is a qualitative difference between Eq. B.9 and Eq. B.16, its effects are small. Fig. B.1 shows the difference between the two equations for a wide parameter-space. Especially for the often used high extractor voltages ($U_{ext} \geq 10 \text{ kV}$) it is smaller than 0.1° .

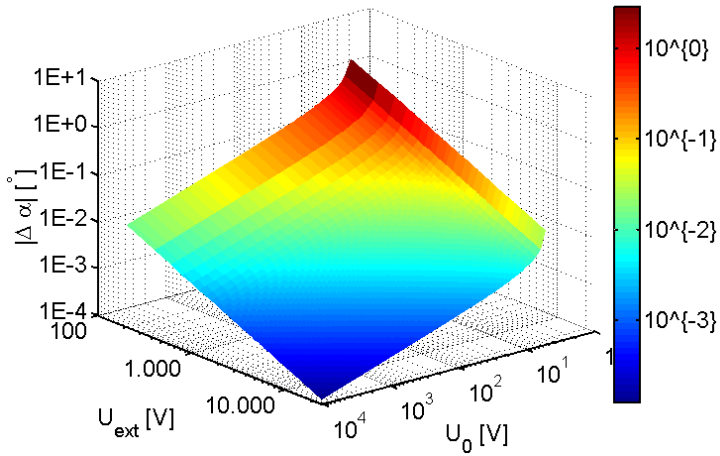


Figure B.1.: Difference between Eq. B.9 and Eq. B.16 for a wide parameter space of the extractor voltage and the kinetic electron energy. The divergence is small over the full parameter space.

Danksagungen

Aufgrund der überwiegenden Benutzung von Synchrotron-Strahlung als Lichtquelle war meine Promotionszeit geprägt von häufigen Reisen. Die in dieser Arbeit verwendeten Probensysteme wurden größtenteils im Forschungszentrum Jülich erstellt und vorcharakterisiert und sind anschließend von mir an verschiedenen europäischen Synchrotrons untersucht worden. An allen diesen Stationen standen mir viele liebe Menschen zur Seite, die mich unterstützt haben und denen ich an dieser Stelle herzlich danken möchte:

Zuerst danke ich meinem Doktorvater **Prof. Dr. Claus Michael Schneider**, der mir die Arbeit mit der spannenden und hoch modernen Methode der energiegefilterten Photoemissions-Mikroskopie mit Synchrotron Strahlung ermöglicht hat. Bei allem instrumentellen und reise-technischen Aufwand, die solche Experimente mit sich bringen, hat er mir stets den Rücken frei gehalten. Seine Tür stand mir stets für wissenschaftliche Diskussionen offen.

Sehr gefreut hat mich, dass **Dr. Nick Barrett** bereit war, die Zweitkorrektur meiner Arbeit zu übernehmen. Ich habe ihn während meiner ersten Synchrotron Strahlzeit am Soleil (Paris) als versierten und engagierten Photoemissions-Experten kennen lernen dürfen und in der Folgezeit während einigen Strahlzeiten in Triest von seiner Erfahrung profitiert.

Ich möchte **Dr. Carsten Wiemann** für die freundliche Aufnahme in die Photoemissions-Mikroskopie Gruppe danken, für die langjährige vertrauensvolle Zusammenarbeit in Jülich, Berlin, Triest und Hamburg, sowie für die stets hilfreichen fachlichen Diskussionen. Für die engagierte experimentelle Unterstützung in Triest gilt mein Dank **Dr. Vitaliy Feyer**, mit dem ich zusammen die Möglichkeiten unseres NanoESCA Setups an der Nanospectroscopy Beamline erkunden durfte. Seine langjährige Erfahrung in Photoemissionsspektroskopie mit Synchrotron Strahlung war stets von großer Hilfe. Des Weiteren danke ich **Dr. Ingo Krug** dafür, dass

er mich schon früh auf seine Strahlzeit nach Paris mitgenommen hat auf der ich von ihm bereits viel über das NanoESCA und das Arbeiten mit Synchrotrons lernen konnte.

An allen Synchrotron-Strahlrohren und Endstationen bin ich sehr warmherzig empfangen und zuvorkommend betreut worden. Ganz besonders möchte ich dafür **Andrea Locatelli** und **Onur Mentés** von der Nanospectroscopy Beamline am Synchrotron Elettra danken. Beim Aufbau unseres Experimentes, der Betreuung des Strahlrohrs und allen kleinen und großen technischen Unterstützungen in Triest waren sie von unschätzbarem Wert. Einige Male durfte ich auch auf ihr Elmitec LEEM/PEEM zurückgreifen, was sich insbesondere in Hinblick auf die STO Messungen als sehr erfolgreich erwies. Für den allgemeinen technischen Support in Triest gilt ein besonderer Dank auch **Matteo Lucian**. Die zweite für mich sehr wichtige Crew besteht aus **Wolfgang Drube**, **Andreij Gloskovskii**, **Sebastian Thiess**, **Frank Okrent** und **Heiko Schulz-Ritter**, denen ich für ihre umfängliche Unterstützung am Synchrotron DESY in Zusammenhang mit sämtlichen Experimenten mit harter Röntgenstrahlung danken möchte.

Für die Unterstützung beim Bau meiner Proben danke ich **Thomas Jansen**, **Dr. Daniel Bürgler**, **Dr. Julius Menning**, **Silke Kleinen-Goebels** und **René Borowski**, sowie **Michael Schnee** und **Fabian Fritz** bei der Hilfe mit dem AFM.

Für die fruchtbare Kooperation bei der Untersuchung resistiv-schaltender Materialien danke ich **Dr. Christian Lenser**, **Dr. Annemarie Köhl** und **Prof. Dr. Regina Dittmann**. Für die vielen anregenden Diskussionen bzgl. Photoemission oder Synchrotronstrahlung möchte ich **Moritz Plötzing**, **Dr. Christian Weier**, **Dr. Stefan Cramm**, **Christoph Schmitz**, **Markus Eschbach**, **Dr. Lukasz Plucinski** und **Dr. Christian Tusche** danken.

Für die technische Unterstützung in Jülich bedanke ich mich bei **Bernd Küpper**, **Konrad Bickmann**, **Jürgen Lauer**, **Heinz Pfeiffer** und das Werkstatt-Team um **Jens Schnitzler**, sowie **Herbert Feilbach** und **Hans Sachsenhausen** von der Konstruktion.

Mein großer Dank für eine konstruktive Zusammenarbeit in Hinblick auf das NanoESCA gilt den Mitarbeitern der **Focus GmbH**, allen voran **Matthias Escher**, **Dr. Nils Weber**, **Dr. Michael Merkel** und **Michael Weber**.

Schließlich möchte ich mich bei allen weiteren Mitarbeitern des **PGL-6** für das äußerst angenehme Institutsklima bedanken. Das schließt in einem großen Maße alle aktuellen und ehemaligen Mitglieder der morgendlichen Kaffeerrunde mit ein, mit denen ich viele spannende und schöne Erfahrungen auch abseits des Institutsalltags teilen durfte. Dieses freundschaftliche Miteinander war auch in anstrengenden Zeiten sehr erbaulich.

Mein letzter und größter Dank gilt meinen **Freunden** und meiner **Familie**, für die ich in den letzten Jahren oft viel zu wenig Zeit hatte und die dennoch immer an mich gedacht und geglaubt haben, für ihre Unterstützung und Zuneigung, allen voran **Marianna Iakhnenko**, **Marion Patt**, **Ulrich Patt** und **Markus Patt**.

Bibliography

- [AE07] Grazyna Antczak and Gert Ehrlich. Jump processes in surface diffusion. *Surface Science Reports*, 62(2):39–61, 2007. 165
- [Ani97] Anisimov, V. I. and Aryasetiawan, F. and Lichtenstein, A. I. First-principles calculations of the electronic structure and spectra of strongly correlated systems: the LDA + U method. *Journal of Physics: Condensed Matter*, 9(4):767, 1997. 17
- [Bau12] Ernst Bauer. A brief history of PEEM. *Journal of Electron Spectroscopy and Related Phenomena*, 185(10):314–322, 2012. 3
- [BCWK12] N. Barrett, E. Conrad, K. Winkler, and B. Krömker. Dark field photoelectron emission microscopy of micron scale few layer graphene. *Review of Scientific Instruments*, 83(8):083706, 2012. 8
- [BLC⁺06] M. M. Beerbom, B. Lägél, A. J. Cascio, B. V. Doran, and R. Schlaf. Direct comparison of photoemission spectroscopy and in situ Kelvin probe work function measurements on indium tin oxide films. *Journal of Electron Spectroscopy and Related Phenomena*, 152(1-2):12–17, 2006. 52
- [Blü10] Stefan Blügel, editor. *Electronic oxides - correlation phenomena, exotic phases and novel functionalities ; lecture notes of the 41st Spring School 2010*, volume 13 of *Schriften des Forschungszentrums Jülich*. Forschungszentrum Zentralbibliothek, Jülich, 2010. 15
- [BN82] O. A. Baschenko and V. I. Nefedov. Relative intensities in X-ray photoelectron spectra. Part IX. Estimates for photoelectron mean free paths taking into account elastic collisions in a solid. *Journal of Electron Spectroscopy and Related Phenomena*, 27(2):109–118, 1982. 19
- [Boh11] Mark Bohr. The evolution of scaling from the homogeneous era to the heterogeneous era. *Electron Devices Meeting (IEDM), 2011 IEEE International*, pages 1.1.1–1.1.6, 2011. 1

- [Brü33] E. Brüche. Elektronenmikroskopische Abbildung mit lichtelektrischen Elektronen. *Zeitschrift für Physik*, 86(7-8):448–450, 1933. 3
- [BWK13] N. Barrett, K. Winkler, B. Kroemker, and E. H. Conrad. Laboratory-based real and reciprocal space imaging of the electronic structure of few layer graphene on SiC(000 $\bar{1}$) using photoelectron emission microscopy. *Ultramicroscopy*, 130:94–100, 2013. 41
- [CCW+76] Chazalviel, J. N., M. Campagna, Wertheim, G. K., Schmidt, P. H., and Y. Yafet. Electronic Structure and 4f-Hole Lifetime in Rare-Earth Borides. *Physical Review Letters*, 37(14):919–922, 1976. 153
- [Chu71] L. Chua. Memristor-The missing circuit element. *IEEE Transactions on Circuit Theory*, 18(5):507–519, 1971. 2
- [Chu11] Leon Chua. Resistance switching memories are memristors. *Applied Physics A*, 102(4):765–783, 2011. 2
- [CMK+99] Daniele Cocco, Marino Marsi, Maya Kiskinova, Kevin C. Prince, Thomas Schmidt, Stefen Heun, and Ernst Bauer. Microfocusing VLS-grating-based beamline for advanced microscopy. *SPIE proc.*, 3767, 1999. 45
- [CVB+12] Sharon H. Chou, Johannes Voss, Igor Bargatin, Aleksandra Vojvodic, Roger T. Howe, and Frank Abild-Pedersen. An orbital-overlap model for minimal work functions of cesiated metal surfaces. *Journal of Physics. Condensed matter : an Institute of Physics journal*, 24(44):445007, 2012. 25, 166
- [Dah00] David A. Dahl. Simion for the personal computer in reflection. *Volume 200: The state of the field as we move into a new millenium*, 200(1–3):3–25, 2000. 59
- [Dav14] M. W. Davidson. Fundamentals of Mercury Arc Lamps. <http://zeiss-campus.magnet.fsu.edu/articles/lightsources/mercuryarc.html>, 2014. 41
- [DDCS07] H. Dery, P. Dalal, Ł. Cywiński, and L. J. Sham. Spin-based logic in semiconductors for reconfigurable large-scale circuits. *Nature*, 447(7144):573–576, 2007. 2

-
- [DDS95] M. S. Dresselhaus, G. Dresselhaus, and R. Saito. Physics of carbon nanotubes. *Carbon*, 33(7):883–891, 1995. 2
- [Dem09] Demtroeder. *Elektrizität und Optik: Mit ... 19 Tabellen, zahlreichen durchgerechneten Beispielen und 145 Übungsaufgaben mit ausführlichen Lösungen*. 5., überarb. und erw. aufl edition, 2009. 82
- [Dem10] Demtroeder. *Kern-, Teilchen- und Astrophysik: Mit 68 Tabellen, zahlreichen durchgerechneten Beispielen und 104 Übungsaufgaben mit ausführlichen Lösungen*. 3., überarb. und erw. aufl edition, 2010. 66
- [DGR⁺74] R. H. Dennard, F. H. Gaensslen, V. L. Rideout, E. Bassous, and A. R. LeBlanc. Design of ion-implanted MOSFET's with very small physical dimensions. *IEEE Journal of Solid-State Circuits*, 9(5):256–268, 1974. 1
- [Dru05] W. Drube. Photoelectron spectroscopy with hard X-rays. *Proceedings of the Workshop on Hard X-ray Photoelectron Spectroscopy HAXPES Proceedings of the Workshop on Hard X-ray Photoelectron Spectroscopy*, 547(1):87–97, 2005. 14
- [Ege07] Ray F. Egerton. *Physical principles of electron microscopy: An introduction to TEM, SEM and AEM*. Springer, New York and NY, 2007. 74, 80
- [EH80] W. Eberhardt and F. J. Himpsel. Dipole selection rules for optical transitions in the fcc and bcc lattices. *Physical Review B*, 21(12):5572–5576, 1980. 16
- [EHC91] D. J. Eaglesham, G. S. Higashi, and M. Cerullo. 370 degree C clean for Si molecular beam epitaxy using a HF dip. *Applied Physics Letters*, 59(6):685, 1991. 146
- [Ein05] A. Einstein. Über einen die Erzeugung und Verwandlung des Lichtes betreffenden heuristischen Gesichtspunkt. *Annal. Phys.*, 1905(322/6):132, 1905. 10
- [EK74] Gerhard Ertl and Jürgen Küppers. *Low energy electrons and surface chemistry*, volume 4 of *Monographs in modern chemistry*. Verl. Chemie, Weinheim, 1974. 25

- [EWM⁺05] M. Escher, N. Weber, M. Merkel, C. Ziethen, P. Bernhard, G. Schonhense, S. Schmidt, F. Forster, F. Reinert, B. Kromker, and D. Funne-
mann. NanoESCA: a novel energy filter for imaging x-ray photoemission
spectroscopy. *J. Phys.: Condens. Matt.*, 17(16):S1329–S1338, 2005. 3,
7, 29, 30, 33, 89
- [EWRB10] M. Escher, K. Winkler, O. Renault, and N. Barrett. Applications of high
lateral and energy resolution imaging XPS with a double hemispheri-
cal analyser based spectromicroscope: Trends in X-ray Photoelectron
Spectroscopy of solids (theory, techniques and applications). *Journal
of Electron Spectroscopy and Related Phenomena*, 178–179(0):303–316,
2010. 3, 35, 39, 40, 75, 81, 89, 90, 96, 101, 149
- [Fad10] C. S. Fadley. X-ray photoelectron spectroscopy: Progress and perspec-
tives. *Trends in X-ray Photoelectron Spectroscopy of solids (theory, tech-
niques and applications)*, 178–179(0):2–32, 2010. 4, 18, 157
- [FM10] Jens Falta and Thomas Möller. *Forschung mit Synchrotronstrahlung:
Eine Einführung in die Grundlagen und Anwendungen*. Studium.
Vieweg + Teubner, Wiesbaden, 1. auff edition, 2010. 44
- [FO74] Enrico Fermi and Jay Orear. *Nuclear physics: A course, given by Enrico
Fermi at the University of Chicago*. Midway reprint. Univ. of Chicago
Press, Chicago [u.a.], rev. ed edition, 1974. 15
- [Foc] Focus GmbH. company - website. <http://www.focus-gmbh.com>. 7
- [Foc12] Focus GmbH. NanoESCA Technical Reference Manual. 2012. 37
- [FSR⁺13] S. Francoual, J. Strempler, D. Reuther, D. K. Shukla, and A. Skaugen.
Double phase-retarder set-up at beamline P09 at PETRA III. *Journal
of Physics: Conference Series*, 425(13):132010, 2013. 46
- [GDN⁺15] Daniel M. Gottlob, Hatice Doğanay, Florian Nickel, Stefan Cramm,
Ingo P. Krug, Slavomír Nemšák, and Claus M. Schneider. Micro-
scopic analysis of the composition driven spin-reorientation transition
in Ni_xPd_{1-x}/Cu(001). *Ultramicroscopy*, 2015. 3
- [GFK81] S. M. Goldberg, C. S. Fadley, and S. Kono. Photoionization cross-
sections for atomic orbitals with random and fixed spatial orientation.

-
- Journal of Electron Spectroscopy and Related Phenomena*, 21(4):285–363, 1981. 13
- [Gos80] Goswami, A. and Lisgarten, N. D. The measurement of the inner potential of diamond. *Journal of Physics C: Solid State Physics*, 13(8):1381, 1980. 138
- [Gos82] Goswami, A. and Lisgarten, N. D. The measurement of inner potentials for copper, silver and gold. *Journal of Physics C: Solid State Physics*, 15(19):4217, 1982. 138
- [Her87] H. Hertz. Ueber einen Einfluss des ultravioletten Lichtes auf die elektrische Entladung. *Annal. Phys.*, 1887(267/8):983, 1887. 10
- [HG12] Alberto Herrera-Gomez. The Peak-Shirley Background: Internal Report. 2012. 172
- [HGWL10] M. G. Helander, M. T. Greiner, Z. B. Wang, and Z. H. Lu. Pitfalls in measuring work function using photoelectron spectroscopy. *Applied Surface Science*, 256(8):2602–2605, 2010. 24
- [Hir75] Hirst, L. L. Mixing-Decay Widths for 4f Ions in Solids. *Physical Review Letters*, 35(20):1394–1396, 1975. 153
- [HMTI⁺88] F. J. Himpsel, McFeely, F. R., A. Taleb-Ibrahimi, Yarmoff, J. A., and G. Hollinger. Microscopic structure of the SiO₂/Si interface. *Physical Review B*, 38(9):6084–6096, 1988. 172, 174, 175
- [HN95] B. Hammer and J. K. Nørskov. Why gold is the noblest of all the metals. *Nature*, 376(6537):238–240, 1995. 153
- [Hor90] K. Horn. Semiconductor interface studies using core and valence level photoemission. *Applied Physics A*, 51(4):289–304, 1990. 11
- [HTWF08] Shaaker Hajati, Sven Tougaard, John Walton, and Neal Fairley. Noise reduction procedures applied to XPS imaging of depth distribution of atoms on the nanoscale. *Surface Science*, 602(18):3064–3070, 2008. 55, 58
- [Hüf03] Stefan Hüfner. *Photoelectron spectroscopy: Principles and applications*. Springer, Berlin [etc.], 2003. 3, 7, 10, 15, 20, 22, 71

- [IAK76] R. E. Imhof, A. Adams, and G. C. King. Energy and time resolution of the 180 degrees hemispherical electrostatic analyser. *Journal of Physics E: Scientific Instruments*, 9(2):138, 1976. 34, 92, 98, 101
- [JE88] A. Jablonski and H. Ebel. Comparison of electron attenuation lengths and escape depths with inelastic mean free paths. *Surface and Interface Analysis*, 11(12):627–632, 1988. 182
- [JEE86] Alexander Jablonski, Maria F. Ebel, and Horst Ebel. Effects of photoelectron elastic scattering on angular distribution of photoemission from solids. *Journal of Electron Spectroscopy and Related Phenomena*, 40(2):125–140, 1986. 182
- [JEE87] A. Jablonski, M. F. Ebel, and H. Ebel. Effect of the analyser acceptance angle on the photoelectron intensity. *Journal of Electron Spectroscopy and Related Phenomena*, 42(3):235–243, 1987. 178
- [J.J93] J.J. Yeh. *Atomic Calculation of Photoionization Cross-Sections and Asymmetry Parameters*. Gordon and Breach Science Publishers, Langhorne and PE (USA), 1993. 13
- [JP99] A. Jablonski and C. J. Powell. Relationships between electron inelastic mean free paths, effective attenuation lengths, and mean escape depths. *Journal of Electron Spectroscopy and Related Phenomena*, 100(1–3):137–160, 1999. 19, 178
- [KBH⁺74] M. Klasson, A. Berndtsson, J. Hedman, R. Nilsson, R. Nyholm, and C. Nordling. Electron escape depth in silicon. *Journal of Electron Spectroscopy and Related Phenomena*, 3(6):427–434, 1974. 175
- [KH06] Charles Kittel and Siegfried Hunklinger. *Einführung in die Festkörperphysik*. Oldenbourg, München [u.a.], 14., überarb. und erw. Aufl. / neu bearb. und aktualisiert von Siegfried Hunklinger edition, 2006. 138
- [KHK⁺06] S. Khan, K. Holldack, T. Kachel, R. Mitzner, and T. Quast. Femtosecond Undulator Radiation from Sliced Electron Bunches. *Physical Review Letters*, 97(7):074801, 2006. 13
- [KIK⁺07] Toyohiko Kinoshita, Eiji Ikenaga, Jungjin Kim, Shigenori Ueda, Masaaki Kobata, James R. Harries, Kenya Shimada, Akihiro Ino, Kenji Tamasaku, Yoshinori Nishino, Tetsuya Ishikawa, Keisuke Kobayashi,

- Wolfgang Drube, and Christof Kunz. How is it possible to obtain buried interface information through very thick films using a hard-X-ray PEEM? *Surface Sci*, 601(20):4754–4757, 2007. 183, 184
- [KKO⁺03] M. Kotsugi, W. Kuch, F. Offi, L. I. Chelaru, and J. Kirschner. Microspectroscopic two-dimensional Fermi surface mapping using a photoelectron emission microscope. *Review of Scientific Instruments*, 74(5):2754–2758, 2003. 3, 8, 21, 22, 138
- [Kna73] A. G. Knapp. Surface potentials and their measurement by the diode method. *Surface Science*, 34(2):289–316, 1973. 25, 27
- [KS67] C. E. Kuyatt and J. Arol Simpson. Electron Monochromator Design. *Review of Scientific Instruments*, 38(1):103–111, 1967. 69, 98, 167
- [LB08] A. Locatelli and E. Bauer. Recent advances in chemical and magnetic imaging of surfaces and interfaces by XPEEM. *Journal of Physics: Condensed Matter*, 20(9):093002, 2008. 4
- [LBC⁺03] A. Locatelli, A. Bianco, D. Cocco, S. Cherif, S. Heun, M. Marsi, M. Pasqualetto, and E. Bauer. High lateral resolution spectroscopic imaging of surfaces: The undulator beamline “nanospectroscopy” at Elettra. *J. Phys. IV France*, 104:99–102, 2003. 46
- [Lie10] Helmut Liebl. *Applied charged particle optics*. Springer, Berlin [u.a.], 2010. 67, 79, 205
- [LKP⁺14] C. Lenser, A. Köhl, M. Patt, C. M. Schneider, R. Waser, and R. Dittmann. Band alignment at memristive metal-oxide interfaces investigated by hard x-ray photoemission spectroscopy. *Physical Review B*, 90(11):115312, 2014. 4
- [LKS⁺15] Christian Lenser, Annemarie Koehl, Ivetta Slipukhina, Hongchu Du, Marten Patt, Vitaliy Feyer, Claus M. Schneider, Marjana Lezaic, Rainer Waser, and Regina Dittmann. Formation and Movement of Cationic Defects During Forming and Resistive Switching in SrTiO₃ Thin Film Devices. *Advanced Functional Materials*, page n/a, 2015. 4, 187
- [LMNB11] Andrea Locatelli, Tevfik Onur Menteş, Miguel Ángel Niño, and Ernst Bauer. Image blur and energy broadening effects in XPEEM. *Ultramicroscopy*, 111(8):1447–1454, 2011. 3, 44, 167

- [Loc] A. Locatelli. Website of the NanoSpectroscopy Beamline at Elettra. <https://www.elettra.trieste.it/elettra-beamlines/nanospectroscopy.html>. 46
- [LPBZ⁺10] F. de La Peña, N. Barrett, L. F. Zagonel, M. Walls, and O. Renault. Full field chemical imaging of buried native sub-oxide layers on doped silicon patterns. *Surface Science*, 604(19–20):1628–1636, 2010. 90, 154, 171, 172
- [LPM⁺14] Christian Lenser, Marten Patt, Stephan Menzel, Annemarie Köhl, Carsten Wiemann, Claus M. Schneider, Rainer Waser, and Regina Dittmann. Insights into Nanoscale Electrochemical Reduction in a Memristive Oxide: the Role of Three-Phase Boundaries. *Advanced Functional Materials*, 24(28):4466–4472, 2014. 4, 187, 189
- [LW79] Joseph Ladislav Wiza. Microchannel plate detectors. *Nuclear Instruments and Methods*, 162(1–3):587–601, 1979. 37, 129
- [Man94] A. N. Mansour. Gold Mg K alpha XPS Spectra from the Physical Electronics Model 5400 Spectrometer. *Surface Science Spectra*, 3(3):197–201, 1994. 152
- [MBME11] J. Minár, J. Braun, S. Mankovsky, and H. Ebert. Calculation of angle-resolved photo emission spectra within the one-step model of photo emission—recent developments. *Journal of Electron Spectroscopy and Related Phenomena*, 184(3–6):91 – 99, 2011. Advances in Vacuum Ultraviolet and X-ray Physics The 37th International Conference on Vacuum Ultraviolet and X-ray Physics (VUVX2010). 11
- [Mic77] Herbert B. Michaelson. The work function of the elements and its periodicity. *Journal of Applied Physics*, 48(11):4729–4733, 1977. 55, 166
- [Mil16] Millikan, R. A. A Direct Photoelectric Determination of Planck's constant. *Physical Review*, 7(3):355–388, 1916. 10
- [ML12] Tefvik Onur Mentemur and Andrea Locatelli. Angle-resolved X-ray photoemission electron microscopy. *Photoelectron microscopy, Time resolved pump-probe PES*, 185(10):323–329, 2012. 3
- [Moo98] G. E. Moore. Cramming More Components Onto Integrated Circuits. *Proceedings of the IEEE*, 86(1):82–85, 1998. 1

- [NGK⁺13] F. Nickel, D. M. Gottlob, I. P. Krug, H. Doganay, S. Cramm, A. M. Kaiser, G. Lin, D. Makarov, O. G. Schmidt, and C. M. Schneider. Time-resolved magnetic imaging in an aberration-corrected, energy-filtered photoemission electron microscope. *Eighth International Workshop on LEEM/PEEM*, 130(0):54–62, 2013. 4, 190
- [NIS12] NIST. NIST X-ray Photoelectron Spectroscopy Database: Version 4.1, 2012. 13, 14
- [NJP⁺09] N M Buckanie, J Göhre, P Zhou, D von der Linde, M Horn-von Hoegen, and F-J Meyer zu Heringdorf. Space charge effects in photoemission electron microscopy using amplified femtosecond laser pulses. *Journal of Physics: Condensed Matter*, 21(31):314003, 2009. 3, 167
- [No106] Nolting. *Quantenmechanik: Methoden und Anwendungen*. Springer-Lehrbuch. 6., überarb. aufl edition, 2006. 16
- [NSS57] Carl Nordling, Evelyn Sokolowski, and Kai Siegbahn. Precision Method for Obtaining Absolute Values of Atomic Binding Energies. *Physical Review*, 105(5):1676–1677, 1957. 10
- [NSS⁺00] S. A. Nepijko, N. N. Sedov, G. Schönhense, M. Escher, Xinxin Bao, and Weixin Huang. Resolution deterioration in emission electron microscopy due to object roughness. *Annalen der Physik*, 9(6):441–451, 2000. 74, 148
- [Pav15] John Pavlus. The Search for a New Machine. *Scientific American*, 312(5):58–63, 2015. 2
- [PCO14] PCO AG. pco.1600 cooled 14 bit CCD camera. <http://www.pco.de/sensitive-cameras/pco1600/>, 2014. 38, 133
- [PCW⁺80] D. T. Pierce, R. J. Celotta, G.-C. Wang, W. N. Unertl, A. Galejs, C. E. Kuyatt, and S. R. Mielczarek. The gas spin polarized electron source. *Review of Scientific Instruments*, 51(4):478–499, 1980. 16
- [PDV10] Yuriy V. Pershin and Massimiliano Di Ventra. Experimental demonstration of associative memory with memristive neural networks. *Neural networks : the official journal of the International Neural Network Society*, 23(7):881–886, 2010. 2

- [Pie49] J. R. Pierce. *Theory and design of electron beams*. Van Nostrand Co, 1949. 167
- [PJ99a] C. J. Powell and A. Jablonski. Evaluation of Calculated and Measured Electron Inelastic Mean Free Paths Near Solid Surfaces. *Journal of Physical and Chemical Reference Data*, 28(1):19–62, 1999. 19
- [PJ99b] C. J. Powell and A. Jablonski. Evaluation of Calculated and Measured Electron Inelastic Mean Free Paths Near Solid Surfaces. *Journal of Physical and Chemical Reference Data*, 28(1):19–62, 1999. 182
- [Pla14] Plano GmbH, 2014. 90
- [Pow84] C. J. Powell. Inelastic mean free paths and attenuation lengths of low-energy electrons in solids. *Scanning electron microscopy*, (1984/IV):1649–1664, 1984. 19
- [PSG06] T. Pfeifer, C. Spielmann, and G. Gerber. Femtosecond x-ray science. *Reports on Progress in Physics*, 69(2):443–505, 2006. 13
- [PWW⁺14] M. Patt, C. Wiemann, N. Weber, M. Escher, A. Gloskovskii, W. Drube, M. Merkel, and C. M. Schneider. Bulk sensitive hard x-ray photoemission electron microscopy. *Review of Scientific Instruments*, 85(11):–, 2014. 3, 5, 37, 157, 159, 169, 179, 181, 183
- [Rep92] M. Repoux. Comparison of background removal methods for XPS. *Surface and Interface Analysis*, 18(7):567–570, 1992. 18
- [RG89] Gertrude F. Rempfer and O. Hayes Griffith. The resolution of photoelectron microscopes with UV, X-ray, and synchrotron excitation sources. *Ultramicroscopy*, 27(3):273–300, 1989. 3, 59, 75, 78, 81, 84
- [RNG80] Gertrude F. Rempfer, Karen K. Nadakavukaren, and O. Hayes Griffith. Topographical effects in emission microscopy. *Ultramicroscopy*, 5(1-3):437–448, 1980. 3
- [Rob] Roberto Pugliese and Giorgio Paolucci. Atomic Calculation of Photoionization Cross-Sections and Asymmetry Parameters. <https://vuoeletra.eu/services/elements/WebElements.html>. 13, 14
- [RSHG91] Gertrude F. Rempfer, Walter P. Skoczylas, and O. Hayes Griffith. Design and performance of a high-resolution photoelectron microscope. *Ultramicroscopy*, 36(1-3):196–221, 1991. 3

-
- [Sai14] Saint-Gobain Crystals. Crystal Scintillation Products, $\text{YAG}(\text{Ce})$, 2014. 38
- [San85] Sanchez, A. and Ochando, M. A. Calculation of the mean inner potential. *Journal of Physics C: Solid State Physics*, 18(1):33, 1985. 21
- [SB13] Petr Schauer and Jan Bok. Study of spatial resolution of $\text{YAG}:\text{Ce}$ cathodoluminescent imaging screens. *Nuclear Instruments and Methods in Physics Research Section B: Beam Interactions with Materials and Atoms*, 308(0):68–73, 2013. 38
- [Sci] Scienta Omicron GmbH. company website. <http://www.scientaomicron.com>. 7
- [SD79] M. P. Seah and W. A. Dench. Quantitative electron spectroscopy of surfaces: A standard data base for electron inelastic mean free paths in solids. *Surface and Interface Analysis*, 1(1):2–11, 1979. 18
- [SH66] K. C. Schmidt and C. F. Hendee. Continuous Channel Electron Multiplier Operated in the Pulse Saturated Mode. *IEEE Transactions on Nuclear Science*, 13(3):100–111, 1966. 131
- [Shi72] Shirley, D. A. High-Resolution X-Ray Photoemission Spectrum of the Valence Bands of Gold. *Physical Review B*, 5(12):4709–4714, 1972. 18
- [SLD⁺12] S. Stille, Ch. Lenser, R. Dittmann, A. Koehl, I. Krug, R. Muenstermann, J. Perlich, C. M. Schneider, U. Klemradt, and R. Waser. Detection of filament formation in forming-free resistive switching SrTiO_3 devices with Ti top electrodes. *Applied Physics Letters*, 100(22):223503, 2012. 2
- [SMT⁺15] G. Schönhense, K. Medjanik, C. Tusche, M. de Loos, van der Geer, B. M. Scholz, F. Hieke, N. Gerken, J. Kirschner, and W. Wurth. Correction of the deterministic part of space-charge interaction in momentum microscopy of charged particles. *Ultramicroscopy*, 2015. 3
- [SS02] Claus M. Schneider and Gerd Schönhense. Investigating surface magnetism by means of photoexcitation electron emission microscopy. *Reports on Progress in Physics*, 65(12):1785, 2002. 3, 74, 84

- [SSSW08] Dmitri B. Strukov, Gregory S. Snider, Duncan R. Stewart, and R. Stanley Williams. The missing memristor found. *Nature*, 453(7191):80–83, 2008. 2
- [SSZ⁺98] H. Spiecker, O. Schmidt, Ch Ziethen, D. Menke, U. Kleineberg, R. C. Ahuja, M. Merkel, U. Heinzmann, and G. Schönhense. Time-of-flight photoelectron emission microscopy TOF-PEEM: first results. *Nuclear Instruments and Methods in Physics Research Section A: Accelerators, Spectrometers, Detectors and Associated Equipment*, 406(3):499–506, 1998. 3, 170
- [Sti15] A. Stiller. Die Moritat von Moores Tat. *c't - magazin fuer computer technik*, 2015(10):72–75, 2015. 1
- [SWP⁺12] C. M. Schneider, C. Wiemann, M. Patt, V. Feyer, L. Plucinski, I. P. Krug, M. Escher, N. Weber, M. Merkel, O. Renault, and N. Barrett. Expanding the view into complex material systems: From micro-ARPES to nanoscale HAXPES: Photoelectron microscopy, Time resolved pump-probe PES. *Journal of Electron Spectroscopy and Related Phenomena*, 185(10):330–339, 2012. 4
- [TEK⁺13] Christian Tusche, Martin Ellguth, Alexander Krasnyuk, Aimo Winkelmann, Dmytro Kutnyakhov, Pavel Lushchyk, Katerina Medjanik, Gerd Schönhense, and Jürgen Kirschner. Quantitative spin polarization analysis in photoelectron emission microscopy with an imaging spin filter. *Eighth International Workshop on LEEM/PEEM*, 130(0):70–76, 2013. 4
- [TEU⁺11] C. Tusche, M. Ellguth, A. A. Unal, C.-T. Chiang, A. Winkelmann, A. Krasnyuk, M. Hahn, G. Schonhense, and J. Kirschner. Spin resolved photoelectron microscopy using a two-dimensional spin-polarizing electron mirror. *Applied Physics Letters*, 99(3):032505–3, 2011. 4, 89
- [THE⁺10] R. M. Tromp, J. B. Hannon, A. W. Ellis, W. Wan, A. Berghaus, and O. Schaff. A new aberration-corrected, energy-filtered LEEM/PEEM instrument. I. Principles and design. *Ultramicroscopy*, 110(7):852–861, 2010. 3, 74
- [THP⁺03] Hungchun Tsai, Emily Hu, Kuoguang Perng, Minkar Chen, Jung-Chun Wu, and Yee-Shyi Chang. Instability of gold oxide Au₂O₃. *Surface Science*, 537(1–3):L447–L450, 2003. 153

-
- [THW⁺13] R. M. Tromp, J. B. Hannon, W. Wan, A. Berghaus, and O. Schaff. A new aberration-corrected, energy-filtered LEEM/PEEM instrument II. Operation and results. *Frontiers of Electron Microscopy in Materials Science*, 127(0):25–39, 2013. 74
- [TMZ⁺15] Maxim Tchapyguine, Mikko-Heikki Mikkilä, Chaofan Zhang, Tomas Andersson, and Olle Björneholm. Gold Oxide Nanoparticles with Variable Gold Oxidation State. *The Journal of Physical Chemistry C*, 119(16):8937–8943, 2015. 153
- [Ton90] B. P. Tonner. Energy-filtered imaging with electrostatic optics for photoelectron microscopy. *Nuclear Instruments and Methods in Physics Research Section A: Accelerators, Spectrometers, Detectors and Associated Equipment*, 291(1–2):60–66, 1990. 34, 98
- [Tou88] Sven Tougaard. Quantitative analysis of the inelastic background in surface electron spectroscopy. *Surface and Interface Analysis*, 11(9):453–472, 1988. 17
- [TPP11] S. Tanuma, C. J. Powell, and D. R. Penn. Calculations of electron inelastic mean free paths. IX. Data for 41 elemental solids over the 50 eV to 30 keV range. *Surface and Interface Analysis*, 43(3):689–713, 2011. 18, 19, 173, 180, 182, 186
- [Ven91] Lee H. Veneklasen. Design of a spectroscopic low-energy electron microscope. *Ultramicroscopy*, 36(1-3):76–90, 1991. 3
- [WB81] M. Wöhlecke and G. Borstel. Symmetry arguments for light-induced electron spin polarization from low-symmetry wave vectors. *Physical Review B*, 24(5):2857–2858, 1981. 16
- [WDSS09] Rainer Waser, Regina Dittmann, Georgi Staikov, and Kristof Szot. Redox-Based Resistive Switching Memories - Nanoionic Mechanisms, Prospects, and Challenges. *Advanced Materials*, 21(25-26):2632–2663, 2009. 2
- [WHS⁺12] M. Wiefner, D. Hauschild, A. Schöll, F. Reinert, V. Feyer, K. Winkler, and B. Krömker. Electronic and geometric structure of the PTCDA/Ag(110) interface probed by angle-resolved photoemission. *Physical Review B*, 86(4):045417, 2012. 8

- [WKCS12] C. Wiemann, A. M. Kaiser, S. Cramm, and C. M. Schneider. Deflection gating for time-resolved x-ray magnetic circular dichroism-photoemission electron microscopy using synchrotron radiation. *Review of Scientific Instruments*, 83(6):063706–5, 2012. 3
- [WPC⁺12] C. Wiemann, M. Patt, S. Cramm, M. Escher, M. Merkel, A. Gloskovskii, S. Thiess, W. Drube, and C. M. Schneider. Probing buried layers by photoelectron spectromicroscopy with hard x-ray excitation. *Applied Physics Letters*, 100(22):223106–3, 2012. 4
- [WPK⁺11] Carsten Wiemann, Marten Patt, Ingo P. Krug, Nils B. Weber, Matthias Escher, Michael Merkel, and Claus M. Schneider. A New Nanospectroscopy Tool with Synchrotron Radiation: NanoESCA@Elettra. *e-Journal of Surface Science and Nanotechnology*, 9:395–399, 2011. 29, 173
- [WTO⁺06] Takanori Wakita, Toshiyuki Taniuchi, Kanta Ono, Motohiro Suzuki, Naomi Kawamura, Masafumi Takagaki, Hayato Miyagawa, FangZhun Guo, Tetsuya Nakamura, Takayuki Muro, Hiroyuki Akinaga, Takayoshi Yokoya, Masaharu Oshima, and Keisuke Kobayashi. Hard X-ray Photoelectron Emission Microscopy as Tool for Studying Buried Layers. *Jpn. J. Appl. Phys.*, 45(3A):1886, 2006. 4
- [YL85] J. J. Yeh and I. Lindau. Atomic subshell photoionization cross sections and asymmetry parameters: $1 < z < 103$. *Atomic Data and Nuclear Data Tables*, 32(1):1–155, 1985. 13
- [YYK⁺06] H. Yasufuku, H. Yoshikawa, M. Kimura, A. M. Vlaicu, M. Kato, M. Kudo, J. Fujikata, and S. Fukushima. On the wide-energy-range tuning of x-ray photoemission electron microscope optics for the observation of the photoelectrons excited by several keV x-rays. *Review of Scientific Instruments*, 77(3):033702, 2006. 4

List of Figures

2.1. Momentum- and Realspace Photoemission microscopy	9
2.2. Three step model of photoemission	12
2.3. Photoionization Cross Sections	14
2.4. Photoexcitation scheme	15
2.5. Photoexcitation transition scheme	17
2.6. Selected IMFP curves	19
2.7. Momentum Conservation in Momentum Microscopy	20
2.8. Brillouin Zone Scheme	22
2.9. Work function schematic	26
2.10. Influence of an accelerating field on the work function	27
3.1. NanoESCA setup at Elettra	29
3.2. Scheme of the NanoESCA	31
3.3. Energy diagram of the analyzer	35
3.4. Detection System	37
3.5. Real space and momentum mode	40
3.6. Comparison UV-Laser and Hg-lamp excitation	42
3.7. NanoESCA beamline at Elettra	46
4.1. work function evaluation scheme	51
4.2. Workfunction-Fit for scripted evaluations	53
5.1. Diagram of an immersion objective lens	60
5.2. Trajectories and geometrical optics	61
5.3. Calculated trajectories	63
5.4. Entrance Angle Conversion	65
5.5. Calculated acceptance angle	69
5.6. Maximal angle entering the energy filter	70
5.7. Photoelectron emission characteristics	72
5.8. Calculated objective lens transmissions	73
5.9. Calculation scheme of the spherical aberration of the accelerating field	76

5.10. Spherical aberration of the objective lens	78
5.11. Chromatic aberration of the accelerating field	79
5.12. Spherical aberration of the objective lens	80
5.13. Chromatic aberration of the objective lens	82
5.14. Diffraction at the contrast aperture	83
5.15. Total aberration of the objective	86
5.16. Ideal contrast aperture diameter	87
6.1. Non-isochromaticity in a PEEM image	91
6.2. Work function mapping	93
6.3. Energy correction of an image spectrum	95
6.4. Sketch of the HSA	97
6.5. Energy Filter Trajectory-Calculation 1	99
6.6. Energy Filter Trajectory Shift at Exit Slit	101
6.7. Energy Filter Trajectory-Calculation 2	102
6.8. Transmission of monochromatic images	104
6.9. Transmission of non-monochromatic images	106
6.10. Magnification of the Projective Lenses	109
6.11. Non-isochromaticity disentanglement	111
6.12. Non-isochromaticity Profile Fit	113
6.13. NISO 3D-fit example	115
6.14. NISO pass energy	116
6.15. NISO Profiles	116
6.16. NISO slit width	117
6.17. NISO trends	119
6.18. Energy shift corrected calculation	121
7.1. Flat field	128
7.2. Dark field	130
7.3. Intensity vs. MCP voltage	131
7.4. Multiplier characteristic of the MCP	132
7.5. SEC vs. standard imaging	134
7.6. SEC quality quantification	135
7.7. Momentum microscopy on Ag (001)	137
7.8. CEC at the Fermi edge and its position in the 3D k-space	139
7.9. Extracted momentum resolved spectra of Ag (001)	140
7.10. Calibration of the k_{\parallel} scale	141

7.11. Determination of the instrumental energy resolution	143
7.12. Limitation of the momentum space with a CA	144
7.13. Influence of the CA on spectra	146
7.14. Microscopy test-samples	146
7.15. Spatial resolution of energy filtered PEEM images	148
7.16. Microspectra from different ROIs	151
7.17. Spectral analysis of the microspectra	151
8.1. Sketch of the HAXPEEM setup	159
8.2. Design of the HAXPEEM test sample	160
8.3. Spectral analysis of HAXPEEM test sample	161
8.4. Work function maps of the HAXPEEM sample	163
8.5. Comparison of work function edges for hard and soft x-ray excitation	164
8.6. Hard x-ray beam profile	165
8.7. Work function profiles	166
8.8. Space charge analysis	169
8.9. Electron time-of-flight differences in the microscope	171
8.10. Compare hard and soft x-rays	173
8.11. Compare Au 3d and Au 4f spectra	177
8.12. HaxPEEM and AFM data	179
8.13. AFM and HAXPEEM profile	181
8.14. Lateral resolution of HAXPEEM	183
9.1. Time resolved measurements on devices	188
9.2. XAS results on STO	189
9.3. HAXPEEM results on STO	190
9.4. Setup for time resolved EF-PEEM	191
9.5. Results with the gating mechanism	192
A.1. Gauss/Step-Function	200
B.1. Comparison between acceptance angle equations	206

List of Tables

6.1. Residual microscope magnifications	113
6.2. Fit parameters of the non-isochromaticity analysis	118
7.1. Fit-results of the line-fits shown in Fig. 7.4.	132
7.2. Fit values from the k-Calibration	142
7.3. Compare CA cut-off energies with calculations	145
7.4. Cross Sections and IMFPs	149
7.5. Fit values for a Au 4f spectrum excited with $h\nu = 180$ eV	153
7.6. Fit values for a Si 2p spectrum excited with $h\nu = 180$ eV	154
8.1. Compare Si spectra for different photon energies	174
8.2. Compare peak intensities for different photon energies	175
8.3. Fit values for Au peaks	177
8.4. Fitted EAL values determined from the HAXPEEM experiment	182
8.5. Results of line fits to the resolution measurements shown in Fig. 8.14	185

List of own publications

Articles

- **A New Nanospectroscopy Tool with Synchrotron Radiation: NanoESCA@ELETTRA** | C. Wiemann, M. Patt, I. P. Krug, N. Weber, M. Escher, M. Merkel, C. M. Schneider | *e-Journal of Surface Science and Nanotechnology* 9 (2011) 395-399
- **Probing buried layers by photoelectron spectromicroscopy with hard x-ray excitation** | C. Wiemann, M. Patt, S. Cramm, M. Escher, M. Merkel, A. Gloskovskii, S. Thiess, W. Drube, C. M. Schneider | *Appl. Phys. Lett.* 100, 223106 (2012)
- **Expanding the view into complex material systems: From micro-ARPES to nanoscale HAXPES** | C.M. Schneider, C. Wiemann, M. Patt, V. Feyer, L. Plucinski, I.P. Krug, M. Escher, N. Weber, M. Merkel, O. Renault, N. Barrett | *J. Electron Spectr. Rel. Phenom.* 185 (2012) 330-339
- **Electric Field-Driven Coherent Spin Reorientation of Optically Generated Electron Spin Packets in InGaAs** | S. Kuhlen, K. Schmalbuch, M. Hagedorn, P. Schlammes, M. Patt, M. Lepsa, G. Güntherodt, B. Beschoten | *Phys. Rev. Lett.* 109, 146603 (2012)
- **Insights into Nanoscale Electrochemical Reduction in a Memristive Oxide: the Role of Three-Phase Boundaries** | C. Lenser, M. Patt, S. Menzel, A. Köhl, C. Wiemann, C. M. Schneider, R. Waser, R. Dittmann | *Adv. Funct. Mater.* 24 (2014) 4466-4472
- **Band alignment at memristive metal-oxide interfaces investigated by hard x-ray photoemission spectroscopy** | C. Lenser, A. Köhl, M. Patt, C. M. Schneider, R. Waser, R. Dittmann | *Phys. Rev. B* 90 (2014) 115312
- **Bulk sensitive hard x-ray photoemission electron microscopy** | M. Patt, C. Wiemann, N. Weber, M. Escher, A. Gloskovskii, W. Drube, M.

Merkel, C. M. Schneider | *Rev. Sci. Instrum.* 85 (2014) 113704

- **Formation and Movement of Cationic Defects During Forming and Resistive Switching in SrTiO₃ Thin Film Devices** | C. Lenser, A. Koehl, I. Slipukhina, H. Du, M. Patt, V. Feyer, C. M. Schneider, M. Lezaic, R. Waser, R. Dittmann | *Adv. Funct. Mater.* (2015), DOI: 10.1002/adfm.201500851

Conference Contributions

- **Time-resolved studies of current-induced spin polarization in strained InGaAs/GaAs structures (talk)** | M. Hagedorn*, S. Kuhlen, M. Patt, P. Schlammes, F. Klein, S. Goebbels, G. Guentherodt, B. Beschoten, M. Lepsa, T. Schaeppers | *DPG condensed matter conference, Regensburg (March 2010)*
- **NanoESCA, a new nanospectroscopy tool with synchrotron radiation (poster)** | M. Patt*, C. Wiemann, I. Krug, M. Escher, N. Weber, M. Merkel and C. M. Schneider | *DPG condensed matter conference, Dresden (March 2011)*
- **Energy-filtered PEEM at ferroelectric nanostructures: Fingerprints of the ferroelectric polarization in the electronic structure of PbZr_{0.52}Ti_{0.48}O₃ (poster)** | I.P. Krug*, M. Patt, C. M. Schneider, N. Barrett, A. Besmehn, A. Morelli, A. R. Chaudhuri, I. Vrejoiu, O. Renault, F. Sirotti | *DPG condensed matter conference, Dresden (March 2011)*
- **Photoemission-Microscopy with Hard X-Rays on SrTiO₃ (poster)** | M. Patt*, C. Wiemann, M. Escher, C. Lenser, A. Gloskovskii, S. Thiess, S. Cramm, W. Drube, M. Merkel, C. M. Schneider | *JARA-FIT conference, Schleiden (Sep 2011)*
- **k-space microscopy with synchrotron radiation on Ag and Bi₂Te₃ (talk)** | M. Patt*, V. Feyer, L. Plucinski, C. Wiemann, and C. M. Schneider | *DPG condensed matter conference, Berlin (Mar 2012)*
- **Electric field-driven coherent spin reorientation and spin rephasing of optically generated electron spin packets in InGaAs (talk)** | S. Kuhlen*, K. Schmalbuch, M. Hagedorn, P. Schlammes, M. Patt, M. Lepsa, G. Guentherodt, B. Beschoten | *DPG condensed matter conference, Berlin (Mar 2012)*

-
- **Studies of oxide-based resistive switches by photoelectron emission microscopy and synchrotron radiation (talk and poster)** | M. Patt*, C. Wiemann, V. Feyer, C. M. Schneider | *SFB 917 workshop, Schleiden (Sep 2012)*
 - **Momentum microscopy with synchrotron radiation on Ag and Bi₂Te₃ (poster)** | M. Patt*, V. Feyer, L. Plucinski, G. Mussler, D. Grützmacher and C. M. Schneider | *LEEM/PEEM 8 conference, Hongkong (Nov 2012)*
 - **Probing Buried Layers with Hard X-Ray Spectromicroscopy (talk)** | C. Wiemann, M. Patt, M. Escher, N.B. Weber, M. Merkel, A. Gloskovskii, W. Drube, C.M. Schneider* | *LEEM/PEEM 8 conference, Hongkong (Nov 2012)*
 - **Signature of n-doping in Gallium Nitride microwires studied by spectroscopic XPEEM (talk)** | J. Morin, O. Renault*, P. Tchouffian, N. Chevalier, V. Feyer, M. Patt, C. M. Schneider | *LEEM/PEEM 8 conference, Hongkong (Nov 2012)*
 - **NanoESCA beamline at Elettra (poster)** | C. M. Schneider, C. Wiemann, M. Patt, V. Feyer* | *LEEM/PEEM 8 conference, Hongkong (Nov 2012)*
 - **HAXPEEM: Bulk-Sensitive Photoemission Electron Microscopy (poster)** | M. Escher*, N.B. Weber, M. Merkel, C. Wiemann, M. Patt, C.M. Schneider | *LEEM/PEEM 8 conference, Hongkong (Nov 2012)*
 - **Mapping of the spin-resolved band structure of fct cobalt films on Cu(100)** | C. Tusche*, M. Ellguth, A. Krasnyuk, C. Wiemann, V. Feyer, M. Patt, C. M. Schneider, J. Kirschner | *DPG condensed matter conference, Regensburg (Mar 2013)*
 - **Towards time-resolved photo-emission-imaging of buried layers of resistive-switching materials (talk and poster)** | M. Patt*, C. Wiemann, V. Feyer, C. M. Schneider | *SFB 917 conference, Kerkrade (Sep 2013)*
 - **Circular Dichroism of Topological Insulators investigated by momentum microscopy and synchrotron radiation (talk)** | M. Patt, V. Feyer, L. Plucinski, G. Mussler, C. Wiemann*, C. M. Schneider | *IVC-19, Paris, (Sep 2013)*
 - **Photoelectron spectromicroscopy using hard x-rays to investigate resistive switching devices (poster)** | C. Wiemann*, M. Patt, A. Gloskovskii,

- S. Thiess, W. Drube, M. Merkel, M. Escher, C. M. Schneider | *IVC-19, Paris, (Sep 2013)*
- **Photoelectron microspectroscopy of resistive switching materials using soft x-ray synchrotron radiation (poster)** | V. Feyer*, C. Wiemann, M. Patt, A. Köhl, R. Dittmann, C.M. Schneider | *IVC-19, Paris, (Sep 2013)*
 - **Efficient mapping of the spin resolved bandstructure of fct cobalt films by spin polarized momentum microscopy (talk)** | C. Tusche*, M. Ellguth, A. Krasnyuk, C. Wiemann, V. Feyer, M. Patt, C. M. Schneider, J. Kirschner | *IVC-19, Paris, (Sep 2013)*
 - **Direct observation of local redox-processes on resistively switching SrTiO₃ with spatially resolved spectroscopy (talk)** | A. Köhl*, C. Lenser, M. Patt, V. Feyer, C.M. Schneider, R. Dittmann, R. Waser | *IVC-19, Paris, (Sep 2013)*
 - **Signature of silicon doping in Gallium Nitride microwires studied by spectroscopic XPEEM (talk)** | J. Morin, O. Renault*, P. Tchouffian, N. Chevalier, V. Feyer, M. Patt, C.M. Schneider | *IVC-19, Paris, (Sep 2013)*
 - **HAXPEEM: Bulk Sensitive Photoemission Electron Microscopy (talk)** | M. Merkel*, M. Escher, N.B. Weber, C. Wiemann, M. Patt and C.M. Schneider | *ALC, Hawaii (Dec 2013)*
 - **Sb₂Te₃ ultrathin films on Si(111): magnetic surface doping and circular dichroism in angle-resolved photoemission spectroscopy (poster)** | M. Eschbach*, M. Patt, L. Plucinski, V. Feyer, G. Mussler, D. Grützmacher, C.M. Schneider | *DPG condensed matter conference, Dresden (Apr 2014)*
 - **Chemical investigation of buried active layers in resistive switching materials by hard x-ray photoemission electron microscopy (poster)** | C. Schmitz*, M. Patt, C. Wiemann, A. von der Heiden, M. Martin, A. Gloskovskii, W. Drube, C. M. Schneider | *DPG condensed matter conference, Dresden (Apr 2014)*
 - **Hard X-ray photoelectron spectromicroscopy to address buried layers in resistive switching devices (poster)** | M. Patt*, C. Wiemann, C. Lenser, N. Weber, M. Escher, A. Gloskovskii, W. Drube, M. Merkel, C.M. Schneider | *LEEM/PEEM 9, Berlin (Mar 2014)*

-
- **Die Entwicklung zeitaufgelöster Photoelektronen-Emissions-Mikroskopie zur Untersuchung resistiv schaltender Bauelemente (poster)** | M. Patt, C. Schmitz, C. Wiemann*, C. Lenser, C. M. Schneider | *SNI, Bonn (Sep 2014)*
 - **Ortsaufgelöste Photoelektronenspektroskopie mit harten Röntgenstrahlen (poster)** | C. Wiemann*, M. Patt, A. Gloskovskii, S. Thiess, W. Drube, C. M. Schneider | *SNI, Bonn (Sep 2014)*

Talks

- **k-space microscopy with synchrotron radiation on Ag and Bi₂Te₃ (talk)** | M. Patt*, V. Feyer, L. Plucinski, C. Wiemann, and C. M. Schneider | *DPG condensed matter conference, Berlin (Mar 2012)*
- **Studies of oxide-based resistive switches by photoelectron emission microscopy and synchrotron radiation** | M. Patt*, C. Wiemann, V. Feyer, C. M. Schneider | *SFB 917 workshop, Schleiden (Sep 2012)*
- **Towards time-resolved photo-emission-imaging of buried layers of resistive-switching materials** | M. Patt*, C. Wiemann, V. Feyer, C. M. Schneider | *SFB 917 conference, Kerkrade (Sep 2013)*

Curriculum Vitae

Personal data

Name Marten Christopher Patt
E-Mail physics@mcpatt.de
Date of birth 30 January 1982 in Waldbröl
Nationality German

Education

08/1988 - 07/1992 Primary school, Rosbach
08/1992 - 06/2001 Bodelschwingh-Gymnasium Herchen
06/2001 Abitur
10/2002 - 07/2009 RWTH Aachen University
07/2009 Diploma in Physics, II. Institute of Physics, RWTH Aachen
Supervisor: Prof. Dr. G. Güntherodt
Time- and spatial resolved detection and manipulation of pulsed-electrical induced, coherent spinpolarisation in III/IV semiconductor-heterostructures

04/2010 - Present Forschungszentrum Jülich / University Duisburg-Essen
Ph.D. in physics, Peter Grünberg Institut, FZ Jülich Supervisor: Prof. Dr. C. M. Schneider
Bulk- and surface sensitive energy-filtered photoemission microscopy using synchrotron radiation for the study of resistive switching memories

Work Experience

07/2001 - 10/2002 Military Service, Mayen
04/2008 - 03/2009 Research Assistant (II. Institute of Physics, RWTH Aachen)
Programming/design of the barrier-free institute-homepage
Teaching Assistant "Physics V" (Prof. G. Güntherodt)

- 10/2009 - 12/2009 Research Assistant (II. Institute of Physics, RWTH Aachen)
Development of a web- and database-based evaluation-system for the "Advanced Physics Internship"
- 03/2010 Research Assistant (II. Institute of Physics, RWTH Aachen)
Programming of a web- and database-based management system for online ordering and transaction of the institute's liquid helium assembly
- 04/2010 - 08/2011 Graduation Stipendium "Research with Synchrotron Radiation in Nano- and Bioscience", TU Dortmund
- 08/2011 - 08/2014 Research Assistant/ Ph.D. student, Forschungszentrum Jülich:
Study of the electronic surface and bulk structure of oxide based Resistive Switching Devices and Topological Insulators with the means of photoelectron spectroscopy and microscopy at several European synchrotron radiation sources (Elettra, Soleil, Bessy II, Petra III) and user support at the FZ Jülich NanoESCA end-station at Elettra (Trieste, Italy).

Erklärung

Hiermit erkläre ich, dass ich die vorliegende Dissertation selbstständig und ohne fremde Hilfe verfasst habe. Außer den angegebenen Quellen habe ich keine weiteren Hilfsmittel benutzt. Alle wörtlich oder inhaltlich entnommenen Textpassagen oder Abbildungen habe ich in jedem Einzelfall kenntlich gemacht. Dieser Dissertation geht weder ein erfolgloser Promotionsversuch voraus, noch wurde sie in einem weiteren Promotionsverfahren eingereicht. Die Ergebnisse dieser Dissertation sind abgesehen von den angegebenen Publikationen unveröffentlicht. Diese Dissertation strebt den Doktorgrad “Dr. rer. nat” an und wurde von Prof. C. M. Schneider betreut.

Jülich, den 31. August 2015

Marten Christopher Patt

List of Abbreviations

AFM	atomic force microscopy
ARPES	angular resolved photoemission spectroscopy
CA	contrast aperture
CED	constant energy distribution
CMP	chemical mechanical polishing
DFT	Density Functional Theory
EAL	effective attenuation length
EDC	energy dispersion curve
ESCA	Electron Spectroscopy for Chemical Analysis
FA	field aperture
FIB	focused ion beam
FWHM	full width at half maximum
HAXPEEM	hard x-ray photoemission electron microscopy
HAXPES	hard x-ray photoemission spectroscopy
HSA	hemispherical sector analyzer
IMFP	inelastic mean free path
MBE	molecular beam epitaxy
PCA	principal component analysis
PEEM	photoemission electron microscopy
PES	photoemission spectroscopy

List of Abbreviations

RF	radio frequency
RIBE	reactive ion beam etching
RMSE	root-mean-square error
SEC	single event counting
SEM	scanning electron microscope
STO	strontium titanate SrTiO_3
XAS	x-ray absorption spectroscopy
XPS	x-ray photoemission spectroscopy

Index

- aberration, 3, 74
 - chromatic-, 78
 - spherical-, 75, 80, 186
- absorption
 - edge, 23
 - spectroscopy, 3, 23
- acceptance angle, 66, 70, 103, 139, 158, 176, 186
- Airy disc, 82
- analogue imaging, 127
- ARPES, *see* photoemission spectroscopy, angular resolved
- atomic force microscopy, 160, 183
- Auger electron, 23

- back focal plane, 39
- band structure, 3, 10
- beam
 - spot, 45, 46, 186
- beamline, 45
 - Nanospectroscopy, 45, 172
 - P09, 46, 172
- bending magnet, 44
- Bessel function, 82
- best fit criterion, 180
- Bethe equation, 18
- binding energy, 7, 11, 36
- Bloch function, 14
- bremsstrahlung, 44

- Brillouin zone, 21, 136, 139
- bulk sensitivity, 18, 157

- camera, 38
- cavity, 44
- CCD sensor, 129
- CCD-sensor, 38
- CED, *see* constant energy distribution
- channeltron, 39, 160, 172
 - spectrum, 92, 176
- checkerboard sample, 90, 108, 158, 171
- chemical contrast, 147
- chemical mechanical polishing, 159
- chemical shift, 153, 174, 186
- Chevron, 37
- circle of least confusion, 77
- Clebsch-Gordon coefficient, 16
- constant energy distribution, 8
- contact potential, 26
- contrast aperture, 32, 39, 52, 67, 68, 81, 103, 144
- core level, 11, 16, 107

- dark field, 129
- de Broglie wavelength, 82
- Density Functional Theory, 11, 14
- detector
 - image-, 37
- diffraction, 81

- dipole approximation, 16
- dynamic range, 38
- EDC, *see* energy dispersion curve
- effective attenuation length, 19, 178
- electron
 - momentum, 20, 21
 - secondary-, 17, 23, 167
- element-selectivity, 177
- Elettra, 43, 127, 190
- emission plane, 139
- energy dispersion curve, 8, 21
- energy filter, 3, 33, 89
 - resolution, 52, 162
- energy shift, 89, 101
 - correction, 94
- energy-filtered photoemission
 - microscopy, 3
- entrance aperture
 - HSA-, 68, 96, 97, 102, 124
- Error function, 199
- ESCA, 11
- EXAFS, 23
- exit slit
 - HSA-, 96
- extractor, 32
- extractor field, 8
- Fermi
 - distribution, 142
 - edge, 43, 136, 142
 - level, 11, 25
 - surface, 22
- Fermi's golden rule, 15
- field aperture, 39, 92
- field of view, 38, 98
- final state, 15
- flat field, 128
 - correction, 91, 129
- focal length, 90
- focus
 - marginal, 76
 - paraxial, 76
- focused ion beam, 147
- Fourier lens, 34, 96
- FOV, *see* field of view
- free electron
 - final-state model, 19
 - parabola, 19
- full width at half maximum, 147
- FWHM, *see* full width at half maximum
- Gauss-profile, 147
- Gauss/Step-Function, 54, 135, 147, 199
- Gaussian function, 199
- Gaussian profile, 107
- generalized extreme value function, 131
- goodness of fit, 162
- hard x-ray photoemission
 - microscopy, 157
 - spectroscopy, 157
- HAXPEEM, 59, 89
- Heaviside step-function, 199
- hemispherical sector analyzer, 33, 96
- high symmetry direction, 139
- HSA, *see* hemispherical sector analyzer
- image potential, 26
- IMFP, *see* inelastic mean free path
- immersion lens, 27, 59, 75

-accelerating field, 27, 158
 inelastic mean free path, 18, 71, 148,
 157, 175, 190
 information depth, 157, 178
 initial state, 15
 inner potential, 138
 isochromaticity, 6, 35, 58, 89, 128,
 161, 168, 172
 kinetic electron energy, 11, 59, 89, 158
 laser, 41
 lattice constant, 138
 law of Helmholtz and Lagrange, 69,
 119
 light
 bandwidth, 45, 162
 polarization, 13, 16, 24, 45
 source, 13, 41, 161
 linear accelerator, 44
 lithography, 159
 Lorentz profile, 107, 201
 magnification
 microscope-, 33, 108
 objective-, 67, 158
 projective, 32
 MCP, *see* microchannel plate
 memristor, 2
 mercury lamp, 41, 91, 161
 micro-spectroscopy, *see* spectroscopy,
 micro-
 microchannel plate, 37
 microscope
 magnification, *see* magnification
 objective, 30
 projection column, 32
 microscopy
 momentum-, 6, 7, 21, 39, 70, 136
 real-space-, 7, 39
 MIM structure, 2
 molecular beam epitaxy, 146, 159
 momentum
 conservation, 20
 microscopy, *see* microscopy
 monochromator, 45
 exit slit, 45
 exit-slit, 152
 grating, 46
 Moore's law, 1
 MOSFET, 1
 multichannel analyzer, 133
 NanoESCA, 10, 26, 30, 59
 NEXAFS, 23
 non-isochromaticity, *see*
 isochromaticity, 200
 objective lens, 59, 108
 -transmission, 158
 one-step model, 11
 optical axis, 112, 114
 overlayer film method, 19, 182
 oxygen vacancy, 2
 pass energy, 33, 115
 PCO.1600, 38
 perovskite oxide, 187
 PES, *see* photoemission spectroscopy
 PETRA-III, 43, 157
 phase space conservation, 204
 photo-current, 17
 photo-excitation, 15
 photo-ionization cross section, 13,
 147, 158, 167, 175, 186
 photoelectric effect, 7, 10

- photoemission
 - background, 17, 177
 - horizon, 52, 141, 145
 - microscopy, 7, 29
 - spectroscopy, 3, 7, 10
 - spectroscopy, angular resolved-, 21
- photon
 - flux, 167, 186
- Planck's constant, 10
- principal component analysis, 56, 89
- projective lens, 108, 110
- radio frequency, *see* synchrotron,
 - radio frequency
- Rayleigh criterion, 82
- reactive ion beam etching, 159
- real-space microscopy, *see* microscopy
- reciprocal lattice vector, 138
- refractive index, 67
- region of interest, 8
- relativistic corrections, 65
- resistive switching, 187
- resistive switching memories, 2
- resolution
 - energy-, 176
 - image-, 89
 - momentum-, 73
 - spatial-, 73, 146, 178, 183
 - total spatial limit, 84
- retardation, 36
- ROI, *see* region of interest
- root-mean-square error, 180
- scanning electron microscope, 147
- Schottky effect, 27
- scintillator, 37
- screening, 153, 175
- secondary electron, *see* electron,
 - secondary-
- secondary electron background, 52
- selection rules, 16
- Shirley background, 18, 172
- Simion, 59
- single crystal, 8, 25, 136
- single event counting, 127, 133, 178, 182, 186
- space-charge, 131, 167
- spectro-microscopy, 6
- spectroscopy
 - absorption-, 23
 - micro-, 39, 41, 92
- spin-filter, 4
- surface diffusion, 165
- surface potential, 25, 50, 138
- surface sensitivity, 18, 148
- synchrotron, 3, 43, 161
 - bunch gap, 44
 - bunch length, 44
 - radio frequency, 44
 - ring current, 45
 - ring energy, 45
- telescopic image, 40
- tetrode lens, 32
- three-step-model, 11
- time resolution, 3, 13, 44, 187
- time-of-flight, 3, 168
- top-up mode, 45
- Tougaard background, 17
- transfer lens, 35, 96
- transmission
 - objective lens-, 70, 167, 185

undulator, 45
 gap, 45
 phase shift, 45
universal curve, 18

vacuum level, 11
Voigt profile, 105, 123, 151, 201
Volta potential, 26

work function, 10, 24, 149
 contrast, 26, 90

analysis, 49, 89, 92, 161
edge, 43, 50, 136, 138, 161
map, 50, 110, 114
shift, 50, 110

XMCD, 24

XMLD, 24

XNLD, 24

YAG-screen, 37

Yamagui method, 138

Band / Volume 109

Study on the electroforming and resistive switching behaviour of nickel oxide thin films for non-volatile memory applications

R. Weng (2015), xxi, 159 pp

ISBN: 978-3-95806-062-3

Band / Volume 110

Microswimmers – From Single Particle Motion to Collective Behaviour

Lecture Notes of the DFG SPP Summer School 2015

edited by G. Gompper, C. Bechinger, S. Herminghaus, R. E. Isele-Holder,

U.B. Kaupp, H. Löwen, H. Stark, R. G. Winkler (2015)

ISBN: 978-3-95806-083-8

Band / Volume 111

Long range order in 3D nanoparticle assemblies

E. Josten (2015), 238 pp

ISBN: 978-3-95806-087-6

Band / Volume 112

Silicon nanowire structures for neuronal cell interfacing

S. Pud (2015), 153 pp

ISBN: 978-3-95806-089-0

Band / Volume 113

Memristive Phenomena -

From Fundamental Physics to Neuromorphic Computing

Lecture Notes of the 47th IFF Spring School 2016

22 February – 04 March 2016, Jülich, Germany

ed. by R. Waser and M. Wuttig (2016), ca 1000 pp

ISBN: 978-3-95806-091-3

Band / Volume 114

Single-Cell Analysis of Microbial Production Strains in Microfluidic Bioreactors

A. M. Grünberger (2015), XIX, 225 pp

ISBN: 978-3-95806-092-0

Band / Volume 115

Magnetic order and spin dynamics in the extended kagome system $\text{CaBaCo}_2\text{Fe}_2\text{O}_7$

J. Reim (2015), viii, 144 pp

ISBN: 978-3-95806-097-5

Band / Volume 116

Structural and electronic investigations on homo- and hetero-organic layers involving CuPc on silver single crystal surfaces

K. M. Schönauer (2015), x, 148 pp

ISBN: 978-3-95806-112-5

Band / Volume 117

First-principles investigation of inelastic magnetic excitations in nanostructures deposited on surfaces

B. J. Schweflinghaus (2016), v, 204 pp

ISBN: 978-3-95806-115-6

Band / Volume 118

Magnetic, structural, and electronic properties of NiFe₂O₄ ultrathin films

M. Hoppe (2016), vii, 118 pp

ISBN: 978-3-95806-122-4

Band / Volume 119

First-principle investigation of displacive response in complex solids

D. A. Klüppelberg (2016), xi, 179 pp

ISBN: 978-3-95806-123-1

Band / Volume 120

Beam Cooling at COSY and HESR - Theory and Simulation - Part 1 Theory

H. Stockhorst, T. Katayama and R. Maier (2016), v, 192 pp

ISBN: 978-3-95806-127-9

Band / Volume 121

Scanning tunneling microscopy of single-molecule magnets and hybrid-molecular magnets: Two approaches to molecular spintronics

V. Heß (2016), x, 127 pp

ISBN: 978-3-95806-128-6

Band / Volume 122

Bulk and surface sensitive energy-filtered photoemission microscopy using synchrotron radiation for the study of resistive switching memories

M. C. Patt (2016), viii, 247 pp

ISBN: 978-3-95806-130-9

Weitere **Schriften des Verlags im Forschungszentrum Jülich** unter

<http://www.zb1.fz-juelich.de/verlagextern1/index.asp>

**Schlüsseltechnologien /
Key Technologies
Band / Volume 122
ISBN 978-3-95806-130-9**

